Elongated Microswimmers: Influence of Hydrodynamics

vorgelegt von
Master of Science

Arne Wolf Zantop

ORCID: 0000-0002-6537-3292

an der Fakultät II – Mathematik und Naturwissenschaften
der Technischen Universität Berlin
zur Erlangung des akademischen Grades

Doktor der Naturwissenschaften
– Dr. rer. nat. –

genehmigte Dissertation

Promotionsausschuss:

Vorsiztender:	Prof. Dr. Dieter Breitschwerdt
Erster Gutachter:	Prof. Dr. Holger Stark
Zweiter Gutachter:	Prof. Dr. Roland Netz

Termin der wissenschaftlichen Aussprache: 14. Dezember 2022

Berlin 2023

Abstract

Our nature is full of microscopic organisms such as algae, which are at the basis of the marine food chain and thus establish entire ecosystems, or bacteria, which are important for our nutrition and health, and also find a broad application in industrial processes. Thus, a broad research field is concerned with the many aspects of the biology, chemistry and physics of microorganisms. Physicists are particularly interested in the swimming motion of organisms such as algae, bacteria, spermatozoa and others. In collective motion, these microswimmers exhibit a diverse behavior such as the formation of swarms, vortices, convection rolls and plumes, and active turbulence. Therby, most microswimmers are elongated, and are otherwise characterized by different swimming mechanisms. Consequently, their dynamics arises from the interplay of different interactions, *i.e.*, direct collisions and long-range flow fields. It is subject of current research to determine the role of the different interactions for the fascinating collective dynamics.

In this context, we consider the squirmer rod, a model microswimmer that consists of several spherical squirmers, in order to create an elongated body shape. To realize the swimming mechanisms of bacteria and algae, *i.e.*, pushers and pullers, we concentrate the surface slip-velocity field on the rear end or front side of the rod. This generates the force dipole, which these swimming mechanisms exert on the fluid. Using the simulation method of multi-particle collision dynamics (MPCD), we analyze the flow fields of the squirmer rods both in the bulk fluid as well as in the Hele-Shaw geometry, *i.e.*, in narrow confinement between two parallel plates. Using hydrodynamic multipole expansions, we categorize the different multipole contributions created by neutral, and pusher squirmer rods in the bulk fluid as well as in the Hele-Shaw geometry. Thereby, we show how the confinement changes the radial decay of the flow fields of the force or source multipoles, and hence the characteristic flow fields compared to the bulk fluid.

Further, we present a detailed study of the collective dynamics of neutral squirmer rods moving in the midplane of the Hele-Shaw geometry. From small to a large aspect ratio and density, we observe a disordered state, dynamic swarms, a single swarm, and a jammed cluster state and characterize them accordingly. We also investigate a wide range of aspect ratios and densities for pushers and pullers and provide corresponding state diagrams. The flow field of pushers destabilizes ordered structures and favors the disordered state at small densities and aspect ratios. As soon as geometric interactions become relevant for longer squirmer rods, we observe a turbulent state, as well as a dynamic cluster, while a single swarm and jammed clusters reappear at large aspect ratios. The power spectrum of the turbulent state shows two distinct energy cascades at small and large wave numbers, which follow power laws with non-universal exponents. Pullers show a strong tendency to form swarms so that no disordered state occurs at the investigated densities. For larger aspect ratios, the single swarm and jammed cluster are observed again.

Another part of this work deals in more detail with the multi-particle collision dynamics (MPCD) method, which is widely used in soft matter physics to simulate fluid flows at micrometer scale. In general, in this model the fluid exhibits the equation of state of an ideal gas, making it highly compressible. This is in contrast to real fluids, which are incompressible for velocities well below the speed of sound. Therefore, we propose a modified collision rule that leads to a MPCD algorithm with a non-ideal equation of state and a significantly reduced compressibility. At the same time, our algorithm requires less computational resources compared to conventional MPCD algorithms. To further establish the algorithm, we provide analytic expressions for the equation of state and shear viscosity, which show a good agreement with simulations of the pressure in a fluid at rest, the shear viscosity in linear shear flow, and the velocity field of a Poiseuille flow. Using two exemplary squirmer rod systems, we further compare the results of the dynamics under the extended MPCD method to those with the established MPCD version with Andersen thermostat. Thereby, we investigate the dynamic swarm state and single swarm state, which create large pressure gradients due to the sum of the many individual squirmer-rod flow fields. For the single swarm state the extended MPCD fluid shows more homogeneous fluid density, and we make the interesting observation that dynamic swarms are more pronounced and exhibit a higher polar order for the extended MPCD method.

Zusammenfassung

Unsere Natur ist voll von mikroskopisch kleinen Organismen wie Algen, die an der Basis der marinen Nahrungskette stehen und damit ganze Ökosysteme begründen, oder Bakterien, die für unsere Ernährung und Gesundheit wichtig sind und auch in industriellen Prozessen eine breite Anwendung finden. Daher befasst sich ein breites Forschungsfeld mit den vielfältigen Aspekten der Biologie, Chemie und Physik von Mikroorganismen. Physiker:innen interessieren sich dabei besonders für die Schwimmbewegungen von Organismen wie Algen, Bakterien, Spermatozoen und Anderen. In kollektiver Bewegung zeigen diese Mikroschwimmer ein vielfältiges Verhalten, wie die Bildung von Schwärmen, Wirbeln, Konvektionsrollen und Plumes sowie aktive Turbulenz. Dabei sind die meisten Mikroschwimmer länglich, und zeichnen sich sonst durch verschiedene Schwimmmechanismen aus. Ihre Dynamik entsteht folglich durch das Zusammenspiel der verschiedenen Wechselwirkungen also durch direkte Zusammenstöße und weitreichenden Flussfelder. Die Rolle der verschiedenen Wechselwirkungen für die faszinierende kollektive Dynamik zu bestimmen, ist Gegenstand aktueller Forschung.

In diesem Kontext betrachten wir den Squirmer-Rod, ein Mikroschwimmermodell, das wir aus mehreren kugelförmigen Squirmern zusammensetzen, um eine längliche Körperform zu erzeugen. Um die Schwimmmechanismen von Bakterien und Algen zu realisieren, d.h. Pusher und Puller, konzentrieren wir das Oberflächengeschwindigkeitsfeld auf die Rückseite oder die Vorderseite des Rods und können so den Kraft-Dipol dieser Schwimmmechanismen generieren. Mit Hilfe der Simulationsmethode der Vielteilchenstoßdynamik (MPCD) analysieren wir die Strömungsfelder dieser Squirmer-Rods sowohl in der freien Flüssigkeit, sowie in der Hele-Shaw-Geometrie, d.h. eingeschlossen zwischen zwei dichten parallelen Platten. Mittels der hydrodynamischen Multipolentwicklung kategorisieren wir die unterschiedlichen Anteile der Flussfelder von neutralen und Pusher Squirmer-Rods in der freien Flüssigkeit, sowie eingeschlossen zwischen zwei Platten. Dabei zeigen wir wie der Einschluss in der Hele-Shaw-Geometrie die radiale Reichweite der Flussfelder der Kraft- oder Quellmultipole, und somit der charakteristischen Flussfelder, im Vergleich zur freien Flüssigkeit verändert.

Weiter präsentieren wir eine ausführliche Studie der kollektiven Dynamik neutraler Squirmer-Rods, die sich in der Mittelebene einer Hele-Shaw-Geometrie bewegen. Von einem kleinen bis zu einem großen Längenverhältnis und einer großen Dichte beobachten wir einen ungeordneten Zustand, dynamische Schwärme, einen einzelnen Schwarm, sowie ein blockiertes Cluster und charakterisieren diese entsprechend.

Auch für Pusher und Puller untersuchen wir eine breite Spanne von Längenverhältnissen und Dichten und liefern entsprechende Zustandsdiagramme. Das Strömungsfeld von Pushern destabilisiert dabei geordnete Strukturen und begünstigt den ungeordneten Zustand bei kleinen Dichten und Längenverhältnissen. Sobald

geometrische Wechselwirkungen bei längeren Squirmer-Rods relevant werden, beobachten wir einen turbulenten Zustand, sowie ein dynamisches Cluster, während bei großen Längenverhältnissen wieder ein einzelner Schwarm und blockierte Cluster auftreten. Die spektrale Leistungsdichte des turbulenten Zustands zeigt dabei zwei unterschiedliche Energiekaskaden bei kleinen und großen Wellenzahlen die Potenzgesetzen mit nicht-universellen Exponenten folgen. Puller hingegen zeigen eine starke Tendenz zur Bildung von dynamischen Schwärmen, sodass bei den dabei untersuchten Dichten gar keine ungeordneten Zustände auftreten. Bei größerem Längenverhältnis tritt wieder ein einzelner Schwarm oder ein blockiertes Cluster auf.

Ein weiterer Teil dieser Arbeit befasst sich eingehender mit der Methode der Vielteilchenstoßdynamik (MPCD), welche in der Physik der weichen Materie häufig verwendet wird, um Hydrodynamik im Mikrometerbereich zu simulieren. In der Regel weist in diesem Modell die Flüssigkeit die Zustandsgleichung eines idealen Gases auf, wodurch sie stark kompressibel ist. Dies steht jedoch im Widerspruch zu realen Flüssigkeiten, welche für Geschwindigkeiten weit unterhalb der Schallgeschwindigkeit inkompressibel sind. Wir schlagen daher eine modifizierte Kollisionsregel vor, die zu einem MPCD-Algorithmus mit einer nicht idealen Zustandsgleichung und einer deutlich reduzierten Kompressibilität führt. Gleichzeitig benötigt unser Algorithmus im Vergleich zu herkömmlichen MPCD-Algorithmen weniger Rechenressourcen. Um dem Algorithmus ein theoretisches Fundament zu geben, liefern wir analytische Ausdrücke für die Zustandsgleichung und die Scherviskosität, die eine gute Übereinstimmung mit Simulationen des Drucks in einem ruhenden Fluid, der Scherviskosität bei linearer Scherströmung und dem Geschwindigkeitsfeld einer Poiseuille-Strömung zeigen. Anhand zweier exemplarischer Squirmer-Rod-Systeme vergleichen wir außerdem die Ergebnisse der Dynamik der Squirmer-Rods unter der erweiterten MPCD-Methode mit denen der etablierten MPCD-Version mit Andersen-Thermostat. Dabei betrachten wir die Zustände der dynamischen Schwärme und des einzelnen Schwarms, die durch die Summe der vielen Flussfelder einzelner Squirmer-Rods große Druckgradienten erzeugen. Für den Zustand des einzelnen Schwarms zeigt die erweiterte MPCD-Methode eine homogenere Fluiddichte, und wir machen die interessante Beobachtung, dass die dynamischen Schwärme bei der erweiterten MPCD-Methode stärker ausgeprägt sind und eine höhere polare Ordnung aufweisen für die erweiterte MPCD-Methode.

Contents

CHAPTER 1

Introduction

Despite often unnoticed in our everyday life, our worlds flora and fauna consist of microscopic organisms to a major fraction. Their omnipresence becomes especially obvious when regarding the plant biomass that performs photosynthesis in the carbon cycle. In fact, microscopic swimming algae amount to about 50% of the total biomass involved in the carbon cycle, as estimated by satellite measuring of chlorophyll concentration [1–3].

Bacteria exist right next to us and even in our bodies. For example, the normal strains of the well-known bacterium *Escherichia coli* are a part of our gut microbiota [4], where it plays an important role for nutrition, our health, our immune system [5–8] and even performs tasks such as the production of vitamins [9].

Also in industrial processes, microorganisms find a broad application. In biotechnological and medical industry, straits of the *E. coli* and *Bacillus subtilis* bacteria are used for the synthesis of different biochemicals. Examples are the production of bio fuels [10–12], enzymes for the food and other branches of industry [13–16], ecological plant protectives [17, 18], pharmaceuticals [19, 20] or supplemental vitamins [21]. Another important application is found in the process of waste water recycling [22, 23]. As this collection implies, a broad research field is concerned with the biology, chemistry and physics of microorganisms and the many aspects of their behavior is subject of current research.

For physicists, these self-propelled organisms – algae, bacteria, spermatozoa and others – are particularly interesting because they swim in aqueous solutions. Rather than only passively diffusing around, they perform an active swimming motion to explore their environment [24, 25]. For this reason, physicists speak of microswimmers. The microswimmers' active motion introduces a whole variety of new fascinating phenomena that go beyond the physics of passive particles [26, 27]. We illustrate this with a few examples from the dynamics of microswimmers.

In order to steer or navigate, microswimmers have developed various strategies like the run-and-tumble motion pattern [28, 29]. Through the modulation of the time

between tumbling events in response to chemical concentrations microswimmers are able to approach nutrients [30–34]. For sperm cells, steering in response to the rheology of the fluid [35] and boundary-following navigation [36] is observed.

In collective motion, microswimmers exhibit a particularly interesting and diverse dynamic behavior that arises form their complex interactions [37, 38]. Examples are the formation of swarms [39–42] or vortices [43–46], convection rolls and plumes [47], fluid pumps [48, 49], active nematic patterns [50–52], and active turbulence [53–57].

Thereby, the phenomenon of active turbulence is currently receiving special attention, because it forms an interesting counterpart to the classical turbulence in passive fluids. While turbulence in passive fluids is caused by external driving, active turbulence occurs due to the motion of the self-propelled particles. In both cases, the supplied energy is transported and dissipated over different length scales. Thereby, active turbulence exhibits a specific length scale, which appears as the characteristic size of vortices and patterns, whereas classical turbulence is scale invariant [58–60]. Furthermore, the power spectrum of the velocity fluctuation is no longer universal but depends on the specific type of active particles and parameters [60–62]. Systems, which exhibit active turbulence, include bacteria [53], bio-filaments within the cytoplasm [50, 56] and cells in growing tissue [63, 64].

On the one hand, microswimmers interact through steric collisions, which typically cause an alignment due to their mostly elongated body shapes [24]. On the other hand, swimming microorganisms interact via long-ranged flow fields created by their swimming motion [65]. This second type of interaction depends fundamentally on the biological propulsion strategy of the species under consideration. While bacteria propel with flagella that extent from the back of the cell body, also other propulsion strategies exist [65, 66]. For example, algae like *Chlamydomonas reinhardtii* propel with two short flagella that extent from the front of their body and perform a breast stroke to swim forward [67, 68]. Other organisms like *Paramecium* are covered entirely with hair-like appendages called cilia, which perform a synchronized wave-like motion to propel [69, 70]. On the microscopic scale, where hydrodynamic flows are dominated by viscous dissipation, these mechanisms generate entirely different long-ranged flow fields, which results in the impressive variety of observed phenomena [71–76]. Besides experiments with biological entities like bacteria, synthetic microswimmers like the famous Janus particles [25, 77] or active emulsion droplets [78, 79] are employed. However, the physics of active matter is not limited to microswimmers, but is also found with slightly different mechanisms or interactions in herds of sheep, flocks of birds, school of fish or human crowds.

On the theoretical side, a range of different particle-based models are employed. Examples range from the famous Vicsek model that employs coarse-grained interactions [80–82], to Langevin dynamics simulation with more realistic steric interactions [83–88] and implicit hydrodynamic interactions [89, 90]. Models which explicitly simulate the flow field use the method of multi-particle collision dynamics [41, 47,

73, 74, 76, 91–97] or the lattice Boltzmann approach [98–101].

A suspension of microswimmers can also be considered in the continuum limit, where they become the constituents of an active fluid [102, 103]. Continuum models for polar active particles, which combine elements of the Toner-Tu [104] and Swift-Hohenberg [105] equations, are able to reproduces active turbulence [58, 106] or clustering [107]. In general, continuum models are distinguish between polar or nematic symmetry, and dry or wet systems. For example, continuum models for wet active nematic fluids include equations of motion for the order-parameter field and extend the constitutive relation of stress tensor by an active contribution [108].

Nevertheless, it is still subject of current research to precisely determine the influences of both steric and hydrodynamic interactions of the constituting particles on the swarm formation, active turbulence, or other phenomena [75, 109–113]. In this context, we introduced the elongated squirmer rod as a model for elongated microswimmers in their fluid environment. The squirmer rod thereby extend the well known squirmer model swimmer [69, 74, 114] for spherical microswimmers such as synthetic Janus particles [115–117] or biological organisms such as *Volvox* [118]. Commonly, squirmers propel themselves by imposing an axisymmetric surface-velocity field on the surrounding fluid [74, 119, 120], which models the propulsion through the beating motion of cilia in biological systems. The spherical squirmer has been employed in various hydrodynamic studies of the collective behavior of microswimmers [73, 74, 92, 94, 100, 121–124]. To model the hydrodynamic flow of the solvent, we use the method of multi-particle collision dynamics (MPCD) [125]. In general, MPCD is well suited for numerical simulations of highly viscous hydrodynamic flows in the context of microscopic solute particles. As stochastic solver, it includes thermal fluctuations [126, 127] and also complex geometric boundaries can be implemented precisely with this method [128–131]. Furthermore, the MPCD algorithms are well suited for parallel computing on graphic cards, such that large systems can be simulated efficiently already on desktop computers [132, 133]. Besides the application to model solvent dynamics in the context of microswimmers, MPCD algorithms have been used to study colloidal suspensions [134–138], polymers [139–141], blood cells [142], the African trypanosome as the causative agent of the sleeping sickness [143], or fish schools [144]. The MPCD method itself has been extended to multi component fluids [145], liquid crystals [146–148], or fluids with chemical reactions [149].

Scientific questions

The large variety of different microswimmers described so far is mainly characterized by different body shapes and the flow fields generated by specific locomotion mechanisms. Despite the multitude of microswimmers now known to researchers, it remains an open question to identify the respective influences of mutual interaction by hydrodynamic flow fields and steric collisions on collective behavior [109, 110,

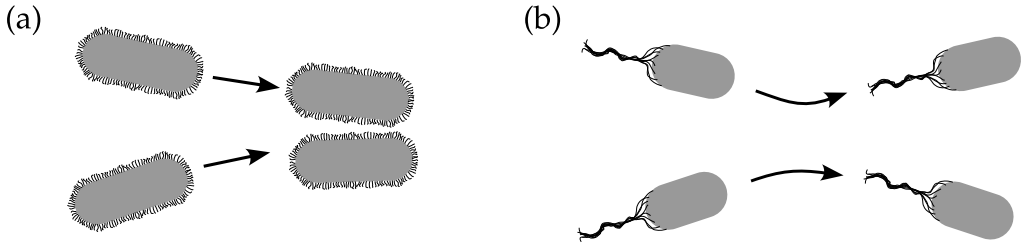

Figure 1.1: Different interactions between colliding microswimmers. (a) Dominated by steric interaction, the collision leads to an alignment of the particles. (b) Hydrodynamic interactions can cause a torque on both particles, which leads to a deflection [65].

112].

With the introduction of the elongated squirmer rod, we therefore first want to explore the direct relationship between the flow field and the cell body shape. We also investigate the influence of narrow confining walls in a Hele-Shaw geometry on the hydrodynamic flow fields of the squirmer rods. This geometry enables us to better understand the physics in experimental systems such as Petri dishes or microscope slides. Furthermore, we also want to use our model to investigate the respective influences of the hydrodynamic and steric interactions on the collective dynamics of many microswimmers.

As depicted in Fig. 1.1(a), purely steric interactions mainly lead to an alignment of elongated microswimmers such that they preferentially form swarming clusters [150]. In contrast, hydrodynamic interactions can lead to an aligning or anti-aligning torque depending on the type of swimmer and relative position, as shown for pushers in Fig. 1.1(b) [65, 94].

Outline

This thesis is written in cumulative form, and organized as follows. Chapter 2 introduces the theoretical background of the physics of swimming microorganisms. To begin with, the hydrodynamic transport equations that satisfy the continuity equations for mass, momentum and energy, are discussed. After motivating Newtonian fluids, the limit of highly viscous Stokes flow is discussed. On the basis of hydrodynamic multipoles, the swimming strategies of different microorganisms are reviewed and the interactions due to their characteristic flow fields are discussed. Lastly, the squirmer-rod model for elongated microswimmers is introduced.

Chapter 3 introduces the multi-particle collision dynamics (MPCD) method, a stochastic solver for hydrodynamic flows. Here, different variants of the original algorithm are compared. Subsequently, the coupling to solute particles and integration of their equation of motion are discussed. We end with some notes on the

efficient implementation of MPCD on modern computer graphic cards.

Since this thesis is written in cumulative form, the results of the research will be presented in the form of their publication in scientific journals. The relevant four articles are introduced and set into context in chapter 4. The first article in Sec. 4.2 introduces the squirmer-rod model and explores the resulting flow field for different aspect ratios in the bulk fluid and in confinement between two parallel plain walls. In Sec. 4.3 we introduce an extended variant of the MPCD method with a non-ideal equation of state for the pressure, and we present the application to simulations of squirmer rods in Sec. 4.4. Thereby, we present an in-depth study of the collective dynamics of neutral squirmer rods for different aspect ratios and area fractions. In the last article in Sec. 4.5 we then investigate the collective dynamics of pusher and puller-type squirmer rods. Chapter 5 draws conclusions from the combination of the articles and gives responses to the scientific questions that were posed above.

CHAPTER 2

Physics of swimming microorganisms

As we saw at the beginning of chapter 1, the large variety of motile microscopic lifeforms predominantly lives in aquatic habitats in the oceans, lakes or other bodies of water. Consequently, we approach the subject of active microswimmers starting from the physics of fluids in motion. This will lead us from the more general hydrodynamic transport equations to the Newtonian fluids, which are described by a linear relation of the fluid stress and the strain rate. The dynamics of microswimmers is further characterized by the limiting case of highly viscous flow. In the context of this so-called Stokes flow, we introduce the theoretical framework to understand the hydrodynamic interaction of microswimmers. As we will see in the following sections, the fluid environment introduces fascinating hydrodynamic interactions between organisms. Together with the active motion of the particles, this leads to a particularly rich collective behavior.

2.1 Hydrodynamic flows

The physical properties of the matter that surrounds us — gases, liquids and solids — can be described at different levels of detail. In our everyday life matter appears as continuum because the complex microscopic state and dynamics smear out on the macroscopic scale of the physical processes relevant for us. From our macroscopic perspective, the number of the constituting particles is so large that even for a small parcel of matter the microscopic dynamics can be described with the framework of statistical mechanics. Thus, we may work with the dynamics of an ensemble average because the microscopic detail vanishes in the thermodynamic limit. For the relevant physical phenomena, this suggests a classical continuum description of matter, for the dynamics of the fields of macroscopic variables like mass, momentum and energy. In the case of gases and liquids, the constituting particles are not bound to a fixed

configuration such that their continuum description deals with deformation, flows and transport. Due to this similarity, gases and liquids are typically combined under the terminology of fluids.

Hydrodynamic flows are most commonly described by the so-called Navier-Stokes equations, which apply to conventional length scales much larger than the inter-particle distance. In addition to the simpler Euler equations, they take into account internal friction in the fluid. In their mathematical form, they are a continuum formulation of the basic physical principle of the conservation of momentum with the addition of constitutive relations for the viscous stress tensor for the class of Newtonian fluids. These equations governing the motion of fluids can be derived starting from different basic premises. Most fundamentally, starting from the physics of collisions between the constituting particles in the kinetic theory of gases, the famous Chapman-Enskog approach can be used to derive hydrodynamic equations of motion to different order in the Knudsen number from the Boltzmann equation [151, 152]. The Knudsen number is thereby defined as the ratio of the mean free path for the fluid particles to a characteristic physical length scale. Here, we follow a more direct approach that starts with continuity equations as first principles and directly leads to the hydrodynamic transport equations following Ref. [153]. In Section 2.2, we then introduce the constitutive relations for the stress tensor and heat flux in a Newtonian fluid, which then leads us to the Navier-Stokes equations.

2.1.1 Hydrodynamic transport equations

In the following, we derive the hydrodynamic transport equations following the seminal work of Irving and Kirkwood [153]. In this approach, we derive continuity equations for the fluid density, momentum and energy. For the momentum and energy, pressure and viscous forces will become relevant.

We begin by considering a small stationary volume V inside the fluid of mass density $\rho(\mathbf{r}, t)$. The local velocity of the fluid is described by the vector field $\mathbf{u}(\mathbf{r}, t)$. The rate of change in the total mass of the volume is due to transport of fluid mass by the velocity field $\mathbf{u}(\mathbf{r}, t)$ through the surface ∂V of the volume V

$$\partial_t m(\mathbf{r}, t) \;=\; \partial_t \int_V \rho(\mathbf{r}, t) \mathrm{d}^3 r \;=\; -\int_{\partial V} \rho(\mathbf{r}, t) \mathbf{u}(\mathbf{r}, t) \cdot \mathrm{d}\mathbf{A}. \tag{2.1}$$

Here, $\mathrm{d}\mathbf{A}$ is an infinitesimal oriented surface element normal to ∂V. For simplicity and clarity, we will omit writing the dependence of the fields ρ and $\mathbf{u}$ on the position $\mathbf{r}$ and time t in the following. According to Gauß' theorem, the surface integral can be rewritten as a volume integral

$$\int_{\partial V} \rho \mathbf{u} \cdot d\mathbf{A} \;=\; \int_V \boldsymbol{\nabla} \cdot (\rho \mathbf{u}) \mathrm{d}^3 r. \tag{2.2}$$

Since the choice of the integration volume V is arbitrary, the equality also applies to the integrand, so that with Eq. (2.1) we obtain the continuity equation for the mass density

$$\partial_t \rho \;=\; -\boldsymbol{\nabla} \cdot (\rho \mathbf{u}). \tag{2.3}$$

If we consider an incompressible fluid ($\boldsymbol{\nabla} \cdot \mathbf{u} = 0$), we can use the so-called *substantial* or *co-moving* derivative $\frac{\mathrm{D}(\circ)}{\mathrm{D}t} = (\partial_t + \mathbf{u} \cdot \boldsymbol{\nabla})(\circ)$ to rewrite Eq. (2.3) as $\frac{\mathrm{D}\rho}{\mathrm{D}t} = 0$. Put in words, this means that as we move with a fluid parcel, the density of the incompressible fluid remains constant.

To obtain the continuity equation for the momentum transport, we consider the rate of change in total momentum

$$\partial_t \int_V (\rho \mathbf{v}) \mathrm{d}^3 r \tag{2.4}$$

in the fluid volume V. As for mass transport, we consider the transport of the three components of momentum with the velocity field through the surface of the stationary volume V. In vector notation this momentum flux through the surface is

$$\int_{\partial V} (\rho \mathbf{u} \otimes \mathbf{u}) \mathrm{d}\mathbf{A} \;=\; \int_V \boldsymbol{\nabla} (\rho \mathbf{u} \otimes \mathbf{u}) \mathrm{d}^3 r \tag{2.5}$$

However, in contrast to the conserved mass regarded before, the momentum of the fluid is also changed by forces that act on the fluid inside V and at the surface ∂V. These are (i) external forces such as gravity, that act in the whole volume, and (ii) pressure and frictional surface forces arising from the interaction with the neighboring fluid. The total external force (i) follows from the integration over the whole volume of the force densities $\mathbf{f}_{\text{ext}}$

$$\int_V \mathbf{f}_{\text{ext}}(\mathbf{r}, t) \mathrm{d}^3 r. \tag{2.6}$$

The surface forces (ii) are described by the symmetric stress tensor $\boldsymbol{\sigma}(\mathbf{r}, t)$ that assigns every infinitesimal surface element $\mathrm{d}\mathbf{A}$ an infinitesimal surface force $\mathrm{d}\mathbf{f}_A = \boldsymbol{\sigma}(\mathbf{r}, t)\mathrm{d}\mathbf{A}$. The specific form of the stress tensor $\boldsymbol{\sigma}$ depends on the physical properties of the fluid under consideration, and will be addressed later. To obtain the total surface force $\mathbf{F}_A(t)$, the infinitesimal surface force is integrated over the whole surface ∂V

$$\mathbf{F}_A(t) \;=\; \int_{\partial V} \mathrm{d}\mathbf{f}_A \;=\; \int_{\partial V} \boldsymbol{\sigma}(\mathbf{r}, t) \mathrm{d}\mathbf{A} \;=\; \int_V \boldsymbol{\nabla} \boldsymbol{\sigma}(\mathbf{r}, t) \mathrm{d}^3 r, \tag{2.7}$$

where we have used Gauß' theorem again. In total, the change of momentum in Eq. (2.4) is equal to the sum of Eq. (2.5), (2.6) and (2.7). Again using the arbitrary choice of the integration volume V, we obtain Cauchy's equation of motion for the

momentum transport

$$\partial_t(\rho\mathbf{v}) + \boldsymbol{\nabla}(\rho\mathbf{u}\otimes\mathbf{u}) \;=\; \boldsymbol{\nabla}\sigma(\mathbf{r},t) + \mathbf{f}_{\text{ext}}(\mathbf{r},t). \tag{2.8}$$

Here, the external force acts as a source or sink of momentum, and can be, for example, a uniform gravitational field $\mathbf{f}_{\text{ext}} = \rho\mathbf{g}$.

To complete the description of the fluid flow, we also have to derive an equation for the rate of change of energy. As for mass and momentum, we consider the energy $E(\mathbf{r},t)$ in an arbitrary stationary volume V in the fluid. This energy changes due to advective transport, heat conduction, heat production and transfer of mechanical work through the surface ∂V. Similar to before, integrals of flows across the surface are transformed using Gauß' theorem, such that we arrive at the equation for the energy transport

$$\partial_t E + \boldsymbol{\nabla}\cdot(E\mathbf{u} + \mathbf{q} - \sigma\mathbf{u}) \;=\; 0. \tag{2.9}$$

Here, $E\mathbf{u}$ is the advective flow of energy, $\mathbf{q}$ is the heat current yet to be defined. The term $\boldsymbol{\nabla}(\sigma\mathbf{u})$ describes the heat production due to friction and work performed by the pressure. For isothermal systems, where the energy transport is not relevant for the dynamics, the evaluation of Eq. (2.9) can be omitted. This is also the case for the hydrodynamic flows around bacteria, which we consider in this work.

As became apparent in this section, the present hydrodynamic transport equations are quite general requiring only basic physical conservation laws and basic vector calculus. However, we still need expressions for the viscous stress tensor σ, the heat flux $\mathbf{q}$ and the thermodynamic pressure p, to close the set of equations [154]. These so-called constitutive relations are defined by the transport phenomena of the physical fluid under consideration. In general they can be very model specific. In the next section we derive the constitutive relations for the most common class of the Newtonian fluids based on simple assumptions on the underlying materials.

2.2 Newtonian fluids

In the most simple case that applies to most ordinary liquids, the shear stress and heat flux both depend linearly on the shear rate and temperature gradient, respectively. This common behavior is expressed in the constitutive relations of the so-called Newtonian fluids [151].

The hydrodynamic behavior of the Newtonian Fluids is described by the Navier-Stokes equations, which combines these constitutive relations and the transport equation derived above. In other words, Newtonian fluids are characterized in how they react to deformations in the velocity field. To give a few counter-examples, non-Newtonian fluids can exhibit shear stress which is non-linear in the strain rate or viscoelastic stress that depends on the history of the deformation [154].

In the following, we first rationalize the constitutive relation of the heat flux. We

then describe how stress arises due to internal friction and pressure in the fluid and express the dependence of the viscous part of the stress tensor on the velocity field. Inserting the constitutive relation of the stress tensor into the Cauchy momentum equations, we are then able to derive the Navier-Stokes equations.

2.2.1 Heat flux

Our intention is to express the conduction of heat in the most simple, linear dependence on the temperature gradient. To justify this at the microscale, we have to consider the transport of heat between two neighboring fluid elements due to molecular motion and interactions. Clearly, the distribution of thermal energy has to vary sufficiently smoothly in order to describe the fluxes resulting from inhomogeneities as linear function locally. In view of the molecular processes, this requires that the temperature gradient $\boldsymbol{\nabla} T$ itself does not vary significantly over the length scale of the molecular interaction λ, *i.e.* $|\partial_x T|/|\partial_x^2 T| \gg \lambda$, which is usually satisfied in practice [155]. In addition, the second law of thermodynamics requires that the heat flux vanishes in the uniform distribution. Given these assumptions, the heat current can be described by Fourier's law of heat conduction $\mathbf{q} = -\kappa \boldsymbol{\nabla} T$ [154]. Here κ denotes the scalar thermal conductivity that applies for isotropic materials [155]. It is worth noting that, with this definition, the energy transport equation describes diffusion of thermal energy in the absence of flow, $\mathbf{u} = 0$.

2.2.2 The fluid stress tensor

The constitutive relation for the stress tensor can be derived as follows [156, 157]. First, we separate out the thermodynamic pressure p which is a material property of the fluid at equilibrium and not related to the derivatives of the velocity field $\mathbf{v}(\mathbf{r})$. Thus, we write $\sigma = -p\mathbf{I} + \sigma'$, where $\mathbf{I}$ is the identity matrix and the second term σ' the viscous stress tensor. In contrast to the pressure contribution, viscous stress arises from the friction of two neighboring fluid layers moving relative to each other. The viscous stress tensor is therefore only proportional to derivatives of the velocity field and vanishes when the fluid is in uniform motion or at rest. For small velocity gradients it is sufficient to consider only the first order derivatives. The fact that no internal friction occurs in uniform rotational fields further constrains σ' to the symmetric part of the velocity gradient. All together, we obtain the following for the viscous stress tensor

$$\sigma' \;=\; \eta \left[(\boldsymbol{\nabla} \otimes \mathbf{u})^T + \boldsymbol{\nabla} \otimes \mathbf{u} - \frac{2}{3}\mathbf{I}(\boldsymbol{\nabla} \cdot \mathbf{u}) \right] + \eta' \mathbf{I}(\boldsymbol{\nabla} \cdot \mathbf{u}). \tag{2.10}$$

Here, the first term in square brackets is the traceless rate of deformation tensor while the second term describes pure isotropic compression given by the trace of the symmetric velocity gradient. The viscosity coefficients η and η' are thereby intrinsic

properties of the fluid and independent of the fluid motion, but depend on the density ρ and temperature T of the fluid. The viscosity η' related to volume changes is generally referred to as *bulk viscosity* and is sometimes written as $\eta' = \gamma - 2\eta/3$, with the new parameter γ, to rearrange Eq. (2.10) [157]. Inserting the stress tensor into Eq. (2.9) for the hydrodynamic transport of energy one obtains the conditions that $\eta \geqslant 0$ and $\eta' \geqslant 0$ to guarantee the positivity of the entropy production rate in accordance with the second law of thermodynamics [154].

In the case of incompressible fluids ($\boldsymbol{\nabla} \cdot \mathbf{u} = 0$) the viscous stress tensor reduces to

$$\boldsymbol{\sigma}' \;=\; \eta \left[(\boldsymbol{\nabla} \otimes \mathbf{u})^T + \boldsymbol{\nabla} \otimes \mathbf{u} \right]. \tag{2.11}$$

This simplification is justified if the typical flow speed $|\mathbf{u}|$ is much smaller than the speed of sound u_{sound} and the Mach number $\mathrm{M} = |\mathbf{u}|/u_{\text{sound}} \ll 1$ is small. In this case, the motion of the fluid $\mathbf{u}$ is not subject to compressibility effects, and that the fluid appears incompressible [154].

2.2.3 The Navier-Stokes equations

Using the continuity equation (2.3), we may first transfer the Cauchy momentum equation from its conservation form to the convective form

$$\rho \left(\partial_t \mathbf{u} + \mathbf{u} \cdot \boldsymbol{\nabla} \mathbf{u} \right) \;=\; \boldsymbol{\nabla} \boldsymbol{\sigma} + \mathbf{f}_{\text{ext}}. \tag{2.12}$$

Since the typical flow velocity in the context of microscopic self-propelled particles is very small compared to the speed of sound, we restrict ourselves to the case of incompressible fluids $\boldsymbol{\nabla} \cdot \mathbf{u} = 0$ in the following. Consequently, also the density $\rho(\mathbf{r}, t) = \rho$ becomes a constant. Inserting the stress tensor in the above equation, we note that the divergence of the first term $\eta(\boldsymbol{\nabla} \otimes \mathbf{u})^T$ vanishes due to the incompressibility condition, such that we arrive at the Navier-Stokes equations for incompressible fluids

$$\rho \left(\partial_t \mathbf{u} + \mathbf{u} \cdot \boldsymbol{\nabla} \mathbf{u} \right) \;=\; -\boldsymbol{\nabla} p + \eta \boldsymbol{\nabla}^2 \mathbf{u} + \mathbf{f}_{\text{ext}}. \tag{2.13}$$

In this form, a moving fluid parcel is accelerated due to gradients of pressure and external force densities. Additionally, it exchanges momentum with the rest of the fluid via momentum diffusion, described by the second order derivative $\eta \boldsymbol{\nabla}^2 \mathbf{u}$. To solve the Navier-Stokes equations for the unknown velocity field $\mathbf{u}(\mathbf{r})$, additional boundary conditions are necessary. In the case of solid walls this is the so-called no-slip condition, which states that $\mathbf{u}(\mathbf{r}) = 0$ at the wall. Note that the co-moving derivative on the left hand side of the equation is non-linear in the velocity which greatly complicates solving it in practice [158].

To further characterize the flow, we require a knowledge of the geometry and the typical flow velocity such that characteristic scales of the length L, flow velocity U and time T can be specified. Using these characteristic parameters along with the

density ρ and viscosity η the Navier-Stokes equation can be converted into a non-dimensional form that contains only a few dimensionless parameters that further characterize the flow [154, 159]. In this manner we use the characteristic length L, flow velocity U and time $T = L/U$ to introduce dimensionless variables according to

$$\tilde{\mathbf{u}} \equiv \mathbf{u}/U, \quad \tilde{t} \equiv tU/L, \quad \widetilde{\boldsymbol{\nabla}} \equiv L\boldsymbol{\nabla}, \quad \tilde{p} \equiv pL/\eta U, \quad \tilde{\mathbf{f}} \equiv \mathbf{f}_{\text{ext}} L^2/\eta U.$$

For a flow inside a channel, U is the maximum velocity in the center, while in an unbounded flow it is chosen as the flow velocity at infinity. For a microswimmer U corresponds to the self-propulsion velocity. These choices are not unique, especially the choice of the inherent time scale $T = L/U$ applies to stationary flow problems, and the non-dimensional pressure may also be defined as $\tilde{p} = p/\rho U^2$ [154]. Inserting these definitions into the Navier-Stokes equations, we obtain the dimensionless form

$$\text{Re}\left(\frac{\partial \tilde{\mathbf{u}}}{\partial \tilde{t}} + \tilde{\mathbf{u}} \cdot \widetilde{\boldsymbol{\nabla}} \tilde{\mathbf{u}}\right) = -\widetilde{\boldsymbol{\nabla}} \tilde{p} + \widetilde{\boldsymbol{\nabla}}^2 \tilde{\mathbf{u}} + \tilde{\mathbf{f}}. \tag{2.14}$$

Here, we have introduced the Reynolds number

$$\text{Re} \equiv \frac{\rho L U}{\eta}, \tag{2.15}$$

which describes the ratio between the inertial forces (numerator) and viscous forces (denominator) of the Navier-Stokes equations [160]. An important implication for systems with the same Reynolds number is that their flows are similar and can be transformed into each other by a simple re-scaling of the lengths, velocities, and time [156]. As a very illustrative consequence, aerodynamic studies can be performed using miniaturized models immersed in water. In this particular example the change in length scale L and viscosity η cancel in the Reynolds number and the two flows are called similar. For large Reynolds numbers the non-linear term $\mathbf{u} \cdot \boldsymbol{\nabla} \mathbf{u}$ is relevant and makes the general solution of the Navier-Stokes equation complicated. In this case, steady flows are unstable to small disturbances, which may lead to turbulent flows [154, 160]. Of particular interest for us is the case of low Reynolds number $\text{Re} \ll 1$, where the Navier-Stokes equation can be further simplified to the so-called Stokes equation.

2.2.4 The Stokes equations

For hydrodynamic flows in the context of bacteria and other microscopic particles, length scales and typical flow velocities are small. Both of these conditions imply that the Reynolds numbers $\text{Re} \ll 1$ is small and thus the hydrodynamic flows are dominated by the viscous terms on the right-hand side of Eq. (2.14) of the Navier-Stokes equation. For this reason microscopic flows are termed strongly viscous [157]. Given these circumstances, the inertial terms on the left hand side of Eq. (2.14) can

be neglected, and we arrive at the so-called Stokes equations for creeping motion [159]

$$\begin{aligned} \eta \boldsymbol{\nabla}^2 \mathbf{u} - \boldsymbol{\nabla} p + \mathbf{f} &= 0 \\ \boldsymbol{\nabla} \cdot \mathbf{u} &= 0 \end{aligned} \tag{2.16}$$

in terms of the dimensional variables. However, one should note that low Reynolds numbers may also occur in very dilute aerodynamic flows [157].

The Stokes equations (2.16) manifest some important implications for hydrodynamic flows at low Reynolds numbers. Most crucially, without the convective derivative in the inertial term the Stokes equation becomes a linear partial differential equation of the velocity and the pressure, such that flow problems can be solved using Green's formalism and boundary integral methods [159]. Another consequence is the absence of a time derivative, such that solutions of the Stokes equations are instantaneous and steady flows.

Note that there is also the so-called transient Stokes flow which also comprises the acceleration term $\rho \partial_t \mathbf{u}$. This hydrodynamic regime appears when the characteristic acceleration time does not occur on the slow time scale L/U chosen in Eq. (2.14) before, but over the much faster time scale $L^2\rho/\eta$ that is required for the vorticity to diffuse over the characteristic length L. In this case the acceleration term $\rho \partial_t \mathbf{u}$ is of the same order as the viscous terms and only the nonlinear term $\mathbf{u} \cdot \boldsymbol{\nabla} \mathbf{u}$ can be neglected for the Navier-Stokes equations [154, 158].

2.2.4.1 Fundamental solution of Stokes flow

The fundamental solution or Green's function for Stokes flow is the flow field generated by a point force acting on the fluid. It can be derived from the Fourier transformation of the Stokes Eq. (2.16) and the incompressibility condition [158]. To account for an arbitrary orientation of the force the most general form of this solution has the tensorial form

$$\mathbf{O}(\mathbf{r}) \;=\; \frac{\mathbf{G}(\mathbf{r})}{8\pi\eta} \;=\; \frac{1}{8\pi\eta}\left(\frac{\mathbf{I}}{r} + \frac{\mathbf{r}\otimes\mathbf{r}}{r^3}\right), \tag{2.17}$$

for a point force located at the origin [161]. Thereby, the term $\mathbf{O}(\mathbf{r})$ is called the Oseen tensor, but often we use $\mathbf{G}(\mathbf{r})$ in calculations without the factor $(8\pi\eta)^{-1}$ for simplicity. The associated pressure field has the form

$$\mathbf{p}(\mathbf{r}) \;=\; \frac{1}{4\pi}\frac{\mathbf{r}}{r^3}. \tag{2.18}$$

The solution $\mathbf{u}^{\mathrm{FM}}(\mathbf{r}) = \mathbf{O}(\mathbf{r})\mathbf{F}$ and $p = \mathbf{p}(\mathbf{r}) \cdot \mathbf{F}$ for a given point force $\mathbf{F}$ is called Stokeslet. Due to its appearance in response to a point force, the Stokeslet is also called hydrodynamic force-monopole. The flow field for an arbitrary distribution of

forces $\mathbf{F}(\mathbf{r})$ can then be obtained by convolution with the Oseen tensor [161]

$$\mathbf{u}(\mathbf{r}) \;=\; \int_V \mathbf{O}(\mathbf{r}-\mathbf{r}')\mathbf{F}(\mathbf{r}')\mathrm{d}^3 r' \tag{2.19}$$

and the associated pressure field

$$p(\mathbf{r}) \;=\; \int_V \mathbf{p}(\mathbf{r}-\mathbf{r}')\cdot\mathbf{F}(\mathbf{r}')\mathrm{d}^3 r'. \tag{2.20}$$

Additional to the Stokeslet, the Stokes equations have another branch of solutions for constant pressure p. In this case, the Stokes equation takes the form of the Laplace equation with the vectorial solution [159]

$$\mathbf{u}^{\mathrm{SM}}(\mathbf{r}) \;=\; c\frac{\mathbf{r}}{r^3}, \tag{2.21}$$

which describes a sink or a source with a flux of fluid into or out of the origin, depending on the sign of the constant c.

2.2.5 Higher order singularities

Similar to electrostatics, the flow field of an arbitrary object can the be expressed as a series of multipoles. To do so, the Oseen tensor in Eq. (2.19) for an arbitrary disturbance is expressed in a Taylor series

$$\mathbf{G}(\mathbf{r}-\mathbf{r}') \;=\; \sum_{n=0}^{\infty} \frac{(-\mathbf{r}'\cdot\boldsymbol{\nabla})^n}{n!}\mathbf{G}(\mathbf{r}). \tag{2.22}$$

We may then separate the primed and unprimed variables. The integration over the primed variable yields the multipole coefficients of $\mathbf{F}(\mathbf{r})$, while the higher-order gradients of $\mathbf{G}(\mathbf{r})$ represent the Stokes multipole moments, which are also solutions to the Stokes equations. Note that in the context of the multipole expansion the factor $(8\pi\eta)^{-1}$ is integrated into the multipole coefficients so that we write $u_i(\mathbf{r}) = f_j G_{ij}(\tilde{\mathbf{r}})$ with $f_j = F_j/(8\pi\eta)$ for the Stokeslet, and so on.

In the most general form, the Stokes multipoles moments are directional derivatives $\prod_{i=1}^{n}(\hat{\mathbf{d}}_i\cdot\boldsymbol{\nabla}')^n$ that differentiate in the direction of the unit vectors $\hat{\mathbf{d}}_i$ with respect to the position of the singularity. In the following we will write these derivatives as gradients of the force and source monopole fields such that a singular solution of n-th order is described by a tensor of rank $(n+2)$. The flow fields then follow from the contraction with a tensorial multipole coefficient $\mathbf{d}_{1,\ldots,i} = \mathbf{d}_1\otimes\mathbf{d}_2\otimes\ldots\otimes\mathbf{d}_n$ of rank-$(n+1)$ that describes the directional derivatives [158, 159].

Applying one directional derivative to the source monopole results in the flow field of two sources with opposite sign, separated by the vector $\mathbf{d}$. Denoting the distance to the singularity with $r = |\tilde{\mathbf{r}}|$, where $\tilde{\mathbf{r}} = \mathbf{r}-\mathbf{r}'$ and $\mathbf{r}'$ is the position of the

singularity, the resulting source dipole is described by the tensor

$$G_{ij}^{\mathrm{SD}}(\tilde{\mathbf{r}}) \;=\; \frac{\partial}{\partial r_i'}\frac{\tilde{r}_j}{\tilde{r}^3} \;=\; -\frac{\delta_{ij}}{\tilde{r}^3} + \frac{3\tilde{r}_i\tilde{r}_j}{\tilde{r}^5}, \tag{2.23}$$

and the resulting flow field is $u_i^{\mathrm{SD}}(\mathbf{r}) = d_j G_{ij}^{\mathrm{SD}}(\tilde{\mathbf{r}})$ (using the Einstein sum convention). The source dipole is also related to the force monopole through the relation $G_{ij}^{\mathrm{SD}}(\tilde{\mathbf{r}}) = -\frac{1}{2}\boldsymbol{\nabla}'^2 G_{ij}(\tilde{\mathbf{r}})$.

Higher order solutions derived from the Oseen tensor are the force dipole

$$G_{ijk}^{\mathrm{FD}}(\tilde{\mathbf{r}}) \;=\; \partial_k' G_{ij}(\tilde{\mathbf{r}}) \;=\; \frac{\delta_{ij}\tilde{r}_k - \delta_{ik}\tilde{r}_j - \delta_{jk}\tilde{r}_i}{\tilde{r}^3} + \frac{3\tilde{r}_i\tilde{r}_j\tilde{r}_k}{\tilde{r}^5}, \tag{2.24}$$

and the force quadrupole $G_{ijkl}^{\mathrm{FQ}}(\tilde{\mathbf{r}}) = \partial_l' G_{ijk}^{\mathrm{FD}}(\tilde{\mathbf{r}})$. Two other notable solutions are a uniform rotation of the flow field — also called rotlet — which follows from the combination of two force dipoles, *i.e.*, anti-symmetric part of the gradient of the Stokeslet $G_{ij}^{\mathrm{R}}(\tilde{\mathbf{r}}) = -\frac{1}{2}\epsilon_{klj}\partial_l G_{ik}(\tilde{\mathbf{r}}) = \epsilon_{ijk}\frac{\tilde{r}_k}{\tilde{r}^3}$ and its gradient, the rotlet dipole $G_{ijk}^{\mathrm{RD}}(\mathbf{r}) = \partial_k'\epsilon_{ijl}\frac{\tilde{r}_l}{\tilde{r}^3}$ [159]. The latter of these two is encountered in the context of microswimmers for the rotating flagella of bacteria [162]. For microswimmers, additional symmetry arguments are used to simplify the tensorial forms as we show in the following.

2.2.5.1 Multipole expansion for axisymmetric microswimmers

We investigate the multipole expansion of the flow field $\mathbf{u}(\mathbf{r})$ of our model microswimmers to provide an understanding of their hydrodynamic pair interactions. To introduce the multipole expansion in the context of microswimmers, a few simplifications are made. First of all, we consider microswimmers as axisymmetric around their direction of swimming $\hat{\mathbf{e}}$ [65, 74]. In this case, the symmetry requires that all gradients in Sec. 2.2.5 reduce to directional derivatives of the Stokeslet $(\hat{\mathbf{e}}\cdot\boldsymbol{\nabla}')^n[\mathbf{G}(\tilde{\mathbf{r}})\hat{\mathbf{e}}]$ and source dipole $(\hat{\mathbf{e}}\cdot\boldsymbol{\nabla}')^n[\mathbf{G}^{\mathrm{SD}}(\tilde{\mathbf{r}})\hat{\mathbf{e}}]$ and all multipole coefficients reduce to scalars. Furthermore, self-propelled particles are typically free of external forces and do not consume fluid such that the force and source monopole moments are not present in their flow fields [65, 162]. In Fig. 2.1 we show a collection of the first axisymmetric multipoles beginning with the Stokeslet [Fig. 2.1(a)] and its first two derivatives [Figs. 2.1(b) and (c)], along with the source monopole in Fig. 2.1(d) and its first two derivatives [Figs. 2.1(e) and (f)].

At large distances to the microswimmer located at the origin of the coordinate system, the flow field can then be written as a sum of the velocity fields of a force dipole ($\mathbf{u}^{\mathrm{FD}}$), source dipole ($\mathbf{u}^{\mathrm{SD}}$), force quadrupole ($\mathbf{u}^{\mathrm{FQ}}$), and rotlet dipole ($\mathbf{u}^{\mathrm{RD}}$)

$$\mathbf{u}(\mathbf{r}) \;=\; \mathbf{u}^{\mathrm{FD}}(\mathbf{r}) \;+\; \mathbf{u}^{\mathrm{SD}}(\mathbf{r}) \;+\; \mathbf{u}^{\mathrm{FQ}}(\mathbf{r}) \;+\; \mathbf{u}^{\mathrm{RD}}(\mathbf{r}) \;+\; \mathcal{O}(r^{-4}) \tag{2.25}$$

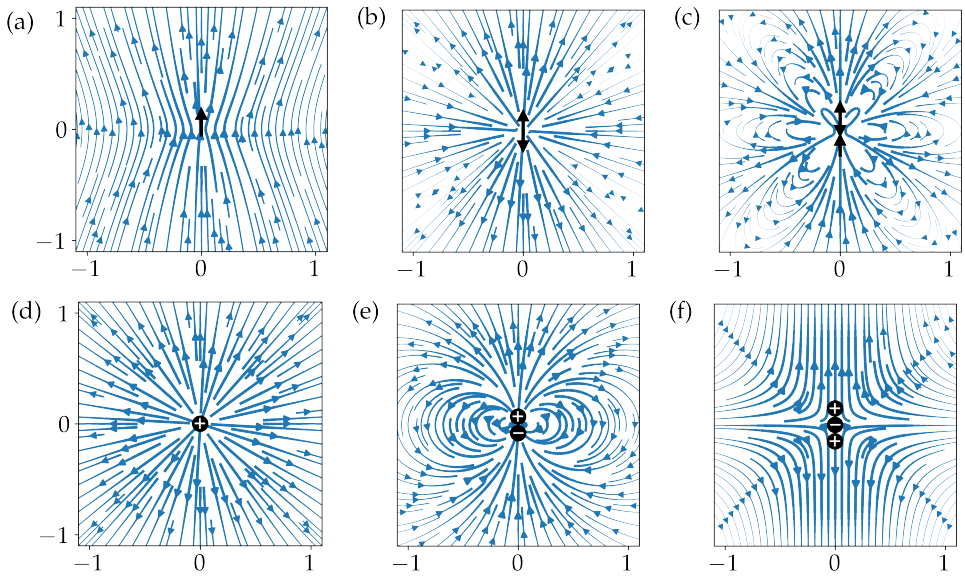

Figure 2.1: Flow fields of different singular solutions of Stokes flow in the laboratory frame of reference. The top row shows the solutions based on point forces (a) Stokeslet/hydrodynamic force monopole ($\mathbf{u}^{\mathrm{FM}}$), (b) force dipole ($\mathbf{u}^{\mathrm{FD}}$), (c) force quadrupole ($\mathbf{u}^{\mathrm{FQ}}$). The bottom row shows the potential flow solutions for constant pressure p, namely (d) source monopole ($\mathbf{u}^{\mathrm{SM}}$), (e) source dipole ($\mathbf{u}^{\mathrm{SD}}$), (f) source quadrupole ($\mathbf{u}^{\mathrm{SQ}}$)

up to 3-*rd* order in $1/r$. Among these moments, the force-dipole field $|\mathbf{u}^{\mathrm{FD}}| \propto 1/r^2$ has the longest range. If it is present for a type of microswimmer, it is usually the dominant mode for pair interactions in the far field [74]. In the following, we omit the rotlet dipole since it does not appear for the microswimmer model used in this work.

In the case of axisymmetric flow fields, the multipoles can be expressed using spherical coordinates with the swimmer located at the origin of the coordinate system [69, 74, 114]. We introduce the polar angle θ relative to the swimmer axis according to $\cos\theta = \hat{\mathbf{e}} \cdot \mathbf{r} \,/\, r$. Then, in spherical coordinates r, ϕ, and θ the respective radial and polar components of the multipole expansion of the velocity field become

$$u_r(r,\theta) = \sum_{n=1}^{\infty} \left[A_n r^{-n} + B_n r^{-n-2} \right] P_n(\cos\theta), \tag{2.26}$$

$$u_\theta(r,\theta) = \sum_{n=1}^{\infty} \left[\left(\frac{n}{2} - 1 \right) A_n r^{-n} + \frac{n}{2} B_n r^{-n-2} \right] V_n(\theta). \tag{2.27}$$

Here, $P_n(\cos\theta)$ are the ordinary Legendre polynomials and

$$V_n(\theta) = \frac{2\sin\theta}{n(n+1)} P_n'(\cos\theta)\,, \tag{2.28}$$

where $'$ denotes the derivative with respect to $\cos\theta$. The coefficients A_n and B_n describe the strength of the respective n^{th}-order force and source multipoles, *e.g.*, B_1 belongs to the source dipole. Due to the restriction to axisymmetric flow fields $u_r(r,\theta)$ and $u_\theta(r,\theta)$ are independent of the azimuthal angle ϕ. Furthermore, the azimuthal velocity component u_ϕ vanishes since the swimmer is torque-free and we do not consider a rotlet-dipole or derivatives of it.

The form of Eq. (2.26) may be used to decompose a flow field $\mathbf{u}(\mathbf{r})$ measured in experiments or simulations into the series of multipole moments A_n and B_n [163]. To determine the terms A_n and B_n, we calculate the n^{th} Legendre coefficient of the radial component $u_r(r,\theta)$ from the integral

$$\begin{aligned} u_{r,n}(r) &\equiv \frac{2n+1}{2}\int_0^\pi u_r(r,\theta) P_n(\cos\theta)\sin\theta\,\mathrm{d}\theta \\ &= A_n r^{-n} + B_n r^{-n-2}, \end{aligned} \tag{2.29}$$

due to the completeness relation of the Legendre polynomials. With the knowledge of a flow field and, in particular, the radial decay of the n^{th} Legendre coefficient $u_{r,n}(r)$, we can then infer the multipole coefficients A_n and B_n. Force and source multipole moments can thereby be distinguished using their different radial decay.

Note that for a spherical rigid body each pair of A_n and B_n for $n > 1$ is not independent because the radial velocity $u_r(r,\theta)$ has to vanish on the surface of the body, due to the no-slip boundary condition.

2.3 Swimming at low Reynolds number

2.3.1 Flow field of a moving sphere

With regard to the hydrodynamic flow fields of arbitrary microswimmer models, which will be considered in the following, it is instructive to look at the flow field of a rigid sphere moving in a bulk fluid with the velocity $\mathbf{U}$. To do so, we consider the multipole expansion in spherical coordinates given in Eqs. (2.26) and (2.27). With $P_1(\cos\theta) = \cos\theta$ and $V_1(\theta) = \sin\theta$ we see that only terms of order $n = 1$ are suitable to fulfill the boundary condition of a rigid moving sphere. For a sphere of radius R the no-slip boundary condition gives $u_r(R,0) = |U|$ and $u_\theta(R,\pi/2) = -|U|$. For the terms in the square brackets in Eqs. (2.26) and (2.27) we then find $A_1 = 3|\mathbf{U}|/2$ and

$B_1 = -R^2|\mathbf{U}|/2$. In Cartesian coordinates we obtain the velocity field

$$\mathbf{u}(\mathbf{r}) \;=\; 6\pi\eta\mathbf{U}\left(1+\frac{R^2}{6}\boldsymbol{\nabla}'^2\right)\mathbf{O}(\mathbf{r}-\mathbf{r}') \tag{2.30}$$

as combination of the Stokeslet with magnitude A_1 and a source dipole with magnitude B_1 for a sphere located at $\mathbf{r}'$, where we used the relation $\mathbf{G}^{\mathrm{SD}}(\tilde{\mathbf{r}}) = -1/2\boldsymbol{\nabla}'^2\mathbf{G}(\tilde{\mathbf{r}})$ [158]. Due to the different radial decay of the two hydrodynamic multipoles, the Stokeslet dominates the flow field at large distances $r \gg R$. Furthermore, we can deduce the force acting on the moving sphere

$$\mathbf{F} = 6\pi\eta R\mathbf{U} \tag{2.31}$$

which follows from the prefactor of the Stokeslet term. This force is related to the inhomogeneity in the Stokes equation $\mathbf{f}_{\mathrm{ext}}$ which drives the sphere.

2.3.2 Biological microswimmers

The fact that microorganisms swim in the regime of low Reynolds number governed by the Stokes equation, has important implications for their propulsion strategies. Phenomenologically speaking, low Reynolds numbers imply the dominance of viscous friction such that microswimmers are not able to exploit their own inertia during their propulsion as human swimmers do. More precisely, since the Stokes equation is linear and contains no time derivative, its solutions are instantaneous and exhibit kinetic reversibility. This means that for a solution $\mathbf{u}$, $\boldsymbol{\nabla}p$ and $\mathbf{f}_{\mathrm{ext}}$, also the reverse flow $-\mathbf{u}$ is a solution for $-\boldsymbol{\nabla}p$ and $-\mathbf{f}_{\mathrm{ext}}$ [159]. As a consequence, the propulsion strategies of microswimmers must use non-reciprocal deformations to achieve a net displacement [164], which is know by the term *Scallop theorem* [165].

To solve this constraint on swimming strokes, nature has found a number of different strategies. Organisms as *Opalina, Paramecium* or *Volvox* [70, 166] are entirely covered by hair-like appendages, called cilia, which perform a non-reciprocal beating motion [see Fig. 2.2(a)]. On a large scale, neighboring cilia synchronize via hydrodynamic interactions such that metachronal waves form and push the swimmer forward [69]. Pusher-type organisms as the bacteria *E. coli* or *B. subtilis* [28, 38] possess a number of flagella joined in a bundle, which are shaped similar to a cork-screw [see Fig. 2.2(b)]. The rotation of this flagella bundle pushes the fluid backward similar to a propeller, and thus pushes the swimmer forward through the fluid. Puller-type organisms as the *Chlamydomonas* algae [167, 168] have developed two shorter flagella extending from the front of the cell body performing a beating pattern similar to a breast stroke as depicted in see Fig. 2.2(c).

The three swimming strategies described so far differ decisively in their flow fields. As we have seen in Sec. 2.3.1, a moving sphere free of external forces generates the flow field of a source dipole. Even more, the source dipole is in fact present for

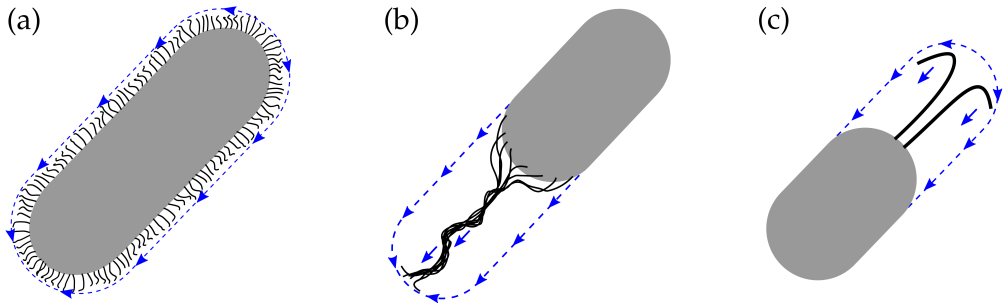

Figure 2.2: Sketches of the three fundamental types of biological microswimmer propulsion. (a) Ciliated organisms such as *Opalina, Paramecium* or *Volvox* [70, 166] are entirely covered by hair-like cilia, which transport fluid along their surface. (b) Pusher type organisms as the bacteria *E. coli* or *B. subtilis* [28, 38] use a bundle of rotating flagella to push themselves through the fluid. (c) Puller type organisms as the *Chlamydomonas* algae [167] use two beating flagella that fulfill a breast-stroke-like motion to pull themselves through the fluid [168]. Dashed blue lines are used to sketch the effective stroke averaged body shape of the swimmers including their cilia or flagella. As depicted in the sketches, the cell bodies of all three microswimmer types are rather elongated than spherical.

all self-propelled particles [162]. Fascinatingly, the surface slip-velocity of the source dipole closely resembles the stroke averaged biological cilia beating patterns such that the source dipole corresponds to ciliates like *Opalina* or *Paramecium* [114].

The swimming patterns of pushers and pullers generate an asymmetric distribution of forces, which results in the flow field of a force dipole in leading order. For pushers the flagella create a backward pushing force, while the cell body pushes fluid forward, for pullers the situation is reversed [74]. Consequently the flow field of pushers and pullers possesses a force dipole moment of opposite sign as shown in Fig. 2.1(b). The force dipole decays as $\sim r^{-2}$ with the distance to the swimmer, such that the flow fields of pushers and pullers are more long-ranged than the source dipole $\sim r^{-3}$ characteristic for ciliates. More complex shapes, such as elongated particles, result in higher order multipole moments which are necessary to fulfill the boundary conditions of the surface of the swimmer.

2.3.3 Flow fields of elongated particles

Different analytical approaches exist for the treatment of the flow field of elongated particles. To begin with, the ordinary multipole expansion given in Eqs. (2.41), (2.26) and (2.27) may be applied. This description results in higher-order terms to fulfill the no-slip boundary condition on the non-spherical surface of the elongated particle, and as we will see also the distribution of the surface slip velocity plays a role. A more detailed picture of microswimmers and resulting boundary conditions will be

given in Sec. 2.6.

Another approach exists for ellipsoidal particles, which are relatively simple to treat mathematically. In this case, the Stokes equation can be solved in elliptical coordinates resulting in a multipole expansion in ellipsoidal harmonics [169–171]. Relating this solution to the ordinary multipole series the flow field may be written in terms of a distribution of Stokeslets. However, the formulation of these solutions are quite intricate, for more details we refer to Ref. [158].

Lastly, the so-called slender body theory is applied in the limit of thin elongated particles as, for example, rigid polymers or fibers. In a nutshell, instead of considering a volume distribution of Stokeslets as in Eq. (2.19), the distribution of the disturbance forces is approximated by a line distribution of Stokeslets, source dipoles, and force dipoles. The resulting velocity field is then obtained from a line integral over the distribution of the singularities. In the limit of thin spheroids, the ellipsoidal solution is consistent with the slender body theory [158].

2.4 Swimming in confinement

Although many microswimmers live in vast habitats that resemble a bulk fluid, confined geometries are also a common environment. For example, on solid surfaces or at air interfaces [172, 173]. Furthermore, Stokes flow in channels is relevant in the context of blood flow [131, 142, 143], and also experimental setups using droplets, Petri dishes or microscope slides [174].

In the presence of solid walls or interfaces, the solution of the Stokes equations has to be adjusted such that it fulfills the boundary conditions, *i.e.*, the no-slip condition on the walls. In the following, we will therefore first consider the case of a Stokeslet in the presence of a single plane no-slip wall. Then, we will proceed to the Hele-Shaw geometry of a microswimmer between two parallel plane no-slip walls, which is used throughout this work.

2.4.1 Stokes flow near a plain wall

A showcase of swimming in confinement is in the presence of a single plain wall. In this case, analytical formulas have been derived by Blake *et al.* for a Stokeslet [175] and other multipoles [178]. In the presence of a wall, the so-called Lorentz image technique is used to fulfill the boundary condition for the velocity field similar to electrostatics [158]. For a Stokeslet the mirrored image Stokeslet is accompanied by a force dipole and a source dipole in order to fulfill the no-slip boundary condition at the wall [175]. The resulting flow field for a point force pointing towards the wall is shown in Fig. 2.3(a). The combined image system fulfills the no-slip boundary condition and is often called Blake tensor. For the Stokeslet located at $\mathbf{r}'$ with the position $\mathbf{r}''$ mirrored at the plane perpendicular to the z-direction it takes the form

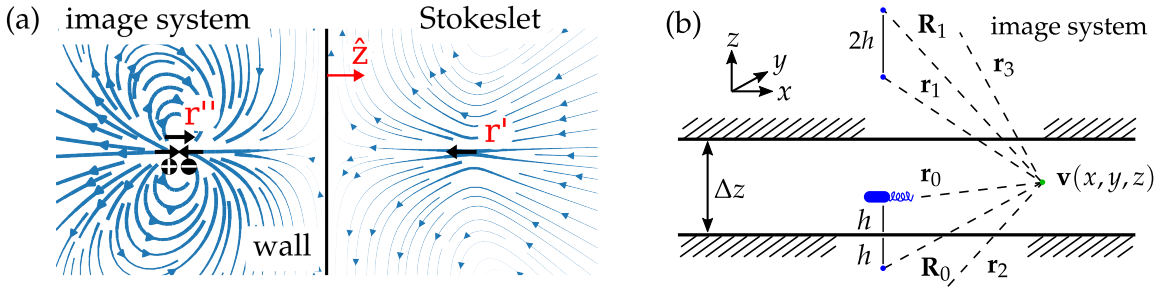

Figure 2.3: Image systems for a Stokeslet in the presence of solid walls. (a) In the presence of a single infinite wall with no-slip boundary conditions, the image system consisting of a Stokeslet, force dipole and source dipole is known as the so-called *Blake* tensor [175, 176]. (b) In the Hele-Shaw geometry, the system is confined by two parallel infinite walls with no-slip condition. In this case, the image system consists of an infinite recursion of reflections, which results in a different characteristic of hydrodynamic flow fields [177].

[159, 175, 176]

$$B_{ij}(\mathbf{r}, \mathbf{r}''(\mathbf{r}')) = (-\delta_{jk} - 2r''_z\delta_{k3}\nabla''_j + (r''_z)^2 M_{kj}\boldsymbol{\nabla}''^2)O_{ik}(\mathbf{r} - \mathbf{r}'') \tag{2.32}$$

where $\mathbf{M} = \mathrm{diag}(1, 1, -1)$. For a plane that lies in the origin of the coordinate system $\mathbf{r}'' = \mathbf{r}' - 2(\mathbf{r}' \cdot \hat{\mathbf{z}})$. The total flow field at $\mathbf{r}'$ due to a point force $\mathbf{f}$ then reads $\mathbf{u}(\mathbf{r}) = [\mathbf{O}(\mathbf{r} - \mathbf{r}') + \mathbf{B}(\mathbf{r}, \mathbf{r}'')]\mathbf{f}$. In Eq. (2.32), we can recognize the reflected Stokeslet, force dipole and source dipole from left to right. The additional image system near the plane wall affects the far field of the force monopole such that it behaves as a force dipole if it is oriented parallel to the wall, or like a source dipole if it oriented normal to the wall. Likewise, a rotlet near a plane wall appears as a rotlet dipole [178].

2.4.2 The Hele-Shaw geometry

The geometry which we use throughout this work is the so-called Hele-Shaw geometry where the fluid is confined between two parallel plane walls with small distance Δz as shown in Fig. 2.3(b). This geometry describes for instance the fluid between microscope slides or a thin fluid film in Petri dishes. Similar to the presence of a single plane wall presented before, image singularities are used recursively to solve the boundary conditions. However, an infinite number of recursive image singularities are necessary in order to fulfill the boundary conditions at both walls.

As Liron and Mochon showed, an analytical solution can also be derived in this geometry [177]. The solution involves a Fourier transformation in two dimensions, where the infinite series of image singularities can be separated into an algebraic far field contribution and an exponentially decaying near field term. The approach was recently generalized to fluids in a thin film, *i.e.*, with one no-slip and one slip wall,

and higher order singularities by Mathijssen *et al*. [176]. For a point force located at position $\mathbf{r}'$ the modified Green's tensor at the position $\mathbf{r}$ is given by

$$\mathcal{G}_{ij}(\mathbf{r},\mathbf{r}') \;=\; -24\Delta z\frac{r_z}{\Delta z}\left(1-c\frac{r_z}{\Delta z}\right)\frac{r'_z}{\Delta z}\left(1-c\frac{r'_z}{\Delta z}\right)\left[\frac{\delta_{\alpha\beta}}{2\tilde{\rho}^2}-\frac{\tilde{r}_\alpha\tilde{r}_\beta}{\tilde{\rho}^4}\right]\delta_{i\alpha}\delta_{j\beta}+\mathcal{O}\left(\mathrm{e}^{-\tilde{\rho}/\Delta z}\right). \tag{2.33}$$

Here, $\tilde{\mathbf{r}}=\mathbf{r}-\mathbf{r}'$ denotes the distance to the point force, $\tilde{\rho}=\sqrt{\tilde{r}_x^2+\tilde{r}_y^2}$, and the coefficient c distinguishes the parallel plates geometry ($c=1$) and thin film case with one *slip* boundary condition ($c=1/2$). The corresponding pressure reads

$$\mathcal{P}_j(\mathbf{r},\mathbf{r}') \;=\; -\frac{12\eta}{\Delta z}\frac{r'_z}{\Delta z}\left(1-c\frac{r'_z}{\Delta z}\right)\frac{\tilde{r}_\alpha}{\tilde{\rho}^2}\delta_{j\alpha}+\mathcal{O}\left(\mathrm{e}^{-\tilde{\rho}/\Delta z}\right). \tag{2.34}$$

Here, the Greek indices α,β denote the first two dimensions parallel to the confining walls.

As we see here, the solution contains a leading order far-field term with an algebraic radial decay if the force is oriented parallel to the walls (square brackets) and an additional near field term with exponential decay. The structure of this far-field term thereby behaves as a two-dimensional source dipole in the direction parallel to the walls [176], and has a parabolic or shape in the direction perpendicular to the walls. If the force is oriented perpendicular to the walls, the entire flow field decays exponentially.

As in the bulk fluid, higher-order force moments follow from applying the directional derivative $(\hat{\mathbf{e}}\cdot\boldsymbol{\nabla}')$ to the Green's function [176]. Likewise, applying the Laplace operator $\boldsymbol{\nabla}'^2$ to the Green's function flow field yields the flow field of a source dipole, which here is up to a factor identical to the Green's function [176]. Higher source-multipole moments are again generated by directional derivatives. For an axisymmetric microswimmer oriented in the direction of $\hat{\mathbf{e}}$ the contributions to the flow field are [162, 176]

$$\mathbf{u}^{\mathrm{FD}}(\mathbf{r}) \;=\; \kappa(\hat{\mathbf{e}}\cdot\boldsymbol{\nabla}')\boldsymbol{\mathcal{G}}(\mathbf{r},\mathbf{r}')\hat{\mathbf{e}} \tag{2.35}$$

$$\mathbf{u}^{\mathrm{FQ}}(\mathbf{r}) \;=\; \nu(\hat{\mathbf{e}}\cdot\boldsymbol{\nabla}')^2\boldsymbol{\mathcal{G}}(\mathbf{r},\mathbf{r}')\hat{\mathbf{e}} \tag{2.36}$$

$$\mathbf{u}^{\mathrm{SD}}(\mathbf{r}) \;=\; -\sigma\frac{1}{2}\boldsymbol{\nabla}'^2\boldsymbol{\mathcal{G}}(\mathbf{r},\mathbf{r}')\hat{\mathbf{e}} \tag{2.37}$$

$$\mathbf{u}^{\mathrm{SQ}}(\mathbf{r}) \;=\; -\chi(\hat{\mathbf{e}}\cdot\boldsymbol{\nabla}')\boldsymbol{\mathcal{G}}^{\mathrm{SD}}(\mathbf{r},\mathbf{r}')\hat{\mathbf{e}} \tag{2.38}$$

where $\boldsymbol{\nabla}'$ denotes the derivative with respect to the position of the singularity at $\mathbf{r}'$. In general, the multipole coefficients can be transferred from the bulk flow since the same strength of the singularity is considered for the derivation of *e.g.*, Eq. (2.33). In order to discuss the implications of the modified multipole terms, we calculate the expressions for the force dipole and source dipole terms. In the following, we restrict ourselves to the case where the microswimmer is oriented parallel to the confining

walls. In the Hele-Shaw geometry, the flow field of the source dipole resulting from Eq. (2.37) reads

$$\mathcal{G}_{ij}^{\mathrm{SD}} \;=\; -\frac{24c}{\Delta z}\frac{r_z}{\Delta z}\left(1-c\frac{r_z}{\Delta z}\right)\left[\frac{\delta_{ij}}{2\tilde{\rho}^2}-\frac{\tilde{r}_j\tilde{r}_i}{\tilde{\rho}^4}\right]. \tag{2.39}$$

Here, we neglected the exponentially decaying terms of the near field in Eq. (2.33), such that this far-field limit of the flow field is independent of the swimmer height r_z'. For the force dipole we obtain

$$\mathcal{G}_{ij}^{\mathrm{FD}}(\mathbf{r},\mathbf{r}') \;=\; -24\Delta z\frac{r_z}{\Delta z}\left(1-c\frac{r_z}{\Delta z}\right)\frac{r_z'}{\Delta z}\left(1-c\frac{r_z'}{\Delta z}\right)\left[\frac{2\delta_{ij}\tilde{r}_j}{\tilde{\rho}^4}+\frac{\tilde{r}_i}{\tilde{\rho}^4}-\frac{4\tilde{r}_i\tilde{r}_j^2}{\tilde{\rho}^6}\right]. \tag{2.40}$$

As we can read from Eqs. (2.33), (2.39) and (2.40) an important characteristic of the Hele-Shaw geometry is that the flow fields decay with different exponents in $\tilde{\rho}$ compared to the bulk fluid. For the force multipoles, this means that the velocity fields decay more rapidly with the order of $\boldsymbol{\mathcal{G}}\propto\tilde{\rho}^{-2}$ and $\boldsymbol{\mathcal{G}}^{\mathrm{FD}}\propto\tilde{\rho}^{-3}$, whereas in the bulk fluid $\mathbf{G}\propto\tilde{r}^{-1}$ and $\mathbf{G}^{\mathrm{FD}}\propto\tilde{r}^{-2}$. At the same time, the source dipole and other source multipoles become more long ranged such that the velocity fields decay as $\boldsymbol{\mathcal{G}}^{\mathrm{SD}}\propto\tilde{\rho}^{-2}$ compared to the bulk case where $\mathbf{G}^{\mathrm{SD}}\propto\tilde{r}^{-3}$. This transformation of the radial decay radically changes the nature of the flow fields and also hydrodynamic interactions in comparison to the flow fields in bulk [179].

Independent of the geometry, the source dipole is the lowest-order multipole term for microswimmers free of external forces, which occurs for all self propelled particles [162].

However, in the bulk flow the force dipole which is more long-ranged and therefore always the dominant term of the far field, if it exists [179]. As we saw, this changes in the Hele-Shaw geometry such that the source dipole becomes the dominant term of the flow field, being most long-ranged. Although this seems to implicate that it becomes irrelevant to distinguish between pusher and puller type microswimmers, this is not the case. As we show, the force dipole still dominates the intermediate range of the flow field, while the source dipole dominates the far field [125].

Comparing the source dipole in Eq. (2.39) and the Green's function in Eq. (2.33), which are of the same order $\tilde{\rho}^{-2}$, note that they both have the same shape $[\delta_{ij}/2-\tilde{r}_i\tilde{r}_j/\tilde{\rho}^2]$ of a two-dimensional source dipole. Furthermore, in the Hele-Shaw geometry force and source singularities of equal order n also possess the same radial decay $\tilde{\rho}^{-(n+1)}$.

Consequentially, the pairs of singularities of order n only differ in their dependence on the confinement strength Δz, which can be identified from the remaining factors Δz and $1/\Delta z$ in Eqs. (2.33) and (2.39), respectively. For the force monopole in Eq. (2.33) and higher-order force multipoles, the factor Δz is factored out from the hyperbolic profiles in r_z and r_z'. For the source multipoles, the identity

$\mathbf{u}^{\mathrm{SD}}(\mathbf{r}) \propto \boldsymbol{\nabla}'^2(\boldsymbol{\mathcal{G}}(\mathbf{r},\mathbf{r}')\hat{\mathbf{e}})$ results in a factor of $1/\Delta z$ instead.

In other words, the magnitude of the force multipoles increases with the height of the Hele-Shaw geometry. At the same time, the magnitude of the source multipole increases with the strength of the confinement. Thus, force and source multipoles of the same order in $\tilde{\rho}$ may only be identified in a given flow field by using their dependence on Δz.

2.4.3 Multipole expansion in the Hele-Shaw geometry

With the multipoles presented in Sec. 2.4.2 it is possible to construct a series expansion for the flow field of a microswimmer similar to the bulk fluid. Again, we consider the relevant flow fields of the source dipole ($\boldsymbol{u}_{\mathrm{SD}}$), force dipole ($\boldsymbol{u}_{\mathrm{FD}}$), force quadrupole ($\boldsymbol{u}_{\mathrm{SD}}$), and source octupole ($\boldsymbol{u}_{\mathrm{SD}}$) in the Hele-Shaw geometry

$$\mathbf{u}(\mathbf{r}) \;=\; \boldsymbol{u}_{\mathrm{SD}}(\mathbf{r}) \;+\; \boldsymbol{u}_{\mathrm{FD}}(\mathbf{r}) \;+\; \boldsymbol{u}_{\mathrm{FQ}}(\mathbf{r}) \;+\; \boldsymbol{u}_{\mathrm{SO}}(\mathbf{r}) \;+\; \dots\,. \tag{2.41}$$

Although the source quadrupole behaves equally to the force dipole in the Hele-Shaw geometry, it is omitted here because we neither observe in the bulk fluid nor in the Hele-Shaw geometry. This series is converted into a form similar to the bulk case, such that a measured or simulated flow field can be decomposed into its multipole moments and thereby determine the contributions in Eq. (2.41).

First, we switch to cylindrical coordinates (ρ, φ, z). We eliminate the z-dependence by averaging over the z coordinate, restricting the height of the singularity r'_z to $r'_z = \Delta z/2$, and then obtain the average radial component from the projection on $\hat{\mathbf{e}}_\rho$,

$$\tilde{u}_\rho(\rho,\varphi) \;\equiv\; \frac{\hat{\mathbf{e}}_\rho}{\Delta z} \cdot \int_0^{\Delta z} \mathbf{u}(\rho,\varphi,z)\,\mathrm{d}z. \tag{2.42}$$

Applying this transformation to the flow fields of the multipoles presented in Sec. 2.4.2 we identify that the radial coordinates of the velocity can be written in terms of Chebyshev polynomials of the first kind $T_n(\cos\varphi) = \cos\big(n\varphi\big)$ [125]. For example, for the force monopole we obtain

$$\tilde{u}_\rho^{\mathrm{FM}}(\rho,\varphi) = \mathcal{A}_1 \rho^{-2} T_1(\cos\varphi) \tag{2.43}$$

and for the source dipole

$$\tilde{u}_\rho^{\mathrm{SD}}(\rho,\varphi) = \mathcal{B}_1 \rho^{-2} T_1(\cos\varphi) \tag{2.44}$$

for a motion along the x axis, $\hat{\mathbf{e}} = \hat{\mathbf{e}}_x$. This form again shows the force monopole and source dipole have the same dependence on ρ and φ, resulting in the same factor $\rho^{-2}T_1(\cos\varphi)$, similar to other multipoles of the same order. Here, we have integrated the Δz dependence and remaining factors into the coefficients such that they scale as $\mathcal{A}_1 \propto \Delta z$ and $\mathcal{B}_1 \propto \Delta z^{-1}$, respectively. Applying the identities (2.35) to

(2.38) repeatedly also to higher order multipoles, one obtains a multipole series

$$\tilde{u}_\rho(\rho,\varphi) \;=\; \sum_{n=1}^{\infty} \frac{\mathcal{A}_n + \mathcal{B}_n}{\rho^{n+1}}\, T_n(\cos\varphi)\,. \tag{2.45}$$

Here, $\mathcal{A}_n \sim \Delta z$ and $\mathcal{B}_n \sim \Delta z^{-1}$ are the respective coefficients of the force and source multipole moments which all show the same scaling with the confinement strength $\sim \Delta z$ and $\sim \Delta z^{-1}$, respectively. Again we can recognize that in case of a force-free swimmer, $\mathcal{A}_1 = 0$, the source dipole becomes the most long-ranged multipole for microswimmers in the Hele-Shaw geometry.

We may use the orthogonality relations of $\cos(n\varphi) = T_n(\cos\varphi)$ to extract the multipole moments from Eq. (2.45) by projecting $\tilde{u}_\rho(\rho,\varphi)$ on the Chebyshev polynomials,

$$\tilde{u}_{\rho,n}(\rho) \;\equiv\; \frac{1}{\pi}\int_0^{2\pi} \tilde{u}_\rho(\rho,\varphi)\, T_n(\cos\varphi)\,\mathrm{d}\varphi, \tag{2.46}$$

which yields

$$\tilde{u}_{\rho,n}(\rho) = \frac{\mathcal{A}_n + \mathcal{B}_n}{\rho^{n+1}}. \tag{2.47}$$

We again stress that, in contrast to the bulk fluid [Eq. (2.29)], force and source multipoles of same order n cannot be distinguished in a given flow field in the form of Eq. (2.42) at constant Δz. Principally, the different scaling with the slab width Δz may be used to infer the coefficients $\mathcal{A}_n$ and $\mathcal{B}_n$, although in practice our simulation data presented in Section 4.2 is not always sufficiently accurate to distinguish both cases.

However, the relevant multipole coefficients may be transferred from the bulk fluid, which can be rationalized as follows. On the one hand, both multipole expansions capture the disturbance created by a microswimmer in leading order, and the characteristic distribution of force and source multipoles should remain the same in the Hele-Shaw geometry. On the other hand, in contrast to a point-like singularity higher-order terms enter to fulfill the boundary conditions on the surface of a voluminous microswimmer and on the bounding plates. However, these are short-ranged and do not contribute to the far field.

2.5 Hydrodynamic interactions

Hydrodynamic interactions emerge through the advection of particles in the flow fields created by other particles, or the by the effective flow field resulting through the reflection at a boundary as in, for example, Eq. (2.32). In the first case, the particle interacts with another particle, in the second case with a wall.

In this section we will give a brief overview over the dynamical response of spherical and elongated particles to arbitrary flow fields. Subsequently, we will

argue how this affects interactions between particles. We start with Faxén's law for spherical particles which describes velocity and reorientation resulting from a background flow. We will then describe the generalization to the case of prolate spheroids, which will also lead us to the Jeffery orbits of elongated particles in shear flow.

2.5.1 Faxén's law

Faxén's law describes the advection $\mathbf{v}$ and rotation $\boldsymbol{\omega}$ of a particle in a background flow $\mathbf{u}(\mathbf{r})$. The formalism uses a formulation of the Lorentz' reciprocal theorem, an integral theorem that follows from Green's second identity and the structure of the stress tensor [158]. The formulation

$$\oint_S \mathbf{u}(\sigma' \cdot \mathrm{d}\mathbf{S}) - \int_V \mathbf{u}(\boldsymbol{\nabla} \cdot \sigma')\mathrm{d}^3 r \;=\; \oint_S \mathbf{u}'(\sigma \cdot \mathrm{d}\mathbf{S}) - \int_V \mathbf{u}'(\boldsymbol{\nabla} \cdot \sigma)\mathrm{d}^3 r. \tag{2.48}$$

relates two different solutions $\mathbf{u}, \sigma$ and $\mathbf{u}', \sigma'$ of the Stokes equation. Choosing different solutions for $\mathbf{u}$ and $\mathbf{u}'$, the reaction of different particles shapes to specific flows can be calculated. To specifically obtain the force acting on a moving sphere of radius R, the first solution $\mathbf{u}, \sigma$ is the flow field of the sphere moving with velocity $\mathbf{v}$ which is yet to be determined. As second solution $\mathbf{u}', \sigma'$ serves the flow field of a sphere in the flow of a point force acting on the fluid. For a sphere at the position $\mathbf{r}$ the resulting hydrodynamic force is given by [157, 180]

$$\mathbf{v} \;=\; \frac{\mathbf{F}}{6\pi\eta R} + \left[1 + \frac{R^2\boldsymbol{\nabla}^2}{6}\right]\mathbf{u}(\mathbf{r}). \tag{2.49}$$

Here, the first term coincides with Stokes-law for the velocity of a sphere due to the external force $\mathbf{F}$ in the case of $\mathbf{u}(\mathbf{r}) = 0$. The first term in the square brackets is the leading order direct advection in the flow field, while the additional term $\boldsymbol{\nabla}^2\mathbf{u} = \boldsymbol{\nabla} p/\eta$ can be understood as proportional to the pressure gradient. Equivalently, the torque on a sphere is obtained by considering the flow field of a rotating sphere as first solution $\mathbf{u}, \sigma$, which results in [158]

$$\boldsymbol{\omega} \;=\; \frac{1}{2}\boldsymbol{\nabla} \times \mathbf{u}(\mathbf{r}) - \frac{\mathbf{T}}{8\pi\eta R^3} \tag{2.50}$$

For elongated particles the multipole solution of Stokes flow for prolate spheroidal particles can be inserted into the reciprocal theorem resulting in Faxén's law for prolate spheroids. The resulting advection velocity has a similar structure to Eq. (2.49), but contains a line integral over the spheroid axis. This can be understood recalling that the flow field of prolate spheroids can also be written as a superposition of lowest-order singularities. Likewise, an expression for the torque on a

prolate spheroid may be calculated. Refer to [158] for more details and complete expressions.

2.5.2 Jeffery orbits of elongated microswimmers

In contrast to spherical particles, which only rotate in response to a vortex in the velocity field, anisotropic particles also react to a shearing motion of the solvent depending on their instantaneous orientation. As a result, force-free anisotropic particles perform a periodic tumbling motion in shear flow, known as Jeffery orbits. The equations of motion may be derived using resistance tensors for the spheroid and the velocity of the solvent [171], or the corresponding Faxén law for the rotation of a prolate ellipsoid [158]. For uniaxial spheroids with director $\hat{\mathbf{e}}$, the corresponding equation for the angular velocity $\boldsymbol{\omega}(t)$ is

$$\boldsymbol{\omega}(t) = \frac{1}{2}\boldsymbol{\nabla} \times \mathbf{u}(\mathbf{r}) + \gamma \left\{ \hat{\mathbf{e}}(t) \times \left[\mathbf{E}(\mathbf{r})\hat{\mathbf{e}}(t) \right] \right\}, \tag{2.51}$$

where $\mathbf{E}(\mathbf{r}) = [(\boldsymbol{\nabla} \otimes \mathbf{u})^T + \boldsymbol{\nabla} \otimes \mathbf{u}]/2$ is the local strain rate tensor at the position $\mathbf{r}$, which we already encountered in the context of the fluid stress tensor in Eq. (2.11) [171, 181]. Further, the geometric factor $\gamma = \frac{\alpha^2-1}{\alpha^2+1} \in [0, 1]$ depends on the aspect ratio α of the elongated particles [158]. The equation of motion for the director $\hat{\mathbf{e}}$ of the spheroid is $\partial_t \hat{\mathbf{e}} = \boldsymbol{\omega}(t) \times \hat{\mathbf{e}}(t)$. The resulting solution for $\hat{\mathbf{e}}(t)$ describes orbits on a unit sphere, called Jefferey orbits. As we can also read from Eq. (2.51), in the case of a spherical particle $\alpha = 1$ only a fluid vortex with vorticity $\boldsymbol{\nabla} \times \mathbf{u}$ results in a rotation of the particle.

2.5.3 Hydrodynamic interaction between microswimmers

Hydrodynamic interactions between pairs of microswimmers are decisively characterized by the dominant hydrodynamic multipoles of their flow fields and their shapes or aspect ratios. Together with their velocities, these enter Faxén's law and describe the resulting interaction by advection and reorientations. Additionally, short-ranged interactions are described by the so-called lubrication theory [158]. We begin with the most fundamental types of interactions, which can be understood already in the context of spherical microswimmers. Considering emergent advection and reorientations described by Eqs. (2.49) and (2.50), we realize that advection resulting from the friction force $6\pi\eta R(\mathbf{u}(\mathbf{r}) - \mathbf{U})$ is most long ranged and dominates the interaction for the flow field $\mathbf{u}(\mathbf{r})$ of a given multipole. The reason is that this term decays with the inter-particle distance just as the multipole itself, while all other terms contain derivatives of $\mathbf{u}(\mathbf{r})$, which decay faster. While the leading order advection in the flow field always occurs, the pressure gradient $\boldsymbol{\nabla}^2\mathbf{u} = \boldsymbol{\nabla} p$ vanishes for source multipoles, which fulfill the harmonic equation $\boldsymbol{\nabla}^2\mathbf{u} = 0$.

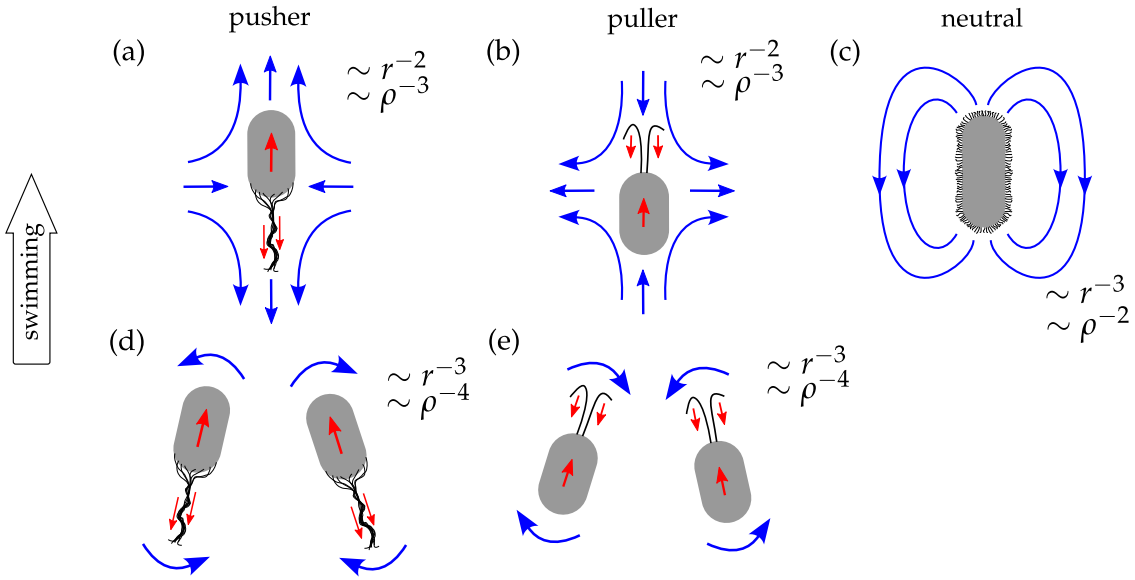

Figure 2.4: Hydrodynamic interactions between different types of microswimmers adapted from [65]. Sketch of the flow fields of (a) pusher-, (b) puller- and (c) neutral-type microswimmers. Both propulsion mechanisms create a pair of opposing forces (red arrows) distinguished by a change of sign. Advection along the stream lines (blue arrows) is the main manifestation of hydrodynamic interaction. Hydrodynamic reorientations for pairs of (d) pusher and (e) puller type microswimmers resulting from the vorticity of the flow fields shown in (a) and (b). Two pushers on an approaching trajectory are reoriented towards the swimming in parallel configuration. For pullers, the rotation is opposite such that they are reoriented towards a perpendicular configuration. In contrast, neutral microswimmer types do not impose a rotation on each other since the flow field of the source dipole has zero vorticity. For elongated microswimmers, Jeffery orbits arise due to the local strain rate tensor $\mathbf{E}(\mathbf{r})$ according to Eq. (2.51). The radial decay of the interactions is denoted in powers of r (bulk fluid) and ρ (Hele-Shaw geometry).

For pushers and pullers, which impose the flow field of a force dipole as shown in Fig. 2.4(a) and (b), this has the following implications. Pushers swimming side-by-side in parallel attract each other while pullers repel each other in the same configuration, following the stream lines. Swimming behind one another pushers repel while pullers attract each other [65]. The additional term $\sim \boldsymbol{\nabla}^2\mathbf{u}$ is more short ranged. For *neutral* swimmers, for which the source dipole is the leading-order multipole contribution, the mutual advection in the side-by-side and head-to-tail configurations cancels and therefore does not introduce a characteristic attraction or repulsion [Fig. 2.4(c)].

Regarding the reorientations, we look at the vorticity of the flow fields of the force dipole, as shown in Fig. 2.4(a) and (b). As the streamlines indicate, the sign

of the vorticity alternates in four quadrants. For pairs of swimmers, this affects a converging trajectory in two different ways. As depicted in Fig. 2.4(d), pushers on a converging path are reoriented towards a configuration swimming side-by-side in parallel. If the force dipole changes the sign for pullers, swimmers approaching each other are reoriented even more towards each other, as depicted in Fig. 2.4(e). Lastly, the source-dipole flow field does not possess a vorticity, such that neutral spherical microswimmers do not reorient. For elongated microswimmers, the local strain rate tensor $\mathbf{E}(\mathbf{r})$ creates to Jeffery orbits according to Eq. (2.51).

However, compared to the reorientation arising from the vorticity in the Faxén theorem, the effect of these periodic oscillations about a fixed axis is small.

Distinguishing between the bulk fluid and the Hele-Shaw geometry, we note that the general shape of the flow fields remain the same such that interactions qualitatively remain the same. On the other hand, the radial decay of the hydrodynamic multipoles change in the Hele-Shaw geometry such that the source dipole becomes the most-long ranged contribution of the flow field. However, as we elaborated before, the interaction via advection and reorientation mainly arise from the force dipole such that the Hele-Shaw geometry primarily implies more short-ranged interactions compared to the bulk fluid.

2.6 The squirmer model for microswimmers

The squirmer is a model for spherical microswimmers of radius R, which covers, among others, the major microswimmer types presented in Sec. 2.3. For the ciliary propulsion, the squirmer model enforces the flow velocity of a source dipole as slip velocity on surface of the microswimmer [69, 114]. This resembles the analytical solution of a moving sphere without external forces in Eq. (2.30). For spherical pusher - and puller-type microswimmers, a pair of the force dipole and source quadrupole, where the second term ensures that the normal velocity $u_r(r, \theta)$ in Eq. (2.26) vanishes on the squirmer surface [120]. In the same manner, pairs of higher order multipoles can be added to model, for example, Janus particles [182]. However, for simplicity, we restrict ourselves to terms up to $n = 2$ in Eq. (2.27) in the following. All together, we obtain the slip-velocity at the surface of the spherical microswimmer

$$\mathbf{v}_s(\hat{\mathbf{x}}_s) \;=\; B_1^s(1 + \beta\hat{\mathbf{e}} \cdot \hat{\mathbf{x}}_s)\left[(\hat{\mathbf{e}} \cdot \hat{\mathbf{x}}_s)\hat{\mathbf{x}}_s - \hat{\mathbf{e}}\right] \tag{2.52}$$

that acts on the surrounding fluid [73, 119]. Here, $\hat{\mathbf{x}}_s$ is the unit vector pointing from the squirmer center to the respective surface point, and the unit vector $\hat{\mathbf{e}}$ indicates the orientation of the squirmer. The squirmer parameter β is used to control the swimmer type by changing the ratio between source-dipole and force-dipole moment. Thereby, a value of $\beta < 0$ results in a pusher, where the slip velocity is concentrated at the rear of the sphere. Likewise, values of $\beta > 0$ concentrate the slip velocity at the front of the sphere and result in a puller. The absence of a force dipole, $\beta = 0$,

results in a neutral squirmer, as depicted in Fig. 2.5(a). For a neutral squirmer, the induced flow field in the bulk fluid is given by the flow field of a pure source-dipole singularity with strength $B_1 = B_1^s R^3$. It can be shown that the squirmer parameter B_1^s also determines the swimming speed $v_0 = 2/3 B_1^s$ [114]. The resulting surface slip-velocity field may then be used in computer simulations by enforcing the boundary condition within the MPCD method [74, 120], the Lattice-Boltzmann method [183] or the boundary-element method [184].

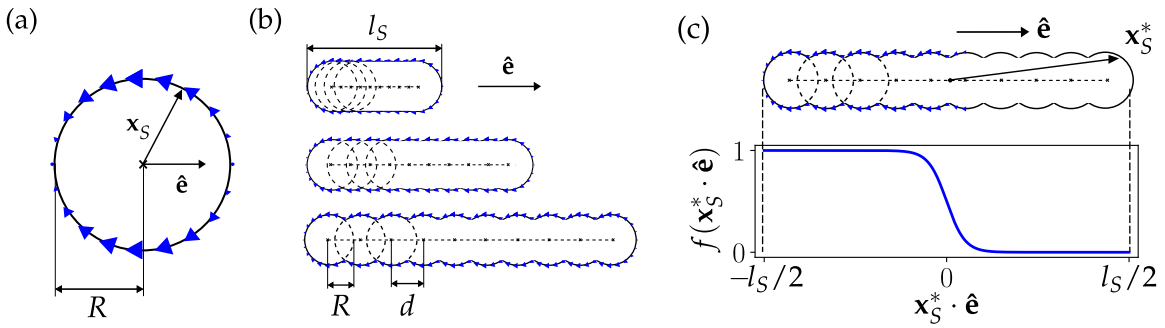

Figure 2.5: (a) Schematic of a single squirmer of radius R and with orientation given by the unit vector $\hat{\mathbf{e}}$. The surface slip-velocity field of a neutral squirmer is indicated by blue arrows. (b) Schematic of the squirmer-rod model consisting of $n_{sq} = 10$ spherical squirmers placed on a straight line separated by the distance d. All squirmer orientations $\hat{\mathbf{e}}$ are aligned with the rod axis. (c) Realization of a pusher type squirmer rod. The surface slip velocity on the rod surface is multiplied with the scalar envelope function $f(\mathbf{x}_s^* \cdot \hat{\mathbf{e}})$ given by Eq. (2.53), such that the slip-velocity is concentrated on the rear of the rod.

2.6.1 The squirmer-rod model

To pursue our main objective and investigate how the interplay of shape anisotropy of microswimmers and their hydrodynamic interactions determine their collective motion, we introduce the new squirmer-rod model [125]. Squirmer rods consist of a number of $N_{sq} = 10$ spherical squirmers [*cf.* Fig. 2.5(a)] arranged on a line to form a rigid body as shown in Fig. 2.5(b). The resulting shape mimics the actual rod shape of many biological microswimmers such as bacteria or *Paramecium*. Furthermore, the model can be extended to flexible shapes by introducing bending rigidity between the beads in future works, see chapter 5. To form rods of different aspect ratios $\alpha = l_S/2R$, where l_S is the rod length, we vary the squirmer distance d [*cf.* Fig. 2.5(b)]. To ensure a smooth surface and enable swimmers to slide past each other easily, we do not exceed a maximum squirmer distance of $d \approx 0.8R$, which amounts to a maximum aspect ratio of $\alpha = 5$. This closely resembles the aspect ratio of bacteria such as *E. coli* or *B. subtilis*. The squirmer rod propels itself via the axisymmetric

surface slip-velocity field of the neutral squirmer, which is imposed on the surface of its individual squirmers to the surrounding fluid [74, 119, 120].

To encompass pusher and puller-type microswimmers in the squirmer rod model, we concentrate the surface slip velocity either to the back or the front of the squirmer rod as shown in Fig. 2.5(c). This is achieved by multiplying the magnitude of the slip velocity by using the envelope function

$$f(\mathbf{x}_s^* \cdot \hat{\mathbf{e}}, \chi) \;=\; 1 + \chi \tanh(10\mathbf{x}_s^* \cdot \hat{\mathbf{e}}/l_S) \tag{2.53}$$

where $\mathbf{x}_s^*$ is the vector that points from the rod center to a location on the rod surface [*cf.* Fig. 2.5(c)] and $l_S/10$ is the step width of the envelope function [185]. The parameter $\chi \in [-1, 1]$ determines the swimmer type and force-dipole strength, such that for $\chi < 0$ a pusher-type swimmer is realized and likewise a puller-type swimmer for $\chi > 0$. Choosing either $\chi = -1$ or $\chi = 1$ results in one completely passive half of the rods, while for intermediate values the relative contributions of the source dipole and force dipole to the flow field vary. For $\chi = 0$, the model resembles the neutral squirmer rod [185]. With the definition that ensures that the average $\langle f(x, \chi)\rangle_x = 1$ is independent of χ, also the swimming velocity is nearly independent of χ. Note that the squirmer rod model is also related to the ellipsoidal squirmer model, which is also elongated [184, 186]. However, it features a more realistic rod shape [187, 188] and the surface-slip velocity is distributed evenly over the cell body independent of the aspect ratio [186].

2.7 Brownian motion

Additional to the self-propelled motion, microswimmers are also subject to a diffusive Brownian motion, which describes a random walk through the fluid. This motion is a result of the random collisions with the solvent particles. The combination of the diffusive and active motion is described by the so-called Langevin equation [152, 189]. In the overdamped limit of high viscosity, the particles velocity $\mathbf{v}$ and angular velocity $\boldsymbol{\omega}$ are given by [150, 161]

$$\begin{aligned} \mathbf{v}(t) \;&=\; v_0\hat{\mathbf{e}} + \boldsymbol{\mu}_T\left[-\boldsymbol{\nabla} V(\mathbf{x}, \hat{\mathbf{e}}) + \mathbf{f}_{\text{rand}}(t)\right] \quad \text{and} \\ \boldsymbol{\omega}(t) \;&=\; \boldsymbol{\mu}_R\left[-\boldsymbol{\nabla}_{\hat{\mathbf{e}}} V(\mathbf{x}, \hat{\mathbf{e}}) + \boldsymbol{\tau}_{\text{rand}}(t)\right] \end{aligned} \tag{2.54}$$

Here, $\boldsymbol{\mu}_T$ and $\boldsymbol{\mu}_R$ are the respective translational and rotational mobility tensors. In this picture, the particle moves with the self-propulsion velocity $v_0\hat{\mathbf{e}}$ and is subject to two forces. The first deterministic force due to a potential $V(\mathbf{x}, \hat{\mathbf{e}})$ corresponds to an external force or the interaction with other particles. The second force and last term $\mathbf{f}_{\text{rand}}(t)$ describes a random force, which results from the random thermal motion of the solvent particles. With the mobility $\boldsymbol{\mu}_T$ we obtain the stochastic velocity $\boldsymbol{\eta}(t) = \boldsymbol{\mu}_T\mathbf{f}_{\text{rand}}(t)$. Likewise, the angular velocity is given by the deterministic torque due to

the potential $V(\mathbf{x}, \hat{\mathbf{e}})$, and a stochastic torque $\boldsymbol{\tau}_{\text{rand}}(t)$ transferred from the solvent. The dynamic of the particle orientation then follows from $\partial_t \hat{\mathbf{e}}(t) = \boldsymbol{\omega}(t) \times \hat{\mathbf{e}}(t)$.

The stochastic velocity $\boldsymbol{\eta}(t)$ has zero mean $\langle \boldsymbol{\eta}(t) \rangle = 0$ and is delta-correlated in time with the variance $\langle \boldsymbol{\eta}(t) \otimes \boldsymbol{\eta}(t') \rangle = 2\mathbf{D}_T \delta(t - t')$, where $\mathbf{D}_T = k_\mathrm{B} T \boldsymbol{\mu}_T$ is the translational diffusion tensor given by the Stokes-Einstein relation [152]. A similar expression applies for the stochastic angular velocity $\boldsymbol{\zeta}(t) = \boldsymbol{\mu}_R \boldsymbol{\tau}_{\text{rand}}(t)$, which also has zero mean $\langle \boldsymbol{\zeta}(t) \rangle = 0$ and is delta-correlated in time $\langle \boldsymbol{\zeta}(t) \otimes \boldsymbol{\zeta}(t') \rangle = 2\mathbf{D}_R \delta(t - t')$. For the rotational diffusion tensor, the Stokes-Einstein relation reads $\mathbf{D}_R = k_\mathrm{B} T \boldsymbol{\mu}_R$. These relations for the autocorrelation of the stochastic noise terms are also a consequence of the fluctuation-dissipation theorem, because they relate the fluctuations of the random force and torque to the dissipation described by the friction tensor $\boldsymbol{\gamma}_T = \mathbf{D}_T^{-1} / k_\mathrm{B} T$ and $\boldsymbol{\gamma}_R = \mathbf{D}_R^{-1} / k_\mathrm{B} T$, respectively.

For spherical particles as, for example, the squirmers, the friction and hence diffusion tensors are rotationally symmetric and given by $\mathbf{D}_T = \mathbf{1} k_\mathrm{B} T / (6\pi\eta R)$ and $\mathbf{D}_R = \mathbf{1} k_\mathrm{B} T / (8\pi\eta R^3)$. If rod-like particles move through a fluid, they are subject to an anisotropic friction force, so that also the diffusion becomes anisotropic as a result of the Stokes-Einstein relation. In this case, the diffusion tensors are given by

$$\begin{aligned} \mathbf{D}_T &= k_\mathrm{B} T \left[\mu_\parallel (\hat{\mathbf{e}} \otimes \hat{\mathbf{e}}) + \mu_\perp (\mathbf{1} - \hat{\mathbf{e}} \otimes \hat{\mathbf{e}}) \right] \quad \text{and} \\ \mathbf{D}_R &= k_\mathrm{B} T \mu_R, \end{aligned} \tag{2.55}$$

with the mobilities [190]

$$\begin{aligned} \mu_\parallel &= \frac{\mu_0}{2\pi} \left[\ln(\alpha) - 0.207 + \frac{0.980}{\alpha} - \frac{0.133}{\alpha^2} \right], \\ \mu_\perp &= \frac{\mu_0}{4\pi} \left[\ln(\alpha) + 0.839 + \frac{0.185}{\alpha} + \frac{0.233}{\alpha^2} \right], \\ \mu_R &= \frac{3\mu_0}{\pi\alpha^2} \left[\ln(\alpha) - 0.662 + \frac{0.917}{\alpha} - \frac{0.050}{\alpha^2} \right]. \end{aligned} \tag{2.56}$$

Here, α denotes the aspect ratio of the rod-like particles and μ_0 is the Stokes mobility of a spherical particle with radius R. The rotational mobility μ_R thereby relates to rotation perpendicular to the rod axis $\hat{\mathbf{e}}$.

To discuss the resulting dynamics, we restrict ourselves to the case of a spherical active Brownian particle free of external influences $V(\mathbf{x}, \hat{\mathbf{e}}) = 0$. In this case, the random torque leads to an exponential decay of the orientational autocorrelation [26]

$$\langle \hat{\mathbf{e}}(t) \cdot \hat{\mathbf{e}}(0) \rangle = e^{-t/\tau_R},$$

where $\tau_R = [(d-1) D_R]^{-1}$ is the orientational persistence time in d dimensions. As a result, the persistent motion becomes irrelevant at large time scale. The mean square displacement is obtained by integration of the equations of motion Eq. (2.54),

resulting in

$$\langle |\mathbf{r}(t) - \mathbf{r}(0)|^2 \rangle = 2dD_T t + 2v_0^2 \tau_r t - 2v_0^2 \tau_r^2 (1 - e^{-t/\tau_r}). \tag{2.57}$$

Here, we can identify two special cases depending on the time scale of t. At times shorter that the persistence time $t \ll \tau_R$, the mean square displacement describes a persistent ballistic motion due to the active swimming velocity v_0, such that the mean square displacement

$$\langle |\mathbf{r}(t) - \mathbf{r}(0)|^2 \rangle = (v_0 t)^2 + 2dD_T t$$

grows quadratically in time $\propto t^2$. At long time scales $t \gg \tau_R$, the motion becomes diffusive due to the stochastic reorientation of the particles, such that the mean square displacement

$$\langle |\mathbf{r}(t) - \mathbf{r}(0)|^2 \rangle = 2t(dD_T + v_0^2 \tau_R)$$

grows linear in time $\propto t$. For a discussion of the motion of elongated particles we refer to ten Hagen *et al*. [191]. In order to compare the relative influences of the active persistent motion and diffusive motion to the dynamics of the active particle, another dimensionless quantity is introduced. The so-called Péclet number

$$\mathrm{Pe} = \frac{t_d}{t_a} = \frac{2Rv_0}{D_T} \tag{2.58}$$

describes the ratio of the time scales $t_d = (2R)^2/D_T$ and $t_a = 2R/v_0$, required for active Brownian particles to travel the length of the particle diameter $2R$ due to diffusion or active motion, respectively. Hence, active motion is negligible if $\mathrm{Pe} \ll 1$, while diffusive motion is not relevant for $\mathrm{Pe} \gg 1$

Also hydrodynamic interactions can be integrated into the Langevin equation via the mobility or diffusion tensors within the Rodne-Prager framework for spherical particles [161] or rods [192]. Thereby, the Faxén theorem of Eq. (2.49) is used to calculate the acting hydrodynamic forces in pairs of particles within the so-called method of reflection. Lastly, we note that the Langevin equation is physically equivalent to the Smoluchowski equation for the evolution of the probability distribution function of the active Brownian particles.

CHAPTER 3

Multi-particle collision dynamics (MPCD)

3.1 Introduction

When it comes to the numerical simulations of hydrodynamic flows, there are numerous approaches at different levels of detail and abstraction. Most commonly, differential equations that describe hydrodynamic flows are discretized and then solved using finite elements or finite volume schemes [193]. For limiting cases there are specific schemes like the boundary element method for Stokes flow that exploits the Lorentz reciprocal theorem to describe the entire flow at the boundary of the domain [159].

Another approach is followed in the so-called mesoscopic schemes, which includes the methods of multi-particle collision dynamics (MPCD), dissipative-particle dynamics [194, 195], smoothed-particle hydrodynamics [194, 196] and the lattice-Boltzmann method [197]. Common for this class is the utilization of coarse-grained fluid particles that evolve according to simple dynamic rules [74, 194]. These rules are defined such that the resulting hydrodynamic flow field fulfills the Navier-Stokes equations [126, 198] In contrast, the lattice-Boltzmann method begins at a lower level of description and discretizes the Boltzmann equation for the velocity distribution function of the solvent particles [197, 199].

Since their introduction in 1999 [126], algorithms belonging to the method of multi-particle collision dynamics (MPCD) have become a standard tool for the simulation of fluid flows in the field of soft-matter physics [74, 200, 201]. In particular, MPCD algorithms have been used extensively in the context of microswimmers [41, 47, 73, 76, 91–96, 125, 202, 203], to cite only a few examples. Other studies with MPCD cover polymers [139–141], colloidal suspensions [134–138], blood cells [142], the African trypanosome as the causative agent of the sleeping sickness [143], and even schools of fish [144]. Also extensions to binary fluid mixtures [145], liquid

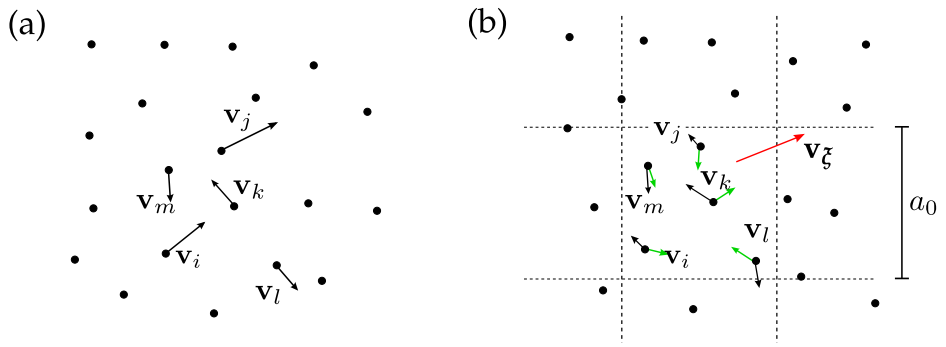

Figure 3.1: Sketch of the particle motion and collision rule in the MPCD method. The fluid is represented by point like-particles (back dots) with continuous positions and velocities (back arrows). The two steps mimic the ballistic motion and collision of particles. In the streaming step (a) particles move ballistically for the duration of Δt. For the collision step (b) the space is divide in a cubic lattice with lattice constant a_0 to form groups of particles. The particles in these cells then exchange momentum (green arrows) and energy according to a collision rule, while conserving the total momentum $m_0 n_\xi \mathbf{v}_\xi$. Some methods resemble the micro-canonical ensemble, such that also the energy in the cell is conserved.

crystals [146–148], and chemically reacting systems[149] exist.

In our simulations, we employ a specific MPCD method that incorporates a so-called Andersen thermostat and features angular-momentum conservation (MPCD-AT+a) [73, 204]. Furthermore, we developed an extended version of MPCD with a non-ideal equation of state and thus a reduced compressibility that enables accurate simulations of dense microswimmer configurations [205, 206]. By solving the Navier-Stokes equations, the method treats hydrodynamic interactions between active squirmer rods and also with the confining walls of the Hele-Shaw geometry [126, 201]. Furthermore, thermal fluctuations are included in the method.

In concrete, the MPCD method considers point-like particles with number density n_0 and defines simplified rules for the two dynamic stages in their motion, which are ballistic motion and collisions, as sketched in Fig. 3.1. These rules are then applied in alternating steps [126]. In the following we will first introduce the streaming step which is common to all MPCD variants. We will then give a brief overview over the most common collision rules and discuss their specific properties.

3.2 Streaming step

During the streaming step the point particles with masses m_0, positions $\mathbf{x}_i(t)$, and velocities $\mathbf{v}_i(t)$ move ballistically during the time Δt according to

$$\mathbf{x}_i(t + \Delta t) = \mathbf{x}_i(t) + \mathbf{v}_i(t)\Delta t. \tag{3.1}$$

This motion represents the free motion of a particle in the fluid before a collision occurs, which is represented by the collision step. During the streaming step, particles collide with confining walls or moving objects such as squirmers in our case [47, 73, 74, 76, 94, 125] and thereby transfer both linear and angular momentum, in particular, to the squirmers. The so-called bounce-back rule [126, 128] enforces the no-slip boundary condition at confining walls or the slip-velocity field at the squirmer surfaces [125].

3.3 Collision step

The key of the MPCD collision step is to define a simplified multi-particle collision rule, which ensures momentum conservation. It can be shown that this is sufficient to guarantee that the model fulfills the Navier-Stokes equations [126]. The resulting methods are efficient for the numerical solution of hydrodynamic flows, and enable the usage of powerful parallel computing architectures [132]. Furthermore, model parameters can be derived by analytical calculations [194, 207].

To approach the MPCD collision rule, we begin with the very intuitive variant of the so-called stochastic rotation dynamics (SRD), which was formulated by Malevanets and Kapral [126]. We will then cover variants with different thermodynamic and mechanical properties as the utilization of a thermostat and the incorporation of angular momentum conservation. We will then approach more complex collision rules that generate different thermodynamic equations of state as a result of a tailored inherent momentum transport mechanism [205, 206, 208]. However, we stress again that all collision rules conserve momentum, and therefore obey the Navier-Stokes equations.

Generic for all collision rules, the simulation volume is first divided into a cubic lattice and the fluid particles are grouped into cubic unit cells of linear size a_0 and centered around $\boldsymbol{\xi}$ as depicted in Fig. 3.1(b). Thereby, the total number of particles is chosen such that, on average, a number of n_0 particles resides in each cell of unit volume a_0^3. Then, for the $n_{\boldsymbol{\xi}}$ particles in each cell volume $\mathcal{V}_{\boldsymbol{\xi}} = a_0^3$ around $\boldsymbol{\xi}$ the mean velocity $\mathbf{v}_{\boldsymbol{\xi}}$ and center-of-mass position $\mathbf{x}_{\boldsymbol{\xi}}$ are determined. At this point one of the following collision rules is applied to the particles within each cell. Lastly, before the following collision step, the cubic lattice is randomly shifted to ensure Galilean invariance [208].

3.3.1 Stochastic rotation dynamics (SRD)

The collision rule of the SRD method consists of a rotation of the thermal velocities $\mathbf{v_i} - \mathbf{v}_{\boldsymbol{\xi}}$ around a randomly chosen axis $\hat{\mathbf{n}}_{\boldsymbol{\xi}}$, which is different for each cell $\boldsymbol{\xi}$ and time step, by the constant angle α [126]. With the rotation matrix $\mathbf{R}(\hat{\mathbf{n}}_{\boldsymbol{\xi}}, \alpha)$ the collision

step can be summarized as

$$\mathbf{v}_i^{\text{new}} \;=\; \mathbf{v}_\xi + \mathbf{R}(\hat{\mathbf{n}}_\xi, \alpha)\left(\mathbf{v}_i - \mathbf{v}_\xi\right). \tag{3.2}$$

As can be easily proven, this rule conserves the momentum $m_0 n_\xi \mathbf{v}_\xi$, thermal energy $E_\xi = \frac{m_0}{2n_\xi}\sum_{\mathbf{x}_i\in\mathcal{V}_\xi}(\mathbf{v}_i - \mathbf{v}_\xi)^2$ and, trivially, the number of particles n_ξ within each collision cell. With these properties, it can be shown that the resulting flow field obey the Navier-Stokes equation and the hydrodynamic equation of energy transport. Furthermore, it can be proven that the dynamics fulfills the Boltzmann H-theorem such that the system evolves towards thermodynamic equilibrium under the SRD algorithm [126]. The model parameter α decisively controls the local redistribution of momentum and energy and therefore describes other parameters of the SRD fluid, as the viscosity [207]. Typically, values are chosen around 120°. In two dimensions, the rotation axis is perpendicular to the xy-plane, and the rotation angle randomly selected between $\pm\alpha$ [207].

Due to the rotation of the relative velocities, the method does not conserve angular momentum locally at the scale of the collision cells. This leads to incorrect angular diffusion of immersed solute particles [209]. Angular-momentum conservation can be restored by declaring the collision angle within each cell $\alpha_\xi(\{\mathbf{x}_i \mid \mathbf{x}_i \in \mathcal{V}_\xi\})$ a function of the instantaneous position of the particles. This extension was proposed by Ryder for SRD in two dimensions [201, 210].

To realize simulations in the canonical ensemble, a thermostat can be added to the SRD method. In this case, the total kinetic energy in each cell E_ξ relative to $\mathbf{v}_\xi$ is calculated. Then, a random new thermal energy E'_ξ is generated from the appropriate gamma distribution, which follows from the Maxwell-Boltzmann distribution for the $3(n_\xi - 1)$ velocities. Lastly, all thermal velocities are rescaled with the factor E'_ξ/E_ξ [211]. In the canonical ensemble the SRD method has further been extended to restore angular-momentum conservation of the collision rule. In this case, a correction is added to the new velocities following from Eq. (3.2) and the rescaling with the thermostat [212]. We elaborate this procedure in detail in the context of the MPCD method with Andersen thermostat in Sec. 3.3.2.

3.3.2 MPCD with Andersen thermostat

The MPCD algorithm with Andersen thermostat (MPCD-AT) describes fluids in the thermodynamic canonical ensemble. In the collision step, fluid particles are assigned new random thermal velocities $\delta\mathbf{v}_i$ relative to the center-of-mass velocity which are drawn from a Boltzmann-distribution with variance $\sqrt{k_B T_0/m_0}$ [74, 125, 204].

To restore overall momentum conservation, the change in linear momentum per particle, $m_0\Delta\mathbf{v}_\xi = \frac{m_0}{n_\xi}\sum_{\mathbf{x}_i\in\mathcal{V}_\xi}\delta\mathbf{v}_i$, is subtracted from each particle velocity, such that

the final new velocity reads

$$\mathbf{v}_i^{\text{new}} \;=\; \mathbf{v}_\xi + \delta\mathbf{v}_i - \Delta\mathbf{v}_\xi. \tag{3.3}$$

The collision step of the MPCD-AT method can be adapted to realize angular momentum conservation, and is then denoted by (MPCD-AT+a). To achieve this, a correction term is added to Eq. (3.3) containing the angular momentum before the collision $\mathbf{L}_\xi = \frac{m_0}{n_\xi}\sum_{\mathbf{x}_i\in\mathcal{V}_\xi}\mathbf{x}_{i,c}\times\mathbf{v}_i$, and the angular momentum introduced by the random velocities $\Delta\mathbf{L}_\xi = \frac{m_0}{n_\xi}\sum_{\mathbf{x}_i\in\mathcal{V}_\xi}\mathbf{x}_{i,c}\times\delta\mathbf{v}_i$. Here $\mathbf{x}_{i,c}$ denotes the particle position relative to the center-of-mass position $\mathbf{x}_\xi$. With the additional correction term, the collision step can be summarized by

$$\mathbf{v}_i^{\text{new}} \;=\; \mathbf{v}_\xi + \delta\mathbf{v}_i - \Delta\mathbf{v}_\xi - \mathbf{x}_{i,c}\times\mathbf{I}_\xi^{-1}(\,\mathbf{L}_\xi - \Delta\mathbf{L}_\xi\,), \tag{3.4}$$

Here, $\mathbf{I}_\xi$ is the moment-of-inertia tensor of the configuration of particles inside $\mathcal{V}_\xi$ relative to the center-of-mass, such that $\Delta\boldsymbol{\omega} = \mathbf{I}_\xi^{-1}(\mathbf{L}_\xi - \Delta\mathbf{L}_\xi)$ corresponds to a correcting contribution in the angular velocity. Similar to the stochastic rescaling of the thermal energy in the SRD method in Sec. 3.3.1, rescaling the thermal energy in the MPCD-AT to the value before the collision can be used to perform simulations in the micro-canonical ensemble [194].

In general, the MPCD-AT and SRD versions of MPCD show a similar performance in simulations, and can be applied almost interchangeably. However, one difference is the relaxation time to thermodynamic equilibrium. For SRD the relaxation time increases with the mean density n_0, while it decreases for MPCD [201]. At the same time, the numerical implementation poses different challenges. For MPCD efficient and fast random number generators are required to generate $3n_\xi$ random numbers for the normal distribution. In contrast, SRD requires only 2 random floating point numbers to generate a rotation axis, but generating a random energy E'_ξ, which follows the gamma distribution, is numerically intensive. In our experience the computational cost of the two different collision steps with thermostat and angular momentum conservation are rather similar. In implementations on graphic cards, which have immense numerical capabilities, the performance is instead dominated by the efficient organization of the data transfer between the memory and the processor. This is common for all MPCD algorithms, which require multiple gigabytes of data to describe the state of the fluid particles.

3.3.3 Equation of state

In this section, we address how the macroscopic thermodynamic pressure of the MPCD fluid can be derived from the microscopic dynamics of the streaming and collision step. To calculate the equation of state for the pressure, we use the experimental definition of pressure as the normal component of the momentum flux

through an arbitrarily oriented plane for the fluid in thermal equilibrium, *i.e.*, without gradients in the velocity field [207]. This is important to avoid contributions to the normal component of the momentum flux which arise from the bulk viscosity in the presence of gradients in the velocity field. In general, both the MPCD streaming and collision step contribute to the pressure:

$$P \;=\; P_{\mathrm{str}} + P_{\mathrm{coll}}\,. \tag{3.5}$$

During the streaming step, particles do not interact and simply transport momentum by moving across any plane considered. This results in the ideal gas contribution $P_{\mathrm{str}} = n_0 k_{\mathrm{B}} T / a_0^3$, which is common for all MPCD methods [145].

To evaluate the contribution P_{coll} from the collision step, we consider the momentum flux across a plane with unit area a_0^2, which lies inside a collision cell. Without loss of generality, we choose the plane perpendicular to the y-axis at position y_0 and then average over all y_0. During the collision step momentum is transported from the region $y < y_0$ across the plane into the region $y > y_0$ during time Δt. Thus, for the pressure as momentum transfer per area and time we obtain

$$P_{\mathrm{coll}} \;=\; \frac{m_0}{a_0^2 \Delta t} \left\langle \hat{\mathbf{y}} \cdot \sum_{\{i | y_i > y_0\}} (\mathbf{v}_i^{\mathrm{new}} - \mathbf{v}_i) \right\rangle . \tag{3.6}$$

Here, i is restricted to all particles $y_i > y_0$ and $m_0 \hat{\mathbf{y}} \cdot (\mathbf{v}_i^{\mathrm{new}} - \mathbf{v}_i)$ is the change in the normal momentum component of particle i during collision as given in, for example, Eq. (3.4). The change in momentum is thereby transferred to the particles $y_i < y_0$, such that these particles are included in this consideration implicitly. The average goes over all possible collisions, particle configurations, and positions y_0. For the traditional MPCD methods presented above, the collisional contribution vanishes since there is no correlation between the velocity change $(\mathbf{v}_i^{\mathrm{new}} - \mathbf{v}_i)$ and the positions y_i. In consequence, traditional MPCD possesses the thermodynamic equation of state of the ideal gas [145]. In simulations of Stokes flow far from mechanical equilibrium this may cause artifacts, because large density inhomogeneities arise to resolve the Stokes pressure in an ideal gas [41, 206]. This, in turn, leads to inhomogeneous material properties, such as the viscosity of the fluid [206].

As Ihle, Tützel, and Kroll demonstrated, introducing position and velocity dependent collision rules in two dimensions results in different material properties, in particular, a non-ideal equation of state [213]. As depicted in Fig. 3.2, pairs of neighboring collision cells connected by red arrows are chosen randomly between the configurations (i)-(iv). Using a stochastic collision with a probability that depends on the densities and relative velocities in the pairs of cells, the method mimics hard-sphere collisions. Most importantly, the collision is only initiated if the particle groups move towards each other. Exchanging the relative velocities of the two particle groups, the modified collision rule introduces a directed momentum flux at equilibrium [213].

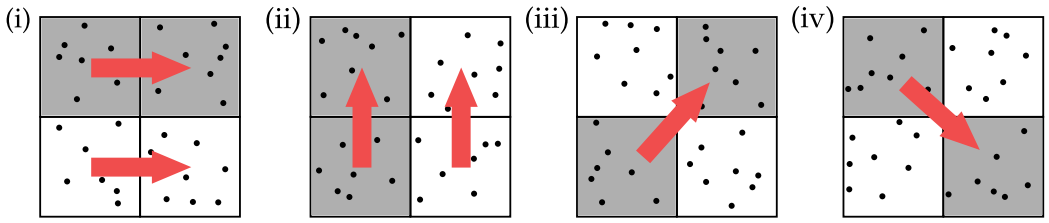

Figure 3.2: Sub-divided collision cells used to implement a position, velocity and density dependent collision rule in two dimensions adapted from Ref. [213].

3.3.4 Shear viscosity

Similar to the pressure and equation of state, the shear viscosity consists of two contributions from the streaming and collision step, respectively,

$$\eta \;=\; \eta_{\text{str}} + \eta_{\text{coll}}\,. \tag{3.7}$$

The dynamic shear viscosity thereby relates the off-diagonal component of the viscous stress tensor $\sigma'_{xy} = \eta\partial_y v_x = \eta\dot{\gamma}$ in the linear shear flow $\mathbf{v}(y) = \dot{\gamma}y\hat{\mathbf{x}}$ with the constant shear rate $\dot{\gamma}$. As for the pressure in Sec. 3.3.3, we may use that the momentum flux through a plane in the fluid is equivalent to components of the viscous stress tensor $\boldsymbol{\sigma}'$ to determine the shear viscosity of the MPCD method [207].

The contribution of the streaming step is determined by the correlation between the velocity components $\langle v_x v_y\rangle$ of a fluid particle, since only correlated velocity components result in a flux of the x component of momentum along the y direction. The velocity correlation function $\langle v_x v_y\rangle$ changes during both the streaming and collision step, but should recover its initial state after one step cycle in the steady state. Using this self-consistency condition, one can ultimately determine $\langle v_x v_y\rangle$ and the contribution to σ'_{xy} (see Refs. [205] and [207] for more details).

For the contribution of the collision step, we again consider momentum transported within a collision cell from the region $y < y_0$ across the plane into $y > y_0$ during time Δt. Compared to Eq. (3.6) for the pressure, we now need the transfer of the x component of momentum per area and time, thus

$$\sigma'_{xy} \;=\; -\frac{m_0}{a_0^2\Delta t}\left\langle \hat{\mathbf{x}}\cdot\sum_{i|y_i>y_0}\mathbf{v}_i^{\text{new}} - \mathbf{v}_i\right\rangle. \tag{3.8}$$

To obtain η_{coll}, Eq. (3.8) is then evaluated in the linear shear flow using that $\sigma'_{xy} = \eta\dot{\gamma}$.

The time step Δt naturally determines the ratio of the two contributions to the viscosity. The collisional contribution, $\eta_{\text{coll}} \sim 1/\Delta t$, scales with the frequency of the collision, while in the streaming step, $\eta_{\text{str}} \sim \Delta t$. Large mean-free paths $\lambda \sim \Delta t$ imply that the models behave more like a gas. Thus, $\Delta t \ll 1$ are applied to realize highly

viscous flows in the context of microswimmers. Then, the collisional contribution η_{coll} dominates.

For the SRD method with or without thermostat one obtains the expressions [207]

$$\begin{aligned} \eta_{\text{str}}^{\text{SRD}} &= \frac{nk_BT\Delta t}{a^3}\left[\frac{5n}{(n-1+e^{-n})[4-2\cos(\alpha)-2\cos(2\alpha)]}-\frac{1}{2}\right] \quad \text{and} \\ \eta_{\text{coll}}^{\text{SRD}} &= \frac{m_0\left(n-1+e^{-n}\right)}{18a_0\Delta t}\left(1-\cos(\alpha)\right). \end{aligned} \tag{3.9}$$

in the case of three spatial dimensions.

For the MPCD method with Andersen thermostat, one obtains [194]

$$\begin{aligned} \eta_{\text{str}}^{MPCD-AT} &= \frac{n_0k_{\text{B}}T\Delta t}{m_0}\left(\frac{n_0}{n_0-1+e^{-n_0}}-\frac{1}{2}\right) \quad \text{and} \\ \eta_{\text{coll}}^{MPCD-AT} &= \frac{a_0^2\left(n_0-1+e^{-n_0}\right)}{12\Delta t}. \end{aligned} \tag{3.10}$$

It is important to note that for MPCD-AT the collisional contribution to the stress tensor is not symmetric, which means the violation of angular-momentum conservation [201]. To restore the symmetry of the stress tensor of a Newtonian fluid, the antisymmetric part of the velocity gradient $\widetilde{\sigma}' = \sigma' + \widetilde{\eta}\left[(\boldsymbol{\nabla}\otimes\mathbf{u})^T - \boldsymbol{\nabla}\otimes\mathbf{u}\right]$ is added. Here, $\tilde{\eta}$ is the antisymmetric part of the viscosity, which vanishes in angular momentum conserving systems $\tilde{\eta}=0$. With the Cauchy momentum equation Eq. (2.8) and assuming an incompressible fluid, this results in [209]

$$\rho\left(\partial_t\mathbf{u}+\mathbf{u}\cdot\boldsymbol{\nabla}\mathbf{u}\right) = -\boldsymbol{\nabla}p+(\eta+\widetilde{\eta})\boldsymbol{\nabla}^2\mathbf{u}+\mathbf{f}_{\text{ext}}. \tag{3.11}$$

Although flow fields are not affected, this leads to spurious torques which influence the dynamics of solute particles [209, 214]. Using a kinetic theory, one can show that both contributions to the viscosity need to be equal, $\eta_{\text{coll}} = \widetilde{\eta}_{\text{coll}}$ [215]. This can be understood considering that the angular momentum of the particles in the collision cell is induced by the vorticity of the shear flow, which generates the angular velocity $\boldsymbol{\omega} = (\boldsymbol{\nabla}\times\mathbf{v})/2 = -(\dot{\gamma}/2)\hat{\mathbf{z}}$. Hence, preserving the associated velocity $\boldsymbol{\omega}\times\mathbf{x}_{i,c}$ during the collision step essentially reduces the viscous momentum transport by a factor of two by eliminating $\widetilde{\eta}_{\text{coll}}$.

This is reflected in the expressions for the collisional viscosity of the collision rule MPCD-AT+a with conserved angular momentum [194]. For sufficiently large n_0, the

streaming and collisional viscosity contributions read

$$\eta_{\mathrm{str}}^{MPCD-AT+a} = \frac{n_0 k_{\mathrm{B}} T \Delta t}{m_0} \left[\frac{n_0}{n_0 - (d+2)/4} - \frac{1}{2} \right] \quad \text{and}$$
$$\eta_{\mathrm{coll}}^{MPCD-AT+a} = \frac{a_0^2 \, (n_0 - 7/5)}{24 \Delta t}, \tag{3.12}$$

where d denotes the number of spatial dimensions.

For the SRD method with thermostat and angular-momentum conservation, values for the viscosity are obtained by simulations [41]. As elaborated before, the angular momentum conservation reduces the collisional viscosity by a factor of two. For common collision angles around $\alpha = 130^\circ$, the values of the collisional viscosity are comparable to MPCD-AT+a.

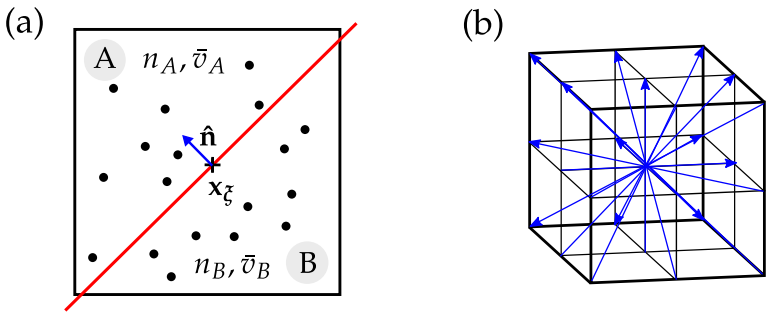

Figure 3.3: (a) Side view of a collision cell divided by a plane (red line) through the center-of-mass position $\mathbf{x}_\xi$ and with the unit normal vector $\hat{\mathbf{n}}$. (b) Normal vectors $\hat{\mathbf{n}}$ of the 13 possible collision directions. They point to the corners, as well as the centers of the edges and faces of the collision cell [205].

3.4 Extended MPCD method with non-ideal equation of state

In Ref. [205] we suggested an alternative MPCD algorithm compared to the original SRD [126] or MPCD-AT method [74]. In the following, we briefly describe the most important properties of the algorithm based on Ref. [205]. The main difference of this extended MPCD method is that the collision rule depends on both the positions and velocities of the fluid particles. This mechanism generates a momentum flux, which contributes to the pressure in the isotropic part of the stress tensor and, thereby, generates a non-ideal equation of state. The collision rule thus generalizes the method introduced in Ref. [213] to three dimensions.

In particular, collisions occur among two groups of particles at random, with a probability that depends on the local density and velocities, and only if the two

groups move towards each other. To select two groups of particles in three dimensions, we divide each collision cell into two halves A and B by a plane with the unit normal vector $\hat{\mathbf{n}}$ and containing the center-of-mass position $\mathbf{x}_\xi$ [see Fig. 3.3(a)]. At each collision step $\hat{\mathbf{n}}$ is chosen at random from a discrete set of 13 possible orientations for each cell, as shown in Fig. 3.3(b). This enables the analytic calculation of transport properties [205]. Alternatively, $\hat{\mathbf{n}}$ may also be chosen randomly on the unit sphere, which even increases the viscosity of the model slightly.

To introduce a momentum flux during the collision, the particle groups exchange the relative momentum along the unit vector $\hat{\mathbf{n}}$. To define the rate of the random collisions, we use the mean velocities $\bar{v}_A$ and $\bar{v}_B$ along the normal vector $\hat{\mathbf{n}}$ on both sides of the plane to define the relative velocity $\Delta u = \bar{v}_B - \bar{v}_A$. Thereby, we define $\hat{\mathbf{n}}$ such that it always points towards region A, and $\Delta u > 0$ when the groups approach each other. With the numbers of particles n_A an n_B in the two groups and the scattering cross section c, the collision rate $c\,\Delta u\,n_A\,n_B$ is similar to the rate of collision in two clouds of hard-core particles and can be derived from the collision term of the Boltzmann equation [216]. Accordingly, we introduce the collision probability

$$p(\Delta u) \equiv \Theta(\Delta u)\, c\Delta u\, n_A n_B \tag{3.13}$$

$$\approx \Theta(\Delta u)\left[1 - \exp\Big(-c\Delta u\, n_A n_B\Big)\right], \tag{3.14}$$

where the exponential ensures that $p(\Delta u) \leqslant 1$, assuming a sufficiently small c. Further, the Heaviside step function $\Theta(\Delta u)$ ensures that collisions only occur when the groups approach each other.

3.5 Boundary conditions and solute particles

If boundaries like walls or solute particles are immersed in the MPCD fluid, they are coupled to the fluid in both the streaming and collision step. During the streaming step, fluid particles collide with the boundaries and thereby exchange momentum, in particular, with the solute particles. To implement a no-slip boundary condition for the fluid flow, the so-called bounce-back rule is applied. This means that the velocity of a fluid particle is reversed $\mathbf{v}_i^{\text{new}} = -\mathbf{v}_i$ upon collision with a solid wall, as shown in Fig. 3.4(a).

In the case of a moving colloid or with the imposed slip velocity field on the surface of a squirmer $\mathbf{v}_\text{s}(\hat{\mathbf{x}}_i)$ given in Eq. (2.52), the bounce-back rule implies that

$$\mathbf{v}_i^{\text{new}} \;=\; -\mathbf{v}_i + 2\left[\mathbf{p}/m + \boldsymbol{\omega}\times(\mathbf{x}_i - \mathbf{r}) + \mathbf{v}_\text{s}(\hat{\mathbf{x}}_{i,s})\right]. \tag{3.15}$$

Here, $\mathbf{r}$ and $\mathbf{p}/m$ are the center-of-mass position and velocity of the solute particle and $\hat{\mathbf{x}}_{i,s}$ is a unit vector that points from the center of the squirmer to the position of the fluid particle $\mathbf{x}_i$ [see Fig. 3.4(a)]. The change of momentum of the fluid particle is

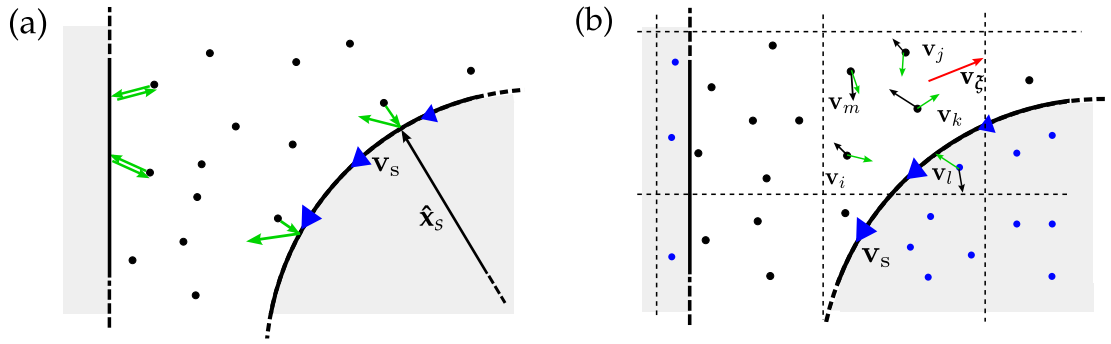

Figure 3.4: Coupling of the MPCD fluid to immersed boundaries. (a) During the streaming step, particles collide with the solid walls according to the bounce-back rule and exchange momentum with solute particles. (b) In the collision step, ghost particles are distributed in the region of the boundaries with density n_0. These participate in the collision and their momentum change is assigned to the respective solute particles.

thereby subtracted from the solute particle, such that the total linear and angular momenta of solvent and solute particles are conserved.

In the MPCD collision step, the walls and solute particles contain so-called "ghost" or "virtual" particles, which are randomly distributed in the collision cells which overlap with the boundaries, as shown in blue in Fig. 3.4(b). The ghost particles thereby guarantee that the number density remains equal to n_0. Before the collision step, their velocities are initialized as the local velocity of the translating and rotating solute particles with the addition of a random thermal velocity $\delta\mathbf{v}_{\mathrm{MB}}$ drawn from the Boltzmann distribution

$$\mathbf{v}_{\mathrm{ghost}} = \mathbf{p}/m + \boldsymbol{\omega} \times (\mathbf{x}_{\mathrm{ghost}} - \mathbf{r}) + \mathbf{v}_{\mathrm{s}}(\hat{\mathbf{x}}_{\mathrm{ghost},s}) + \delta\mathbf{v}_{\mathrm{MB}}. \tag{3.16}$$

Here, $\hat{\mathbf{x}}_{\mathrm{ghost},s}$ is a unit vector that points from the center of the squirmer to the nearest point on the surface. In case of solid walls, only a random thermal velocity is assigned. After the collision step, the changes in linear and angular momentum of the ghost particles are assigned to the relevant squirmer, which ensures the conservation of linear and angular momentum.

On the one hand, the use of ghost particles improves the validity of the no-slip condition, on the other hand, they prevent that the density dependent fluid properties do not deviate due to partially empty collision cells at boundaries [128].

3.6 Molecular dynamics of solute particles

Treating solute particles immersed in the MPCD fluid requires additional integration methods known from molecular dynamics (MD) or event driven simulations. In our case, interactions between solute particles are described by smooth potentials such

that MD methods apply to solve the equations of motion for the solute positions $\mathbf{r}$ and orientations $\mathbf{e}$.

In particular, repulsive forces act between pairs of squirmers that were introduced in Sec. 2.6, and also when they belong to different squirmer rods introduced in Sec. 2.6.1. The forces are described by the Weeks-Chandler-Andersen (WCA) potential, which is a purely repulsive modification of the well-known Lennard-Jones potential [217]. The WCA potential is defined as

$$V_{\mathrm{WCA}}(r) \;=\; \begin{cases} 4\epsilon\left[(\sigma/r)^{12}-(\sigma/r)^{6}\right]+\epsilon & \text{if } r/\sigma < \sqrt[6]{2}, \\ 0 & \text{else,} \end{cases} \tag{3.17}$$

where r is the particle-particle distance, ϵ describes the interaction energy, and σ the interaction range. The first part of the potential thereby is the Lennard-Jones potential shifted by ϵ, which has a minimum at the distance $r_{\min} = \sigma\sqrt[6]{2}$ with $V_{\mathrm{WCA}}(r_{\min}) = 0$. The step-wise definition guarantees that the potential is continuously differentiable and goes to zero at the cutoff distance. For squirmer rods, we set $\sigma = 2R_{\mathrm{sq}}/\sqrt[6]{2}$ as the diameter of the squirmer and choose a large interaction energy $\epsilon \sim 10^4 k_{\mathrm{B}}T$ to mimic hard-core interactions [205].

Because the squirmer rods are considered as rigid bodies, these squirmer interactions result in respective forces and torques acting on the rods [218],

$$\mathbf{F} \;=\; -\boldsymbol{\nabla}\sum_{ij} V_{\mathrm{WCA}}(r_{ij}) \quad \text{and} \quad \boldsymbol{\tau} \;=\; -\sum_{ij} \mathbf{r}_{i,c} \times \left[\boldsymbol{\nabla} V_{\mathrm{WCA}}(r_{ij})\right]. \tag{3.18}$$

Here, i iterates over squirmers in the rod under consideration, j over all squirmers of different rods and $\mathbf{r}_{i,c}$ denotes the squirmer position in the center-of-mass frame of the rod.

The motion of the squirmer rods is therefore characterized by the forces $\mathbf{F}$, torques $\boldsymbol{\tau}$, their mass m, and their moment-of-inertia tensor $\mathbf{I} = \mathrm{diag}(I_1, I_2, I_3)$, written in their center-of-mass frame aligned along the principle axes. The rotational symmetry of the squirmer rods implies $I_1 = I_2$ with $\hat{\mathbf{e}} = \hat{\mathbf{e}}_z$ in the body-fixed frame [125, 219]. The equations of motion for momentum $\mathbf{p}$ and angular momentum $\mathbf{L}$ of the squirmer rods are

$$\frac{\mathrm{d}\mathbf{p}}{\mathrm{d}t} \;=\; \mathbf{F} \quad \text{and} \quad \frac{\mathrm{d}\mathbf{L}}{\mathrm{d}t} = \boldsymbol{\tau}. \tag{3.19}$$

Further, the orientation of the squirmer rod evolves as $\dot{\mathbf{e}} = \boldsymbol{\omega} \times \mathbf{e}$, where $\boldsymbol{\omega} = \mathbf{I}^{-1}\mathbf{L}$. To integrate these dynamics into our simulation method, we alternate between the MPCD steps and the MD integration. During the MPCD steps, the fluid particles exchange energy and momentum with the solute particles (squirmer rods) as described in Sec. 3.5. During the MD integration the exchanged momenta are considered together with the acting forces and torques. One cycle of the combined integration scheme consist of

1. the MPCD streaming step,
2. the MPCD collision step,
3. the MD integration with the refined time step $\delta t = \Delta t/10$,
4. resolving the overlap of solutes and fluid particles.

The MD integration **3** is performed with a symplectic splitting method for rigid body dynamics, which provides a high accuracy through a precise conservation of energy [219]. To tune the precision of the MD integration independent of the MPCD time step Δt, which determines the fluid properties, we introduce the MD time step $\delta t = \Delta t/10$. The coupling to the fluid, which is subject to the Andersen thermostat, guarantees that the whole system is in the canonical ensemble.

In the following, we provide a brief overview of the symplectic splitting method for the integration of the rigid-body positions $\mathbf{r}(t)$ and orientations $\hat{\mathbf{e}}(t)$ according to Ref. [219]. The MD method uses the leapfrog variant of the well-known velocity Verlet method to integrate the translational degrees of freedom [218] and includes additional steps to integrate the orientations $\hat{\mathbf{e}}(t)$ of, for example, the squirmer rods [219]. The MD method is initiated by advancing the linear and angular momentum by half a time step $\delta t/2$

$$\begin{aligned} \mathbf{p}(t+\delta t/2) &= \mathbf{p}(t) + \mathbf{f}(t)\delta t/2, \\ \mathbf{L}(t+\delta t/2) &= \mathbf{L}(t) + \boldsymbol{\tau}(t)\delta t/2. \end{aligned} \tag{3.20}$$

Then, the positions are advanced by a complete time step δt

$$\mathbf{r}(t+\delta t) = \mathbf{r}(t) + \mathbf{p}(t+\delta t/2)\delta t/m, \tag{3.21}$$

Before advancing the momenta to the full time step $t+\delta t$ with the updated forces and torques in the second step, we integrate the angular degrees of freedom, in particular, the orientations $\hat{\mathbf{e}}(t)$ of the squirmer rods.

The scheme by Dullweber *et. al* [219] thereby considers the dynamics of the rotation matrix $\mathbf{Q}(t)$, that describes the reorientation $\hat{\mathbf{e}}(t) = \mathbf{Q}^T(t)\hat{\mathbf{e}}_0$ that the rigid body has undergone with respect to a fixed reference frame $\hat{\mathbf{e}}_0 = \hat{\mathbf{z}}$. For our case of a rotationally symmetric rigid body, the update of $\mathbf{Q}(t)$ is

$$\mathbf{Q}(t+\delta t) = \mathbf{Q}(t)\mathbf{R}_z^T\mathbf{R}_{\mathbf{L}(t)}^T, \tag{3.22}$$

where $\mathbf{R}_{\mathbf{L}(t)}^T$ is the rotation matrix about the axis $\mathbf{L}(t)$ by the angle $\delta t|\mathbf{L}(t)|/I_1$ [219]. For our case of a truly rotationally symmetric rigid body, we may omit the factor $\mathbf{R}_\mathbf{z}^T$ in the update of $\mathbf{Q}(t)$ and directly apply the change of the transformation matrix on the orientation vector of the rigid body $\mathbf{e}(t+\delta t) = \mathbf{R}_{\mathbf{L}(t)}\mathbf{e}(t)$. Note that in the absence of external forces the integration scheme is is exact [219]. Lastly, the method is completed by advancing the linear and angular momentum to the full time step

δt, respectively,

$$\begin{aligned} \mathbf{p}(t+\delta t) &= \mathbf{p}(t+\delta t/2) + \mathbf{f}(t+\delta t)\delta t/2 \quad \text{and} \\ \mathbf{L}(t+\delta t) &= \mathbf{L}(t+\delta t/2) + \boldsymbol{\tau}(t+\delta t)\delta t/2. \end{aligned} \tag{3.23}$$

In the last step **4**, overlaps between fluid particles and the solute resulting from the MD step **3** are corrected by correcting the motion of the fluid particles similar to Ref. [220]. Then, another cycle begins at step **1**.

3.7 Efficient implementation of MPCD on graphic cards (GPUs)

Over the recent years, computer graphic cards and their centerpiece, the graphics processing unit (GPU), have become a very powerful tool that can replace small computer clusters for applicable algorithmic problems. Their strength compared to traditional computer clusters lies in their low price and superior efficiency regarding electric power consumption [221].

However, the way GPUs process instructions and data is entirely different from multi-core computers or clusters, and therefore require different programming approaches or even algorithms [222]. In particular, processor cores combined in the so-called vector processing units in GPUs are not independent and always apply the same instruction on multiple data (SIMD) in contrast to multi-core computers which apply multiple instructions on multiple data (MIMD). Otherwise, modern GPUs possess multiple levels of hierarchies such that multiple SIMD vector processors can work independently on different tasks, as shown in Fig. 3.5.

The collision rule of MPCD — which is simultaneously applied to millions of fluid particles almost independently — is a good example for an algorithm suitable for a GPU. Although already elementary implementations of MPCD on GPUs achieve immense performance benefits compared to conventional computers, a set of optimizations can again provide large performance increases.

The difficulty in a MPCD collision step is that in a naive implementation the fluid particles have to be loaded into the processor repeatedly, in order to calculate the center of mass, mean velocity, angular momentum, and moment of inertia tensor. If the fluid particles that belong to one collision cell are located in different memory locations, the GPU hardware cannot access their memory in a combined read instruction, and instead has to use separate read instructions on different memory locations [223]. To solve this issue, the memory array containing the fluid particles is frequently sorted based on the index of the collision cell in which the fluid particles lie [125, 132]. We thereby use the counting sort algorithm [224] by calculating a parallel prefix sum [225]. This way, memory accesses can be combined and the performance increases by a factor of two.

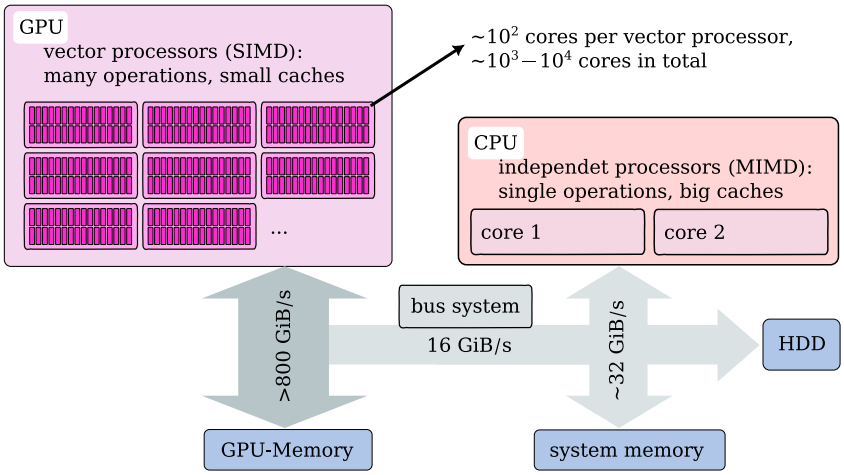

Figure 3.5: Sketch of a computer system consisting of a graphic card (GPU) and main processor (CPU). When running programs, the CPU mainly orchestrates the GPU, without computing itself. The GPU can access and process the large number of MPCD particles fast, due to the high bandwidth of its memory ($> 800\text{GiB/s}$) and large number of vector-processor cores ($\sim 10^3 - 10^4$) [222].

To avoid the repeated memory accesses in the collision step, which further limit the performance, we make use of the small shared data caches inside of the GPU's vector processors. However, to be able to store all fluid particles residing in one collision cell into this memory, the number of collision cells is typically lower than the number of vector-processor cores (threads). To maximize performance, we dynamically allocate shared memory and form groups of threads that work on each collision cell. To synchronize work in the groups of threads (SIMD), we use parallel summation and prefix sum algorithms.

CHAPTER 4

Published Articles of the Thesis

In this chapter, I will present the four articles published in scientific journals as part of this thesis. To begin with, I will give a brief overview of the overall content and place the different articles in line. The articles will then be presented in the following sections.

During my thesis work, I have developed the new squirmer rod model for elongated microswimmers, as well as an extended version of the MPCD algorithm to improve simulations of dense configurations of squirmer rods. Using both models, we investigated the flow fields of individual squirmer rods and the collective dynamics of squirmer rods as a function of the aspect ratio, density and swimmer type. Our first two articles are thereby concerned with the introduction of the squirmer rod (**1.**, see below) and the extended MPCD method (**2.**). In the following articles, we concentrated on the collective dynamics of neutral squirmer rods (**3.**) as well as pusher and puller-type squirmer rods (**4.**).
Below, I provide an overview over the relevance of the articles.

1. A. W. Zantop and H. Stark. *Squirmer rods as elongated microswimmers: flow field and confinement*. Soft Matter, **16**, 6400-6412, (2020).
doi: https://doi.org/10.1039/D0SM00616E

Contribution: First author, performed research and wrote of the manuscript, see Sec. 4.2 for more details.

Relevance: This work introduces the squirmer-rod model for elongated microswimmers and its implementation in the MPCD method. Its flow fields in the bulk fluid and Hele-Shaw geometry are investigated by means of a hydrodynamic multipole decomposition for multiple aspect ratios and confinement strengths.

Status: published in peer reviewed journal.

2. A. W. Zantop and H. Stark. *Multi-particle collision dynamics with a non-ideal equation of state. I.* The Journal of Chemical Physics, **154**, 024105, (2021).
doi: https://doi.org/10.1063/5.0037934

Contribution: First author, performed research and wrote of the manuscript, see Sec. 4.3 for more details.

Relevance: This work introduces an extended MPCD method with a collision rule that results in a non-ideal equation of state. Analytic expressions for the equation of state and the shear viscosity are derived and show excellent agreement with results from simulations.

Status: published in peer reviewed journal.

3. A. W. Zantop and H. Stark. *Multi-particle collision dynamics with a non-ideal equation of state. II. Collective dynamics of elongated squirmer rods.* The Journal of Chemical Physics, **155**, 134904, (2021).
doi: https://doi.org/10.1063/5.0064558

Contribution: First author, performed research and wrote of the manuscript, see Sec. 4.4 for more details.

Relevance: This work provides a study of the collective dynamics of squirmer rods at different aspect ratio and density. Thereby, it is shown that the extended MPCD method improves the precision of simulations in dense configurations of squirmer rods and the flow field shows excellent agreement with the analytical solution.

Status: published in peer reviewed journal.

4. A. W. Zantop and H. Stark. *Emergent collective dynamics of pusher and puller squirmer rods: swarming, clustering, and turbulence.* Soft Matter, **18**, 6179-6191, (2022).
doi: https://doi.org/10.1039/D2SM00449F

Contribution: First author, performed research and wrote of the manuscript, see Sec. 4.5 for more details.

Relevance: This work provides an in-depth analysis of the collective dynamics of pusher and puller-type squirmer rods as a function of the aspect ratio, density, and force dipole strength. It is found that swarming states dominate the behavior of pullers, while pushers exhibit turbulence.

Status: published in peer reviewed journal.

4.1 Synopsis

In our first article presented in Sec. 4.2, we introduce the squirmer-rod model for elongated microswimmers motivated by the shape of biological microscopic organisms [226, 227]. The model covers the different biological propulsion strategies of ciliates, as for example *Paramecium* [70, 166], pushers like the *E. coli* or *B. subtilis* bacteria [28, 228, 229], or pullers as the algae *Chlamydomonas reinhardtii* [38, 167]. To model the hydrodynamic flow of the solvent, we employ the multi-particle collision dynamics (MPCD) method [74, 120].

Thereby, we focus on the flow fields created by single squirmer rods in the bulk fluid and Hele-Shaw geometry, where the squirmer rod swims between two parallel plates. The flow fields are characterized using a decomposition into hydrodynamic multipoles to identify the dominant contributions. For the bulk fluid, the decomposition into hydrodynamic multipoles was introduced by de Graaf *et al.* [163]. In our work, we extend their idea further to the Hele-Shaw geometry based on the appropriate Green's function of the Stokes equations derived by Liron and Mochon [177] and Mathijssen *et al*. [176]. This allows us to formulate an alternative multipole expansion for the far field in the Hele-Shaw geometry. Thereby, all multipoles are modified with the transition from the bulk fluid to the confinement in the Hele-Shaw geometry [176, 177, 179]. More specifically, this means that the algebraic radial decays of the multipoles change; the force-multipoles become more short-ranged, while the source-multipoles become more long-ranged. At the same time, the distance of the confining plates controls the absolute strength of the multipoles. This has the fundamental consequence that the source dipole dominates the far field of the fluid flow of every type of self-propelled particle [74, 162].

For the neutral squirmer rod, we observe that the flow field is accurately described by solely adding a force-quadrupole term compared to the spherical squirmer. This additional term possesses the same $1/r^3$ radial decay as the source dipole and, therefore, it does not alter the far-field behavior. The strength of this additional term increases linearly with the aspect ratio of the rod. For the pusher-type squirmer rod the modified surface slip-velocity results in the expected characteristic force-dipole moment in the flow field, which is more long-ranged and, therefore, dominates flow field in the bulk fluid.

In the Hele-Shaw geometry, we verify both the different radial decay of the flow fields of the source and force multipoles as well as the scaling with the distance of the confining walls. In particular, the characteristic source-dipole moment in the flow field of neutral squirmer rods becomes more long-ranged, while the force-dipole moment in the flow field of pushers becomes more short-ranged. The appropriate multipole expansion for the Hele-Shaw geometry fits well in the far field and in strong confinement. For larger separations of the walls, deviations appear at short distances due to terms neglected from the full form of the appropriate Green's function of the Stokes equations. For the pusher-type squirmer rod in the Hele-Shaw

geometry an interesting crossover of the source-dipole to the force-dipole appears as a function of the confinement strength.

In our second article presented in Sec. 4.3, we introduce an extended MPCD method with improved thermodynamic properties for simulations of the collective dynamics of squirmer rods. This work is separated into two articles. In the present first article, we introduce the extended MPCD method and derive analytic expressions for the equation of state and the shear viscosity, which are compared with simulations. In the second article, we evaluate the new method in the context of squirmer rods and perform an in-depth study of the phase diagram of neutral squirmer rods.

Our starting point is that the traditional MPCD fluid has the equation of state of the ideal gas and is thus very compressible [126, 145, 230]. On this basis, we formulated a new MPCD collision step, which extends the concept of Tüzel, Ihle, and collaborators, who integrated geometric properties of collisions between hard-core particles into a two-dimensional variant of MPCD [231, 232].

The definition of the extended collision rule resembles properties of collisions in clouds of hard-core particles. This is realized as follows. Additionally to dividing MPCD particles into collision cells, each cell is divided into two groups using a randomly oriented plane. To mimic geometric properties of hard-core particles, collisions exchange the relative momentum of these groups if they approach each other. Moreover, the collision frequency in the MPCD collision cell increases with the density and relative velocity of the two particle groups. To realize different collision frequencies for each MPCD cell, collisions occur at random with a probability that depends both on the local density and velocities of the particles. This is motivated by the collision term in the Boltzmann equation for clouds of particles [216] and appears in a similar form for chemical reactions of second order [233].

The extended MPCD method creates an inherent momentum flux that adds to the pressure term of the stress tensor. As we show, this results in a non-ideal equation of state of the model fluid and achieves a low compressibility at a high numeric efficiency. Furthermore, we derive analytic expressions for pressure and the shear viscosity, which are in good agreement with values obtained from numerical simulations of the bulk fluid, constant linear shear and Poiseuille flow.

In our third article presented in Sec. 4.4 we continue our work on the extended MPCD method [205], assess its properties and performance, and apply it for an in-depth study of the collective dynamics of neutral squirmer rods.

As we are able to show, the extended MPCD method accurately reproduces the analytic solution of the flow field of a pusher-type spherical squirmer in both the bulk flow as well as in the Hele-Shaw geometry.

We further compare the extended MPCD method to the traditional MPCD-AT+a method in simulations of a dense configuration of squirmer rods with large aspect

ratio α, for the same viscosity η and Péclet number Pe. Simulations of the collective dynamics of squirmer rods are thereby performed in a Hele-Shaw geometry, where the squirmer rods are confined to move in the center plan between the confining walls. In both MPCD methods, the squirmer rods form a large stable swarm, but as expected the extended MPCD fluid indeed behaves more incompressible, and the properties of the fluid remain more uniform. In a second comparison, we consider squirmer rods with small aspect ratio α, which exhibit the dynamic formation of small swarms with a finite lifetime for both MPCD methods. However, in this case, the collective dynamics differs and the emergent swarms in the extended MPCD method have larger velocities and reach larger sizes.

We further determine the state diagram of neutral squirmer rods for variations of the aspect ratio α and the density, described by the two-dimensional area fraction ϕ in the center plane. Overall, four different states emerge. In dilute systems, where distances between particles are large, a disordered state without any correlations between squirmer rods occurs. For higher aspect ratios, $\alpha > 3.25$, the rods exhibit a dynamic swarming state, in which small to medium size swarms frequently form and dissolve. If the aspect ratio is further increased, swarms become stable, and ultimately a single big swarm forms. Lastly, at large density the rod configuration reaches a jammed state with a large stationary cluster.

In our latest article presented in Sec. 4.5, we extend our study to the collective dynamics of pusher and puller-type squirmer rods. In this regard, we adapt the squirmer-rod model to include arbitrary values of the force-dipole strength, in order to smoothly vary from strong pusher to strong puller type. We then investigate the state diagram of squirmer rods in the Hele-Shaw geometry, as a function of the force-dipole parameter χ, the aspect ratio α, and the density or area fraction ϕ.

For pusher-type squirmer rods we observe a new turbulent state alongside with a dynamic cluster state, which emerges intermediate between active turbulence and jammed clustering. We find that the dynamic states emerge in an interplay between hydrodynamic interactions, described by the force-dipole strength χ, and the steric interactions, described by the combination of α and ϕ. In dilute systems, where particles collide less and steric interactions are less important, the hydrodynamic interactions of pushers result in a complete destabilization of the swarming state that emerges for neutral squirmer rods. Instead, we observe a disordered state that exists also for higher aspect ratios α and densities ϕ. For larger α and ϕ, we observe that short-ranged steric interactions that align rods are more important and the turbulent state emerges in a competition with the more long-ranged hydrodynamic disordering interactions. This results in positive and negative velocity correlations that alternate on the length scale of a few swimmer lengths. The corresponding power spectral density exhibits two distinct regimes with power-law scaling and non-universal exponents and a maximum, indicating a characteristic patter length-scale. For larger aspect ratios and denser systems, the steric interactions dominate

and induce the single swarm and jammed cluster states already found for neutral squirmer rods.

In contrast, the hydrodynamic interactions of pullers enhance the formation of dynamic swarms, which then occur for all aspect ratios already at low densities. Accordingly, also the single-swarm state and the jammed cluster state are shifted towards smaller densities.

The variation of the swimmer-type parameter χ supports the previous findings. For pullers, we observe that the dynamic swarming state dominates at low densities for also small dipole strengths. The turbulent state is again found for intermediate strengths of both hydrodynamic and steric interactions, and we observe that it is destroyed if hydrodynamic interactions dominate.

Soft Matter

PAPER

View Article Online
View Journal | View Issue

Cite this: *Soft Matter*, 2020, **16**, 6400

Squirmer rods as elongated microswimmers: flow fields and confinement

Arne W. Zantop * and Holger Stark *

Received 8th April 2020,
Accepted 9th June 2020

DOI: 10.1039/d0sm00616e

rsc.li/soft-matter-journal

Microswimmers or active elements, such as bacteria and active filaments, have an elongated shape, which determines their individual and collective dynamics. There is still a need to identify what role long-range hydrodynamic interactions play in their fascinating dynamic structure formation. We construct rods of different aspect ratios using several spherical squirmer model swimmers. With the help of the mesoscale simulation method of multi-particle collision dynamics we analyze the flow fields of these squirmer rods both in a bulk fluid and in Hele-Shaw geometries of different slab widths. Based on the hydrodynamic multipole expansion either for bulk or confinement between two parallel plates, we categorize the different multipole contributions of neutral as well as pusher-type squirmer rods. We demonstrate how confinement alters the radial decay of the flow fields for a given force or source multipole moment compared to the bulk fluid.

1 Introduction

Swimming at the micron scale and understanding how microorganisms overcome the constraints of low-Reynolds-number hydrodynamics have attracted a lot of attention among physicists.[1–3] Intriguing features such as active turbulence,[4,5] swarming,[6,7] polar patterns,[8] and vortex formation,[8,9] which arise from the active nature of the fluid, still pose challenges to scientists. The fluid environment and the flow fields initiated by microswimmers strongly determine both their isolated motion and their appealing collective patterns, which they develop in non-equilibrium.[10] But also the elongated body shapes[4,7,8] and geometric confinement[11–15] of microswimmers significantly contribute to their single and collective dynamics. However, it is still a matter of current debate to completely identify the individual contributions of direct steric and long-range hydrodynamic interactions.[2,16,17] By introducing an active squirmer rod in this article, we aim to contribute to the discussion with a detailed analysis of its flow field in bulk and Hele-Shaw geometry.

Artificial microscopic swimmers with various locomotion mechanisms have recently been constructed to study the principal properties of their individual and collective motion. Examples mostly include spherical microswimmers.[6,18–21] Elongated and flexible active constituents are realized by polar biofilaments in motility assays[8] or at a fluid–fluid interface,[7] while bacteria provide a natural realization of active rods.[4]

Combining elements of the Toner–Tu[22] and Swift–Hohenberg[23] theories, continuum models for bacterial microswimmers have been developed that are able to reproduce pattern formation such as vortices and active turbulence.[4,24–26] Alternative continuum theories for active matter based on liquid-crystal hydrodynamics reproduce the creation, annihilation, and motion of liquid-crystal defects[27] or are able to describe the dynamics of the intracellular cytoskeleton gel.[2,28]

In contrast, particle-based simulations are employed to study the collective dynamics of active rods. In the famous Vicsek model coarse-grained aligning interactions are able to reproduce dynamical states such as flocking and swarming.[29–31] Langevin dynamics simulations of active rods[4,32,33] or active filaments[34,35] suggest that many properties might already emerge from short-ranged steric interactions. However, also implicit hydrodynamic pair interactions are included in such simulations to provide more realistic models with novel dynamic states.[36,37] An extension to single active filaments exists.[38,39] Explicit hydrodynamic simulation schemes have been applied, as well. For example, the lattice Boltzmann method was used to investigate the properties of microswimmers with various shapes[40–42] while with the method of multi-particle collision dynamics collective phases of spherical[43–45] and ellipsoidal microswimmers[46,47] were studied, as well as realizations of pusher and puller-type swimmers.[48,49]

In this work, we introduce and characterize single squirmer rods with the idea to model elongated microswimmers in their fluid environment. They then can be used to disentangle the effect of direct steric and long-range hydrodynamic interactions in their collective behavior. The squirmer model swimmer[45,50,51] is a good model for spherical artificial microswimmers such as Janus particles[52–54] and also biological organisms such as *Volvox*.[55] Squirmers have in common that they propel themselves by an axisymmetric surface–velocity field, which acts on the surrounding fluid.[45,56,57] In biological systems this is realized

Institut für Theoretische Physik, Technische Universität Berlin, Hardenbergstraße 36, 10623 Berlin, Germany. E-mail: a.zantop@tu-berlin.de, holger.stark@tu-berlin.de

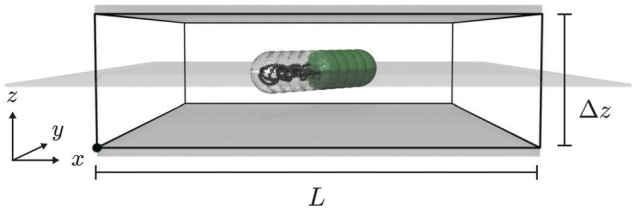

Fig. 1 Perspective view of a squirmer rod moving in the midplane (in light gray) of a Hele-Shaw cell with slab width Δz. Periodic boundary conditions along the x and y directions are used.

by cilia, located all over the cell surface, which perform synchronized collective non-reciprocal motions. The squirmer has frequently been used in hydrodynamic simulations of the collective behavior of microswimmers[42,58,59] and also by our own group,[43–45,60–62] where we rely on the mesoscale method of multi-particle collision dynamics.[45,63,64]

In this article we use squirmers to build rigid rod-shaped microswimmers of different aspect ratios and perform large-scale simulations with multi-particle collision dynamics. We explore their hydrodynamic flow fields both in a bulk fluid and in a Hele-Shaw geometry with varying cell width, where we keep the squirmer rod in the midplane to mimic the fluid interface in the experiments of ref. 7 (*cf.* Fig. 1).

In our analysis, we rely on the hydrodynamic multipole expansion both in the bulk fluid[10,40,50,65] and between two parallel plates.[12–14] This will enable us to categorize the different multipoles of both neutral as well as pusher-type squirmer rods and to determine the different radial decays of their multipole flow fields.

The paper is organized as follows. In Section 2 we introduce the squirmer rod and the methods to generate and analyze its flow fields. We present the results of our analysis in Section 3 and conclude in Section 4.

2 System and methods

The hydrodynamics of the squirmer rod at small Reynolds numbers is determined by the Stokes equations including the incompressibility condition,

$$\eta\nabla^2\mathbf{u} - \nabla p + \mathbf{f} = 0 \quad \nabla\cdot\mathbf{u} = 0. \tag{1}$$

Here, η is the viscosity of the fluid, $\mathbf{u}(\mathbf{r})$ the fluid velocity, $p(\mathbf{r})$ the pressure, and $\mathbf{f}(\mathbf{r})$ denotes a body force at point $\mathbf{r}$. In the following we introduce the squirmer-rod model, the fundamental solutions of the Stokes equations both in bulk and a Hele-Shaw cell, in order to characterize its hydrodynamic multipole moments, and details of the method of multi-particle collision dynamics (MPCD) to simulate the flow fields together with the relevant parameters.

2.1 Squirmer rod model

To investigate the influence of shape anisotropy of microswimmers and their hydrodynamic interactions on collective motion, we introduce a new model of squirming active rods. To construct them, we arrange several spherical squirmers [*cf.* Fig. 2(a)] on a line to form

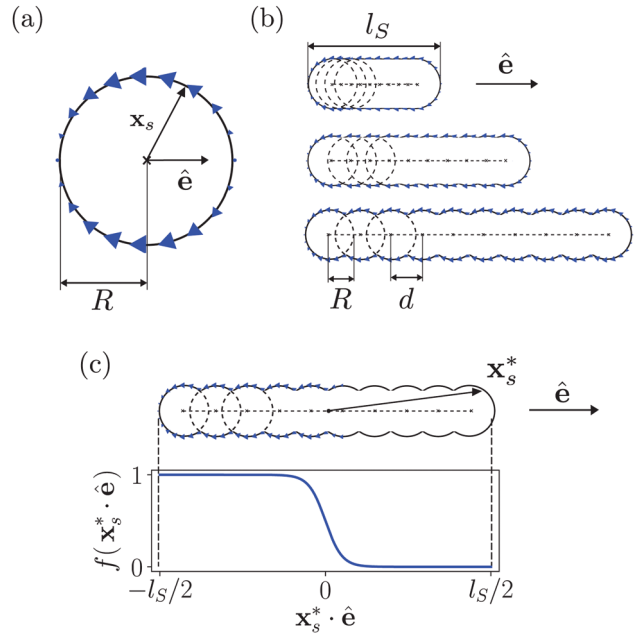

Fig. 2 (a) Schematic of a single squirmer of radius R and with orientation given by the unit vector $\hat{\mathbf{e}}$. The surface slip-velocity field of a neutral squirmer is indicated by blue arrows. (b) Schematic of the squirmer rod model. Always, $n_{sq} = 10$ spherical squirmers are placed on a straight line with distance d to form active rods. All squirmer orientations $\hat{\mathbf{e}}$ are aligned with the rod axis. (c) Implementation of a pusher type squirmer rod. The surface slip velocity on the rod surface is multiplied by the envelop function $f(\mathbf{x}_s^*\cdot\hat{\mathbf{e}})$ of eqn (3) such that the slip-velocity field is concentrated on the rear of the rod.

a rigid body as shown in Fig. 2(b). On the one hand, this closely resembles the actual rod shape of many biological microswimmers such as bacteria, on the other hand the model can be extended to a flexible swimmer body by introducing bending rigidity in future works. In concrete, we always take $N_{sq} = 10$ spherical squirmers and vary the squirmer distance d [*cf.* Fig. 2(b)] to form rods of different aspect ratios $\alpha = l_S/2R$, where l_S is the rod length. We do not go beyond a maximum squirmer distance of $d \approx 0.8R$, which amounts to a maximum rod length $l_S = 9.5R$, so that the surface is still smooth enough that swimmers can slide past each other. Each of the individual squirmers of a rod propels itself by an imposed axisymmetric surface slip-velocity field of a neutral squirmer,[45,56,57]

$$\mathbf{v}_s = B_1^s[(\hat{\mathbf{e}}\cdot\hat{\mathbf{x}}_s)\hat{\mathbf{x}}_s - \hat{\mathbf{e}}] \tag{2}$$

that acts on the surrounding fluid. Here, $\hat{\mathbf{x}}_s$ is the unit vector along $\mathbf{x}_s$, which points from the squirmer center to its surface, and unit vector $\hat{\mathbf{e}}$ indicates the orientation and swimming direction of the squirmer. In the case of a single squirmer, the induced flow field in a bulk fluid agrees with the velocity field of a pure source-dipole singularity with strength $B_1 = B_1^s R^3$ as explained in the following section. The squirmer parameter B_1^s also determines the swimming speed v_0, which amounts to $v_0 = 2/3B_1^s$ for a single squirmer.

Having the surface velocity field distributed over the whole squirmer rod [*cf.* Fig. 2(b)], our model resembles ciliated microorganisms such as *Paramecium*. In contrast, bacteria like

E. coli propel themselves with a bundle of rotating flagella that pushes fluid backwards while the cell body does not have any surface velocity field. To implement squirmer rods of such a pusher or also of puller type, we use the envelope function

$$f(\mathbf{x}_s^* \cdot \hat{\mathbf{e}}) = \frac{1 \mp \tanh(10\mathbf{x}_s^* \cdot \hat{\mathbf{e}}/l_S)}{2}. \quad (3)$$

Here, $\boldsymbol{x}_s^*$ is a vector from the center of mass of the rod to any point on the surface [*cf.* Fig. 2(c)] and $10/l_S$ is the step width of the envelope function. Multiplying the surface velocity field with $f(x_s^* \cdot \hat{\mathbf{e}})$, concentrates the slip velocity field on the rear half of the rod for the – sign in f and thereby a pusher squirmer rod is realized, while the + sign generates a puller.

2.2 Fundamental solutions of Stokes flow in bulk

To provide an understanding of the flow field $\mathbf{u}(\mathbf{r})$ that squirmer rods initiate in a bulk fluid and how they interact hydrodynamically, we review the multipole expansion of $\mathbf{u}(\mathbf{r})$.[50,66] It is composed of singular solutions of the Stokes equations including the Stokeslet as the flow field of the leading force monopole, which has to vanish for force-free microswimmers, the flow field of the source dipole, and their higher-order derivatives. We introduce the polar angle θ relative to the squirmer-rod axis *via* $\cos\theta = \hat{\mathbf{e}}\cdot\mathbf{r}/r$. Then, in spherical coordinates r, ϕ, and θ the respective radial and polar components of the velocity field can be written as[50,66]

$$\begin{aligned} u_r(r,\theta) &= \sum_{n=1}^{\infty}\left[A_n r^{-n} + B_n r^{-n-2}\right] P_n(\cos\theta), \\ u_\theta(r,\theta) &= \sum_{n=1}^{\infty}\left[\left(\frac{n}{2}-1\right)A_n r^{-n} + \frac{n}{2}B_n r^{-n-2}\right] V_n(\theta). \end{aligned} \quad (4)$$

Here, $P_n(\cos\theta)$ are the ordinary Legendre polynomials and

$$V_n(\theta) = \frac{2\sin\theta}{n(n+1)} P_n'(\cos\theta), \quad (5)$$

where $'$ means derivative with respect to $\cos\theta$. Due to the rotational symmetry of a squirmer rods about its axis, the flow field is independent of the azimuthal angle ϕ and the azimuthal velocity component u_ϕ vanishes. The multipole coefficients A_n and B_n describe the strength of the nth-order force and source multipoles, where B_1 belongs to the source dipole. To determine them, we calculate the nth expansion or Legendre coefficient of the radial component of the flow field in eqn (4),

$$u_{r,n}(r) \equiv \frac{2n+1}{2}\int_0^\pi u_r(r,\theta) P_n(\cos\theta)\sin\theta \mathrm{d}\theta, \quad (6)$$

using the completeness relation of the Legendre polynomials, which gives

$$u_{r,n}(r) = A_n r^{-n} + B_n r^{-n-2}. \quad (7)$$

Thus, from the simulated flow fields of the squirmer rods, in particular, from the radial decay of $u_{r,n}(r)$, we can infer their leading force and source multipole moments. We will demonstrate this in Section 3.1. Note that the nth force and source monopole can be clearly distinguished by their radial decay.

2.3 Fundamental solutions of Stokes flow in Hele-Shaw geometry

In a seminal paper Liron and Mochon[12] determined the Stokeslet solution between two infinitely extended parallel plates with no-slip boundary condition (*cf.* Hele-Shaw geometry in Fig. 1) using an infinite series of image forces. For a force parallel to the plates ($x-y$ plane), the x, y components of the resulting Stokeslet flow field are long-range and consist of a Poiseuille flow profile $g(z)$ along the plate normal times the flow field of a two-dimensional source dipole in the plane (*cf.* Appendix A). As in the bulk fluid[65] one can generate the flow fields of higher-order force moments by applying the directional derivative $\hat{\mathbf{e}}\cdot\nabla_p$ to the Stokeslet flow field.[14] Here, ∇_p is the nabla operator acting on the position of the Stokeslet singularity and the unit vector $\hat{\mathbf{e}}$ gives the direction of the force multipole in the $x-y$ plane, which we assume to be uniaxial for simplicity. Likewise, by applying the Laplace operator ${\nabla_p}^2$ to the Stokeslet flow field, one obtains the flow field of a source dipole, which here is up to a factor identical to the Stokeslet flow field.[14] Higher source multipole moments are again generated by directional derivatives.

Relevant for the squirmer rod will be the flow fields of the source dipole ($\mathbf{u}_{SD}$), force dipole ($\mathbf{u}_{FD}$), force quadrupole ($\mathbf{u}_{SD}$), and source octupole ($\mathbf{u}_{SD}$):†

$$\mathbf{u}(\mathbf{r}) = \mathbf{u}_{SD}(\mathbf{r}) + \mathbf{u}_{FD}(\mathbf{r}) + \mathbf{u}_{FQ}(\mathbf{r}) + \mathbf{v}_{SO}(\mathbf{r}) + \ldots. \quad (8)$$

To determine these contributions from the simulated flow field of the squirmer rod, we first average over the z coordinate and then treat the resulting velocity field $\tilde{\mathbf{u}}(\rho,\varphi)$ in the x–y plane using polar coordinates ρ, φ. As we demonstrate in Appendix A, for a microswimmer oriented along the x axis, $\hat{\mathbf{e}} = \hat{\mathbf{e}}_x$, the multipole expansion for the radial component of the flow field gives

$$\tilde{u}_\rho(\rho,\varphi) = \sum_{n=1}^{\infty}\frac{\mathscr{A}_n + \mathscr{B}_n}{\rho^{n+1}} T_n(\cos\varphi). \quad (9)$$

Here, $T_n(\cos\varphi) = \cos(n\varphi)$ are the Chebyshev polynomials of the first kind and $\mathscr{A}_n$, $\mathscr{B}_n$ are the respective coefficients of the force and source multipole moments. They start with $\mathscr{A}_1$ for the force monopole, which does not exist for a force-free swimmer, and $\mathscr{B}_1$ for the source dipole, and so on.

It immediately becomes obvious that in contrast to the bulk fluid one cannot distinguish the flow fields of force and source multipoles with the same angular dependence (same order n) by the radial decay. We note that the coefficients scale differently with the slab width Δz. In Appendix A we motivate $\mathscr{A}_n \propto \Delta z$ and $\mathscr{B}_n \propto 1/\Delta z$. However, our simulated data are not always sufficiently accurate to discriminate both cases. So, we assign the relevant multipole assuming that it is preserved from the bulk fluid. The multipole expansion captures the distribution

† Although the source quadrupole shares the same radial dependence as the force dipole in the Hele-Shaw geometry, it is not considered in this list for two reasons. First, we solely observe a force dipole in the bulk fluid but no source quadrupole. Second, the strength of $\tilde{u}_{\rho,2}(\rho)$ grows with the slab width Δz in our simulations, which identifies it as a force dipole rather than a source quadrupole. We will elaborate on this further below.

of force and source multipoles in leading order. This distribution generated by the rod surface should remain the same in the Hele-Shaw geometry. However, since we deal with a voluminous rod in contrast to a point-like source, higher-order terms enter to fulfill the boundary conditions on both the rod surface and the bounding plates. The flow fields of these terms will decay faster than the leading bulk moments at some distance from the rod.

Finally, exploiting the orthogonality relations of $\cos n\varphi = T_n(\cos\varphi)$, we extract the multipole moments from eqn (9) by projecting $\tilde{u}_\rho(\rho,\varphi)$ on the Chebyshev polynomials,

$$\tilde{u}_{\rho,n}(\rho) \equiv \frac{1}{\pi}\int_0^{2\pi} \tilde{u}_\rho(\rho,\varphi) T_n(\cos\varphi)\mathrm{d}\varphi, \tag{10}$$

which yields

$$\tilde{u}_{\rho,n}(\rho) = \frac{\mathscr{A}_n + \mathscr{B}_n}{\rho^{n+1}}. \tag{11}$$

In both the bulk fluid and Hele-Shaw geometry we can restrict our focus on a particular set of Stokes flow singularities. These will be the source dipole ($\mathscr{B}_1$), force dipole ($\mathscr{A}_2$), force quadrupole ($\mathscr{A}_3$), and source octupole ($\mathscr{B}_3$).

2.4 MPCD fluid model

To model the fluid in our simulations, we apply the method of multi-particle collision dynamics together with the Andersen thermostat and angular momentum conservation (MPCD-AT+a).[44] The method solves the Navier–Stokes equations and thereby can also treat hydrodynamic interactions between the active squirmer rod and the confining walls of the Hele-Shaw geometry.[63,64] Furthermore, it also includes thermal fluctuations. The MPCD method considers point-like particles that represent the fluid and defines rules for (i) their motion and (ii) their collisions such that the resulting hydrodynamic flow field fulfills the Navier–Stokes equations. These rules are applied in alternating steps. We shortly introduce the essential features of the MPCD method and refer to ref. 45 for more details.

During the streaming step (i) the point particles with masses m_0, positions $\mathbf{x}_i(t)$, and velocities $\mathbf{v}_i(t)$ move ballistically during time Δt,

$$\mathbf{x}_i(t+\Delta t) = \mathbf{x}_i(t) + \mathbf{v}_i(t)\Delta t. \tag{12}$$

During this step fluid particles collide with confining walls or the surface of the squirmer rod. By applying the so-called bounce-back rule[44,45] the collisions either enforce the no-slip boundary condition on confining walls or the slip-velocity field on the squirmer-rod surface. In addition, the collisions also transfer both linear and angular momentum, in particular, to the squirmer rod. This changes the center-of-mass and angular momentum of the rigid rod, which is calculated relative to the center-of-mass. In Appendix B we present formulas for the mass m_{rod} and moment-of-inertia tensor $\mathbf{I}_{\mathrm{rod}}$ of the rigid squirmer rod.

For the collision step (ii), the simulation volume is divided by a cubic lattice and the fluid particles are grouped into the cubic unit cells of linear size a_0 and centered around ξ. First, for the n_ξ particles in each cell with volume $\mathscr{V}_\xi$ the mean velocity $\mathbf{v}_\xi$ and center-of-mass position $\mathbf{x}_\xi$ are determined. Then, in the center-of-mass frame the fluid particles are assigned new random velocities $\delta\boldsymbol{v}_i$ from a Boltzmann-distribution with temperature T_0. To restore overall momentum conservation, the total change in linear momentum, $m_0\Delta\mathbf{v}_\xi = \frac{m_0}{n_\xi}\sum_{\mathbf{x}_i\in\mathscr{V}_\xi}\delta\mathbf{v}_i$, has to be subtracted from the new velocities, while an additional term containing the difference of the angular momentum before the collision $\mathbf{L}_\xi = \frac{m_0}{n_\xi}\sum_{\mathbf{x}_i\in\mathscr{V}_\xi}\mathbf{x}_{i,c}\times\mathbf{v}_i$, and the change in angular momentum, $\Delta\mathbf{L}_\xi = \frac{m_0}{n_\xi}\sum_{\mathbf{x}_i\in\mathscr{V}_\xi}\mathbf{x}_{i,c}\times\delta\mathbf{v}_i$, is added to preserve angular momentum. Here $\mathbf{x}_{i,c}$ denotes the particle position relative to the center-of-mass position $\mathbf{x}_\xi$. Thus, the collision step can be summarized by

$$\mathbf{v}_i^{\mathrm{new}} = \mathbf{v}_\xi + \delta\mathbf{v}_i - \Delta\mathbf{v}_\xi - \mathbf{x}_{i,c}\times\mathbf{I}_\xi^{-1}(\mathbf{L}_\xi - \Delta\mathbf{L}_\xi), \tag{13}$$

Here, $\mathbf{I}_\xi$ is the moment-of-inertia tensor of the distribution of particles inside $\mathscr{V}_\xi$ calculated in the center-of-mass frame. During this step immersed boundaries are represented by so-called "ghost" particles. They are added to the collision cells divided by the boundaries and interact with the other fluid particles. These ghost particles are assigned the local velocity of the translating and rotating squirmer rod plus a random thermal velocity drawn from a Boltzmann distribution. The changes of linear and angular momentum of the ghost particles during the collision step are then added to the squirmer rod to ensure linear and angular momentum conservation. Finally, before performing each collision step, the lattice is randomly shifted to ensure Galilean invariance.

Given the center-of-mass and angular momentum of the rigid squirmer rod, its location and orientation are updated 10 times during each collision step using a standard leapfrog algorithm.[67] The rod is treated as single rigid body the position and orientation vector of which is updated following ref. 67. To keep the squirmer rod in the midplane of the Hele-Shaw cell, we only use the x and y component of the fluid force acting on the rod to integrate its motion in time throughout the simulation. Due to the symmetry about the midplane only Brownian forces are acting on the squirmer normal to the midplane. Note due to this constraint we do not observe any oscillatory trajectories between the plates as observed in ref. 68.

We have implemented the MPCD model fluid together with the squirmer-rod model in C++ and CUDA to enable the use of graphic cards. Because the main performance bottleneck in MPCD is memory access, we integrate a sorting algorithm and lookup table following ref. 69. Additionally, we use variable size cooperative thread groups to add dynamic load balancing to our MPCD collision routines in CUDA.

2.5 Geometry and fluid parameters

For the MPCD fluid we use a density of $n_0 = 10/a_0^3$ fluid particles per cell and the same mass density $\rho_0 = m_0 n_0$ for the immersed squirmer rod. With time step $\Delta t = 0.02a_0\sqrt{m_0/k_{\mathrm{B}}T_0}$ one obtains a dynamic fluid viscosity of $\eta = 16.05\sqrt{m_0 k_{\mathrm{B}}T_0}/a_0^2$.[44] Throughout this work, the radius and the squirner parameter of the

single squirmer are chosen as R= $3a_0$ and $B_1^s = 0.1\sqrt{k_B T_0/m_0}$, respectively.

To determine how the hydrodynamic moments of the squirmer flow field in a bulk fluid varies with the aspect ratio α in Section 3.1, we simulate single rods in a cubic box of linear size L = $100a_0$ using periodic boundary conditions in all three dimensions. For all other bulk simulations in Sections 3.1 and 3.3, we use box sizes of L = $180a_0$ with periodic boundary conditions. We begin by simulating the system for a time $10^4\Delta t$ to equilibrate the MPCD fluid flow and then average the flow fields over the time interval from $10^4\Delta t$ to 5 $\times$ $10^6\Delta t$. To determine the radial component $v_r(r,\theta)$ of the velocity field, we also exploit the rotational symmetry of the flow fields by averaging about the rod axis. Using eqn (6), we then obtain the expansion coefficients $u_{r,n}(r)$ for different multipole order n and extract the strengths of the hydrodynamic moments by fitting $u_{r,n}(r)$ from eqn (7) to the curves determined from the simulated flow fields.

For the simulations in Hele-Shaw geometry in Sections 3.2 and 3.3, we use box sizes of L = $200a_0$ with no-slip walls and periodic boundary conditions along the x and y directions. For the slab width we investigate the three values $\Delta z/R$ = 2.7, 6.0, and 9.3. When determining the flow fields in the Hele-Shaw geometry, the total simulation time is increased up to $10^7\Delta t$ to compensate for the fact that the flow field cannot be averaged about the rod axis.

3 Results

In the following, we present our results. We first discuss the flow field of a neutral squirmer rod in the bulk fluid and how it depends on the aspect ratio α. We then study neutral squirmer rods in Hele-Shaw geometries of different slab widths and illustrate the different far-field behavior compared to the bulk fluid. Finally, we look at a squirmer rod of pusher type moving in both bulk fluid and the Hele-Shaw geometry.

3.1 Neutral squirmer rods in bulk fluid

In the bulk fluid, rods of different aspect ratio α create flow fields as shown in Fig. 3. In all panels (a), (b), and (c) only a part of the simulated fluid volume is shown. In the case of the spherical squirmer, α = 1, in Fig. 3(a) we observe a perfect match with the theoretical prediction for the flow field of a source dipole moment. For a short squirmer rod with α = 1.75 the flow field already becomes stretched along the rod [*cf.* Fig. 3(b)]. At higher aspect ratio, α = 4.0, the flow field shows a strong deviation from the one of a source dipole moment, with the streamlines buckling inwards at the sides of the rod. Thus, we expect higher-order moments to contribute strongly to squirmer rods with higher aspect ratios α.

To provide a quantitative analysis, we apply eqn (6) and decompose the flow field into its different angular contributions with the nth-order Legendre coefficients $u_{r,n}(r)$. As an example, we show in Fig. 4(a) the measured $u_{r,n}(r)$ as data points for a squirmer rod of α = 4 and also include fitted polynomials in r^{-1} as solid lines.

All radial velocity components $u_{r,n}(r)$ either show distinct power law behavior as for n = 1 and 3 or vanish. The first-order coefficient $u_{r,1}(r)$ clearly shows a pure $1/r^3$ decay, indicating a zero force monopole moment A_1 while the source dipole moment B_1 is present, as expected. This is consistent with the fact that we consider microswimmers free of external forces. Consistent with the head–tail symmetry of the forces, the squirmer rods exert on the fluid, we do not observe a force dipole moment, A_2 = 0, since the second-order coefficient $u_{r,2}(r)$ vanishes. Furthermore, the third-order contribution $u_{r,3}(r)$ is also present and decays with $1/r^3$, which indicates an additional force quadrupole moment A_3. We elaborate on its origin further below. Both curves $u_{r,1}(r)$ and $u_{r,3}(r)$ fall off from the theoretically predicted power law at large r due to the finite size of the simulation box. They also show small deviations from the power law, which we attribute to the flow fields of the image swimmers introduced by the use of periodic boundary conditions. All other coefficients $u_{r,n}(r)$ are too small to be distinguished from noise and hence can be neglected in the following. Thus, the flow field of a neutral squirmer rod is a superposition of a source dipole moment ($B_1 \neq 0$), and a force quadrupole moment ($A_3 \neq 0$), which both decay as $1/r^3$. In Fig. 4(b) we plot the two moments normalized by the squirmer parameter B_1^s *versus* the aspect ratio α. They both increase roughly linearly in α. While the source-dipole moment B_1 shows

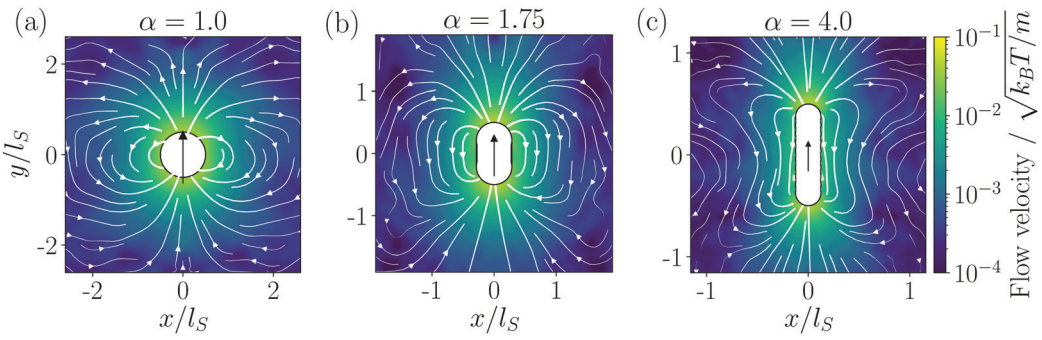

Fig. 3 Simulated flow fields of an active squirmer rod for different aspect ratios α = 1 (a), α = 1.75 (b), and α = 4.0 (c) shown in the laboratory frame. The color-coded magnitude of the velocity field and streamlines are presented. In each case only a part of the simulated fluid volume is shown.

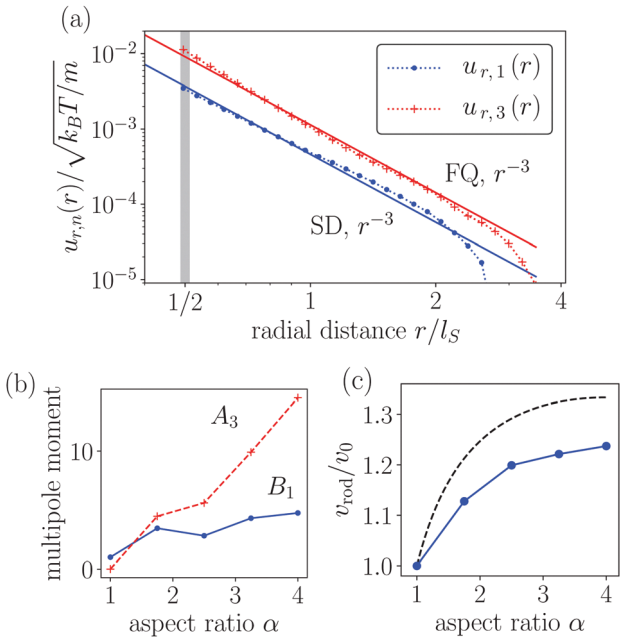

Fig. 4 (a) Radial Legendre coefficients $u_{r,n}(r)$ of the simulated flow field of a neutral squirmer rod with aspect ratio $\alpha = 4.0$ calculated from eqn (6) (symbols) and with fitted power laws (solid lines). SD and FQ stand for source dipole and force quadrupole, respectively. (b) Hydrodynamic multipole moments in units of the squirmer parameter $B_1^s R^3$ plotted *versus* aspect ratio α. (c) Swimming speed v_{rod} of a squirmer rod plotted *versus* α. v_{rod} is normalized by the swimming speed $v_0 = 2/3B_1^s$ of a single squirmer at $\alpha = 1$. Simulation data (blue dots) and analytical values as given by eqn (15) (dashed black line).

a modest increase in α starting from $B_1 = B_1^s R^3$ for $\alpha = 1$, the force quadrupole moment A_3 increases much more strongly from zero and clearly dominates beyond $\alpha = 2$.

The additional force quadrupole does not break the head–tail symmetry of the squirmer rod, which we therefore denote as neutral. However, the corresponding flow field clearly affects the shape of the overall flow field as we saw in Fig. 3. Since its angular dependence is governed by the third-order Legendre polynomial $P_3(\cos\theta)$ compared to $P_1(\cos\theta)$ of the source dipole, it will influence the hydrodynamic interactions with other squirmer rods, also because its flow field shows the same radial decay, $1/r^3$.

To shed some light on the origin of the force quadrupole, we determined the local force $F_{hyd}(y_i)$, with which the spherical squirmer component i placed at y_i along the rod axis acts on the surrounding fluid. Of course, the rod is force free, thus all the forces $F_{hyd}(y_i)$ add up to zero, $\sum_{i=1}^{N_{sq}} F_{hyd}(y_i) = 0$. The forces from the terminal squirmers $i = 1$ and $i = N_{sq}$ are mainly determined by fluid pressure. They cancel each other up to some remaining force, $F_{hyd,p} = F_{hyd}(y_1) + F_{hyd}(y_{N_{sq}})$. In the following, we refer the force of the other squirmers on this remaining force, $\delta F_{hyd}(y_i) = F_{hyd}(y_i) - F_{hyd,p}/(N_{sq} - 2)$, so that they sum up to zero: $\sum_{i=2}^{N_{sq}-1} \delta F_{hyd}(y_i) = 0$. In Fig. 5(a) we plot the relative force $\delta F_{hyd}(y_i)$,

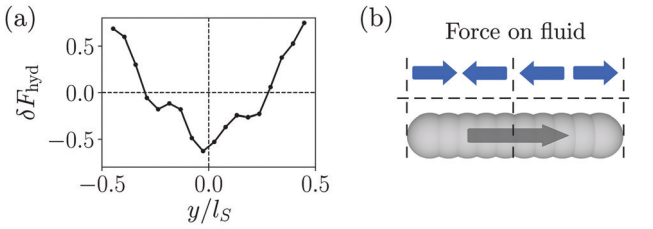

Fig. 5 (a) Local relative force $\delta F_{hyd}(y_i)$, with which the squirmer rod acts on the fluid, plotted along the long axis y of the squirmer rod. The aspect ratio is $\alpha = 4$. The dots correspond to the axial positions y_i of the constituent squirmers and the line is a guide to the eye. Note, in contrast to the rest of the article, $N_{sq} = 20$ squirmers are used to compose the rod in order to generate a smoother surface. (b) Sketch of $\delta F_{hyd}(y)$ (blue arrows) to illustrate the force quadrupole. The grey arrow indicates the swimming velocity.

the schematic in Fig. 5(b) rationalizes the different signs of $\delta F_{hyd}(y_i)$. In the center of the rod ($y = 0$), the relative local force is negative due to the surface velocity of the squirmer rod pushing fluid backwards, while at both ends of the rod the fluid is dragged with the rod. This generates the observed force quadrupole.

Finally, as we show in Fig. 4(c), the swimming speed v_{rod} of the rod increases with α and then saturates. With increasing aspect ratio the swimming speed is more and more determined by the maximum surface velocity around the equator of the constituent squirmers and thus the speed increases. At large α the cap regions of the squirmer rod become irrelevant and the swimming speed saturates. To calculate an analytic expression for the swimming speed, we average the surface slip-velocity field $\boldsymbol{v}_s$ of the squirmer rod over the whole surface with area S_{rod}.[70] For the component along the squirmer axis $\hat{\mathbf{e}}$ we obtain

$$v_{rod} = -\frac{1}{S_{rod}}\int_{S_{rod}} \hat{\mathbf{e}} \cdot \mathbf{v}_s \mathrm{d}S \tag{14}$$

$$= v_0\left(\frac{3}{2} - \frac{1}{2\alpha} - \frac{1}{54} + \frac{1}{162\alpha} + \frac{\alpha}{54} - \frac{\alpha^2}{162}\right). \tag{15}$$

The derivation is sketched in Appendix C. Note that the first two terms on the right-hand side of eqn (15) result when a perfect spherocylinder with the maximum slip velocity $B_1^s = 3v_0/2$ on the straight region is assumed. For $\alpha = 1$ we reproduce the swimming velocity v_0 of the spherical squirmer. Fig. 4(c) shows the analytic expression overestimates the swimming speed. The reason is that the surface average of eqn (14) to calculate the swimming speed only applies to spherical shapes since then the hydrodynamic surface stress for a passive sphere is constant along the surface.[70] This is used in the derivation of eqn (14) and obviously no longer valid for the passive squirmer rod.

3.2 Neutral squirmer rods in Hele-Shaw geometry

To discuss the flow fields of a squirmer rod in the confining Hele-Shaw geometry, we start with Fig. 6 where we show the color-coded strength of the flow field and streamlines in the midplane of the cell (upper panel) and the cross-sectional plane

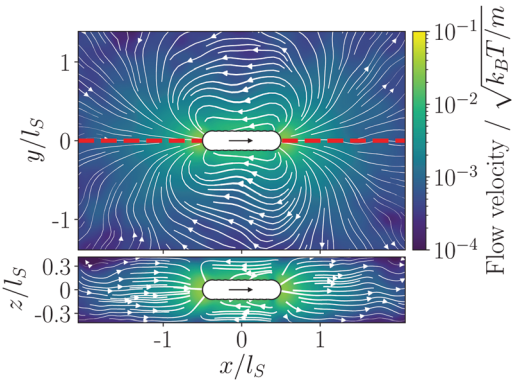

Fig. 6 Simulated flow field of a squirmer rod with aspect ratio $\alpha = 4.0$ in a Hele-Shaw geometry with slab width $\Delta z = 6R = 18a_0$ shown in the laboratory frame. The color-coded magnitude of the velocity field v and streamlines are presented. Upper panel: Flow field in the midplane; lower panel: flow field in the cross-sectional plane indicated by the red dashed line in the upper panel.

(lower panel). For a squirmer rod of $\alpha = 4.0$ and similar to the bulk fluid [*cf.* Fig. 2(c)], we observe how the streamlines at the sides of the rod buckle inwards (upper panel of Fig. 6) due to the flow field of the force quadrupole moment. However, as explained in Section 2.3 and detailed in Appendix A, in the Hele-Shaw geometry the flow field of the source dipole with moment $\mathscr{B}_1$ is of longer range than the one of the force quadrupole with moment $\mathscr{A}_3$. Indeed, already at a distance l_S from the rod the buckling of the flow lines is much weaker compared to the bulk fluid [*cf.* Fig. 3(c)] and the flow field assumes the shape of a pure source dipole.

In the lower panel of Fig. 6, further away from the rod ($|x/l_S| > 1$) the streamlines are approximately parallel to the bounding plates in agreement with the Poiseuille flow profile of the single force and source multipoles as detailed in Appendix A. However, in the direct vicinity of the rod, $|x/l_S| < 3/4$, near-field flow along the z direction occurs, which is due to terms with exponential decay in the full hydrodynamic solution in a slab geometry.

We now present a more quantitative analysis of the simulated flow fields in Fig. 7 and 8. As for the bulk fluid, we decompose the flow fields into the different angular contributions given by the Chebyshev polynomials $T_n(\cos\varphi)$ using eqn (10). Since from the radial decay of the expansion coefficients $\tilde{u}_{\rho,n}(\rho)$ we cannot distinguish between the force multipole of nth order and the source multipole of $n+1$th order, we are guided by the analysis in the bulk fluid from Section 3.1 and attribute the expansion coefficients $\tilde{u}_{\rho,1}(\rho)$ and $\tilde{u}_{\rho,3}(\rho)$, plotted in Fig. 7 and 8, to a source dipole (SD) and force quadrupole (FQ), respectively.

In Fig. 7 we plot $\tilde{u}_{\rho,1/3}(\rho)$ averaged over the cell height for different slab widths Δz. For a small width $\Delta z = 2.7R = 0.34l_S$ the coefficients are in very good agreement with the expected power-law decay: $1/\rho^2$ for the source dipole and $1/\rho^4$ for the force quadrupole. Both power laws fit well over the whole range of the radial distance. For slab width $\Delta z = 6R = 0.75l_S$ the measured coefficients $\tilde{u}_{\rho,n}(\rho)$ approach the predicted power-law decays at a radial distance of approximately $\rho/l_S = 1$. This is larger than the slab width, where we expect the far-field solutions of the different multipoles to become valid. At this distance the corresponding streamlines shown in the lower panel of Fig. 6 are parallel to the bounding plates as predicted by the multipole flow fields. Finally, increasing the slab width further to $\Delta z = 9.3R = 1.2l_S$ the measured coefficients $\tilde{u}_{\rho,n}(\rho)$ show clear deviations from the expected power-law decay over the whole range of the radial distance ρ. All in all, when we vary the slab width, the force quadrupole moment stays the same, while the source dipole moment increases with decreasing Δz.

In Fig. 8 we choose the smallest slab width $\Delta z/R = 2.7$, where we obtained the best agreement in the previous figure and plot the coefficients $\tilde{u}_{\rho,1/3}(\rho)$ for different aspect ratios α. Again there is very good agreement between the coefficients and the expected power law decay. Only at radial distance smaller than l_S one realizes deviations, as expected. This is, in particular, visible in plot (a).

3.3 Pusher-type squirmer rods

As explained in Section 2.1 we also implemented a pusher-type squirmer rod with aspect ratio $\alpha = 4.0$ and show our analysis in Fig. 9. In the bulk fluid, the force dipole now dominates the flow field as the new coefficient $u_{r,2}(r)$ demonstrates, which decays with $1/r^2$ starting from $r \approx l_S$. Compared to the neutral squirmer rod and the dominating force dipole, the flow field of the source dipole is roughly an order of magnitude smaller. We also observe a deviation from the expected $1/r^3$ decay (as indicated by the solid line) to a decay of roughly $1/r^2$. One explanation might be the hydrodynamic interaction of the squirmer rod with its images due to the periodic boundary conditions, which especially affects the weaker multipole moments. Compared to the neutral rod, the force-dipole field is more long-ranged and therefore hydrodynamic interactions between the images are stronger, which especially influences the field of higher-order multipoles. Very different from the neutral squirmer rod, the third-order coefficient $u_{r,3}(r)$ changes sign at a radial distance of $r \approx l_S$ from positive to negative with increasing r. This is why we plot the magnitude of the coefficients $u_{r,n}(r)$. It is tempting to fit the $1/r^5$ decay of a source octupole with positive moment B_3 at distances $r/l_S < 1$, while at $r/l_S > 1$ we indicate the decay of a force quadrupole with negative moment A_3. Again, the latter is probably strongly disturbed by the periodic images, resulting in a decay of roughly $1/r^2$, similar to our observations before. In conclusion, since the flow fields of both the source dipole and force quadrupole are one order of magnitude weaker compared to the force dipole, the overall flow field is well described by the latter.

In Fig. 10 we analyze the flow field of the pusher-type squirmer rod in the Hele-Shaw geometry for different slab widths. In addition to the findings for the neutral squirmer rod (*cf.* Fig. 7), we also observe the force dipole. Compared to the bulk fluid, it now has a stronger radial decay, $\tilde{u}_{\rho,2}(\rho) \propto 1/\rho^3$, as described by theory. At distances $\rho/l_S < 1.3$ the strong but shorter ranged force-dipole flow field dominates, while for $\rho/l_S > 1.3$ the slower decay of the source-dipole field takes over.

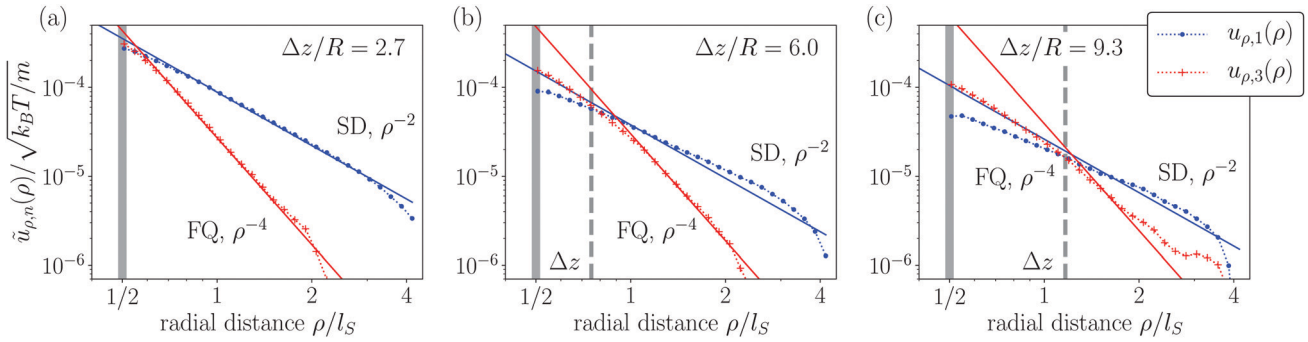

Fig. 7 Multipole analysis of the simulated flow field of a neutral squirmer rod with aspect ratio $\alpha = 4$ for different slab widths of the Hele-Shaw cell: (a) $\Delta z = 2.7R$, (b) $\Delta z = 6.0R$ and (c) $\Delta z = 9.3R$. As in the bulk fluid the radial decays of the expansion coefficients $\tilde{u}_{\rho,n}(\rho)$ feature a source dipole ($n = 1$, blue dots) and force quadrupole ($n = 3$, red pluses). The solid lines show fits with the corresponding power laws of ρ^{-2} and ρ^{-4}, respectively. Grey vertical bar: the coefficients $\tilde{u}_{\rho,n}(\rho)$ were determine for radial distances $\rho \geq l_S/2$. The gray vertical dashed line indicates $\rho = \Delta z$.

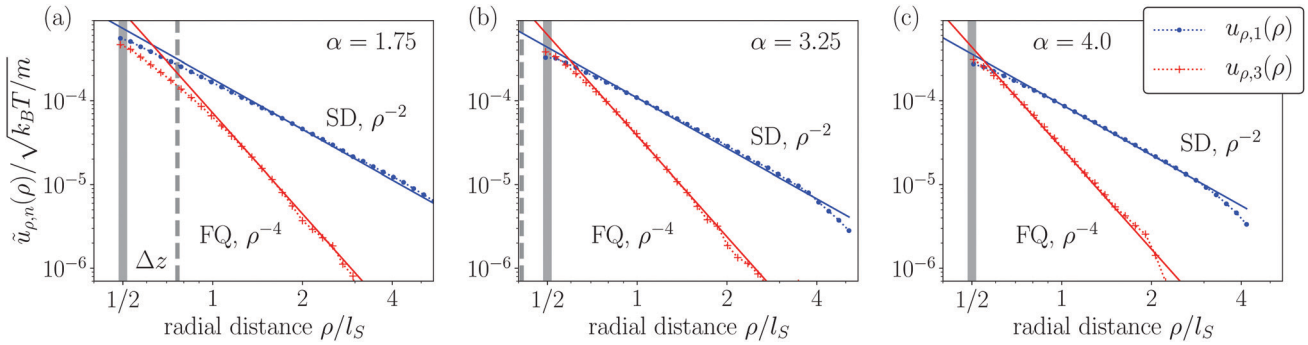

Fig. 8 Multipole analysis of the simulated flow field of a neutral squirmer rod confined in a Hele-Shaw cell with slab width $\Delta z = 2.7R$ for different aspect ratios: (a) $\alpha = 1.75$, (b) $\alpha = 3.25$, and (c) $\alpha = 4.0$. Otherwise, the same description as in Fig. 7 is used.

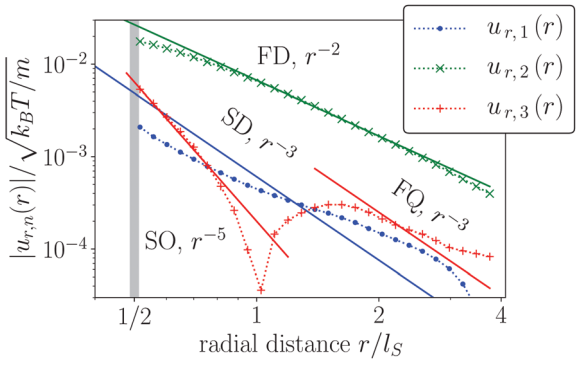

Fig. 9 Absolute values of the radial Legendre coefficients $|u_{r,n}(r)|$ of the simulated flow field of a pusher-type squirmer rod with aspect ratio $\alpha = 4.0$ calculated from eqn (6) (symbols) and with fitted power laws (solid lines). FD, FQ stand for force dipole and quadrupole, while SD, SO mean source dipole and octupole, respectively.

Increasing the slab width, the flow field of the force dipole always dominates in the given radial range [*cf.* Fig. 10(b) and (c)]. The reason is the green curve shifts upwards while the blue curve shifts downwards with increasing Δz. Thus, the dipole-force moment increases with Δz in qualitative agreement with $\mathscr{A}_n \propto \Delta z$ (*cf.* Section 2.3), while the source-dipole moment decreases with Δz again in qualitative agreement with $\mathscr{B}_n \propto 1/\Delta z$.

The third-order coefficient $\tilde{u}_{\rho,3}(\rho) \propto 1/\rho^4$ does not change very significantly in one direction with increasing Δz. We take this as an indication that both the force quadrupole and source octupole contribute to the flow field. A more detailed analysis of $\mathscr{A}_3$ and $\mathscr{B}_3$ is not feasible with the hydrodynamic MPCD method since due to thermal fluctuations it requires long averaging in order to obtain smooth flow lines at large distances. Therefore, larger system sizes would require an immense computational effort.

4 Summary and conclusion

In this paper we introduced the squirmer rod as a new model for elongated microswimmers. By varying aspect ratio and surface slip-velocity field, it is able to describe artificial and biological microswimmers of different shape and propulsion type, such as pushers, pullers, and neutral swimmers. To quantify the generated hydrodynamic flow fields of the squirmer rod, we determined the hydrodynamic multipole moments both in the bulk fluid and the Hele-Shaw geometry, by projecting the simulated flow fields on Legendre or Chebyshev polynomials, respectively. The corresponding expansion coefficients showed the expected radial decay.

The flow field of the neutral squirmer rod in the bulk fluid shows the expected source dipole, while a force quadrupole moment develops linearly with increasing aspect ratio and

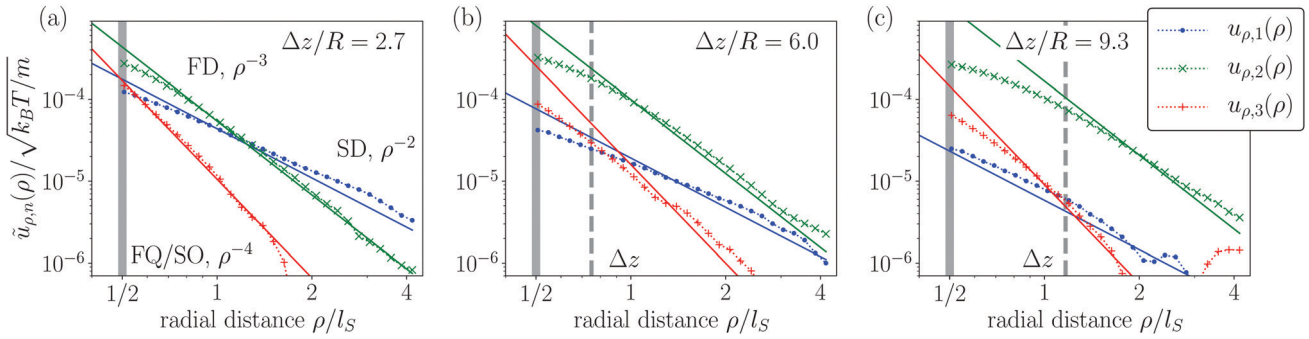

Fig. 10 Multipole analysis of the simulated flow field of a pusher-type squirmer rod with aspect ratio $\alpha = 4$ for different slab widths of the Hele-Shaw cell: (a) $\Delta z = 2.7R$, (b) $\Delta z = 6.0R$ and (c) $\Delta z = 9.3R$. In addition to the source dipole ($n = 1$, blue dots) and force quadrupole/source octupole ($n = 3$, red pluses), the force dipole ($n = 2$, green crosses) is observed. Otherwise, the same description as in Fig. 7 is used.

becomes dominant beyond $\alpha = 2$. It is due to a non-uniform distribution of the force, with which the rod acts on the fluid. By taking an average of the surface slip-velocity field over the rod surface, the actual swimming velocity is overestimated. In the Hele-Shaw geometry the radial decay of the multipole flow fields changes as predicted by theory. Especially at low slab width Δz we find a good match with our simulations. The flow field of the source dipole now decay as $1/\rho^2$ and dominates at radial distances $\rho > \Delta z$ for all α and Δz over the field of the force quadrupole, which now decays as $1/\rho^4$.

For the pusher-type squirmer rod with noticeable elongation we observe that the flow field is composed of four hydrodynamic moments: force dipole, source dipole, force quadrupole, and source octupole. In bulk the force dipole completely dominates the flow field and determines the radial decay with $1/r^2$. However, in the Hele-Shaw geometry the radial decay changes to $1/\rho^3$ and is less long-ranged. Nevertheless, for larger slab widths and the recorded radial distances it dominates the flow field, while for small slab widths we see a cross over to the longer-ranged source-dipole field. This is in qualitative agreement with the expected behavior of the strength of the multipole moments with increasing slab width: the force dipole becomes stronger while the source dipole weakens. Finally, in the Hele-Shaw geometry the flow fields of force quadrupole and source octupole have the same radial decay. Varying slab width suggests that they both contribute.

Our work shows how elongated microswimmers generate additional hydrodynamic multipole moments compared to swimmers of spherical shape, which leads to a more complex appearance of the generated flow field. Since rods experience additional torques in a non-uniform flow field *via* the strain-rate tensor[71] this will generate different behavior in suspensions of squirmer rods compared to their pure steric interactions. Furthermore, the source dipole is predicted to be the dominant hydrodynamic moment in a Hele-Shaw geometry,[13] which we confirm for neutral squirmer rods for varying slab width. However, for pusher and puller rods the dominance of the force dipole depends on the slab width and radial distance.

Therefore, in the continuation of this work, we plan to investigate the collective dynamic behavior of the squirmer rods introduced in this work. Thereby we will gain an understanding how hydrodynamic interactions through the self-generated flow fields contribute to different types of dynamic behavior such as swarming in active nematics or active turbulent phases. As a further extension of the presented model, we plan to introduce bending rigidity between the different components of the squirmer rod to model active flexible filaments used, for example, in ref. 7 and 8.

Conflicts of interest

There are no conflicts to declare.

A Force and source multipole moments in Hele-Shaw geometry

In their seminal paper Liron and Mochon derived Green's function $\mathcal{G}$ for solving the Stokes equations in a Hele-Shaw cell of width Δz (*cf.* Fig. 1) using an infinite series of image point forces.[12] For a point force along the z axis normal to the bounding plates, the Stokeslet decays exponentially and the same applies to the flow field component $u_3(\mathbf{r})$ along the z direction. In the following we concentrate on the case, where the point force is directed along unit vector $\hat{\mathbf{e}}$ in the x–y plane and only flow in this plane is monitored. Then the main feature of the Stokeslet is the long-range flow field of a two-dimensional hydrodynamics source dipole, which appears in the second line,

$$\mathcal{G}_{ij}\hat{e}_j \propto -\frac{3\Delta z}{\pi\eta}\frac{r_3}{\Delta z}\left(1-\frac{r_3}{\Delta z}\right)\frac{r_3^{\mathrm{sw}}}{\Delta z}\left(1-\frac{r_3^{\mathrm{sw}}}{\Delta z}\right) \times \frac{1}{\rho^2}\left[\frac{\delta_{ij}}{2}-\hat{r}_i\hat{r}_j\right]\hat{e}_j. \tag{16}$$

Here, the indices $i, j \in \{1, 2\}$ belong to the x–y plane, ρ is the corresponding radial distance from the point force, and $\hat{\mathbf{r}}$ the radial unit vector. In the first line on the right hand side a Poiseuille flow profile is visible, which vanishes at the plate locations $r_3 = 0$ and Δz, and an equivalent term with the z coordinate of the swimmer, r_3^{sw}, appears.

In the Stokes flow regime any flow field surrounding a solid body can be written as the sum of hydrodynamic multipoles or

singularities, which can be derived from the Stokeslet in eqn (16). For the flow field of the squirmer rod we list the relevant terms:

$$\mathbf{u}(\mathbf{r}) = \mathbf{u}_{\mathrm{FD}}(\mathbf{r}) + \mathbf{u}_{\mathrm{FQ}}(\mathbf{r}) + \mathbf{u}_{\mathrm{SD}}(\mathbf{r}) + \mathbf{u}_{\mathrm{SO}}(\mathbf{r}). \ldots \tag{17}$$

Since the squirmer rod is force free, there only appears the flow field of a force dipole [$\mathbf{u}_{\mathrm{FD}}(\mathbf{r})$] and, in addition, the flow fields of a force quadrupole [$\mathbf{u}_{\mathrm{FQ}}(\mathbf{r})$], a source dipole [$\mathbf{u}_{\mathrm{SD}}(\mathbf{r})$], and a source octupole [$\mathbf{u}_{\mathrm{SO}}(\mathbf{r})$].[14,65]

Following ref. 14 and 65 we derive the flow fields of force multipoles with uniaxial symmetry from the Stokeslet in eqn (16) by applying the directional derivative $\hat{\mathbf{e}}\cdot\nabla_p n$ times on $\mathscr{G}_{ij}\hat{e}_j$, where ∇_p acts on the location of the point force. For $n = 1$ and 2 we thus obtain the respective flow fields of a hydrodynamic force dipole,

$$\begin{aligned} u_{i,\mathrm{FD}}(\mathbf{r}) &= -24\frac{\mathscr{A}_2}{\rho^3}\frac{r_3}{\Delta z}\left(1-\frac{r_3}{\Delta z}\right)\frac{r_3^{\mathrm{sw}}}{\Delta z}\left(1-\frac{r_3^{\mathrm{sw}}}{\Delta z}\right) \\ &\times \left[2\delta_{ij}\hat{r}_i\hat{e}_j + \hat{r}_i - 4\hat{r}_i\hat{r}_j^2\hat{e}_j\right], \end{aligned} \tag{18}$$

and force quadrupole,

$$\begin{aligned} u_{i,\mathrm{FQ}}(\mathbf{r}) &= -24\frac{\mathscr{A}_3}{\rho^4}\frac{r_3}{\Delta z}\left(1-\frac{r_3}{\Delta z}\right)\frac{r_3^{\mathrm{sw}}}{\Delta z}\left(1-\frac{r_3^{\mathrm{sw}}}{\Delta z}\right) \\ &\times \left[\delta_{ij} - 4\delta_{ij}\hat{r}_i^2 - 4\hat{r}_i\hat{r}_j + 8\hat{r}_i\hat{r}_j^3\right]\hat{e}_j. \end{aligned} \tag{19}$$

Note that we allocated a factor Δz from the Stokeslet to the force-multipole moments, so that we have $\mathscr{A}_n \propto \Delta z$. Again following ref. 14 and 65, we derive the flow field of a source dipole by the operation, $u_{i,\mathrm{SD}}(\mathbf{r}) \propto \nabla_p{}^2\mathscr{G}_{ij}\hat{e}_j$. While the second derivative with respect to $r_{\mathrm{s}}^{\mathrm{sw}}$ removes the term with $r_{\mathrm{s}}^{\mathrm{sw}}$ and generates a factor $1/\Delta z^2$, the remaining two-dimensional Laplace operator acting on the source dipole term gives zero. Thus, one arrives at

$$v_{i,\mathrm{SD}}(\mathbf{r}) = -6\frac{\mathscr{B}_1}{\rho^2}\frac{r_3}{\Delta z}\left(1-\frac{r_3}{\Delta z}\right)\left[\frac{\delta_{ij}}{2} - \hat{r}_i\hat{r}_j\right]\hat{e}_j \tag{20}$$

which is nearly identical to the Stokeslet. Flow fields of higher source multipoles are generated by the directional derivate $\hat{\mathbf{e}}\cdot\nabla_p$ acting on $\mathbf{v}_{\mathrm{SD}}(\boldsymbol{r})$. Of relevance is the second derivative, which gives the flow field of a source octupole:

$$\begin{aligned} v_{i,\mathrm{SO}}(\mathbf{r}) &= -6\frac{\mathscr{B}_3}{\rho^4}\frac{r_3}{\Delta z}\left(1-\frac{r_3}{\Delta z}\right) \\ &\times \left[\delta_{ij} - 4\delta_{ij}\hat{r}_i^2 - 4\hat{r}_i\hat{r}_j + 8\hat{r}_i\hat{r}_j^3\right]\hat{e}_j. \end{aligned} \tag{21}$$

Again, we have allocated a factor $1/\Delta z$ to the source-multipole moments, so that we have $\mathscr{B}_n \propto 1/\Delta z$. In the following, we restrict ourselves to a squirmer rod oriented along the x-axis and swimming in the midplane of the Hele-Shaw cell, *i.e.*, $\hat{\mathbf{e}} = \hat{\mathbf{e}}_x$ and $r_3^{\mathrm{sw}} = \dfrac{\Delta z}{2}$. To convert the flow fields in the Hele-Shaw geometry to a form similar to the one used in free Stokes flow, we switch to cylindrical coordinates (ρ,φ,z). We eliminate the z-dependence of the multipole flow fields by integrating over the Poiseuille profile along z, project the resulting velocity field on the radial direction, and arrive at

$$\tilde{u}_\rho(\rho,\varphi) \equiv \frac{\hat{\mathbf{e}}_\rho}{\Delta z}\cdot\int_0^{\Delta z}\mathbf{u}(\rho,\varphi,z)\mathrm{d}z. \tag{22}$$

The resulting radial velocity component can also be decomposed into cell-height averaged multipole moments $\tilde{u}_{\rho,n}$. For the relevant multipole moments we have

$$\tilde{u}_\rho(\rho,\varphi) = \tilde{u}_{\rho,\mathrm{FD}}(\rho,\varphi) + \tilde{u}_{\rho,\mathrm{FQ}}(\rho,\varphi) + \tilde{u}_{\rho,\mathrm{SD}}(\rho,\varphi) + \tilde{u}_{\rho,\mathrm{SO}}(\rho,\varphi) + \ldots. \tag{23}$$

which we calculate using eqn (18)–(21). For the force dipole and quadrupole, we obtain

$$\tilde{u}_{\rho,\mathrm{FD}}(\rho,\varphi) = -\mathscr{A}_2\frac{T_2(\cos\varphi)}{\rho^3} \tag{24}$$

and

$$\tilde{u}_{\rho,\mathrm{FQ}}(\rho,\varphi) = -\mathscr{A}_3\frac{T_3(\cos\varphi)}{\rho^4}, \tag{25}$$

respectively. The source dipole and octupole give

$$\tilde{u}_{\rho,\mathrm{SD}}(\rho,\varphi) = -\mathscr{B}_1\frac{T_1(\cos\varphi)}{\rho^2} \tag{26}$$

and

$$\tilde{u}_{\rho,\mathrm{SO}}(\rho,\varphi) = -\mathscr{B}_3\frac{T_3(\cos\varphi)}{\rho^4} \tag{27}$$

respectively, where the $T_n(\cos\varphi) = \cos(n\varphi)$ are Chebyshev polynomials of the first kind. These formulas agree with the general result given in eqn (9) in the main text. Using eqn (10) and (11), we can then determine the force and source moments $\mathscr{A}_2$, $\mathscr{A}_3$,1, and $\mathscr{B}_3$ by a numerical fit of the power law ρ^{-n} to $\tilde{u}_{\rho,n}(\rho)$.

B Moment-of-inertia tensor of the squirmer rod

The moment-of-inertia tensor $\mathbf{I}_{\mathrm{rod}}$ of the squirmer rod can be calculated applying Steiner's theorem to the constituent parts of the squirmer rod. First, we calculate the masses m_{mid} and m_{cap} as well as the moment-of-inertia tensors $\mathbf{I}_{\mathrm{mid}}$ and $\mathbf{I}_{\mathrm{cap}}$ of the middle segments and end caps relative to their respective centers of mass. Due to the rotational symmetry around the rod axis, $\mathbf{I}_{\mathrm{rod}}$, $\mathbf{I}_{\mathrm{mid}}$ and $\mathbf{I}_{\mathrm{cap}}$ have two degenerate eigenvalues in the x–y plane perpendicular to the rod axis and a different eigenvalue along the rod axis $\hat{\mathbf{e}} = \hat{\mathbf{z}}$.

In each of the constituent parts of the squirmer rods, we use cylindrical coordinates (ρ,φ,z), where $z = 0$ is the center of each spherical squirmer. The constituent parts are sections of spheres of radius R that extend from $z = h_{\mathrm{min}}$ to $z = h_{\mathrm{max}}$. Integration over the enclosed volume with constant mass density ρ_0, gives the mass

$$m = \rho_0\pi\left[R^2 z - \frac{z^3}{3}\right]_{h_{\mathrm{min}}}^{h_{\mathrm{max}}}. \tag{28}$$

For the middle segments of the rod, $-h_{\mathrm{min}} = h_{\mathrm{max}} = d/2$, and for the end caps $h_{\mathrm{min}} = -d/2$ and $h_{\mathrm{max}} = R$.

Based on the known formula for the moment-of-inertia tensor for a solid body with uniform mass density ρ_0, $I_{ij} = \rho_0\int(\mathbf{x}^2 - x_i x_j)\mathrm{d}V$, we first calculate the I_{zz} components of the constituent parts. Integrating $\rho_0\rho^2$ over the enclosed

volume yields

$$I_{zz} = \frac{\pi\rho_0}{4}\left[R^4 z + \frac{2R^2 z^3}{2} - \frac{3z^5}{5}\right]_{h_{\min}}^{h_{\max}} \tag{29}$$

For the component I_{xx} the integrand becomes $\rho_0(z^2 + \rho^2 \sin^2\varphi)$, which yields

$$I_{xx}{}' = \frac{\pi\rho_0}{2}\left[R^4 z - \frac{2R^2 z^3}{2} + \frac{z^5}{5}\right]_{h_{\min}}^{h_{\max}}. \tag{30}$$

We attach a dash here since for the end caps the mass distribution is not symmetric about $z = 0$ and therefore the center of mass of the caps does not coincide with the reference point $\mathbf{x} = 0$, for which $I_{xx}{}'$ was calculated. For further use below, we need the moment of inertia I_{xx} for a rotation axis perpendicular to the z axis through the center of mass and calculate it using Steiner's theorem: $I_{xx} = I_{xx}{}' - m z_{\mathrm{com}}{}^2$. The distance z_{com} between $z = 0$ and the center of mass follows by integrating $z\rho_0/m$ over the enclosed volume,

$$z_{\mathrm{com}} = \frac{\pi\rho_0}{m}\left[\frac{z^2R^2}{2} - \frac{z^3}{3}\right]_{h_{\min}}^{h_{\max}}. \tag{31}$$

For the middle segments the mass distribution is symmetric about $z = 0$ and hence $I_{\mathrm{xx}} = I_{\mathrm{xx}}{}'$.

We now use the previous results to calculate the relevant moments of inertia $I_{\mathrm{rod},ij}$ for the squirmer rod. For the moment $I_{\mathrm{rod},zz}$ the relevant rotational axis along $\hat{\mathbf{z}}$ goes through all the centers of mass of the n_s segments. Thus, we can just add up their moments of inertia:

$$I_{\mathrm{rod},zz} = 2I_{\mathrm{cap},zz} + (n_s - 2)I_{\mathrm{mid},zz}. \tag{32}$$

For the remaining non-zero moments, $I_{\mathrm{rod},xx} = I_{\mathrm{rod},yy}$, we have to shift the respective moments of the middle segments and end caps, $I_{\mathrm{mid},xx}$ and $I_{\mathrm{cap},xx}$, using their distances from the rod's center of mass and Steiner's theorem:

$$I_{\mathrm{rod},xx} = 2\left\{\sum_{i=1}^{n_s/2-1}\left[I_{\mathrm{mid},xx} + m_{\mathrm{mid}}d^2\left(i - \frac{1}{2}\right)^2\right] + I_{\mathrm{cap},xx} + m_{\mathrm{cap}}\left(\frac{n_s - 1}{2}d\right)^2\right\}, \tag{33}$$

for an even number of squirmers per rod n_s.

C Swimming velocity

In principle, following ref. 70 the swimming velocity of a squirmer of arbitrary shape can be calculated analytically using the reciprocal theorem.[70] If $(\mathbf{v},\sigma)$ are the velocity and stress tensor that solve the Stokes equation for the force-free swimmer and $(\mathbf{v}',\sigma')$ the corresponding fields for a passive object of the same shape pulled now by a force $\boldsymbol{F}'$, then

$$\mathbf{F}' \cdot \mathbf{U} = -\int_S \hat{\mathbf{n}} \cdot \sigma' \cdot \mathbf{v}_s \mathrm{d}S. \tag{34}$$

Here $\mathbf{U}$ is the swimming velocity, $\hat{\mathbf{n}}$ the surface normal, $\mathbf{v}_s$ the slip velocity at the swimmer surface and S the surface of the swimmer's body. For a sphere of radius R the acting force is $\mathbf{F}' = -6\pi\eta R\mathbf{U}'$, where $\mathbf{U}'$ is the translational velocity, and the surface force density $\hat{\mathbf{n}} \cdot \sigma' = -\frac{3\eta}{2R}\mathbf{U}'$ is constant and proportional to $\mathbf{U}'$. Thus, for a sphere the swimming velocity $\mathbf{U}$ is simply the negative average of the surface slip velocity $\mathbf{v}_s$

$$\mathbf{U} = -\frac{1}{4\pi R^2}\int_S \mathbf{v}_s \mathrm{d}S. \tag{35}$$

To provide an estimate for the swimming velocity of the squirmer rod, we apply the approximation that the surface force density is constant along the surface of the passive rod, when pulled by force $\mathbf{F}'$ along its long axis. The estimate for the swimming velocity is thus the average of the surface slip velocity $\mathbf{v}_s$ as given in eqn (14).

To determine the swimming velocity, we calculate the surface of the squirmer rod,

$$S_{\mathrm{rod}} = 2\pi R^2\left[\int_0^{\pi}\sin\theta \mathrm{d}\theta + (n_s - 1)\int_{\theta_{\min}}^{\theta_{\max}}\sin\theta \mathrm{d}\theta\right], \tag{36}$$

which adds up the surface of one complete sphere and $n_s - 1$ middle segments of a sphere. The integration limits for the polar angles of the middle segments are $\theta_{\min} = \arccos\left(\frac{\alpha - 1}{n_s - 1}\right)$ and $\theta_{\max} = \pi - \theta_{\min}$. We obtain $S_{\mathrm{rod}} = 4\pi R^2\alpha$. Similarly, we integrate the scalar product of the surface velocity $\mathbf{v}_s$ and the orientation vector $\hat{\mathbf{e}}$

$$\mathbf{v}_s \cdot \hat{\mathbf{e}} = B_1^s(\cos^2\theta - 1) \tag{37}$$

over the surface of one complete sphere and $n_s - 1$ middle segments,

$$\int_{S_{\mathrm{rod}}} \mathbf{v}_s \cdot \hat{\mathbf{e}} \mathrm{d}S = 2\pi R^2 B_1^s\left[\int_0^{\pi}(\mathbf{v}_s \cdot \hat{\mathbf{e}})\sin\theta \mathrm{d}\theta + (n_s - 1)\int_{\theta_{\min}}^{\theta_{\max}}(\mathbf{v}_s \cdot \hat{\mathbf{e}})\sin\theta \mathrm{d}\theta\right], \tag{38}$$

and obtain

$$\int_{S_{\mathrm{rod}}} \mathbf{v}_s \cdot \hat{\mathbf{e}} \mathrm{d}S = 4\pi R^2 B_1^s\left[\alpha - \frac{1}{3} - \frac{n_s - 1}{3}\left(\frac{\alpha - 1}{n - 1}\right)^3\right]. \tag{39}$$

The swimming velocity of the squirmer rod is ultimately given by eqn (15).

Acknowledgements

We thank Felix Rühle and Josua Grawitter for helpful discussions on the topic of the manuscript. We also acknowledge financial support from the Collaborative Research Center 910 funded by Deutsche Forschungsgemeinschaft.

References

1 E. Lauga and T. R. Powers, *Phys. Rev. Lett.*, 2009, **72**, 096601.
2 M. C. Marchetti, J.-F. Joanny, S. Ramaswamy, T. B. Liverpool, J. Prost, M. Rao and R. A. Simha, *Rev. Mod. Phys.*, 2013, **85**, 1143.

3 J. Elgeti, R. G. Winkler and G. Gompper, *Rep. Prog. Phys.*, 2015, **78**, 056601.
4 H. H. Wensink, J. Dunkel, S. Heidenreich, K. Drescher, R. E. Goldstein, H. Löwen and J. M. Yeomans, *Proc. Natl. Acad. Sci. U. S. A.*, 2012, **109**, 14308.
5 D. Nishiguchi, I. S. Aranson, A. Snezhko and A. Sokolov, *Nat. Commun.*, 2018, **9**, 1–8.
6 S. Thutupalli, R. Seemann and S. Herminghaus, *New J. Phys.*, 2011, **13**, 073021.
7 T. Sánchez, D. T. N. Chen, S. J. DeCamp, M. Heymann and Z. Dogic, *Nature*, 2012, **491**, 431.
8 V. Schaller, C. Weber, C. Semmrich, E. Frey and A. R. Bausch, *Nature*, 2010, **467**, 73–77.
9 H. Wioland, F. G. Woodhouse, J. Dunkel, J. O. Kessler and R. E. Goldstein, *Phys. Rev. Lett.*, 2013, **110**, 268102.
10 A. Zöttl and H. Stark, *J. Phys.: Condens. Matter*, 2016, **28**, 253001.
11 J. Blake and A. Chwang, *J. Eng. Mech.*, 1974, **8**, 23–29.
12 N. Liron and S. Mochon, *J. Eng. Mech.*, 1976, **10**, 287–303.
13 T. Brotto, J.-B. Caussin, E. Lauga and D. Bartolo, *Phys. Rev. Lett.*, 2013, **110**, 038101.
14 A. J. Mathijssen, A. Doostmohammadi, J. M. Yeomans and T. N. Shendruk, *J. Fluid Mech.*, 2016, **806**, 35–70.
15 S. Thutupalli, D. Geyer, R. Singh, R. Adhikari and H. A. Stone, *Proc. Natl. Acad. Sci. U. S. A.*, 2018, **115**, 5403–5408.
16 D. L. Koch and G. Subramanian, *Annu. Rev. Fluid Mech.*, 2011, **43**, 637–659.
17 M. Bär, R. Großmann, S. Heidenreich and F. Peruani, *Annu. Rev. Condens. Matter Phys.*, 2019, **11**, 441–466.
18 I. Theurkauff, C. Cottin-Bizonne, J. Palacci, C. Ybert and L. Bocquet, *Phys. Rev. Lett.*, 2012, **108**, 268303.
19 J. Palacci, S. Sacanna, A. P. Steinberg, D. J. Pine and P. M. Chaikin, *Science*, 2013, **339**, 936–940.
20 D. Nishiguchi and M. Sano, *Phys. Rev. E: Stat., Nonlinear, Soft Matter Phys.*, 2015, **92**, 052309.
21 C. C. Maass, C. Krüger, S. Herminghaus and C. Bahr, *Annu. Rev. Condens. Matter Phys.*, 2016, **7**, 171–193.
22 J. Toner and Y. Tu, *Phys. Rev. Lett.*, 1995, **75**, 4326.
23 J. Swift and P. C. Hohenberg, *Phys. Rev. A: At., Mol., Opt. Phys.*, 1977, **15**, 319.
24 J. Dunkel, S. Heidenreich, K. Drescher, H. H. Wensink, M. Bär and R. E. Goldstein, *Phys. Rev. Lett.*, 2013, **110**, 228102.
25 J. Dunkel, S. Heidenreich, M. Bär and R. E. Goldstein, *New J. Phys.*, 2013, **15**, 045016.
26 S. Heidenreich, J. Dunkel, S. H. Klapp and M. Bär, *Phys. Rev. E*, 2016, **94**, 020601.
27 A. Doostmohammadi, J. Ignés-Mullol, J. M. Yeomans and F. Sagués, *Nat. Commun.*, 2018, **9**, 1–13.
28 F. Jülicher, S. W. Grill and G. Salbreux, *Rep. Prog. Phys.*, 2018, **81**, 076601.
29 T. Vicsek, A. Czirók, E. Ben-Jacob, I. Cohen and O. Shochet, *Phys. Rev. Lett.*, 1995, **75**, 1226.
30 G. Grégoire and H. Chaté, *Phys. Rev. Lett.*, 2004, **92**, 025702.
31 H. Chaté, F. Ginelli, G. Grégoire, F. Peruani and F. Raynaud, *Eur. Phys. J. B*, 2008, **64**, 451–456.
32 H. Wensink and H. Löwen, *J. Phys.: Condens. Matter*, 2012, **24**, 464130.
33 M. C. Bott, F. Winterhalter, M. Marechal, A. Sharma, J. M. Brader and R. Wittmann, *Phys. Rev. E*, 2018, **98**, 012601.
34 Ö. Duman, R. E. Isele-Holder, J. Elgeti and G. Gompper, *Soft Matter*, 2018, **14**, 4483–4494.
35 K. Prathyusha, S. Henkes and R. Sknepnek, *Phys. Rev. E*, 2018, **97**, 022606.
36 M. Hennes, K. Wolff and H. Stark, *Phys. Rev. Lett.*, 2014, **112**, 238104.
37 H. Jeckel, E. Jelli, R. Hartmann, P. K. Singh, R. Mok, J. F. Totz, L. Vidakovic, B. Eckhardt, J. Dunkel and K. Drescher, *Proc. Natl. Acad. Sci. U. S. A.*, 2019, **116**, 1489–1494.
38 A. Laskar, R. Singh, S. Ghose, G. Jayaraman, P. S. Kumar and R. Adhikari, *Sci. Rep.*, 2013, **3**, 1–5.
39 A. Laskar and R. Adhikari, *Soft Matter*, 2015, **11**, 9073–9085.
40 J. de Graaf, H. Menke, A. J. Mathijssen, M. Fabritius, C. Holm and T. N. Shendruk, *J. Chem. Phys.*, 2016, **144**, 134106.
41 A. Pandey, P. S. Kumar and R. Adhikari, *Soft Matter*, 2016, **12**, 9068–9076.
42 M. Kuron, P. Stärk, C. Burkard, J. De Graaf and C. Holm, *J. Chem. Phys.*, 2019, **150**, 144110.
43 A. Zöttl and H. Stark, *Phys. Rev. Lett.*, 2014, **112**, 118101.
44 J. Blaschke, M. Maurer, K. Menon, A. Zöttl and H. Stark, *Soft Matter*, 2016, **12**, 9821–9831.
45 A. Zöttl and H. Stark, *Eur. Phys. J. E: Soft Matter Biol. Phys.*, 2018, **41**, 61.
46 M. Theers, E. Westphal, G. Gompper and R. G. Winkler, *Soft Matter*, 2016, **12**, 7372–7385.
47 M. Theers, E. Westphal, K. Qi, R. G. Winkler and G. Gompper, *Soft Matter*, 2018, **14**, 8590–8603.
48 F. J. Schwarzendahl and M. G. Mazza, *Soft Matter*, 2018, **14**, 4666–4678.
49 F. J. Schwarzendahl and M. G. Mazza, *J. Chem. Phys.*, 2019, **150**, 184902.
50 M. Lighthill, *Commun. Pure Appl. Math.*, 1952, **5**, 109–118.
51 J. R. Blake, *J. Fluid Mech.*, 1971, **46**, 199–208.
52 F. Sciortino, A. Giacometti and G. Pastore, *Phys. Rev. Lett.*, 2009, **103**, 237801.
53 S. Jiang, Q. Chen, M. Tripathy, E. Luijten, K. S. Schweizer and S. Granick, *Adv. Mater.*, 2010, **22**, 1060–1071.
54 I. Buttinoni, J. Bialké, F. Kümmel, H. Löwen, C. Bechinger and T. Speck, *Phys. Rev. Lett.*, 2013, **110**, 238301.
55 T. J. Pedley, D. R. Brumley and R. E. Goldstein, *J. Fluid Mech.*, 2016, **798**, 165–186.
56 T. Ishikawa, M. Simmonds and T. Pedley, *J. Fluid Mech.*, 2006, **568**, 119–160.
57 M. T. Downton and H. Stark, *J. Phys.: Condens. Matter*, 2009, **21**, 204101.
58 I. O. Götze and G. Gompper, *Phys. Rev. E: Stat., Nonlinear, Soft Matter Phys.*, 2010, **82**, 041921.
59 G.-J. Li and A. M. Ardekani, *Phys. Rev. E: Stat., Nonlinear, Soft Matter Phys.*, 2014, **90**, 013010.
60 J.-T. Kuhr, J. Blaschke, F. Rühle and H. Stark, *Soft Matter*, 2017, **13**, 7458–7555.

61 F. Rühle, J. Blaschke, J.-T. Kuhr and H. Stark, *New J. Phys.*, 2018, **20**, 025003.
62 J.-T. Kuhr, F. Rühle and H. Stark, *Soft Matter*, 2019, **15**, 5685–5694.
63 A. Malevanets and R. Kapral, *J. Chem. Phys.*, 1999, **110**, 8605–8613.
64 G. Gompper, T. Ihle, D. Kroll and R. Winkler, *Advanced computer simulation approaches for soft matter sciences III*, Springer, Berlin, 2009, pp. 1–87.
65 S. E. Spagnolie and E. Lauga, *J. Fluid Mech.*, 2012, **700**, 105–147.
66 J. Blake, *Math. Proc. Cambridge Philos. Soc.*, 1971, **70**, 303–310.
67 M. P. Allen and D. J. Tildesley, *Computer simulation of liquids*, Oxford University Press, Oxford, 2017.
68 J. de Graaf, A. J. Mathijssen, M. Fabritius, H. Menke, C. Holm and T. N. Shendruk, *Soft Matter*, 2016, **12**, 4704–4708.
69 M. P. Howard, A. Z. Panagiotopoulos and A. Nikoubashman, *Comput. Phys. Commun.*, 2018, **230**, 10–20.
70 H. A. Stone and A. D. Samuel, *Phys. Rev. Lett.*, 1996, **77**, 4102.
71 G. B. Jeffery, *Proc. R. Soc. London, Ser. A*, 1922, **102**, 161–179.

The Journal of Chemical Physics ARTICLE scitation.org/journal/jcp

Multi-particle collision dynamics with a non-ideal equation of state. I

Cite as: J. Chem. Phys. 154, 024105 (2021); doi: 10.1063/5.0037934
Submitted: 17 November 2020 • Accepted: 16 December 2020 •
Published Online: 8 January 2021

Arne W. Zantop and Holger Stark[a]

AFFILIATIONS

Institute of Theoretical Physics, Technische Universität Berlin, Hardenbergstraße 36, 10623 Berlin, Germany

[a]Author to whom correspondence should be addressed: holger.stark@tu-berlin.de

ABSTRACT

The method of multi-particle collision dynamics (MPCD) and its different implementations are commonly used in the field of soft matter physics to simulate fluid flow at the micron scale. Typically, the coarse-grained fluid particles are described by the equation of state of an ideal gas, and the fluid is rather compressible. This is in contrast to conventional fluids, which are incompressible for velocities much below the speed of sound, and can cause inhomogeneities in density. We propose an algorithm for MPCD with a modified collision rule that results in a non-ideal equation of state and a significantly decreased compressibility. It allows simulations at less computational costs compared to conventional MPCD algorithms. We derive analytic expressions for the equation of state and the corresponding compressibility as well as shear viscosity. They show overall very good agreement with simulations, where we determine the pressure by simulating a quiet bulk fluid and the shear viscosity by simulating a linear shear flow and a Poiseuille flow.

I. INTRODUCTION

Since their introduction in 1999,[1] algorithms belonging to the method of multi-particle collision dynamics (MPCD) have become a standard tool to simulate fluid flows in the field of soft matter physics.[2–4] In particular, MPCD algorithms have commonly been used to model solvent dynamics in the context of microswimmers,[5–18] where we can only cite a few examples. Further studies address colloidal suspensions,[19–23] polymers,[24–26] blood cells,[27] the African trypanosome as the causative agent of the sleeping sickness,[28] and even fish schools.[29] Also, extensions to binary and ternary fluid mixtures,[30–32] liquid crystals,[33–35] and chemically reacting systems[36] exist. MPCD methods are particularly suited to simulate solvent flow on the microscopic scale because they solve the Navier–Stokes equations but also incorporate the omnipresent thermal fluctuations.[1,37] The particle-based strategy of MPCD makes the implementation of no-slip boundary conditions in complex geometries very straightforward.[38] Furthermore, the collision rules for the coarse-grained fluid particles are well suited for the implementation on parallel computer hardware[39,40] so that extensive simulations can also be performed on desktop computers with graphic cards.

Although MPCD methods are often used to simulate the dynamics of incompressible solvents, one has to be aware that the coarse-grained fluid particles follow the equation of state of an ideal gas.[1,32,41] Therefore, the fluid is rather compressible and has a low speed of sound c_s.[21] This is tolerable for typical flow velocities well below c_s. In contrast, in the presence of large pressure gradients, pronounced inhomogeneities in the fluid density can occur due to the high compressibility. For example, such a situation has recently been observed in strongly clustered microswimmers,[12] where the overlapping flow fields of many microswimmers are responsible for strong pressure gradients. While variations in fluid density are, in principal, necessary to generate pressure gradients, these variations need to be small to stay close to the limit of an incompressible fluid. Thus, the compressibility needs to be sufficiently small. For the MPCD fluid with its ideal-gas equation of state, this can be achieved by increasing the number n_0 of fluid particles per collision cell and thereby density.[12] However, such an approach causes an immense increase in the simulation time proportional to the square of the fluid density n_0^2 if the system size should be kept constant at an equal Péclet number.

In this paper, we follow a different strategy to decrease compressibility. All the MPCD algorithms consist of a sequence of collision and streaming steps. Here, we propose a new collision rule that results in a non-ideal equation of state for the MPCD fluid. Note that such non-ideal equations of state are required and have

already been introduced in the context of simulating fluid mixtures within MPCD.[31,32] Thus, compressibility is reduced for the constant particle number n_0, and the computational efficiency is enhanced compared to conventional MPCD algorithms, which need to employ a larger particle density. Our approach extends ideas of Tüzel, Ihle, and collaborators, who included geometric properties of hard-core particles in two dimensions into the collision rule to control momentum transport in the fluid.[42,43] This approach has also been extended to the simulation of fluid mixtures.[30] In contrast to conventional MPCD algorithms, where collisions take place at a fixed rate $1/\Delta t$, collisions instead occur stochastically with a probability that depends on the local density and velocities. In the present work, we extent the approach of Refs. 42 and 43 to three dimensions and strongly modify the geometric rules of the collision so that they can be implemented in an existing MPCD code more easily. Furthermore, our new collision rule allows us to keep the typical canonical thermostat and also to take care of angular momentum conservation during collisions, which is particularly important for the simulation of colloids and active particles.[44]

This article is structured as follows: In Sec. II, we introduce the extended MPCD method with its new collision rule including three possible collision probabilities. Then, we derive approximate analytic expressions for the equation of state and the associated compressibility in Sec. III as well as the shear viscosity in Sec. IV. For the shear viscosity, we consider both contributions that arise from the streaming and collision step of the extended MPCD method. In Sec. V, we compare these analytic expressions with the results from simulations and obtain very good agreement for the equation of state. In particular, we demonstrate the reduction of the compressibility for reasonable particle densities. We measure the shear viscosity by determining the collisional and streaming viscosities in a linear shear flow geometry. The total viscosity agrees very well with values determined from simulating a Poiseuille flow and also with the analytic expression above a density of $\sim n_0 = 20$. We close with conclusions and an outlook in Sec. VI.

II. ALGORITHM OF THE EXTENDED MPCD METHOD

Our method shares the common features typical for the group of MPCD algorithms.[1,3,45] Like all MPCD algorithms, it considers point-like particles that represent the fluid at a mesoscopic level of description. They perform a sequence of streaming and collision steps. Since the latter conserves linear momentum, the resulting hydrodynamic flow fields fulfill the Navier–Stokes equations.[1] While we perform the steaming step as in other MPCD algorithms, we alter the collision step as already mentioned in the Introduction. We now explain the extended MPCD method in more detail.

During the streaming step (i), the point particles with masses m_0, positions $\mathbf{x}_i(t)$, and velocities $\mathbf{v}_i(t)$ move ballistically during time Δt,

$$\mathbf{x}_i(t+\Delta t) = \mathbf{x}_i(t) + \mathbf{v}_i(t)\Delta t. \tag{1}$$

They collide with confining walls or moving objects such as model microswimmers called squirmers[4,8,9,16–18] and thereby transfer both linear and angular momentum to these moving objects. By applying the so-called bounce-back rule,[1,38] the collisions either enforce the no-slip boundary condition at confining walls and passive colloids or the slip-velocity field, which are present at squirmer surfaces.

For the collision step (ii), we suggest an alternative algorithm compared to the original SRD method[1] or the collision operator based on the Andersen thermostat.[4] As in all MPCD algorithms, the simulation volume is divided by a cubic lattice and the fluid particles are grouped into the cubic unit cells of linear size a_0 centered around $\boldsymbol{\xi}$ and with volume $\mathcal{V}_\xi$. Each cell then contains n_ξ particles with the mean velocity $\mathbf{v}_\xi$ and center-of-mass position $\mathbf{x}_\xi$. Additionally, each cell is divided into two halves A and B by a plane $P_{\mathbf{x}_\xi,\hat{\mathbf{n}}}$ through the center-of-mass position $\mathbf{x}_\xi$[46] and with an orientation defined by the unit normal vector $\hat{\mathbf{n}}$ [see Fig. 1(a)]. For each cell, $\hat{\mathbf{n}}$ is randomly drawn from a discrete set of 13 possible orientations at each collision step. By definition, $\hat{\mathbf{n}}$ always points to region A. The number of particles on each side of the plane is denoted by n_A and n_B, respectively. Their mean velocities $\bar{v}_A$ and $\bar{v}_B$, respectively, along the normal vector $\hat{\mathbf{n}}$ are given relative to $\mathbf{v}_\xi$.

The main idea of the new collision step is that the particles in region A and B only collide when they move toward each other. Then, they stochastically exchange a momentum $m_0\delta v_i$ along $\hat{\mathbf{n}}$ both with particles in the same half A, B and also on the other side of the plane. The latter mechanism generates momentum flux across the randomly oriented plane and thereby contributes to pressure, which belongs to the isotropic part of the stress tensor.

The collision step can be summarized by

$$\begin{aligned}\mathbf{v}_i^{\text{new}} = \mathbf{v}_i + \chi(\Delta u)\{&\hat{\mathbf{n}}\left[\hat{\mathbf{n}}\cdot(\mathbf{v}_\xi - \mathbf{v}_i) + \delta v_i\right] \\ &- \mathbf{I}_\xi^{-1} m_0 \sum_{\mathbf{x}_j\in\mathcal{V}_\xi}\left[\mathbf{x}_{j,c}\times\hat{\mathbf{n}}\,(\delta v_j - \hat{\mathbf{n}}\cdot\mathbf{v}_j)\right]\times\mathbf{x}_{i,c}\},\end{aligned} \tag{2}$$

where $\mathbf{x}_{i,c}$ denotes the position vector of particle i relative to the center-of-mass position $\mathbf{x}_\xi$. As we explain below, the collision between the particles in region A and B occurs with a certain probability. To initiate a collision, the stochastic variable $\chi(\Delta u)$ is set to one; otherwise, it is zero. The term following $\chi(\Delta u)$ in the square brackets sets the normal velocity components of all particles i to the normal component of the center-of-mass velocity, $\hat{\mathbf{n}}\cdot\mathbf{v}_\xi$. Then, new values for the relative velocity component δv_i are assigned as explained below. They all add up to zero in order to preserve the total momentum. The second term in the curly brackets is added to conserve the angular momentum. Thus, the value $L_\xi = m_0\sum_{\mathbf{x}_i\in\mathcal{V}_\xi}\mathbf{x}_i\times\mathbf{v}_i$

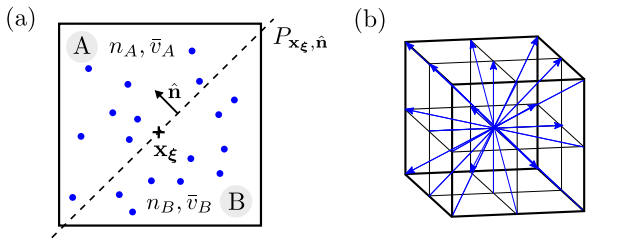

FIG. 1. (a) Side view of a collision cell with the dividing plane $P_{\mathbf{x}_\xi,\hat{\mathbf{n}}}$ through the center-of-mass position $\mathbf{x}_\xi$ and unit normal vector $\hat{\mathbf{n}}$. (b) 13 possible collision or normal vectors $\hat{\mathbf{n}}$ that point to the corners as well as centers of surfaces and edges of the collision cell.

before the collision is preserved. Here, $\mathbf{I}_\xi$ is the moment-of-inertia tensor of all particles in the cell relative to the center of mass.

We have already introduced the mean values of the normal velocity components $\bar{v}_A$ and $\bar{v}_B$ on either side of the collision plane. Then, collisions between the particles of region A and B occur, when, on average, they move toward each other, meaning that the relative velocity

$$\Delta u = \bar{v}_B - \bar{v}_A \tag{3}$$

is positive. Furthermore, collisions between the particle clouds in A and B occur with the rate $c\Delta u n_A n_B$, where c quantifies the scattering cross section. A similar term has been used for the collision rate of two clouds of hard-core particles or in chemical reactions of the second order[47] and can be motivated by the collision term in the Boltzmann equation.[48] Thus, the probability that a collision occurs or that the stochastic variable $\chi(\Delta u)$ is set to one becomes

$$p_\chi(\Delta u) \equiv \Theta(\Delta u)\, c\, \Delta u\, n_A\, n_B \tag{4}$$

$$\approx \Theta(\Delta u)[1 - \exp(-c\, \Delta u\, n_A\, n_B)]. \tag{5}$$

Here, $\Theta(\Delta u)$ is the Heaviside step function so that collisions only occur for $\Delta u > 0$. In the second line, assuming a sufficiently small c, we have introduced the exponential that guarantees $p_\chi(\Delta u) \le 1$. Another possibility to fulfill this constraint using Eq. (4) is[30]

$$p_\chi(\Delta u) = \begin{cases} \Theta(\Delta u)\, c\, \Delta u\, n_A\, n_B & \text{for } p_\chi(\Delta u) \le 1 \\ 1 & \text{else.} \end{cases} \tag{6}$$

We will explore also this form in Sec. V B when we calculate the pressure in the MPCD simulations.

Finally, we introduce the changes δv_i in the velocity component along the normal $\hat{\mathbf{n}}$. It consists of two contributions: $\delta v_i = \delta v_i^t + \delta v_i^s$. The first term transfers momentum from region B of the cell to particles i in the region A and vice versa,

$$\delta v_i^t \equiv \frac{n_{B/A}}{n_{A/B}}\, \bar{v}_{B/A}. \tag{7}$$

Here, the first indices apply to particles i in region A that take over the momentum $m_0 \bar{v}_B$ from region B and the second indices apply to particles i in region B. The ratios n_B/n_A and n_A/n_B guarantee the overall momentum conservation, meaning the total momenta from regions A and B are just swapped. The second contribution,

$$\delta v_i^s \equiv \delta v_i^{\mathrm{MB}} - \Delta v_{\mathrm{A/B}}, \tag{8}$$

assigns each particle a random velocity δv_i^{MB} drawn from a Maxwell–Boltzmann distribution at temperature T, which serves as a thermostat for the fluid. We subtract the mean random velocity

$$\Delta v_{A/B} = \frac{1}{n_{A/B}} \sum_{\{\mathbf{x}_i \in \mathcal{V}_{A/B}\}} \delta v_i^{\mathrm{MB}} \tag{9}$$

to preserve total momentum in both regions A and B, separately.

In particular, the introduction of the momentum transfer in Eq. (7) and the transfer rate Eq. (5) defines the equation of state. As shown in Sec. III, it contains a term proportional to n_ξ^2 resembling a virial expansion and thus extends the ideal gas term.

As in other MPCD algorithms, immersed boundaries are represented by the so-called "ghost" particles during the collision step.[38] These are added to the collision cells to interact with the other fluid particles. In simulations with squirmers, the ghost particles are assigned the local velocity of the translating and rotating squirmers plus a random thermal velocity drawn from a Boltzmann distribution. Then, the changes in linear and angular momentum of the ghost particles following from step (ii) are assigned to the relevant squirmer, which ensures that linear and angular momentum are conserved. Finally, before performing each collision step, the lattice is randomly shifted to ensure Galilean invariance.[49]

III. EQUATION OF STATE

To calculate the equation of state, we use the definition of pressure as the normal component of the momentum flux through an arbitrarily oriented plane.[50] In the extended MPCD method, both streaming (i) and collision step (ii) contribute to the pressure,

$$P = P_{\mathrm{coll}} + P_{\mathrm{str}}. \tag{10}$$

During the streaming step (i), particles do not interact and simply transport momentum across a plane. This results in the ideal gas contribution $P_{\mathrm{str}} = nk_{\mathrm{B}}T/a_0^3$, which we already know from the conventional MPCD methods.[32]

To evaluate the contribution P_{coll} from the collision step (ii), we consider the momentum flux across a plane with area a_0^2 that lies in a single collision cell. Without loss of generality, we choose the plane $P_{\hat{\mathbf{y}},y_0}$ perpendicular to the $\hat{\mathbf{y}}$ axis at position y_0 and then average over all y_0 (see Fig. 2). During the collision step, momentum is transported from the region $y < y_0$ across the plane $P_{\hat{\mathbf{y}},y_0}$ into $y > y_0$ during time Δt. Thus, for the pressure as momentum transfer per area and time, we obtain

$$P_{\mathrm{coll}} = \frac{m_0}{a_0^2 \Delta t} \left\langle \hat{\mathbf{y}} \cdot \sum_{\{i|y_i > y_0\}} (\mathbf{v}_i^{\mathrm{new}} - \mathbf{v}_i) \right\rangle. \tag{11}$$

Here, i is restricted to all particles above $P_{\hat{\mathbf{y}},y_0}$ and $m_0 \hat{\mathbf{y}} \cdot (\mathbf{v}_i^{\mathrm{new}} - \mathbf{v}_i)$ is the change in the normal momentum component of particle i during

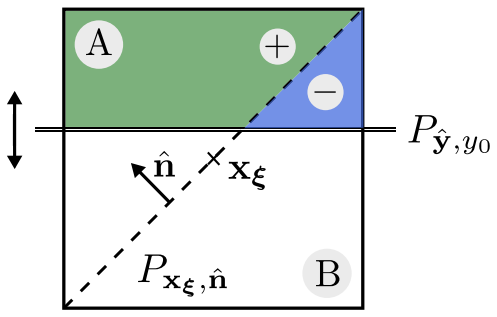

FIG. 2. To derive the equation of state, we consider the momentum transferred to the region above the plane $P_{\hat{\mathbf{y}},y_0}$ with unit normal vector $\hat{\mathbf{y}}$ and at position $y = y_0$. Note that to evaluate $\mathrm{sign}(\mathbf{x} \cdot \hat{\mathbf{n}})$ in Eq. (15), one has to distinguish particles that are located in the green region as part of region A relative to the collision plane with normal $\hat{\mathbf{n}}$ and particles in the blue region as part of B.

collision and given in Eq. (2). The average goes over all possible collisions, particle configurations, orientations $\hat{\mathbf{n}}$ of the collision planes, and positions y_0. The term added to Eq. (2) in the second line to preserve angular momentum does not contribute to $P_{\rm coll}$ since it vanishes when averaging over all possible collisions. Furthermore, since particle i is either in region A and B and we average over all particle velocities relative to $\mathbf{v}_\xi$ with identical velocity distributions, we can ultimately replace $\hat{\mathbf{n}}\cdot(\mathbf{v}_\xi - \mathbf{v}_i)$ in Eq. (2) by the mean velocities $-\bar{v}_{A/B}$ in region A or B of the collision cell. Note that $\bar{v}_{A/B}$ are given relative to $\hat{\mathbf{n}}\cdot\mathbf{v}_\xi$. The choice of index A or B depends on the location of particle i. Thus, we can simplify Eq. (11) to

$$P_{\rm coll} = \frac{m_0}{a_0^2\Delta t}\left\langle \chi(\Delta u)\,\hat{\mathbf{y}}\cdot\hat{\mathbf{n}} \sum_{\{i|y_i>y_0\}} \delta v_i - \bar{v}_{A/B}\right\rangle. \tag{12}$$

The stochastic contribution δv_i^s of δv_i given in Eq. (8) obeys a Gaussian distribution with zero mean and therefore vanishes on average. The remaining part δv_i^t given in Eq. (7) becomes $\bar{v}_{B/A}$ using $n_{A/B} \approx n_\xi/2$. Thus, with the definition of the collision velocity Δu in Eq. (3), we can finally replace $\delta v_i - \bar{v}_{A/B}$ by $\bar{v}_{B/A} - \bar{v}_{A/B} = \Delta u\,\mathrm{sign}(\mathbf{x}_i\cdot\hat{\mathbf{n}})$. The factor $\mathrm{sign}(\mathbf{x}_i\cdot\hat{\mathbf{n}})$ comes in since the first index in $\bar{v}_{B/A} - \bar{v}_{A/B}$ applies if particle i is in region A, while the second index refers to a particle i in B (see Fig. 2). Noting also that Δu and $\mathbf{x}_i$ are independent stochastic variables, we can factorize the average in Eq. (12) and rewrite it as

$$P_{\rm coll} = \frac{m_0}{a_0^2\Delta t}\langle\chi(\Delta u)\Delta u\rangle\left\langle \hat{\mathbf{y}}\cdot\hat{\mathbf{n}} \sum_{\{i|y_i>y_0\}} \mathrm{sign}(\mathbf{x}_i\cdot\hat{\mathbf{n}})\right\rangle, \tag{13}$$

where

$$\langle\chi(\Delta u)\Delta u\rangle = \int_0^\infty \Delta u\, p_\chi(\Delta u)\, p(\Delta u)\,\mathrm{d}\Delta u. \tag{14}$$

Here, $p(\Delta u)$ is the probability distribution for Δu and $p_\chi(\Delta u)$ is the probability for a collision to take place, as introduced in Sec. II.

We now calculate the two averages of Eq. (13). In the second average, we replace the conditional sum by a volume integral introducing the factor $n_\xi/a_0^3\,\Theta(y-y_0)$ and average over y_0. We write the second average as $n_\xi\alpha_P$, where we identify the purely geometrical factor

$$\alpha_P \equiv \left\langle \frac{\hat{\mathbf{y}}\cdot\hat{\mathbf{n}}}{a_0^4}\int_{\mathcal{V}_\xi}\int_{-a_0/2}^{a_0/2}\mathrm{sign}(\mathbf{x}\cdot\hat{\mathbf{n}})\,\Theta(y-y_0)\,\mathrm{d}y_0\mathrm{d}V\right\rangle_{\hat{\mathbf{n}}}. \tag{15}$$

It is the difference between the green and blue volume in Fig. 2 averaged over all $\hat{\mathbf{n}}$ and y_0 and weighted by the projection of $\hat{\mathbf{n}}$ on $\hat{\mathbf{y}}$. The integrals can be calculated for each of the 13 normal vectors $\hat{\mathbf{n}}$ so that we obtain in total

$$\alpha_P = \frac{1}{26}\left[\frac{1}{2} + 4\left(\frac{1}{3\sqrt{2}} + \frac{13}{48\sqrt{3}}\right)\right] \approx 0.08. \tag{16}$$

For the second average, we need the probability distribution for $\Delta u = \bar{v}_B - \bar{v}_A$. Since the components of the single-particle velocities are Gaussian distributed with variance k_BT/m_0, also Δu is Gaussian distributed with variance $4k_BT/(m_0 n_\xi)$, as shown in Appendix A using $n_A = n_B \approx n_\xi/2$. Taking the collision probability from Eq. (4), we then have

$$\langle\chi(\Delta u)\Delta u\rangle = c\,n_A\,n_B\langle\Theta(\Delta u)\,\Delta u^2\rangle = c\,n_\xi\frac{k_BT}{2m_0}. \tag{17}$$

Thus, in total, we obtain from Eq. (13) for the pressure contribution of the collision step,

$$P_{\rm coll} = \frac{c\alpha_P}{2a_0^2\Delta t}k_BT{n_\xi}^2, \tag{18}$$

which is quadratic in the particle density n_ξ. Hence, up to second order in density, the full equation of state reads

$$Pa_0^3 = (P_{\rm str} + P_{\rm coll})\,a_0^3 = n_\xi k_BT\left(1 + \frac{ca_0\alpha_P}{2\Delta t}n_\xi\right). \tag{19}$$

This gives a compressibility

$$\beta = \frac{1}{n_\xi}\frac{\partial n_\xi}{\partial P} = \frac{a_0^3}{n_\xi k_BT}\frac{1}{1 + c\alpha_P a_0 n_\xi/\Delta t}, \tag{20}$$

where the ideal gas contribution from the streaming step, $\beta_{\rm id} = a_0^3/(n_\xi k_BT)$, is diminished by the second-order contribution from the collision step. This means that the MPCD fluid is less compressible.

We add two comments. First, if we take for the collision probability $p_\chi(\Delta u)$ the expression from Eq. (5), which we use as one option in the simulations, one can still evaluate $\langle\chi(\Delta u)\Delta u\rangle$ and then obtain the pressure contribution from the collision step,

$$\begin{aligned} P_{\rm coll} &= \frac{\alpha_P c\,k_BT{n_\xi}^2}{2a_0^2\Delta t}\exp\left(\frac{c^2k_BT}{8m_0}{n_\xi}^3\right)\mathrm{erfc}\left(\sqrt{\frac{k_BT}{2m_0}}\frac{c{n_\xi}^3}{2}\right)\\ &= \frac{c\alpha_P}{2a_0^2\Delta t}k_BT{n_\xi}^2\left[1 - c\sqrt{\frac{k_BT{n_\xi}^3}{2\pi}}\right] + \mathcal{O}({n_\xi}^5). \end{aligned} \tag{21}$$

We will use this form when comparing the pressure in the simulations to the analytic result. Second, in deriving P_c, we have always set $n_A = n_B \approx n_\xi/2$, thus neglecting fluctuations in the particle numbers in regions A and B. For sufficiently large particle numbers, these fluctuations are small. When we compare our analytic results to simulations, we obtain good agreement and the approximation seems to be reasonable.

IV. SHEAR VISCOSITY

To derive an expression for the dynamic shear viscosity η, we consider the linear shear flow

$$\mathbf{v}(y) = \dot{\gamma}y\hat{\mathbf{x}} \tag{22}$$

with constant shear rate $\dot{\gamma}$ (see Fig. 3). We also note that the nonvanishing component of the viscous stress tensor, $\sigma_{xy} = \eta\partial_y v_x = \eta\dot{\gamma}$, describes the negative flux of the x component of momentum along the y direction. Similar to the derivation of the equation of state in Sec. III, the viscosity consists of two contributions from the collision and streaming step, respectively,

$$\eta = \eta_{\rm coll} + \eta_{\rm str}. \tag{23}$$

While the derivation of the collisional viscosity $\eta_{\rm coll}$ requires similar steps used in calculating the collisional contribution of pressure,

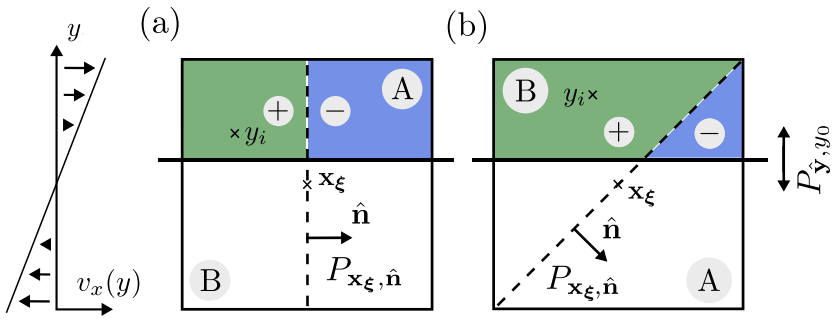

FIG. 3. To derive the shear viscosity, we apply the shear flow $\mathbf{v}(y) = \dot{\gamma} y \hat{\mathbf{x}}$ and consider the momentum transferred to the region above the plane $P_{\hat{\mathbf{y}},y_0}$ with unit normal vector $\hat{\mathbf{y}}$ and at position $y = y_0$. Examples for collision planes with $y_A = 0$ (a) and $y_A \neq 0$ (b) are shown.

the streaming viscosity η_{str} needs special attention. We start with the derivation of η_{coll}.

A. Collisional viscosity

Similar to our derivation of the pressure starting from Eq. (11), we consider the momentum transported during the collision step from the region $y < y_0$ across the plane $P_{\hat{\mathbf{y}},y_0}$ into $y > y_0$ during time Δt (see Fig. 3). However, for σ_{xy}, we need the transfer of the x component of momentum per area and time, and thus,

$$\sigma_{xy} = -\frac{m_0}{a_0^2 \Delta t} \left\langle \hat{\mathbf{x}} \cdot \sum_{i|y_i>y_0} \mathbf{v}_i^{\text{new}} - \mathbf{v}_i \right\rangle. \tag{24}$$

When evaluating the term in the angular bracket using Eq. (2), we concentrate on the first line of Eq. (2) and then at the end following Ref. 45 to include angular momentum conservation, which is the origin of the second line. Replacing δv_i in Eq. (2) by $\bar{v}_{B/A}$ as before in Sec. III, we obtain

$$\sigma_{xy} = -\frac{m_0}{a_0^2 \Delta t} \left\langle \chi(\Delta u)\, \hat{\mathbf{x}} \cdot \hat{\mathbf{n}} \sum_{i|y_i>y_0} [\bar{v}_{B/A} + \hat{\mathbf{n}} \cdot (\mathbf{v}_\xi - \mathbf{v}_i)] \right\rangle.$$

On average, the relative velocity $\Delta u = \bar{v}_B - \bar{v}_A$ is equally distributed on the mean velocities of regions A and B so that we can use $\Delta u/2 \approx \bar{v}_A = -\bar{v}_B$. Furthermore, on average, $\mathbf{v}_\xi$ can be replaced by $\mathbf{v}_i/n_\xi$,[51] and we arrive at

$$\sigma_{xy} = -\frac{m_0}{a_0^2 \Delta t} \left\langle \chi(\Delta u)\, \hat{\mathbf{x}} \cdot \hat{\mathbf{n}} \sum_{i|y_i>y_0} \text{sign}(\mathbf{x}_i \cdot \hat{\mathbf{n}}) \frac{\Delta u}{2} - \hat{\mathbf{n}} \cdot \mathbf{v}_i \left(1 - \frac{1}{n_\xi}\right) \right\rangle. \tag{25}$$

As explained in Sec. III, $\text{sign}(\mathbf{x}_i \cdot \hat{\mathbf{n}})$ is necessary to distinguish between particle i being in either region A or B.

Now, we need to introduce the shear rate $\dot{\gamma}$ from the applied linear shear profile of Eq. (22). It comes in by setting $\mathbf{v}_i$ equal to its deterministic part $\dot{\gamma} y_i \hat{\mathbf{x}}$ and through the Gaussian distribution of Δu. In Appendix B, we show that the conditional distribution for Δu, given the collision vector $\hat{\mathbf{n}}$ and fixed position $\mathbf{x}_i$ of particle i, is Gaussian with the mean value

$$\mu_{i,\hat{\mathbf{n}}} = \langle \Delta u \rangle_{i,\hat{\mathbf{n}}} = -2\, \dot{\gamma}\, \hat{\mathbf{x}} \cdot \hat{\mathbf{n}}\, \frac{y_A(n_\xi - 1) + \text{sign}(\mathbf{x}_i \cdot \hat{\mathbf{n}}) y_i}{n_\xi}. \tag{26}$$

The first factor originates from the orientation of the collision plane with collision vector $\hat{\mathbf{n}}$ relative to the shearing direction $\hat{\mathbf{x}}$ and the second factor from keeping particle i at fixed height y_i. The quantity y_A is the y coordinate of the center of mass of region A defined by the collision plane. For the different collision vectors $\hat{\mathbf{n}}$, we give them in Table I. We need this conditional mean value $\mu_{i,\hat{\mathbf{n}}} = \langle \Delta u \rangle_{i,\hat{\mathbf{n}}}$ when averaging over Δu since in Eq. (25), we also average over the position of particle i. Now, to evaluate the shear viscosity, it is sufficient to only consider the terms of σ_{xy} linear in the shear rate $\dot{\gamma}$. As we demonstrate in the following, they result from either thermal fluctuations of Δu or the deterministic part of $\mathbf{v}_i$ equal to $\dot{\gamma} y_i \hat{\mathbf{x}}$. Thermal fluctuations of $\mathbf{v}_i$ can be neglected since they produce higher-order terms in $\dot{\gamma}$.

To perform the average over Δu in Eq. (25), we first evaluate the required averages using the conditional distribution $p(\Delta u - \mu_{i,\hat{\mathbf{n}}})$ (see Appendix C). Since the shear-induced shift $\mu_{i,\hat{\mathbf{n}}}$ is small compared to the width of the distribution, $m_0 \mu_{i,\hat{\mathbf{n}}}^2 / k_B T \ll 1$, we can always linearize in $\mu_{i,\hat{\mathbf{n}}} \propto \dot{\gamma}$. First, for the mean conditional collision rate using Eq. (4) for $p_\chi(\Delta u)$, we obtain

$$\begin{aligned} \langle \chi(\Delta u) \rangle &= \int_0^\infty p(\Delta u - \mu_{i,\hat{\mathbf{n}}})\, p_\chi(\Delta u)\, \mathrm{d}\Delta u \\ &= c \sqrt{\frac{k_B T n_\xi^3}{8\pi m_0}} + \mathcal{O}(\mu_{i,\hat{\mathbf{n}}}) \equiv \Gamma(n_\xi, c) + \mathcal{O}(\mu_{i,\hat{\mathbf{n}}}). \end{aligned} \tag{27}$$

Only the contribution of the zeroth order in $\mu_{i,\hat{\mathbf{n}}}$ is required, since the last term in Eq. (25) already contributes the required term linear in $\dot{\gamma}$ by setting $\mathbf{v}_i = \dot{\gamma} y_i \hat{\mathbf{x}}$. For the second necessary mean value, we obtain

TABLE I. Values of $|y_A|$ and $|\alpha_{\eta,\hat{\mathbf{n}}}|$ for all collision vectors $\hat{\mathbf{n}}$. Both quantities y_A and $\alpha_{\eta,\hat{\mathbf{n}}}$ have the same sign equal to $-\text{sign}(\hat{\mathbf{n}} \cdot \hat{\mathbf{y}})$ and only appear as product in Eq. (30). Furthermore, note that only collision vectors with $\hat{\mathbf{n}} \cdot \hat{\mathbf{x}} \neq 0$ are relevant for the evaluation of Eq. (30).

$\hat{\mathbf{n}}$	$\lvert y_A \rvert$	$\lvert \alpha_{\eta,\hat{\mathbf{n}}} \rvert$
$\hat{\mathbf{x}}, \hat{\mathbf{z}}, (\hat{\mathbf{x}} \pm \hat{\mathbf{z}})/\sqrt{2}$	0	0
$\hat{\mathbf{y}}$	1/4	1/2
$(\hat{\mathbf{x}} \pm \hat{\mathbf{y}})/\sqrt{2}, (\hat{\mathbf{y}} \pm \hat{\mathbf{z}})/\sqrt{2}$	1/6	1/3
$(\hat{\mathbf{x}} \pm \hat{\mathbf{y}} \pm \hat{\mathbf{z}})/\sqrt{3}$	13/96	13/48

$$\langle\chi(\Delta u)\Delta u\rangle = \int_0^\infty \Delta u\, p(\Delta u - \mu_{i,\hat{\mathbf{n}}})\, p_\chi(\Delta u)\, \mathrm{d}\Delta u$$
$$= c\left(\frac{k_\mathrm{B}T n_\xi}{2m_0} + \sqrt{\frac{k_\mathrm{B}T n_\xi^3}{2\pi m_0}}\,\mu_{i,\hat{\mathbf{n}}}\right) + \mathscr{O}(\mu_{i,\hat{\mathbf{n}}}^2)$$
$$\equiv \Xi(n_\xi, c) + \Omega(n_\xi, c)\mu_{i,\hat{\mathbf{n}}} + \mathscr{O}(\mu_{i,\hat{\mathbf{n}}}^2) \tag{28}$$

up to the linear order in $\mu_{i,\hat{\mathbf{n}}} \propto \dot{\gamma}$. One can show that the zeroth-order term $\Xi(n_\xi, c)$ does not contribute to σ_{xy}, as it should be. The contribution vanishes for collision planes with $y_A = 0$ or in combination with two collision vectors. Using Eqs. (27) and (28) in the expression (25) and only collecting all terms linear in $\dot{\gamma}$, we arrive at

$$\sigma_{xy} = \frac{m_0\dot{\gamma}}{a_0^2\Delta t\, n_\xi}\Big\langle(\hat{\mathbf{x}}\cdot\hat{\mathbf{n}})^2 \sum_{y_i>y_0} y_i\,\Omega + (n_\xi - 1)$$
$$\times\left[\, y_i\Gamma + \mathrm{sign}(\mathbf{x}_i\cdot\hat{\mathbf{n}})\, y_A\Omega\,\right]\Big\rangle. \tag{29}$$

Here, the remaining average $\langle\cdots\rangle$ goes over $\mathbf{x}_i$, the offset y_0 of the plane $P_{\dot{\gamma},y_0}$, and the collision vector $\hat{\mathbf{n}}$.

As in the derivation of the equation of state, we replace the average over all particles and the conditional sum by a volume integral over $n_\xi/a_0^3\,\Theta(y-y_0)$ and also average over y_0. With only the average over the collision vector $\hat{\mathbf{n}}$ remaining, we obtain

$$\sigma_{xy} = \frac{m_0\dot{\gamma}}{a_0^2\Delta t}\Big\langle(\hat{\mathbf{x}}\cdot\hat{\mathbf{n}})^2\big\{\Omega/12 + (n_\xi - 1)\big[\,\Gamma/12 + (\alpha_{\eta,\hat{\mathbf{n}}}\, y_A)\,\Omega\,\big]\big\}\Big\rangle, \tag{30}$$

where

$$\alpha_{\eta,\hat{\mathbf{n}}} \equiv \frac{1}{a_0^4}\int_{\mathscr{V}_\xi}\int_{-a_0/2}^{a_0/2}\mathrm{sign}(\mathbf{x}\cdot\hat{\mathbf{n}})\Theta(y-y_0)\,\mathrm{d}y_0\mathrm{d}V. \tag{31}$$

In Table I, we give the values $\alpha_{\eta,\hat{\mathbf{n}}}$ and y_A for all collision vectors $\hat{\mathbf{n}}$. Averaging over all of them, we obtain for the collisional viscosity without taking into account angular momentum conservation in the collision rule of Eq. (2),

$$\eta_\mathrm{coll}^{-A} = \frac{m_0}{78\,a_0^2\Delta t}\left\{\frac{13}{6}[\Gamma(n_\xi - 1) + \Omega] + \frac{361}{576}\,\Omega(n_\xi - 1)\right\}. \tag{32}$$

For our choice of $c = 1/100$ and $n_\xi = 20$, we obtain $\Omega \approx 5/14$ and $\Gamma = \Omega/2$. If instead of Eq. (4), we use Eq. (5) to have a bounded collision probability $p_\chi(\Delta u)$, we still can evaluate the averages of Eqs. (27) and (28) and expand into $\dot{\gamma}$. The resulting expressions for Ω and Γ are given in Appendix C. For $c = 1/100$ and $n_\xi = 20$, we then obtain $\Omega \approx 1/4$ and $\Gamma \approx 9/65$.

So far, we did not consider the term due to angular momentum conservation in our collision rule (2) when evaluating σ_{xy}. We follow here Ref. 45 to take into account two additional terms. The essential contribution is the rotational motion of the particles in the collision cell induced by the vorticity of the shear flow, which generates the rotational velocity $\boldsymbol{\omega} = \nabla\times\mathbf{v}/2 = -\dot{\gamma}/2\hat{\mathbf{z}}$. The velocity $\boldsymbol{\omega}\times\mathbf{x}_{i,c}$ of particle i due to this rotational flow is removed during the random collision, and we have to add it to $\mathbf{v}_i^\mathrm{new} - \mathbf{v}_i$ considered so far to preserve angular momentum. More precisely, our collision rule (2) only considers the component normal to the collision plane, and when we average over all collision vectors, we realize that only the x component of $\boldsymbol{\omega}\times\mathbf{x}_{i,c}$ is needed. Hence, in total, we need to add to the last term in Eq. (25) the normal velocity component $(\hat{\mathbf{n}}\cdot\hat{\mathbf{x}})\dot{\gamma}y_{ic}/2$. When averaging over all particle positions $j \neq i$, we can set $y_{i,c} = y_i - y_\xi = y_i(1 - 1/n_\xi)$ following a similar reasoning as in footnote 1. Thus, a careful inspection of Eq. (25) and the following steps show that we have to subtract half of the last term in Eq. (25). Ultimately, this replaces Γ in Eq. (32) by $\Gamma/2$.

A minor contribution comes from the random velocity changes δv_j during collision. We mention it here since it gives a near perfect agreement with the simulation results we will present in Fig. 5(a). The random changes δv_j add the angular momentum $\sum_j \mathbf{x}_{j,c}\times\hat{\mathbf{n}}\,\delta v_j$ to the cell, for which we have to subtract a term in the second line of Eq. (2) in order to restore angular momentum conservation. This velocity also has to be considered in $\hat{\mathbf{x}}\cdot(\mathbf{v}_i^\mathrm{new} - \mathbf{v}_i)$ when starting with Eq. (24) for σ_{xy}, and then, the relevant steps carefully have to be repeated. As before, we only need the z component of the angular momentum. Dividing by the moment of inertia for the relevant z direction, $\mathbf{I}_{\xi,zz}/m_0 = \sum_j x_j^2 + y_j^2$, and taking the average over Δu, we obtain the mean angular velocity $\langle\omega_z^{\delta v_i}\rangle_{\Delta u} = \hat{\mathbf{x}}\cdot\hat{\mathbf{n}}\left\langle\chi(\Delta u)\frac{\sum_j y_{j,c}\Delta u/2\,\mathrm{sign}(\mathbf{x}_j\cdot\hat{\mathbf{n}})}{\mathbf{I}_{\xi,zz}/m_0}\right\rangle$. Then, evaluating this average and introducing the mean moment of inertia $\langle\mathbf{I}_\xi\rangle_{zz}/m_0 = a_0^2(n_\xi - 1)/6$ gives $\langle\omega_z^{\delta v_i}\rangle_{\Delta u} = -12(\hat{\mathbf{x}}\cdot\hat{\mathbf{n}})^2 y_A^2\dot{\gamma}\,\Omega/a_0^2$, where we neglected correlations in the product $y_j\Delta u$ and used $\langle\chi(\Delta u)\Delta u\rangle \simeq -2\Omega\hat{\mathbf{x}}\cdot\hat{\mathbf{n}}y_A\dot{\gamma}$. Finally, from the angular velocity, one calculates the mean x component of the velocity correction, $\langle\langle\omega_z^{\delta v_i}\rangle_{\Delta u}y_{ic}\rangle$. Performing the remaining averages, one ultimately realizes that this changes the prefactor of Ω in Eq. (32) from 361/567 to $0.5034 \approx 1/2$. Together with the correction from the previous paragraph, we then obtain the final formula for the shear viscosity,

$$\eta_\mathrm{coll}^{+A} = \frac{m_0}{78\,a_0^2\Delta t}\left\{\frac{13}{6}\left[\frac{\Gamma}{2}(n_\xi - 1) + \Omega\right] + \frac{\Omega}{2}(n_\xi - 1)\right\}. \tag{33}$$

B. Streaming viscosity

To determine the streaming viscosity based on the linear shear flow of Eq. (22), we follow the work of Kikuchi *et al.*[50] They determined the shear stress component σ_{xy} from the momentum along the x direction transported through the plane $y = 0$ during the streaming time Δt. They showed that this results in the expression

$$\sigma_{xy} = \frac{m_0 n_\xi}{a_0^3}\left(\frac{\dot{\gamma}\Delta t}{2}\langle v_y^2\rangle - \langle v_x v_y\rangle\right), \tag{34}$$

where v_x and v_y are velocity components of the fluid particles. The average is performed at the beginning of the streaming step. In the steady state, we can immediately use $\langle v_y^2\rangle = k_\mathrm{B}T/m_0$. However, as we explain now, the velocity correlation $\langle v_x v_y\rangle$ changes when we cycle once through the streaming and collision step. However, in the steady state, it should be back to the value at the start of the cycle. Using this self-consistency condition, one can ultimately determine $\langle v_x v_y\rangle$ and therefore σ_{xy}.

First of all, if $p(v_x, v_y)$ is the velocity distribution of the particles at the beginning of the streaming step, it will evolve toward

the distribution $p(v_x + \dot{\gamma} v_y \Delta t, v_y)$ at the end of the streaming step since particles in the shear flow acquire additional speed along the x axis when moving along the y direction. Based on this altered distribution, the velocity correlation at the end of the streaming step becomes[50]

$$\langle v_x v_y \rangle_{\mathrm{str}}^{\mathrm{new}} = \langle v_x v_y \rangle - \dot{\gamma} \Delta t \langle v_y^2 \rangle. \tag{35}$$

In other words, the value of $\langle v_x v_y \rangle$ decreases by a constant value during the streaming step. Both Eqs. (34) and (35) are common to all MPCD algorithms.[45]

In a second step, $\langle v_x v_y \rangle_{\mathrm{str}}^{\mathrm{new}}$ is altered during the subsequent collision step. This depends on the detailed collision rule. As we demonstrate below and in Appendix D, the velocity correlations change by a constant factor during collision. Thus, $\langle v_x v_y \rangle_{\mathrm{coll}}^{\mathrm{new}} = (1-b)\langle v_x v_y \rangle_{\mathrm{str}}^{\mathrm{new}}$. Inserting Eq. (35) and using the self-consistency condition $\langle v_x v_y \rangle_{\mathrm{coll}}^{\mathrm{new}} = \langle v_x v_y \rangle$ as explained above, we can solve

$$\langle v_x v_y \rangle = \left(1 - \frac{1}{b}\right) \dot{\gamma} \Delta t \langle v_y^2 \rangle. \tag{36}$$

We insert this result into the expression (34) for σ_{xy} and use $\langle v_y^2 \rangle = k_{\mathrm{B}} T / m_0$ to finally arrive at

$$\sigma_{xy} = \frac{\dot{\gamma} n_\xi k_{\mathrm{B}} T \Delta t}{a_0^3} \left(\frac{1}{b} - \frac{1}{2}\right). \tag{37}$$

Thus, after determining the factor $1 - b$ for our collision rule, we will have an expression for the streaming viscosity.

In order to write $\langle v_x v_y \rangle_{\mathrm{coll}}^{\mathrm{new}}$ in a compact way, we abbreviate in the collision rule of Eq. (2) the term added to restore angular momentum conservation by $\mathbf{A}$ and use for the other term $\mathbf{B}_i = \hat{\mathbf{n}}[\hat{\mathbf{n}} \cdot (\mathbf{v}_\xi - \mathbf{v}_i) + \delta v_i]$. Furthermore, right before the collision, the velocity correlation is $\langle v_x v_y \rangle_{\mathrm{str}}^{\mathrm{new}}$ so that we have

$$\begin{aligned} \langle v_x v_y \rangle_{\mathrm{coll}}^{\mathrm{new}} = {} & \langle v_x v_y \rangle_{\mathrm{str}}^{\mathrm{new}} \\ & + \langle \chi(\Delta u) [v_{i,x} B_{i,y} + B_{i,x} v_{i,y} + v_{i,x} A_y + A_x v_{i,y} \\ & + A_x A_y + B_{i,x} B_{i,y} + A_x B_{i,y} + A_y B_{i,x}] \rangle. \end{aligned} \tag{38}$$

Since the value of $\chi(\Delta u)$ is either 0 or 1, we have set $\chi(\Delta u)^2 = \chi(\Delta u)$. Note that in $\delta v_i = \delta v_i^s + \delta v_i^t$, we can drop δv_i^s since it is zero, on average, and also set $\delta v_t = \bar{v}_{B/A}$ using $n_A = n_B \approx n_\xi/2$ in Eq. (7). Hence, we will always use $\delta v_i = \bar{v}_{B/A}$ in the following. For the first term in Eq. (38), we demonstrate here how it is evaluated and refer to Appendix D for the evaluation of all the other terms. We obtain with $\delta v_i = \bar{v}_{B/A}$

$$\langle \chi(\Delta u) v_{i,x} B_{i,y} \rangle = \langle \chi(\Delta u) v_{i,x} n_y [\bar{v}_{B/A} + \hat{\mathbf{n}} \cdot (\mathbf{v}_\xi - \mathbf{v}_i)] \rangle.$$

Here, we recognize that $\bar{v}_{B/A} + \hat{\mathbf{n}} \cdot \mathbf{v}_\xi = 2/n_\xi \sum_{\{j \in \mathscr{V}_{B/A}\}} \hat{\mathbf{n}} \cdot \mathbf{v}_j$ after using the respective definitions of $\bar{v}_{B/A}$ and $\mathbf{v}_\xi$. Since the construction particles i and j lie on different sides of the collision plane and are therefore different, this term vanishes under the typical molecular chaos assumption $\langle v_{i,x} v_{j,y} \rangle = 0$. For the remaining term, we realize that it involves the projector $\hat{\mathbf{n}} \otimes \hat{\mathbf{n}}$, which when averaging over all $\hat{\mathbf{n}}$ gives the unit matrix $\mathbf{1}/3$. Hence, we ultimately have

$$\begin{aligned} \langle \chi(\Delta u) v_{i,x} B_{i,y} \rangle &= -\langle \chi(\Delta u) v_{i,x} v_{i,y} \rangle / 3. \\ &\approx -\langle \chi(\Delta u) \rangle \langle v_{i,x} v_{i,y} \rangle / 3. \end{aligned} \tag{39}$$

In the last line, we used again the molecular chaos assumption and neglected higher correlations for particle i.

For the derivation of the remaining terms in Eq. (38), we refer to Appendix D. Finally, putting all terms in Eqs. (39), (D3), (D1), (D4), and (D8) into Eq. (38), we obtain

$$\langle v_x v_y \rangle_{\mathrm{coll}}^{\mathrm{new}} = \langle v_x v_y \rangle_{\mathrm{str}}^{\mathrm{new}} \left[1 - \langle \chi(\Delta u) \rangle \frac{14 - 13 n_\xi + 8 n_\xi^2}{18 n_\xi^2} \right], \tag{40}$$

from which we read off the factor b as the second term in the brackets. Using it in Eq. (37) together with $\langle \chi(\Delta u) \rangle \approx \Gamma(n_\xi, c)$ from Eq. (27) and dividing by the shear rate, we obtain the streaming viscosity

$$\eta_{\mathrm{str}} = \frac{n_\xi k_{\mathrm{B}} T \Delta t}{a_0^3} \left[\frac{18 n_\xi^2}{(14 - 13 n_\xi + 8 n_\xi^2)\Gamma(n_\xi, c)} - \frac{1}{2} \right]. \tag{41}$$

The sum of this equation and the collisional viscosity from Eq. (33) gives the complete shear viscosity in this new version of MPCD,

$$\eta = \eta_{\mathrm{str}} + \eta_{\mathrm{coll}}^{+A}. \tag{42}$$

V. COMPARISON WITH SIMULATIONS

In this section, we compare the derived analytic expressions (21) for the pressure and (33) and (41) for the collision and streaming viscosities with values obtained from simulations. To calculate the collisional contribution to the pressure, we use with Eq. (11) the same formula with which we started the analytic calculations. Likewise, for the collisional and streaming viscosities, we set up the linear shear–flow profile $\mathbf{v}(y) = \dot{\gamma} y \hat{\mathbf{x}}$ and then explore Eqs. (24) and (34), respectively, to evaluate the viscosities from $\eta = \sigma_{xy}/\dot{\gamma}$. Finally, to test our method in a realistic situation, we also simulate a Poiseuille flow profile and measure the total viscosity from the maximum flow velocity. We start with some computational details.

A. Computational details

To calculate the collisional contribution to the pressure equation of state, we perform MPCD simulations in a box with edge length L using periodic boundary conditions and the parameters introduced further below. The setups of the shear flow profile and the Poiseuille flow need more comments. All the simulations are performed with the bounded collision probability of Eq. (5). For the pressure, we will also show results for the alternative form of Eq. (6).

1. Linear shear flow profile

To generate a steady shear flow profile with constant shear rate $\partial_y v_x = \dot{\gamma}$ in a cubic simulation box with edge length L, we use the so-called Lees–Edwards boundary conditions. We introduce them shortly.[50,52] In the directions along the $\hat{\mathbf{x}}$ and $\hat{\mathbf{z}}$ axes, perpendicular to the shear gradient, regular periodic boundary conditions are applied. However, along the direction of the shear gradient, the boundary conditions are modified such that the periodic images of the system move with velocity $\pm L\dot{\gamma}$. This means that a particle receives a

shift in position and velocity when crossing the boundaries along the y direction. If the particle crosses the lower boundary at time t and position $(x, y = -L/2, z)$, it re-enters the system at the upper boundary at position $((x + L\dot{\gamma}t)_{\mathrm{mod}\,L}, y = +L/2, z)$ with velocity $(v_x + L\dot{\gamma}, v_y, v_z)$. If it crosses the corresponding upper boundary at time t and position $(x, y = +L/2, z)$, it re-enters the system at the lower boundary at position $((x - L\dot{\gamma}t)_{\mathrm{mod}\,L}, y = -L/2, z)$ with velocity $(v_x - L\dot{\gamma}, v_y, v_z)$.

2. Poiseuille flow profile

To generate a Poiseuille flow profile, we do not introduce bounding walls but simulate a driven system with periodic boundaries in all three dimensions and two profiles with opposing flow directions along the $\hat{\mathbf{x}}$ axis.[53] For this, we introduce a pressure difference Δp by acting with a constant body force on all the particles. Particles with positions $y_i < 0$ experience the force $-m_0 g\hat{\mathbf{x}}$, and for particles with positions $y_i > 0$, the force points in the opposite direction, $m_0 g\hat{\mathbf{x}}$. This setup with the box dimensions $L \times 2L \times L$ produces two opposing Poiseuille flow profiles and thereby avoids the implementation of any solid boundaries. With the resulting pressure gradient $\Delta p/L = m_0 n_0 g/a_0^3$, the viscosity then follows from the maximum flow velocity $v_{\max} = \frac{\Delta p L}{8\eta}$.[54]

3. Parameters

For all simulations, we use the edge length $L = 64a_0$, the collision parameter $c = 1/100$, and, in MPCD units, set $k_B T = 1$ and mass $m_0 = 1$. For the Lees–Edwards simulations, the shear rate is chosen as $\dot{\gamma} = \partial_y v_x = 0.006\,25$ in units of the inverse MPCD time scale $t_0 = a_0\sqrt{m_0/k_B T}$.

Each system is initialized by randomly distributing $N = n_0 L^3$ particles in the volume L^3 and by choosing their velocities from the Maxwell–Boltzmann distribution. For the Lees–Edwards simulations, a local offset for the mean velocity component along the x direction is chosen, $\langle v_x \rangle = \dot{\gamma} y$. To equilibrate the system at the beginning, we simulate it for 10^5 time steps Δt. Then, we sample Eqs. (11), (24), and (34) during a simulation time of $5 \times 10^5 \Delta t$. When simulating the Poiseuille flow, we average the flow profile over the same amount of time but use an increased equilibration time of $5 \times 10^5 \Delta t$ to assure that the flow has reached its maximum velocity.

Our goal is to perform the MPCD simulations with defined values of the parameters, which we keep constant throughout the simulations. The collision parameter c introduced in Eq. (4) has to be sufficiently small so that we can explore the dependence on Δu, n_A, and n_B. It turns out that $c = 1/100$ and an average number of $n_0 = 20$ particles per cell is a suitable choice, which yields a collision rate of $\langle \chi(\Delta u) \rangle \approx 0.14$.

Together with a time step of $\Delta t = t_0/200$, our set of parameters is particularly interesting because it yields a total viscosity $\eta = \eta_{\mathrm{str}} + \eta_{\mathrm{coll}}^{+A} \approx 16 a_0 \sqrt{k_B T/m_0}$, which is commonly used for simulating microswimmers with MPCD.[8,9,12,17] Hence, in the following, we focus on densities between $n_0 = 7$ and $n_0 = 35$ and investigate how pressure and viscosities behave in this range of densities centered around $n_0 = 20$.

B. Equation of state

Figure 4 shows the simulated total pressure P, normalized by the ideal gas pressure $P_{\mathrm{id}} = n_0 k_B T/a_0^3$, as a function of density n_0 for

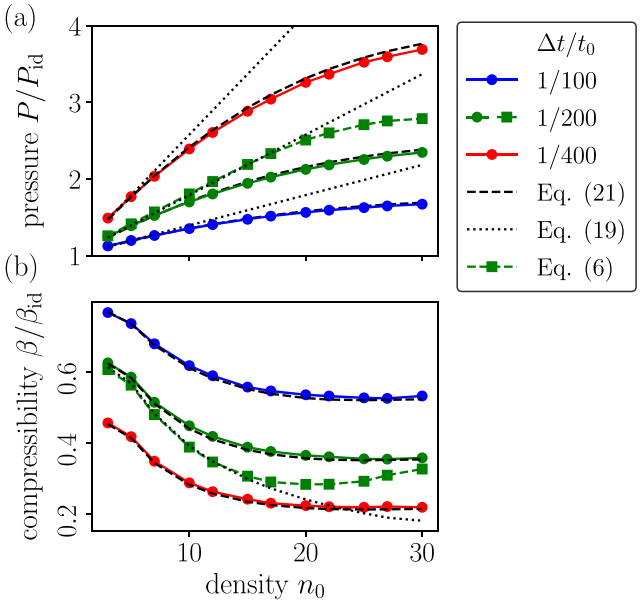

FIG. 4. (a) Total pressure P relative to the ideal gas pressure $P_{\mathrm{id}} = n_0 k_B T/a_0^3$ plotted vs density n_0 for three different values of the time step Δt. Circle symbols show data points obtained from simulations using Eq. (11) together with the bounded collision probability of Eq. (5), and dashed lines show the corresponding theory curves from Eq. (21). The dotted lines show the theory curves from Eq. (19), and the squares show data points obtained from simulations using the bounded collision probability of Eq. (6) for $\Delta t = t_0/200$. (b) The corresponding compressibility β relative to the ideal gas value $\beta_{\mathrm{id}} = a_0^3/(n_\xi k_B T)$ plotted vs n_0.

different time steps Δt. The colored circle symbols are the numerical results using the bounded collision probability from Eq. (5). They are in very good agreement with the analytic result of Eq. (21) plotted as dashed lines. In particular, the simulations confirm the relation $P_{\mathrm{coll}} \propto 1/\Delta t$ according to which a smaller Δt results in a larger pressure. This makes sense since the collision probability is independent of the time step Δt. Hence, there are more collisions in the same time interval when Δt decreases. As dotted lines, we also show the pressure of Eq. (19) calculated with the unbounded collision probability of Eq. (4). They are in very good agreement with the simulated pressure only until $\sim n_0 = 10$. With the idea to enhance the pressure in the simulations further, we also used the alternative bounded collision probability of Eq. (6). Indeed, for the example of $\Delta t = t_0/200$, we obtain a larger pressure (square symbols) since we keep the linear dependence in $\Delta u n_A n_B$ until the probability becomes one. It starts to deviate from the dotted line not until $n_0 = 20$.

In Fig. 4(b), we plot the corresponding compressibility as a function of n_0 relative to its ideal-gas value $\beta_{\mathrm{id}} = 1/P_{\mathrm{id}}$. Using $P = P_{\mathrm{id}}[1 + f(n_0)]$, the compressibility

$$\beta = \frac{1}{n_0}\left(\frac{\partial P}{\partial n_0}\right)^{-1} = \beta_{\mathrm{id}} \frac{1}{1 + f + \frac{\partial f}{\partial n_0}} \tag{43}$$

can be directly related to the deviation of pressure from P_{id}. The dashed and dotted lines in Fig. 4(b) represent the analytic results calculated from the formulas for pressure, while the derivative $\partial f/\partial n_0$

for the numerical results was determined with the standard Python toolchain. Relative to the ideal-gas value, compressibility is further reduced and, in particular, β also decreases with the decrease in Δt. For example, at $\Delta t = t_0/200$ and with $n_0 = 20$ as a reasonable density, compressibility is reduced to $0.4\beta_{\mathrm{id}}$. Now, applying the bounded collision probability of Eq. (6), the compressibility is down to $0.3\beta_{\mathrm{id}}$. To obtain such a reduction with conventional MPCD methods and the ideal-gas pressure, one would need to increase the particle number per cell by a factor of three. Thus, the new collision rule with its non-ideal equation of state reduces the computational efforts.

C. Shear viscosity

We first discuss the collisional viscosity. Figure 5(a) shows the simulated collisional viscosity $\eta_{\mathrm{coll}}^{+A}$ in MPCD units $m_0/(a_0 t_0)$ as a function of the density n_0 for three values of Δt. The circle symbols show data points from simulations using the bounded collision rule Eq. (5). Over a wide range of densities, the values are in very good agreement with the analytical result of Eq. (33) shown as dashed lines. Hence, there is a quantitative agreement between simulations and theory. Similar to the pressure, the simulations confirm the scaling $\eta_{\mathrm{coll}}^{+A} \propto 1/\Delta t$. For the two larger time steps $\Delta t = t_0/100 \Delta t = t_0/200$, we see a deviation at densities $n_0 \leq 10$. We attribute this to the following reasons: first, our collision rule is not constructed for small numbers of particles, and second, to derive Eq. (33), we neglected fluctuations of the center of mass position, which also requires a higher number of particles.

We now continue with the streaming viscosity η_{str} that we extract from the same simulations. Figure 5(b) shows η_{str} in MPCD units $m_0/(a_0 t_0)$ as a function of the density n_0 and for different values of Δt. Again, the circle symbols show data points for the bounded collision rule from Eq. (5), while dotted lines refer to the analytic values given by Eq. (41). Although we observe an approximate quantitative agreement of the simulated values for η_{str} with Eq. (41) for larger densities n_0, there are clear differences. First, Eq. (41) predicts an increase in the streaming viscosity toward smaller n_0, which then falls sharply to zero at $n_0 = 0$ (not shown). The simulated streaming viscosities only show a slight increase for $\Delta t = t_0/100$; otherwise, they are roughly independent of n_0. Second, while we do not reproduce the predicted scaling $\eta_{\mathrm{str}} \propto \Delta t$, we observe a clear increase in the streaming viscosity with Δt, and thus, the expected trend is reproduced qualitatively. As a main reason for the disagreement of the simulated viscosities with Eq. (41), we consider the approximation $\langle \chi(\Delta u) v_{i,x} v_{i,y} \rangle \approx \langle \chi(\Delta u) \rangle \langle v_{i,x} v_{i,y} \rangle$ made during the derivation of Eq. (41). Nevertheless, factoring out the collision rate $\langle \chi(\Delta u) \rangle$ in the previous expression provides a rough quantitative estimate of the streaming viscosity η_{str} as demonstrated.

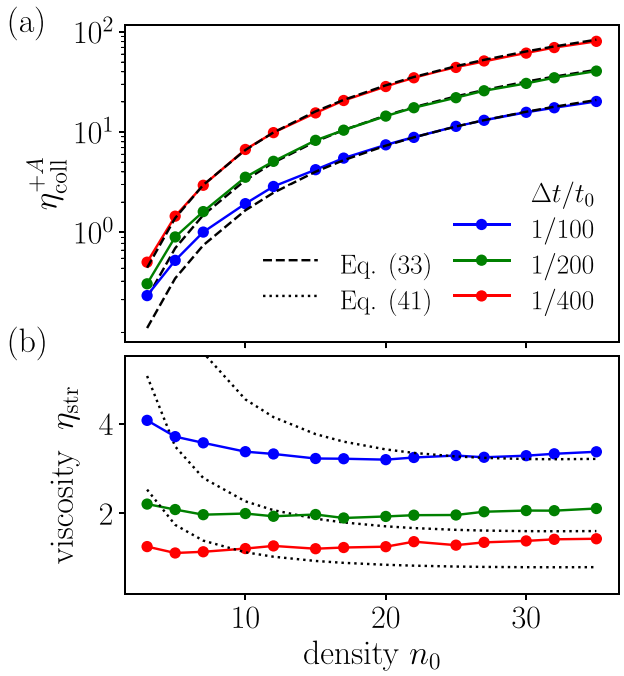

FIG. 5. (a) Collisional viscosity $\eta_{\mathrm{coll}}^{+A}$ in MPCD units $m_0/(a_0 t_0)$ plotted vs density n_0 for three values of the time step Δt. Circle symbols show data points obtained from simulations using Eq. (24), and the dashed lines show the corresponding analytical values as given by Eq. (33). (b) Streaming viscosity η_{str} in MPCD units $m_0/(a_0 t_0)$ plotted vs density n_0 for the same values of Δt. Here, the circle symbols show data points obtained from the same simulations using Eq. (34), and the dotted lines refer to the analytic expression of Eq. (41).

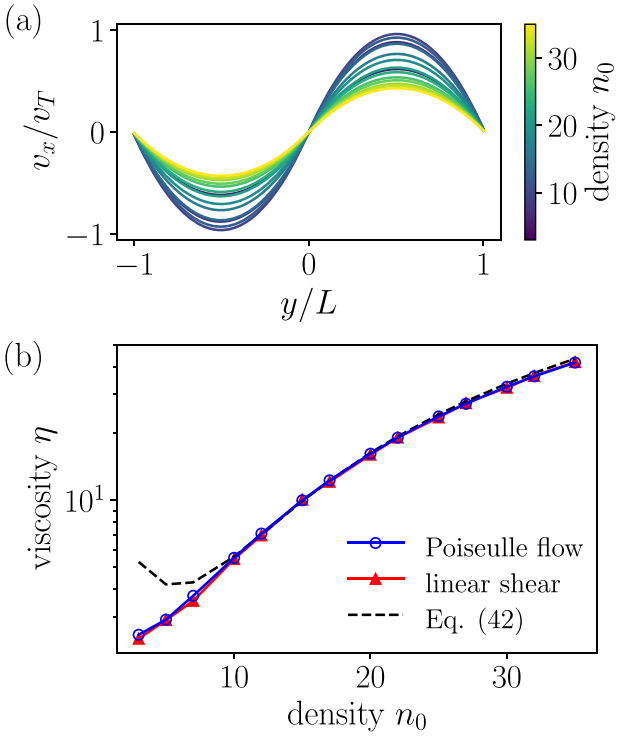

FIG. 6. (a) Poiseuille flow profiles v_x vs lateral channel position y determined in simulations for different densities n_0. The velocity unit is the thermal velocity $v_T = \sqrt{k_B T/m_0}$. (b) Total viscosity in MPCD units $m_0/a_0 t_0$. Blue circle symbols show data points for the viscosity determined from the flow profiles in (a). The red triangle symbols refer to data points resulting from the sum of viscosities, $\eta_{\mathrm{str}} + \eta_{\mathrm{coll}}^{+A}$, determined in Sec. V C. The black dashed line shows the analytical expression of Eq. (42).

D. Poiseuille flow

To simulate the Poiseuille flow profiles, we used the time step $\Delta t = t_0/200$. After averaging the velocity field over the time $5 \times 10^4 \Delta t$, the final flow profiles are generated by also averaging along the x and z directions. The resulting profiles v_x as a function of the y position are shown in Fig. 6(a) for different densities n_0. The two opposing profiles are clearly visible, and in both regions $y < 0$ and $y > 0$, we observe excellent agreement with the expected parabolic shape. The decrease in the flow velocity toward higher densities n_0 already indicates an increase in the total viscosity η with n_0. This increase is even more pronounced since also the pressure difference Δp increases with n_0 because we always use the same body force per fluid particle.

In Fig. 6(b), we plot the total viscosity η as a function of the density n_0. The blue circle symbols show data points obtained by extracting $v_{\max}$ from the Poiseuille flow profiles shown in Fig. 6(a) and using $\eta = \Delta p L/(8 v_{\max})$. The red triangle symbols show the total viscosity $\eta^{+A}_{\text{coll}} + \eta_{\text{str}}$ consisting of the collisional and streaming viscosity, which we determined in Sec. V C from the simulated linear shear profile. The numerical data are compared to the analytical result of Eq. (42), which is shown as the dashed line.

First of all, the values for the viscosities, determined in the simulations by analyzing either momentum transfer in linear shear flow or the maximum flow speed of the Poiseuille profile, are in excellent agreement over the whole range of densities. In addition, we also observe a good agreement with the analytical expression of Eq. (42) for densities $n_0 \geq 10$, where the collisional viscosity η^{+A}_{coll} dominates. For low densities $n_0 < 10$, the deviations occur due to η_{str} as discussed before.

VI. CONCLUSIONS AND OUTLOOK

The new collision rule in our extended MPCD method provides the fluid with a non-ideal equation of state by introducing stochastic collisions between two particle clouds in the collision cell. In short, the collision frequency is quadratic in density and collisions only occur if the particle clouds move toward each other. In contrast to prior approaches, the extended MPCD method is designed for three dimensions, conserves angular momentum, and features a thermostat. The main goal of our method is to guarantee a low fluid compressibility for simulations in which significant pressure gradients occur. Since with the reduced compressibility, we can keep the particle number per collision cell at reasonably small values, our method requires significantly less simulation time compared to raising the fluid density in classical MPCD algorithms.[12] We provide an example in footnote.[55] At the same time, our method saves computer memory necessary to store MPCD particles so that we do not need to reduce the system size. We will explore this more in a planned second publication.

Based on the new collision rule, we have derived the equation of state and also demonstrated the impact of different collision probabilities. Indeed, in the regime where the collision probability is quadratic in density, we observe the nonlinear quadratic variation of pressure with density. For larger densities, where the collision frequency is bounded by the maximum value $1/\Delta t$, the pressure again becomes linear in density, albeit at a higher value, which increases with $1/\Delta t$. For typical values of $\Delta t/t_0 = 1/200$ and $n_0 = 20$ together with the most effective collision probability, compressibility is reduced by a factor three compared to the ideal-gas value at $n_0 = 20$. Overall, we find very good agreement with values obtained from simulations in the regime where our analytic expressions apply.

Moreover, for the shear viscosity, we have derived analytic expressions for the contributions of the collision and streaming step. For the collisional viscosity, we find very good agreement with the values obtained from simulating a linear shear flow and determining momentum transport, while for the streaming viscosity, the analytic expression only provides a rough estimate. However, for density values n_0 above 10, the collisional viscosity starts to dominate and we obtain a very good agreement with the simulated values. This is also demonstrated by simulating a Poiseuille flow and extracting viscosity from the maximum flow velocity.

In a planned second publication, we will use our extended MPCD method for selected flow problems to demonstrate its applicability. Furthermore, we intend to apply it to dense systems of microswimmers, where large pressure fields arise naturally. Preliminary simulations of such systems show that the extended MPCD method keeps the inhomogeneities in fluid density small. This will help us to obtain reliable insight into how hydrodynamic flow fields influence the collective dynamics of clustering and swarming microswimmers.

ACKNOWLEDGMENTS

We thank Josua Grawitter and Christian Schaaf for helpful discussions on the topic of the manuscript. We also acknowledge financial support from the Collaborative Research Center 910 funded by Deutsche Forschungsgemeinschaft.

APPENDIX A: GAUSSIAN DISTRIBUTION FOR Δu

For the derivation of the pressure, the fluid is considered at rest. Assuming molecular chaos, the velocities $\mathbf{v}_j$ of the individual particles all obey the Maxwell–Boltzmann distribution. For the scalar product with the collision vector $\hat{\mathbf{n}}$, this implies the probability density

$$p(\mathbf{v}_j \cdot \hat{\mathbf{n}}) = \sqrt{\frac{m_0}{2\pi k_B T}} \exp\left(-\frac{m_0 (\mathbf{v}_j \cdot \hat{\mathbf{n}})^2}{2 k_B T}\right). \tag{A1}$$

The probability distribution for $\Delta u = \bar{v}_B - \bar{v}_A$ then follows from

$$p(\Delta u) = \int \delta\left(\Delta u - \left[\sum_{\{\mathbf{x}_j \in \mathcal{V}_B\}} \frac{\mathbf{v}_j \cdot \hat{\mathbf{n}}}{n_B} - \sum_{\{\mathbf{x}_j \in \mathcal{V}_A\}} \frac{\mathbf{v}_j \cdot \hat{\mathbf{n}}}{n_A}\right]\right) \times \prod_{j=1}^{N} p(\mathbf{v}_j \cdot \hat{\mathbf{n}}) d(\mathbf{v}_j \cdot \hat{\mathbf{n}}), \tag{A2}$$

where $\delta(\cdots)$ stands for the delta function. Eliminating it by integrating over one normal velocity component and then carefully performing the rest of the $N - 1$ integration finally gives the Gaussian distribution

$$p(\Delta u) = \frac{1}{\sqrt{2\pi\langle\Delta u^2\rangle}} \exp\left(-\frac{\Delta u^2}{2\langle\Delta u^2\rangle}\right). \tag{A3}$$

It has zero mean, $\langle\Delta u\rangle = 0$, and variance

$$\langle\Delta u^2\rangle = \frac{k_B T}{n_A m_0} + \frac{k_B T}{n_B m_0} = \frac{4k_B T}{m_0 n_\xi}, \tag{A4}$$

where we used the approximation $n_{A/B} \approx n_\xi/2$ in the last step. Thus, the sum over Gaussian distributed random numbers follows again a Gaussian distribution.

APPENDIX B: CONDITIONAL DISTRIBUTION OF Δu IN SHEAR FLOW

For deriving the collisional shear viscosity in Sec. IV A, we need the distribution for Δu under the condition that the collision vector $\hat{\mathbf{n}}$ and the position $\mathbf{x}_i$ of particle i are given. We again start with the single-particle velocity distributions. Relative to the applied shear flow, the velocities still follow the Maxwell–Boltzmann distribution,

$$p(\mathbf{v}_j \cdot \hat{\mathbf{n}}, y_j) = \sqrt{\frac{m_0}{2\pi k_B T}} \exp\left(-\frac{m_0[(\mathbf{v}_j - \dot\gamma y_j \hat{\mathbf{x}}) \cdot \hat{\mathbf{n}}]^2}{2k_B T}\right). \tag{B1}$$

Following the same reasoning as in Appendix A, this implies that the conditional distribution for Δu is again Gaussian with the same variance as before: $\langle(\Delta u - \langle\Delta u\rangle)^2\rangle = 4k_B T/(m_0 n_\xi)$.

However, the conditional mean of Δu under the applied shear flow and for fixed $\hat{\mathbf{n}}$ and $\mathbf{x}_i$ is non-zero. Starting from the definition of Δu and averaging over all particle velocities and all positions besides particle i, one obtains

$$\langle\Delta u\rangle_{i,\hat{\mathbf{n}}} = \dot\gamma\, \hat{\mathbf{x}} \cdot \hat{\mathbf{n}} \left[\sum_{\{\mathbf{x}_j \in \mathscr{V}_B/\mathbf{x}_i\}} \frac{\langle y_j\rangle}{n_B} - \sum_{\{\mathbf{x}_j \in \mathscr{V}_A/\mathbf{x}_i\}} \frac{\langle y_j\rangle}{n_A}\right] - \operatorname{sign}(\mathbf{x}_i \cdot \hat{\mathbf{n}})\, \frac{y_i}{n_{A/B}}, \tag{B2}$$

where the subscripts $i, \hat{\mathbf{n}}$ indicate the conditions that the particle i resides at $\mathbf{x}_i$ and the collision vector takes the value $\hat{\mathbf{n}}$. When we introduce the center-of-mass in the respective regions $\langle y_j\rangle = y_{A/B}$ for $\mathbf{x}_j \in \mathscr{V}_{A/B}$ and use $y_A = -y_B$ and $n_{A/B} \approx n_\xi/2$, we can ultimately write the conditional mean as

$$\langle\Delta u\rangle_{i,\hat{\mathbf{n}}} = -2\dot\gamma\, \hat{\mathbf{x}} \cdot \hat{\mathbf{n}}\, \frac{y_A(n_\xi - 1) + \operatorname{sign}(\mathbf{x}_i \cdot \hat{\mathbf{n}})\, y_i}{n_\xi} \equiv \mu_{i,\hat{\mathbf{n}}}. \tag{B3}$$

Based on the conditional distribution $p(\Delta u - \mu_{i,\hat{\mathbf{n}}})$, we can now calculate the required mean values $\langle\chi(\Delta u)\rangle$ and $\langle\chi(\Delta u)\Delta u\rangle$ in shear flow.

APPENDIX C: MEAN VALUES $\langle\chi(\Delta u)\rangle$ AND $\langle\chi(\Delta u)\Delta u\rangle$ IN SHEAR FLOW

We start with the unbounded form of the collision rate $p_\chi(\Delta u)$ in Eq. (4) and find for the mean collision rate

$$\begin{aligned}\langle\chi(\Delta u)\rangle &= \int_0^\infty p(\Delta u - \mu_{\mathbf{x}_i,\hat{\mathbf{n}}})\, p_\chi(\Delta u)\, \mathrm{d}\Delta u \\ &= \frac{cn_\xi}{2}\left\{\sqrt{\frac{k_B T n_\xi}{2\pi m_0}} \exp\left(-\frac{\mu_{i,\hat{\mathbf{n}}}^2 m_0 n_\xi}{4k_B T}\right)\right. \\ &\quad \left. + \frac{\mu_{i,\hat{\mathbf{n}}} n_\xi}{8}\left[1 + \operatorname{erf}\left(\mu_{i,\hat{\mathbf{n}}}\sqrt{\frac{m_0 n_\xi}{8k_B T}}\right)\right]\right\} \qquad \text{(C1)} \\ &= c\sqrt{\frac{k_B T n_\xi^3}{8\pi m_0}} + \mathscr{O}(\mu_{i,\hat{\mathbf{n}}}) \equiv \Gamma(n_\xi, c) + \mathscr{O}(\mu_{i,\hat{\mathbf{n}}}), \qquad \text{(C2)}\end{aligned}$$

where in the last line, we show the relevant zeroth-order term after expansion in $\mu_{i,\hat{\mathbf{n}}}$. For the second mean value, we obtain

$$\begin{aligned}\langle\chi(\Delta u)\Delta u\rangle &= \int_0^\infty \Delta u\, p(\Delta u - \mu_{\mathbf{x}_i,\hat{\mathbf{n}}})\, p_\chi(\Delta u)\, \mathrm{d}\Delta u \\ &= \frac{cn_\xi}{2}\left\{\left(\frac{k_B T}{m_0} + \frac{\mu_{i,\hat{\mathbf{n}}}^2 n_\xi}{4}\right)\left[1 + \operatorname{erf}\left(\mu_{i,\hat{\mathbf{n}}}\sqrt{\frac{m_0 n}{8k_B T}}\right)\right]\right. \\ &\quad \left. + \mu_{i,\hat{\mathbf{n}}}\sqrt{\frac{k_B T n_\xi}{2\pi m_0}} \exp\left(-\frac{\mu_{i,\hat{\mathbf{n}}}^2 m_0 n_\xi}{8k_B T}\right)\right\} \qquad \text{(C3)}\end{aligned}$$

and, after expanding to first order in $\mu_{i,\hat{\mathbf{n}}}$,

$$\begin{aligned}\langle\chi(\Delta u)\Delta u\rangle &= c\left(\frac{k_B T n_\xi}{2m_0} + \sqrt{\frac{k_B T n_\xi^3}{2\pi m_0}}\,\mu_{i,\hat{\mathbf{n}}}\right) + \mathscr{O}(\mu_{i,\hat{\mathbf{n}}}^2) \\ &\equiv \Xi(n_\xi, c) + \Omega(n_\xi, c)\mu_{i,\hat{\mathbf{n}}} + \mathscr{O}(\mu_{i,\hat{\mathbf{n}}}^2). \qquad \text{(C4)}\end{aligned}$$

For the bounded form of the collision rate $p_\chi(\Delta u)$ in Eq. (5), we can also calculate the mean values. The mean collision rate becomes

$$\begin{aligned}\langle\chi(\Delta u)\rangle &= \int_0^\infty p(\Delta u - \mu_{\mathbf{x}_i,\hat{\mathbf{n}}})\, p_\chi(\Delta u)\, \mathrm{d}\Delta u \\ &= \frac{1}{2}\left\{1 + \operatorname{erf}\left(\mu_{i,\hat{\mathbf{n}}}\sqrt{\frac{m_0 n_\xi}{8k_B T}}\right)\right., \qquad \text{(C5)} \\ &\quad - \exp\left[\frac{cn_\xi^2}{8}\left(cn_\xi\frac{k_B T}{m_0} - 2\mu_{i,\hat{\mathbf{n}}}\right)\right] \\ &\quad \left.\times \operatorname{erfc}\left[\sqrt{\frac{n_\xi}{8}}\left(cn_\xi\sqrt{\frac{k_B T}{m_0}} - \mu_{i,\hat{\mathbf{n}}}\sqrt{\frac{m_0}{k_B T}}\right)\right]\right\} \\ &= 1 - \exp\left(\frac{c^2 k_B T n_\xi}{8m_0}\right)\operatorname{erfc}\left(c\sqrt{\frac{k_B T n_\xi^3}{8m_0}}\right) + \mathscr{O}(\mu_{i,\hat{\mathbf{n}}}) \\ &\equiv \Gamma(n_\xi, c) + \mathscr{O}(\mu_{i,\hat{\mathbf{n}}}^2), \qquad \text{(C6)}\end{aligned}$$

where the last line shows the relevant zeroth-order term after expansion in $\mu_{i,\hat{\mathbf{n}}}$. The second mean value becomes

$$\begin{aligned}\langle\chi(\Delta u)\Delta u\rangle &= \int_0^\infty \Delta u\, p(\Delta u - \mu_{\mathbf{x}_i,\hat{\mathbf{n}}})\, p_\chi(\Delta u)\, \mathrm{d}\Delta u \\ &= \frac{1}{2}\Bigg\{\mu_{i,\hat{\mathbf{n}}}\left[1+\mathrm{erf}\left(\mu_{i,\hat{\mathbf{n}}}\sqrt{\frac{m_0 n_\xi}{8k_\mathrm{B}T}}\right)\right] \\ &\quad + \left(cn_\xi\frac{k_\mathrm{B}T}{m_0} - \mu_{i,\hat{\mathbf{n}}}\right) \\ &\quad \times \exp\left[\frac{cn_\xi}{8}^2\left(cn_\xi\frac{k_\mathrm{B}T}{m_0} - 2\mu_{i,\hat{\mathbf{n}}}\right)\right] \\ &\quad \times \mathrm{erfc}\left[\sqrt{\frac{n_\xi}{8}}\left(cn_\xi\sqrt{\frac{k_\mathrm{B}T}{m_0}} - \mu_{i,\hat{\mathbf{n}}}\sqrt{\frac{m_0}{k_\mathrm{B}T}}\right)\right]\Bigg\},\end{aligned}$$

and after expanding to first order in $\mu_{i,\hat{\mathbf{n}}}$, one has

$$\begin{aligned}\langle\chi(\Delta u)\Delta u\rangle &= \frac{ck_\mathrm{B}Tn_\xi}{2m_0}\exp\left(c^2\frac{k_\mathrm{B}Tn_\xi}{8m_0}^3\right)\mathrm{erfc}\left(c\sqrt{\frac{k_\mathrm{B}Tn_\xi}{8m_0}}\right) \\ &\quad + \frac{\mu_{i,\hat{\mathbf{n}}}}{2}\left[1 + c\sqrt{\frac{k_\mathrm{B}Tn_\xi}{2\pi m_0}}^3 - \left(1+c^2\frac{k_\mathrm{B}Tn_\xi}{4m_0}^3\right)\right. \\ &\quad \left.\times\exp\left(c^2\frac{k_\mathrm{B}Tn_\xi}{8m_0}^3\right)\mathrm{erfc}\left(c\sqrt{\frac{k_\mathrm{B}Tn_\xi}{8m_0}}^3\right)\right] + \mathscr{O}\left(\mu_{i,\hat{\mathbf{n}}}^2\right) \\ &\equiv \Xi(n_\xi, c) + \Omega(n_\xi, c)\mu_{i,\hat{\mathbf{n}}} + \mathscr{O}\left(\mu_{i,\hat{\mathbf{n}}}^2\right). \qquad \text{(C7)}\end{aligned}$$

APPENDIX D: VELOCITY CORRELATION DURING COLLISIONS

To derive of the streaming viscosity in Sec. IV B, we consider the evolution of the velocity correlation $\langle v_{i,x}v_{i,y}\rangle_{\mathrm{coll}}^{\mathrm{new}}$ during a collision step. In the main text, we have already evaluated the term $\langle\chi(\Delta u)v_{i,x}B_{i,y}\rangle$. Here, we calculate the remaining terms $\langle\chi(\Delta u)v_xA_y\rangle$, $\langle\chi(\Delta u)A_xA_y\rangle$, $\langle\chi(\Delta u)B_{i,x}B_{i,y}\rangle$, and $\langle\chi(\Delta u)A_xB_{i,y}\rangle$.

We begin by applying some transformations on the abbreviations $\mathbf{B}_i$ and $\mathbf{A}$ that we introduced to write Eq. (38) in a compact way. First, we note that we may drop the stochastic part δv_i^s of $\delta v_i = \delta v_i^t + \delta v_i^s$ because it averages to zero. Furthermore, we replace $\delta v_i^t = \bar{v}_{A/B}$ using $n_A = n_B \approx n_\xi/2$. With the definitions of $\mathbf{v}_\xi$ and $\bar{v}_{A/B}$, the quantity $\mathbf{B}_i$ reads

$$\mathbf{B}_i = -\hat{\mathbf{n}}\cdot\mathbf{v}_i + \frac{2\hat{\mathbf{n}}}{n_\xi}\sum_{\{j\in\mathscr{V}_{B/A}\}}\hat{\mathbf{n}}\cdot\mathbf{v}_j.$$

Furthermore, we can insert the quantity $\mathbf{B}_j$ into $\mathbf{A}$,

$$\begin{aligned}\mathbf{A} &\equiv -\mathbf{I}_\xi^{-1}m_0\sum_{\mathbf{x}_j\in\mathscr{V}_\xi}\left[\mathbf{x}_{j,c}\times\hat{\mathbf{n}}\left(\delta v_j - \hat{\mathbf{n}}\cdot\mathbf{v}_j\right)\right]\times\mathbf{x}_{i,c} \\ &= -\mathbf{I}_\xi^{-1}m_0\sum_{\mathbf{x}_j\in\mathscr{V}_\xi}\left(\mathbf{x}_{j,c}\times\mathbf{B}_j\right)\times\mathbf{x}_{i,c},\end{aligned}$$

and using that, we are free to add the constant velocity $\mathbf{v}_\xi$ inside the round brackets.

With these simplifications, we now begin considering the next most simple term $\langle\chi(\Delta u)B_{i,x}B_{i,y}\rangle$ of the new velocity correlation $\langle v_{i,x}v_{i,y}\rangle_{\mathrm{coll}}^{\mathrm{new}}$.

We first note that the single term and the sum in $\mathbf{B}_i$ always contain different particles $i \neq j$. Hence, the product of these terms vanishes under the usual molecular chaos assumption $\langle v_{i,x}v_{j,y}\rangle = 0$. If we further use that particles are interchangeable so that $\langle\chi(\Delta u)v_{i,x}v_{i,y}\rangle = \langle\chi(\Delta u)v_{j,x}v_{j,y}\rangle$, we obtain

$$\langle\chi(\Delta u)B_{i,x}B_{i,y}\rangle = \left(\frac{2}{n_\xi}+1\right)\langle\chi(\Delta u)n_xn_y(\hat{\mathbf{n}}\cdot\mathbf{v}_i)^2\rangle.$$

Finally, averaging over $\hat{\mathbf{n}}$ and neglecting higher correlations for particle i, we arrive at

$$\langle\chi(\Delta u)B_{i,x}B_{i,y}\rangle \approx \frac{2}{9}\left(\frac{2}{n_\xi}+1\right)\langle\chi(\Delta u)\rangle\langle v_{i,x}v_{i,y}\rangle. \qquad \text{(D1)}$$

In the next term $\langle\chi(\Delta u)v_{i,x}A_y\rangle$, we note that the quantity $\mathbf{A}$ also depends on the positions of the particles so that these must be included in the average. We may perform this average over the particle positions separately on $\mathbf{A}$ to obtain

$$\begin{aligned}\langle\mathbf{A}\rangle &= -\left\langle\mathbf{I}_\xi^{-1}m_0\sum_{\mathbf{x}_{j,c}\in\mathscr{V}_\xi}\left[\left(\mathbf{x}_{i,c}\cdot\mathbf{x}_{j,c}\right)\mathbf{B}_j - \left(\mathbf{B}_j\cdot\mathbf{x}_{i,c}\right)\mathbf{x}_{j,c}\right]\right\rangle \\ &= -\left\langle\mathbf{I}_\xi^{-1}m_0\left[\mathbf{x}_{i,c}^2\mathbf{B}_i - \left(\mathbf{x}_{i,c}\cdot\mathbf{B}_i\right)\mathbf{x}_{i,c}\right]\right\rangle \\ &= -2\langle\mathbf{I}_\xi^{-1}\rangle m_0\langle x_{i,c}^2\rangle\mathbf{B}_i = -\frac{\mathbf{B}_i}{n_\xi}, \qquad \text{(D2)}\end{aligned}$$

where $x_{i,c}$ denotes any of the components of $\mathbf{x}_{i,c}$. In the last line, we assumed that the contribution of the single particle i is low so that we can average $\langle\mathbf{I}_\xi\rangle = (n_\xi - 1)m_0a_0^2\mathbf{I}/6$ separately. Furthermore, we used that $\langle x_{i,c}^2\rangle = a_0^2/12(1 - 1/n_\xi)$ for any of the components of the position and that different components of the position $\mathbf{x}_{i,c}$ are uncorrelated.

Putting Eq. (D2) into $\langle\chi(\Delta u)v_{i,x}A_y\rangle$ and using Eq. (39), we obtain

$$\langle\chi(\Delta u)v_{i,x}A_y\rangle = -\frac{\langle\chi(\Delta u)v_{i,x}B_{i,y}\rangle}{n_\xi} \approx \frac{\langle\chi(\Delta u)\rangle\langle v_{i,x}v_{i,y}\rangle}{3n_\xi}. \qquad \text{(D3)}$$

We proceed with the term $\langle\chi(\Delta u)B_{i,x}A_y\rangle$. Since the term $B_{i,x}$ does not depend on the position of the particle, we can immediately apply Eq. (D2) and insert Eq. (D1) to arrive at

$$\langle\chi(\Delta u)B_{i,x}A_y\rangle \approx -\frac{2}{9n_\xi}\left(\frac{2}{n_\xi}+1\right)\langle\chi(\Delta u)\rangle\langle v_{i,x}v_{i,y}\rangle. \qquad \text{(D4)}$$

The last term to calculate is

$$\begin{aligned}&\langle\chi(\Delta u)A_xA_y\rangle \\ &= \left\langle\chi(\Delta u)\left[\mathbf{I}_\xi^{-1}m_0\sum_{\mathbf{x}_{j,c}\in\mathscr{V}_\xi}\left(\mathbf{x}_{i,c}\cdot\mathbf{x}_{j,c}\right)\mathbf{B}_j - \left(\mathbf{B}_j\cdot\mathbf{x}_{i,c}\right)\mathbf{x}_{j,c}\right]_x\right. \\ &\quad\left.\times\left[\mathbf{I}_\xi^{-1}m_0\sum_{\mathbf{x}_{k,c}\in\mathscr{V}_\xi}\left(\mathbf{x}_{i,c}\cdot\mathbf{x}_{k,c}\right)\mathbf{B}_k - \left(\mathbf{B}_k\cdot\mathbf{x}_{i,c}\right)\mathbf{x}_{k,c}\right]_y\right\rangle. \qquad \text{(D5)}\end{aligned}$$

Similarly, we separately average $\langle \mathbf{I}_\xi^2 \rangle = (19/360 + (n_\xi - 1)/36)(n_\xi - 1) m_0 a_0^2 \mathbf{I} \approx (n_\xi - 1)^2 m_0 a_0^2 \mathbf{I}/36$ based on the assumption of molecular chaos and that the contribution of single pairs of particles is small. Multiplying out yields three terms,

$$\begin{aligned}
&\langle \chi(\Delta u) A_x A_y \rangle \\
&\quad = \langle \mathbf{I}_\xi^{-2} \rangle m_0^2 \Bigg\langle \chi(\Delta u) \sum_{\mathbf{x}_{j,c}, \mathbf{x}_{k,c} \in \gamma_\xi} \Bigg[B_{j,x} B_{k,y} \sum_\alpha x_{i,c,\alpha}^2 x_{j,c,\alpha} x_{k,c,\alpha} \\
&\qquad - 2 \sum_{\alpha,\beta} x_{i,c,\alpha} x_{j,c,\alpha} B_{j,x} B_{k,\beta} x_{i,c,\beta} x_{k,c,y} \Bigg] \Bigg\rangle, \qquad \text{(D6)}
\end{aligned}$$

of which the last is zero because $\langle x_{j,x} x_{k,y} \rangle = 0$ for all j, k. We continue with the averages over the positions inside the sums. In the first summand of Eq. (D6), we recognize that $\langle x_{j,c,\alpha} x_{k,c,\alpha} \rangle = \langle x_{j,c,\alpha}^2 \rangle \delta_{kj}$, and in the second one, we may rewrite $\langle x_{i,c,\alpha} x_{i,c,\beta} \rangle = \langle x_{i,c,\alpha}^2 \rangle \delta_{\alpha\beta}$ and $\langle x_{j,c,\alpha} x_{k,c,y} \rangle = \langle x_{j,c,\alpha}^2 \rangle \delta_{\alpha y} \delta_{kj}$. This follows from the usual molecular chaos assumption that different particles are uncorrelated and the assumption that the components of a position are also uncorrelated. Performing the sums with these replacements, we obtain

$$\begin{aligned}
&\langle \chi(\Delta u) A_x A_y \rangle \\
&\quad = \langle \mathbf{I}_\xi^{-2} \rangle m_0^2 \big\langle \chi(\Delta u) 3 B_{j,x} B_{j,y} \big[(n_\xi - 1) \langle x_{i,c}^2 \rangle^2 + \langle x_{i,c}^4 \rangle \big] \\
&\qquad - 2 B_{i,x} B_{i,y} \big[(n_\xi - 1) \langle x_{i,c}^2 \rangle^2 + \langle x_{i,c}^4 \rangle \big] \big\rangle \\
&\quad = \langle \mathbf{I}_\xi^{-2} \rangle m_0^2 \big[(n_\xi - 1) \langle x_{i,c}^2 \rangle^2 + \langle x_{i,c}^4 \rangle \big] \langle \chi(\Delta u) B_{i,x} B_{i,y} \rangle. \qquad \text{(D7)}
\end{aligned}$$

For the term $\langle \chi(\Delta u) B_{j,x} B_{j,y} \rangle$, we may refer to Eq. (D1). If we approximate $\langle x_{i,c}^4 \rangle \approx a_0^4/80$ and $\frac{n_\xi - 1}{4 n_\xi^2} \approx \frac{1}{4 n_\xi}$, we arrive at

$$\begin{aligned}
&\langle \chi(\Delta u) A_x A_y \rangle \\
&\quad = \langle \mathbf{I}_\xi^{-2} \rangle a_0^4 m_0^2 \left[\frac{(n_\xi - 1)^3}{144 n_\xi^2} + \frac{1}{80} \right] \langle \chi(\Delta u) B_{i,x} B_{i,y} \rangle \\
&\quad = \left[\frac{1}{4 n_\xi} + \frac{9}{20 (n_\xi - 1)^2} \right] \langle \chi(\Delta u) B_{i,x} B_{i,y} \rangle \\
&\quad \approx \frac{1}{18 n_\xi} \left(\frac{2}{n_\xi} + 1 \right) \langle \chi(\Delta u) \rangle \langle v_{i,x} v_{i,y} \rangle. \qquad \text{(D8)}
\end{aligned}$$

In the last line, we have furthermore neglected the term $\frac{9}{20(n_\xi - 1)^2}$, which is small compared to $\frac{1}{4 n_\xi}$.

DATA AVAILABILITY

The data that support the findings of this study are available from the corresponding author upon reasonable request.

REFERENCES

[1] A. Malevanets and R. Kapral, "Mesoscopic model for solvent dynamics," J. Chem. Phys. **110**, 8605–8613 (1999).

[2] R. Kapral, "Multiparticle collision dynamics: Simulation of complex systems on mesoscales," Adv. Chem. Phys. **140**, 89 (2008).

[3] G. Gompper, T. Ihle, D. Kroll, and R. Winkler, "Multi-particle collision dynamics: A particle-based mesoscale simulation approach to the hydrodynamics of complex fluids," in *Advanced Computer Simulation Approaches for Soft Matter Sciences III* (Springer, 2009), pp. 1–87.

[4] A. Zöttl and H. Stark, "Simulating squirmers with multiparticle collision dynamics," Eur. Phys. J. E **41**, 61 (2018).

[5] G. Rückner and R. Kapral, "Chemically powered nanodimers," Phys. Rev. Lett. **98**, 150603 (2007).

[6] I. O. Götze and G. Gompper, "Mesoscale simulations of hydrodynamic squirmer interactions," Phys. Rev. E **82**, 041921 (2010).

[7] P. de Buyl and R. Kapral, "Phoretic self-propulsion: A mesoscopic description of reaction dynamics that powers motion," Nanoscale **5**, 1337–1344 (2013).

[8] A. Zöttl and H. Stark, Phys. Rev. Lett. **112**, 118101 (2014).

[9] J. Blaschke, M. Maurer, K. Menon, A. Zöttl, and H. Stark, Soft Matter **12**, 9821–9831 (2016).

[10] T. Eisenstecken, J. Hu, and R. G. Winkler, "Bacterial swarmer cells in confinement: A mesoscale hydrodynamic simulation study," Soft Matter **12**, 8316–8326 (2016).

[11] M. Wagner and M. Ripoll, "Hydrodynamic front-like swarming of phoretically active dimeric colloids," Europhys. Lett. **119**, 66007 (2017).

[12] M. Theers, E. Westphal, K. Qi, R. G. Winkler, and G. Gompper, "Clustering of microswimmers: Interplay of shape and hydrodynamics," Soft Matter **14**, 8590–8603 (2018).

[13] A. Zöttl and J. M. Yeomans, "Enhanced bacterial swimming speeds in macromolecular polymer solutions," Nat. Phys. **15**, 554–558 (2019).

[14] F. J. Schwarzendahl and M. G. Mazza, "Maximum in density heterogeneities of active swimmers," Soft Matter **14**, 4666–4678 (2018).

[15] F. J. Schwarzendahl and M. G. Mazza, "Hydrodynamic interactions dominate the structure of active swimmers' pair distribution functions," J. Chem. Phys. **150**, 184902 (2019).

[16] J.-T. Kuhr, F. Rühle, and H. Stark, "Collective dynamics in a monolayer of squirmers confined to a boundary by gravity," Soft Matter **15**, 5685–5694 (2019).

[17] A. W. Zantop and H. Stark, "Squirmer rods as elongated microswimmers: Flow fields and confinement," Soft Matter **16**, 6400–6412 (2020).

[18] F. Rühle and H. Stark, "Emergent collective dynamics of bottom-heavy squirmers under gravity," Eur. Phys. J. E **43**, 26 (2020).

[19] P. Kanehl and H. Stark, "Self-organized velocity pulses of dense colloidal suspensions in microchannel flow," Phys. Rev. Lett. **119**, 018002 (2017).

[20] P. Kanehl and H. Stark, "Hydrodynamic segregation in a bidisperse colloidal suspension in microchannel flow: A theoretical study," J. Chem. Phys. **142**, 214901 (2015).

[21] J. Padding and A. Louis, "Hydrodynamic and Brownian fluctuations in sedimenting suspensions," Phys. Rev. Lett. **93**, 220601 (2004).

[22] A. Moncho-Jordá, A. Louis, and J. Padding, "Effects of interparticle attractions on colloidal sedimentation," Phys. Rev. Lett. **104**, 068301 (2010).

[23] M. Yang, A. Wysocki, and M. Ripoll, "Hydrodynamic simulations of self-phoretic microswimmers," Soft Matter **10**, 6208–6218 (2014).

[24] A. Malevanets and J. M. Yeomans, "Dynamics of short polymer chains in solution," Europhys. Lett. **52**, 231 (2000).

[25] A. Zöttl and J. M. Yeomans, "Driven spheres, ellipsoids and rods in explicitly modeled polymer solutions," J. Phys.: Condens. Matter **31**, 234001 (2019).

[26] K. Qi, E. Westphal, G. Gompper, and R. G. Winkler, "Enhanced rotational motion of spherical squirmer in polymer solutions," Phys. Rev. Lett. **124**, 068001 (2020).

[27] H. Noguchi and G. Gompper, "Shape transitions of fluid vesicles and red blood cells in capillary flows," Proc. Natl. Acad. Sci. U. S. A. **102**, 14159–14164 (2005).

[28] D. Alizadehrad, T. Krüger, M. Engstler, and H. Stark, "Simulating the complex cell design of *Trypanosoma brucei* and its motility," PLoS Comput. Biol. **11**, e1003967 (2015).

[29] C. Hemelrijk, D. Reid, H. Hildenbrandt, and J. Padding, "The increased efficiency of fish swimming in a school," Fish Fish. **16**, 511–521 (2015).

[30] E. Tüzel, G. Pan, T. Ihle, and D. M. Kroll, "Mesoscopic model for the fluctuating hydrodynamics of binary and ternary mixtures," Europhys. Lett. **80**, 40010 (2007).

[31] T. Hiller, M. S. de La Lama, and M. Brinkmann, "Stochastic rotation dynamics simulations of wetting multi-phase flows," J. Comput. Phys. **315**, 554–576 (2016).
[32] T. Eisenstecken, R. Hornung, R. G. Winkler, and G. Gompper, "Hydrodynamics of binary-fluid mixtures—An augmented multiparticle collison dynamics approach," Europhys. Lett. **121**, 24003 (2018).
[33] K.-W. Lee and M. G. Mazza, "Stochastic rotation dynamics for nematic liquid crystals," J. Chem. Phys. **142**, 164110 (2015).
[34] T. N. Shendruk and J. M. Yeomans, "Multi-particle collision dynamics algorithm for nematic fluids," Soft Matter **11**, 5101–5110 (2015).
[35] S. Mandal and M. G. Mazza, "Multiparticle collision dynamics for tensorial nematodynamics," Phys. Rev. E **99**, 063319 (2019).
[36] K. Rohlf, S. Fraser, and R. Kapral, "Reactive multiparticle collision dynamics," Comput. Phys. Commun. **179**, 132–139 (2008).
[37] C.-C. Huang, G. Gompper, and R. G. Winkler, "Hydrodynamic correlations in multiparticle collision dynamics fluids," Phys. Rev. E **86**, 056711 (2012).
[38] A. Lamura, G. Gompper, T. Ihle, and D. M. Kroll, "Multi-particle collision dynamics: Flow around a circular and a square cylinder," Europhys. Lett. **56**, 319 (2001).
[39] E. Westphal, S. P. Singh, C.-C. Huang, G. Gompper, and R. G. Winkler, "Multiparticle collision dynamics: GPU accelerated particle-based mesoscale hydrodynamic simulations," Comput. Phys. Commun. **185**, 495–503 (2014).
[40] M. P. Howard, A. Z. Panagiotopoulos, and A. Nikoubashman, "Efficient mesoscale hydrodynamics: Multiparticle collision dynamics with massively parallel GPU acceleration," Comput. Phys. Commun. **230**, 10–20 (2018).
[41] E. Tüzel, M. Strauss, T. Ihle, and D. M. Kroll, "Transport coefficients for stochastic rotation dynamics in three dimensions," Phys. Rev. E **68**, 036701 (2003).
[42] E. Tüzel, T. Ihle, and D. M. Kroll, "Constructing thermodynamically consistent models with a non-ideal equation of state," Math. Comput. Simul. **72**, 232–236 (2006).
[43] T. Ihle, E. Tüzel, and D. M. Kroll, "Consistent particle-based algorithm with a non-ideal equation of state," Europhys. Lett. **73**, 664 (2006).
[44] I. O. Götze, H. Noguchi, and G. Gompper, "Relevance of angular momentum conservation in mesoscale hydrodynamics simulations," Phys. Rev. E **76**, 046705 (2007).
[45] H. Noguchi and G. Gompper, "Transport coefficients of off-lattice mesoscale-hydrodynamics simulation techniques," Phys. Rev. E **78**, 016706 (2008).
[46] In our analytic calculations in the following sections we always make the approximation that it coincides with the cell center.
[47] S. K. Upadhyay, *Chemical Kinetics and Reaction Dynamics* (Springer Science & Business Media, 2007).
[48] J.-P. Hansen and I. R. McDonald, *Theory of Simple Liquids* (Elsevier, 1990).
[49] T. Ihle and D. Kroll, "Stochastic rotation dynamics: A Galilean-invariant mesoscopic model for fluid flow," Phys. Rev. E **63**, 020201 (2001).
[50] N. Kikuchi, C. M. Pooley, J. F. Ryder, and J. M. Yeomans, "Transport coefficients of a mesoscopic fluid dynamics model," J. Chem. Phys. **119**, 6388–6395 (2003).
[51] This follows from the definition $\mathbf{v}_\xi = \sum_j \mathbf{v}_i/n_\xi$, taking the average over all particles $j \neq i$, and using $\langle \mathbf{v}_j \rangle = 0$. The last relation also holds for our definition of the shear flow being symmetric about the cell center since the particle can be anywhere in the collision cell.
[52] M. P. Allen and D. J. Tildesley, *Computer Simulation of Liquids* (Oxford University Press, Oxford, 2017).
[53] J. A. Backer, C. P. Lowe, H. C. J. Hoefsloot, and P. D. Iedema, "Poiseuille flow to measure the viscosity of particle model fluids," J. Chem. Phys. **122**, 154503 (2005).
[54] A. Zöttl, "Hydrodynamics of mircoswimmer in confinement and in Poiseuille flow," Ph.D. thesis, Technisch Universität Berlin, 2014.
[55] To compare our method to classical MPCD in an example, we consider how the compressibility is reduced by a factor of six at equal Péclet numbers. To achieve this reduction in classical MPCD, the particle number has to be increased by a factor of six from $n_0 = 10$ to 60. However, this also increases the viscosity by a factor of six. Therefore, to keep the Péclet number constant, the active velocities of microswimmers have to be reduced by a factor of six. As a result, the time required for a simulation is increased by a factor of $6 \times 6 = 36$.

This is in contrast to our method, where we increase the particle number from $n_0 = 10$ to 20.To compensate that the collision rate is effectively lowered due to the stochastic collision rule, we further divide the time step by four and typically take $\Delta t/t_0 = 1/200$, which also keeps the viscosity at the same value as the reference case of classical MPCD. Thus, we achieve a decrease in compressibility by a factor of $2 \times 3 = 6$ at an equal Péclet number. In total, the time required for a simulation is increased by a factor of $2 \times 4 = 8$. Additionally, the implementation of our collision rule only resulted in 5% computational overhead compared to classical MPCD, Therefore, our new method reduces the computational effort by a factor of 4.5.

The Journal of Chemical Physics ARTICLE scitation.org/journal/jcp

Multi-particle collision dynamics with a non-ideal equation of state. II. Collective dynamics of elongated squirmer rods

Cite as: J. Chem. Phys. 155, 134904 (2021); doi: 10.1063/5.0064558
Submitted: 24 July 2021 • Accepted: 14 September 2021 •
Published Online: 6 October 2021

Arne W. Zantop[a] and Holger Stark[b]

AFFILIATIONS

Institute of Theoretical Physics, Technische Universität Berlin, Hardenbergstraße 36, 10623 Berlin, Germany

[a]Author to whom correspondence should be addressed: a.zantop@tu-berlin.de
[b]holger.stark@tu-berlin.de

ABSTRACT

Simulations of flow fields around microscopic objects typically require methods that both solve the Navier–Stokes equations and also include thermal fluctuations. One such method popular in the field of soft-matter physics is the particle-based simulation method of multi-particle collision dynamics (MPCD). However, in contrast to the typically incompressible real fluid, the fluid of the traditional MPCD methods obeys the ideal-gas equation of state. This can be problematic because most fluid properties strongly depend on the fluid density. In a recent article, we proposed an extended MPCD algorithm and derived its non-ideal equation of state and an expression for the viscosity. In the present work, we demonstrate its accuracy and efficiency for the simulations of the flow fields of single squirmers and of the collective dynamics of squirmer rods. We use two exemplary squirmer-rod systems for which we compare the outcome of the extended MPCD method to the well-established MPCD version with an Andersen thermostat. First, we explicitly demonstrate the reduced compressibility of the MPCD fluid in a cluster of squirmer rods. Second, for shorter rods, we show the interesting result that in simulations with the extended MPCD method, dynamic swarms are more pronounced and have a higher polar order. Finally, we present a thorough study of the state diagram of squirmer rods moving in the center plane of a Hele-Shaw geometry. From a small to large aspect ratio and density, we observe a disordered state, dynamic swarms, a single swarm, and a jammed cluster, which we characterize accordingly.

I. INTRODUCTION

Simulations of hydrodynamic flows in the context of microscopic colloidal and active particles share a long history with the method of multi-particle collision dynamics (MPCD).[1–3] Different modifications of the original algorithm[4] have been applied in studies of colloidal suspensions,[5–9] microswimmers,[10–23] polymers,[24–26] and even complex deformable bodies such as red blood cells[27,28] or the African trypanosome,[29,30] the causative agent of the sleeping sickness, to name a few examples. Our particular interest lies in the collective dynamics of elongated microswimmers and active filaments for which interesting states, such as swarming,[21,31–33] vortex formation,[34–37] active nematic patterns,[38–40] and active turbulence,[41–45] have been observed. Many of these features can already be described by continuum models[46–49] that combine elements of the Toner–Tu[50] and Swift–Hohenberg[51] equations. However, it is still a matter of current debate to identify the importance of purely steric and hydrodynamic interactions on the scale of the constituting particles.[52–57] In this context, we introduced elongated squirmer rods as a model for elongated bacteria using MPCD to simulate their flow fields.[17] Our model thereby adds to the topmost layer of detail in a wide range of models ranging from coarse-grained interactions in the famous Vicsek model[58–60] over Langevin dynamics simulation[41,61–67] with implicit hydrodynamic interactions[68,69] to explicit hydrodynamic simulations using the MPCD and lattice Boltzmann approach.[70–73]

In this context, solving the Navier–Stokes equations at vanishing Reynolds numbers with the particle-based mesoscale method of MPCD has few advantages. It inherently includes the omnipresent thermal fluctuations,[4,74] and complex geometries are straightforward to implement with this method.[28,75–77] Furthermore, the collision rules of MPCD algorithms suit well for parallel computing on graphic cards so that also on desktop computers, one can perform extensive simulations.[78,79]

However, a property that most MPCD algorithms share is that the MPCD fluid particles obey the equation of state of an ideal gas.[4,80,81] This makes the model fluid rather compressible and results in a low speed of sound c_s,[5] which is in conflict with simulating the dynamics of incompressible solvents at a low Reynolds number. It is a matter of current debate how this affects the dynamics of immersed particles,[20] especially for strongly inhomogeneous systems, such as clustered microswimmers.[21] To render the MPCD fluid more incompressible, different strategies can be used. For the ideal-gas models, increasing the density of fluid particles n_0 naturally decreases the compressibility.[21] However, this comes with an immense increase in simulation time proportional to n_0^2 if the system size is held constant. Alternatively, auxiliary field equations can be coupled to the dynamics of the MPCD particles to alter the equation of state of the model.[81]

In a recent publication,[82] we introduced an extended version of MPCD with a modified collision step that transfers momentum across a randomly oriented plane within the collision cell in order to generate a non-ideal equation of state. In addition, the collision probability depends on the local density and velocities. This is different from traditional MPCD algorithms, where collisions occur at a fixed rate. Our approach is motivated by the collision rate in the Boltzmann equation[83] and has the advantage that it can easily be integrated into an existing MPCD program. A similar approach has been formulated for two-dimensional systems in Refs. 84 and 85. While we have already derived expressions for the equation of state and the viscosity in our previous publication,[82] in the present work, we demonstrate its application to the dynamics of single squirmers and squirmer rods, but most importantly to explore their collective dynamics.[17]

In Sec. II, we start by shortly reviewing the extended MPCD method[82] and the squirmer-rod model for elongated microswimmers[17] introduced by us in earlier publications. We then demonstrate the applicability of the extended MPCD method and, in particular, compare it to the traditional MPCD version. First, in Sec. III, we show that our new method accurately reproduces the leading hydrodynamic multipoles contributing to the flow field of a single squirmer in the bulk fluid and in confinement. Second, in Sec. IV, we explicitly demonstrate the lower compressibility of the extended MPCD method considering the specific example of a cluster of squirmer rods. Then, for shorter rods, we illustrate quantitative differences in their swarming behavior between both MPCD methods. Finally, in Sec. V, we employ the extended MPCD method to study in-depth the collective dynamics of squirmer rods. We present a state diagram of squirmer rods for variable aspect ratio and density, which includes dynamic swarms, single swarms, and jammed clusters, and we discuss their structural and dynamic properties. We finish with concluding remarks and an outlook in Sec. VI.

II. METHODS

A. Extended MPCD method

As common to all MPCD algorithms, the fluid is modeled by point-like particles, the dynamics of which proceeds in two alternating steps: ballistic motion along the mean free path followed by a collision. Because the collision rule conserves linear and also angular momentum, the simulated fluid flow solves the Navier–Stokes equations.[4] In MPCD, these steps occur simultaneously for all particles. During the streaming step (i), particles with masses m_0, positions $\mathbf{x}_i(t)$, and velocities $\mathbf{v}_i(t)$ move ballistically for the duration of the time step Δt,

$$\mathbf{x}_i(t+\Delta t) = \mathbf{x}_i(t) + \mathbf{v}_i(t)\Delta t. \tag{1}$$

Moreover, the particles collide with bounding walls, colloids, or, in our case, squirmers[3,13,14,16–18] and transfer linear and angular momenta. To enforce either the no-slip boundary condition or a predefined slip-velocity at a squirmer surface, the so-called bounce-back rule is applied.[4,75]

Our extended MPCD method[82] now modifies the collision step (ii). As usual, the simulation volume is divided by a cubic lattice with lattice constant a_0 and all particles are grouped into cubic cells with volume $\mathscr{V}_{\boldsymbol{\xi}}$ centered around position $\boldsymbol{\xi}$. Before each collision step, the lattice is randomly shifted against the previous lattice to ensure Galilean invariance.[86] The $n_{\boldsymbol{\xi}}$ particles inside a cell have the mean velocity $\mathbf{v}_{\boldsymbol{\xi}}$, center-of-mass position $\mathbf{x}_{\boldsymbol{\xi}}$, and moment-of-inertia tensor $\mathbf{I}_{\boldsymbol{\xi}}$ defined relative to $\mathbf{x}_{\boldsymbol{\xi}}$.

Now, in our modified collision step, each cell is divided into two halves A and B by a plane $P_{\hat{\mathbf{n}},\mathbf{x}_{\boldsymbol{\xi}}}$ that contains the center of mass $\mathbf{x}_{\boldsymbol{\xi}}$ and has the normal unit vector $\hat{\mathbf{n}}$, which, by definition, always points toward A. For each cell and time step, $\hat{\mathbf{n}}$ is randomly drawn from a discrete set of 13 possible orientations. The modified collision step transfers momentum across the randomly oriented plane and thereby generates a non-linear equation of state. We denote the respective number of particles on each side of the plane by n_A and n_B and their respective mean velocity components along $\hat{\mathbf{n}}$ taken relative to $\mathbf{v}_{\boldsymbol{\xi}}$ by $\bar{v}_A$ and $\bar{v}_B$. We also introduce the relative velocity $\Delta u \equiv \bar{v}_B - \bar{v}_A$ for further use. The collision step introduces for each particle velocity $\mathbf{v}_i$ in cell $\mathscr{V}_{\boldsymbol{\xi}}$ a new value $\mathbf{v}_i^{\text{new}}$ and is defined by

$$\mathbf{v}_i^{\text{new}} = \mathbf{v}_i + \chi(\Delta u)\Big\{\hat{\mathbf{n}}\left[\hat{\mathbf{n}}\cdot(\mathbf{v}_{\boldsymbol{\xi}}-\mathbf{v}_i)+\delta v_i\right] - \mathbf{I}_{\boldsymbol{\xi}}^{-1} m_0 \sum_{\mathbf{x}_j\in\mathscr{V}_{\boldsymbol{\xi}}} \left[\mathbf{x}_{j,c}\times\hat{\mathbf{n}}(\delta v_j - \hat{\mathbf{n}}\cdot\mathbf{v}_j)\right]\times\mathbf{x}_{i,c}\Big\}, \tag{2}$$

where $\mathbf{x}_{i,c}$ denotes the position vector of particle i relative to the center-of-mass position $\mathbf{x}_{\boldsymbol{\xi}}$. In contrast to other MPCD methods, the collision only occurs with a certain probability as explained below. To initiate a collision, the stochastic variable $\chi(\Delta u)$ is set to one, otherwise it is zero. The term in square brackets in the first line sets the normal velocity component of particle i relative to $\hat{\mathbf{n}}\cdot\mathbf{v}_{\boldsymbol{\xi}}$ to a new random value δv_i, which we introduce below. It mainly transfers momentum across the collision plane $P_{\hat{\mathbf{n}},\mathbf{x}_{\boldsymbol{\xi}}}$, and all values add up to zero in order to preserve the total momentum. Finally, the term in the second line is added to preserve the angular momentum $L_{\boldsymbol{\xi}} = m_0\sum_{\mathbf{x}_i\in\mathscr{V}_{\boldsymbol{\xi}}}\mathbf{x}_i\times\mathbf{v}_i$ during collision.

Note that the momentum transfer across the randomly oriented plane is responsible for the decreased compressibility of the MPCD fluid. As we showed in Ref. 82, it generates a term proportional to $n_{\boldsymbol{\xi}}^2$ in the equation of state, which thereby deviates from the ideal-gas equation of the classical MPCD fluid. On average, a collision between particles in regions A and B occurs when the two clouds move toward each other meaning $\Delta u \equiv \bar{v}_B - \bar{v}_A > 0$. Following the collision term in the Boltzmann equation, we take for the collision rate $c\Delta u\, n_A n_B$, where c is the scattering cross section.[83] Thus, we set the probability for a collision to occur to

$$p_\chi(\Delta u) \equiv \Theta(\Delta u)[1 - \exp(-c\Delta u\, n_A n_B)], \tag{3}$$

where $\Theta(\Delta u)$ is the Heaviside step function, and we use the exponential function to guarantee $p_\chi(\Delta u) \leq 1$.

Finally, we introduce the new velocity component along the normal $\hat{\mathbf{n}}$,

$$\delta v_i \equiv \frac{n_{B/A}}{n_{A/B}}\, \tilde{v}_{B/A} + \delta v_i^{\mathrm{MB}} - \Delta v_{A/B}. \tag{4}$$

Here, the first term transfers momentum between regions A and B. The first index applies to particles i in region A. They take over the momentum $m_0\tilde{v}_B$ from region B and vice versa. The prefactor $n_{B/A}/n_{A/B}$ guarantees that the overall momentum is conserved. Essentially, the total momenta from regions A and B are just swapped. The second term assigns each particle a thermal velocity δv_i^{MB} drawn from a Maxwell–Boltzmann distribution at temperature T, which thereby serves as a thermostat for the fluid. The last term subtracts the mean thermal velocities in each region (A and B),

$$\Delta v_{A/B} = \frac{1}{n_{A/B}} \sum_{\{\mathbf{x}_i \in \mathscr{V}_{A/B}\}} \delta v_i^{\mathrm{MB}}, \tag{5}$$

in order to conserve momentum.

As in all MPCD algorithms, the so-called "ghost" particles are introduced to participate in the collision step. They are added where overlap with boundaries leads to partially empty collision cells, thereby improving the validity of the no-slip boundary condition.[75] After the collision step, the changes in the linear and angular momentum of the ghost particles are assigned to movable objects, which in our case are squirmers. This ensures that the linear and angular momenta are conserved.

B. Squirmer and squirmer rods

To investigate the flow fields of microswimmers and their hydrodynamic interactions in collective motion, we use spherical squirmers and build squirmer rods from them. Spherical squirmers propel by an imposed axisymmetric slip-velocity field on their surfaces,[3,87,88]

$$\mathbf{v}_s = B_1^s[(1 + \beta\hat{\mathbf{e}}\cdot\hat{\mathbf{r}}_s)(\hat{\mathbf{e}}\cdot\hat{\mathbf{x}}_s)\hat{\mathbf{x}}_s - \hat{\mathbf{e}}], \tag{6}$$

which initiates flow in the surrounding fluid. Here, the unit vector $\hat{\mathbf{x}}_s$ points from the squirmer center toward the squirmer surface and $\hat{\mathbf{e}}$ indicates the orientation and swimming direction of the squirmer. The resulting flow field in the bulk fluid is a superposition of multipole solutions of the Stokes equations. In particular, it contains a source dipole singularity with strength $B_1 = B_1^s R^3$ and a force dipole singularity with strength $A_2 = \beta B_1^s R^2$. The latter is controlled by the parameter β, which determines the squirmer type, and R denotes the radius of the squirmer. For different values of β, the squirmer represents either a pusher ($\beta < 0$), a neutral swimmer ($\beta = 0$), or a puller ($\beta > 0$). The squirmer parameter B_1^s also determines the swimming speed $v_0 = 2/3\, B_1^s$.

To model the actual rod shape of many biological microswimmers, we use the squirmer rod. It is constructed by arranging several neutral spherical squirmers on a line such that they overlap and form a single rigid body. By varying the squirmer distance d, rods of different aspect ratios $\alpha = l_S/2R$ are realized where l_S is the rod length. In this work, we always use $N_{sq} = 10$ spherical squirmers and a maximum squirmer distance of $d \approx 0.8R$ so that the surface is still smooth enough that swimmers can slide past each other. This amounts to a maximum aspect ratio of $\alpha = 4.75$. To model steric interactions between pairs of squirmer rods, we employ the Weeks–Chandler–Andersen potential[89] that acts between two squirmers from different rods. The force constant is chosen strong enough ($\varepsilon_{\mathrm{WCA}} \approx 10^4 k_{\mathrm{B}}T$) to ensure that there is no significant overlap between two rods.

The squirmer rod model described so far resembles ciliated micro-organisms such as *Paramecium*. To model bacteria, such as *E. Coli*, which are driven by a bundle of rotating flagella extending from its rear, one can concentrate the surface velocity on the back of the rod by multiplying the slip velocity with an envelope or step function.[17]

C. Parameters

We choose the parameters for the extended MPCD method such that the total viscosity $\eta = \eta_{\mathrm{str}} + \eta_{\mathrm{coll}}^{+A} \approx 16\sqrt{m_0 k_{\mathrm{B}}T}/a_0^2$ (see Ref. 82) given in MPCD units matches previous studies where other MPCD methods are employed.[13,14,17,21] In particular, the collision parameter $c = 1/100$ and the average number density $n_0 = 20$ are chosen such that the average collision rate $\langle\chi(\Delta u)\rangle \approx 0.14$ is low enough to be in the quadratic regime of the equation of state.[82] Together with a time step of $\Delta t = 0.005 a_0\sqrt{k_{\mathrm{B}}T/m_0}$, the total viscosity takes the prescribed value. For the squirmers, we use a radius of $R = 3a_0$ and a source dipole strength of $B_1^s = 0.1$, which results in a Péclet number of $\mathrm{Pe} = Rv_0/D_T \approx 354.6$, where D_T is the translational diffusion coefficient of the spherical squirmer.[14]

To initialize a simulation, we distribute the fluid particles randomly and choose thermal velocities from the Maxwell–Boltzmann distribution. In addition, the squirmer rods are randomly distributed in the midplane of the simulation box for area fractions ϕ below 0.6. For $\phi \geq 0.6$, we initiate the simulation by arranging the swimmers in a rectangular pattern and by choosing their orientations at random along the longer side of the rectangular unit cell.

We use the following geometries and simulation times in our computer studies. To simulate the flow fields of pusher-type squirmers, we use periodic boundary conditions for the bulk fluid with an edge length of $L = 150a_0$ of the cubic simulation box. In the Hele-Shaw geometry, the confining parallel plates have a separation of $\Delta z = 8a_0$ and an edge length of $L = 300a_0$, and the squirmers are constrained to move in the midplane of the cell (see Fig. 1) by setting the normal component of the velocity v_z and the components ω_x, ω_y of the angular velocities of the squirmer rods to zero after each time step. The flow fields are first equilibrated during 50 000 time steps Δt, and 20 independent simulation runs are used to average the flow fields over a total of $10^7\Delta t$. To simulate the collective motion of squirmer rods, we choose a Hele-Shaw geometry with a

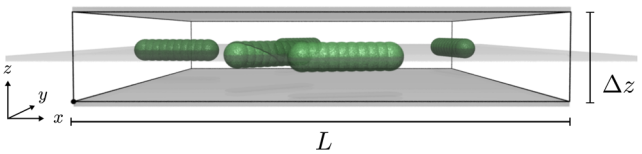

FIG. 1. Schematic of the Hele-Shaw geometry in a perspective view. The squirmers and rods are restricted to move in the midplane between two parallel walls with separation Δz. In the directions parallel to the walls, periodic boundary conditions are applied.

plate separation of $\Delta z = 18a_0$, otherwise the edge length $L = 300a_0$ is the same. The system is equilibrated during 10^7 time steps Δt, and data are sampled during another $10^7 \Delta t$.

III. FLOW FIELDS IN THE EXTENDED MPCD METHOD

In this section, we present a first test for the extended MPCD method by demonstrating the accuracy with which it simulates flow fields of microswimmers. We compare the simulation results of the flow field of a pusher-type squirmer with the analytic multipole expression both in the bulk fluid and in confinement between two parallel plates.

We briefly outline the underlying theory. In the Stokes regime, the flow field generated by an object moving through the bulk fluid can be written as a series of hydrodynamic multipoles. This series contains at the lowest order the Stokeslet or hydrodynamic force monopole, which is not allowed for autonomous swimmers, the source dipole, and their higher-order derivatives. For swimmers with radial symmetry about their swimming direction $\hat{\mathbf{e}}$, the flow fields of these multipoles can be expanded into a Legendre polynomial $P_n(\cos\theta)$. In spherical coordinates r, ϕ, and θ with $\hat{\mathbf{z}} = \hat{\mathbf{e}}$, the radial velocity component of the multipole expansion reads

$$u_r(r,\theta) = \sum_{n=1}^{\infty} \left[A_n r^{-n} + B_n r^{-n-2}\right] P_n(\cos\theta). \tag{7}$$

We use the orthogonality of the Legendre polynomials to extract the coefficients $u_{r,n}(r) = A_n r^{-n} + B_n r^{-n-2}$ from the simulated flow field with the radial component $u_r(r,\theta)$ and then determine the coefficients of the force multipoles A_n and source multipoles B_n by a polynomial fit in r^{-n} and r^{-n-2}.

When the object moves in a fluid confined between two parallel plates with distance Δz (Hele-Shaw geometry), a multipole expansion for the flow field averaged along the plate normal exists.[17,90] Using polar coordinates ρ and φ in the plane, the radial velocity component reads

$$\tilde{u}_\rho(\rho,\varphi) = \sum_{n=1}^{\infty} (\mathscr{A}_n + \mathscr{B}_n)\rho^{-n-1} \cos(n\varphi), \tag{8}$$

where φ is measured against the swimming direction $\hat{\mathbf{e}}$. Along the normal or z direction, the flow field is parabolic, which is integrated out and included into the coefficients $\mathscr{A}_n$ and $\mathscr{B}_n$. Similar to the bulk case, we use the orthogonality of the basis functions $\cos(n\varphi)$ to extract the coefficients $\tilde{u}_{\rho,n}(\rho) = (\mathscr{A}_n + \mathscr{B}_n)\rho^{-n-1}$. The relative strength of the amplitudes $\mathscr{A}_n$ and $\mathscr{B}_n$ can be deduced either by extrapolating from the bulk case or by their different scaling behavior $\mathscr{A}_n \propto \Delta z$ and $\mathscr{B}_n \propto 1/\Delta z$. Most interesting about Eq. (8) is the radial decay of the different multipoles compared to the bulk case. For a force-free microswimmer ($A_1 = \mathscr{A}_1 = 0$), the source dipole moment $\mathscr{B}_1$ becomes the dominant term in the Hele-Shaw geometry, while in the bulk fluid the force dipole A_2 dominates.

In Fig. 2, we demonstrate the multipole analysis of the flow field of the pusher squirmer simulated with the extended MPCD method. Figure 2(a) shows all non-vanishing radial velocity coefficients $u_{r,1}(r)$ and $u_{r,2}(r)$ in the bulk fluid for the squirmer type with $\beta = -1$. In agreement with the analytic expression, each follows a distinctive power law specific for the multipole moment. The radial decay of $u_{r,1}(r)$ clearly has the exponent -3 corresponding to the source dipole moment B_1, and $u_{r,2}(r)$ decays with an exponent -2 in the farfield as expected for the force dipole moment A_2. However, for $u_{r,2}(r)$ close to the squirmer, we also recognize the importance of the short-ranged flow field of the source quadrupole moment B_2, which has the exponent -4. Thus, the polynomial fit deviates from the straight line. The additional source quadrupole moment with a negative value is necessary to balance the force dipole A_2 such that the correct surface velocity field of the pusher squirmer is implemented. In contrast, the flow field of the source dipole moment B_1 obeys the boundary condition by itself so that $u_{r,1}(r)$ follows a pure power law.

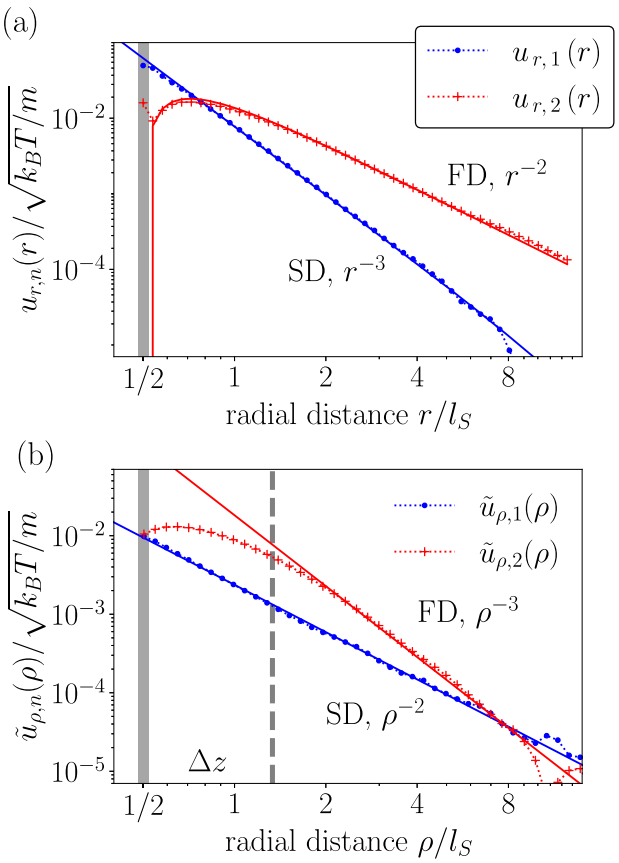

FIG. 2. Radial decay of the radial velocity coefficients of the hydrodynamic multipoles obtained from the Legendre–Fourier decomposition of the flow field of a pusher squirmer. (a) Bulk fluid and squirmer type $\beta = -1$. (b) Hele-Shaw geometry with $\Delta z = 8a_0$ and squirmer type $\beta = -3$.

In the Hele-Shaw geometry, we choose $\beta = -3$ to get a stronger signal from the force dipole. We observe the corresponding radial coefficients $\tilde{u}_{\rho,1}(\rho)$ and $\tilde{u}_{\rho,2}(\rho)$, which perfectly show the expected radial decay [see Fig. 2(b)]. However, note that due to the confinement, the exponents of the moments of force and source dipole are swapped, and hence, the source dipole ultimately dominates the far field. Note that, unlike in the bulk fluid, force and source multipoles in $\tilde{u}_{\rho,n}(\rho)$ decay with the same power law in a Hele-Shaw geometry. Here, the deviation of the force dipole field from theory at $\rho < \Delta z$ (gray dashed line) is due to short-ranged contributions to the flow field that are neglected in Eq. (8).[90,91]

IV. COMPARISON OF TRADITIONAL AND EXTENDED MPCD

A. Fluid density in squirmer-rod systems

In this section, we demonstrate how the low compressibility of the extended MPCD algorithm results in a much more uniform density of the MPCD particles compared to traditional MPCD methods in systems where the fluid is strongly forced. In particular, we consider a dense suspension of squirmer rods that are constrained to move in the center plane between two confining parallel plates, which we will further study in Sec. V. We choose squirmer rods with an aspect ratio of $\alpha = 4.0$ at an area fraction of $\phi = 0.6$.

As a reference, we also perform simulations with the standard MPCD-AT+A algorithm with angular momentum conservation and an Andersen thermostat.[3] We choose the simulation parameters such that the relevant physical quantities characterizing the system, the fluid viscosity and the Péclet number, match in both MPCD algorithms. Hence, for the standard MPCD method, we use $n_0' = 10$ and $\Delta t' = 0.02 a_0 \sqrt{k_B T/m_0}$, which results in the same viscosity $\eta \approx 16\sqrt{m_0 k_B T}/a_0^2$.[14,82] Because the two MPCD algorithms use different time steps, we choose 20×10^6 and 5×10^6 time steps, respectively, to simulate the same period with the extended and conventional MPCD method.

With both algorithms, the initial random distribution of squirmer rods evolves into a stable compact swarm, which moves through the system [insets of Figs. 3(a) and 3(b)]. Above and below the swarm, the fluid experiences strong forcing due to the slip velocity fields on the rod surfaces. This generates a strong pressure gradient between the region of the cluster and the rest of the system. However, the MPCD fluid densities simulated with the traditional and extended MPCD algorithms behave differently, as shown in the main parts of Figs. 3(a) and 3(b). While the relative fluid densities $\langle \rho/\rho_0 \rangle_z$ and $\langle \rho/\rho_0' \rangle_z$, averaged over the z direction, become non-uniform in both simulations, the deviations from the mean density when using the extended MPCD algorithm are much smaller.

For the traditional MPCD algorithm [cf. Fig. 3(a)], the pressure gradient creates regions sparse of fluid particles above and below the swarming cluster as well as between the rods. These fluid particles are pressed into regions outside of the cluster, where the density increases. Note that the density field also includes the ghost particles of the squirmer rods, which are clearly visible in white because their density is held constant at n_0 by definition. In the vicinity of the swarming cluster, the relative density drops to values of about 60% and it rises to 140% in regions outside the cluster. In simulations with stronger confinement, i.e., smaller Δz, this effect becomes even stronger.

In contrast, for the extended MPCD algorithm, the deviations in relative density are significantly lower with around ±6% [cf. Fig. 3(b)]. Thus, the density is only mildly decreased in the vicinity of the cluster and increased in the remaining regions of the system. Note that the fluid density directly between squirmer rods in the midplane follows the trend of the height-averaged density in Figs. 3(a) and 3(b), but the deviations are stronger. With the traditional MPCD method, the relative density drops to 30%, while with the extended MPCD method, the minimum relative density is 90%. All this is in accordance with the low compressibility of the fluid in the extended MPCD method, which is about five times lower

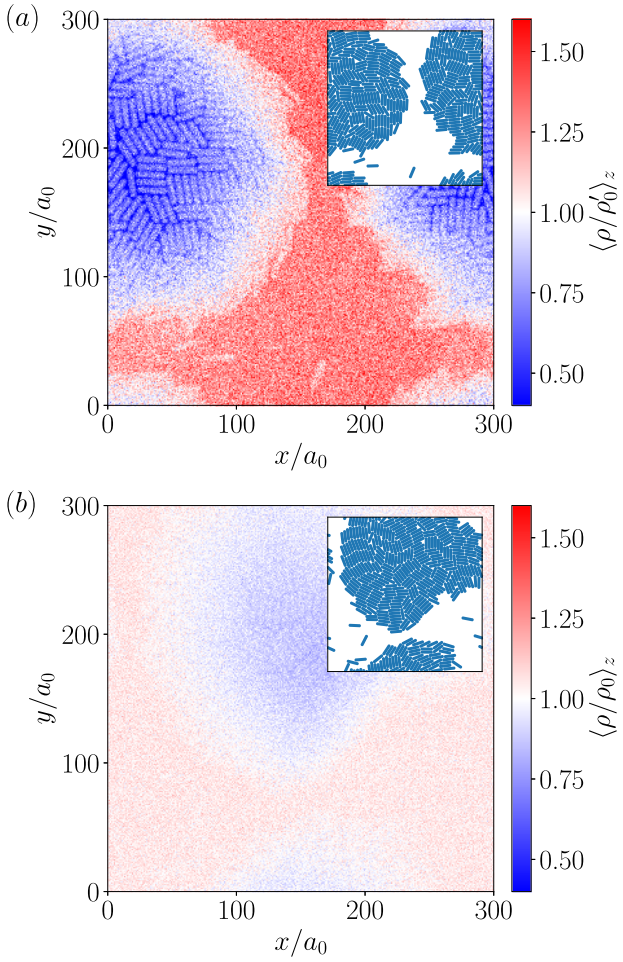

FIG. 3. Density field of the fluid in systems with squirmer rods of an aspect ratio of $\alpha = 4.0$ and an area fraction of $\phi = 0.6$ and in a Hele-Shaw geometry with a plate distance of $\Delta z = 18 a_0$. The relative density is averaged over the height of the system and shown in top view. The insets show snapshots of the configuration of squirmer rods. Results obtained with the traditional MPCD-AT+A algorithm (a) and with the extended MPCD algorithm (b).

compared to the simulations with traditional MPCD.[82] However, note that this comes with an increase in simulation time.

Thus, the extended method better satisfies the incompressibility condition $\nabla \cdot \mathbf{v} = 0$. Furthermore, also the viscosity, which depends on the local density, is more uniform in the extended MPCD method and the simulation thus closer to the Stokes limit. This is particularly important for simulating microswimmers, where typically a constant Péclet number $\mathrm{Pe} \propto \eta$ is assumed for the entire system.

To be more quantitative, we show in Fig. 4 the pressure $\langle p/p_0 \rangle_z$ and viscosity fields $\langle \eta/\eta_0 \rangle_z$ derived from the density fields shown in Fig. 3 using the respective analytical formulas of the traditional method and our extended MPCD method.[2,82] Note that, since both pressure and viscosity depend on density ρ, they are not independent of each other. While the viscosity of the traditional MPCD method is linear in the density and varies accordingly by ±40% [cf. Fig. 4(c)],

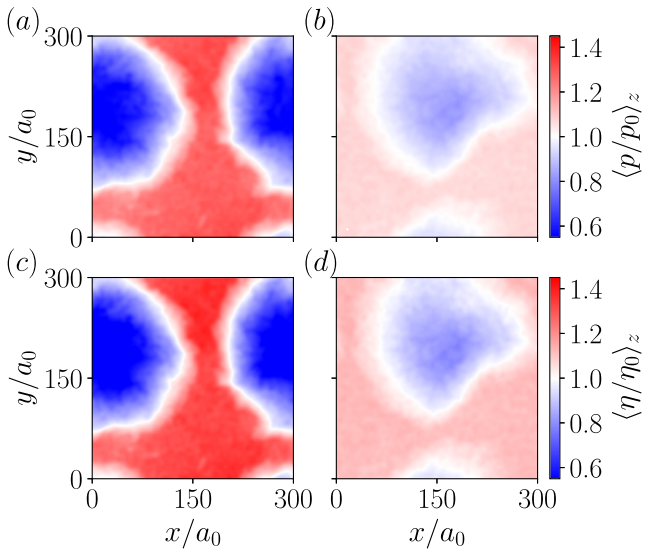

FIG. 4. Fluid pressure (top row) and viscosity (bottom row) fields of the systems shown in Fig. 3 in top view. Both quantities are averaged over the height of the system and smoothed with a Gaussian filter using $\sigma = 3a_0$. Results obtained with the traditional MPCD-AT+A algorithm in the left panels [(a) and (c)] and with the extended MPCD algorithm in the right panels [(b) and (d)]. Note that p_0 is different for the two methods.

variations are much smaller for the extended method. Here, the relation between density and viscosity is more complex and only results in a variation of ±10% [cf. Fig. 4(d)]. The pressure fields show a similar behavior. A closer inspection shows that the deviations from the mean value are marginally smaller compared to the viscosity variations, as one can see in Fig. 4(a) for the traditional method and Fig. 4(b) for the extended method.

Now, with the significant increase in the local Péclet number $\mathrm{Pe} \propto \eta$ outside of the cluster for the traditional MPCD method, we would assume enhanced clustering compared to the much less compressible fluid, which has been reported for spherical squirmers.[21] However, clustering in the two simulations reported here is very similar, suggesting that steric interactions between the elongated rods dominate. In Subsection IV B, we will therefore compare two simulations with shorter rods such that the alignment due to the elongated shape is less pronounced and hydrodynamic interactions between the rods become more important.

B. Influence on hydrodynamic interactions

To investigate how the lower compressibility of the extended MPCD method affects the hydrodynamic interactions between the rods and ultimately their clustering, we choose a lower aspect ratio of $\alpha = 2.5$ and an area fraction of $\phi = 0.4$ to reduce the effect of steric interactions. Otherwise, we use the same system parameters as in Sec. IV A and perform simulations with the two different MPCD algorithms.

In the temporal evolution of both systems, small clusters form due to direct collisions. However, only with the extended MPCD method, they begin to form swarms that grow to a significant size, while with the traditional MPCD method the collision clusters remain small and dissolve rather quickly. The snapshots of Figs. 5(a) and 5(b) as well as videos V1 and V2 illustrate this difference. To quantify it, we identify individual rod clusters such that all spherical squirmers that are separated by a center-to-center distance less than $\Delta x < 1.02R$ belong to one cluster. The cluster size N_c then is the number of rods within a cluster determined by the ratio of squirmer number in the cluster to squirmers per rod. Additionally, we define the cluster velocity as the instantaneous average of rod velocities over the cluster.

Figure 5(c) shows the mean cluster velocity $\langle v_c \rangle$ relative to the squirmer velocity v_0, and Fig. 5(d) shows the probability density for a rod to lie in a cluster with size N_c. Note that the swimming speed of single squirmer rods is $\sim 1.1 v_0$.[17] The difference between both methods is immediately visible. For small groups $N < 10$, we observe similar velocities $v_c \approx 1.1 v_0$ in Fig. 5(c) close to the value of a single rod in the bulk fluid. These rods form a dilute background, which exists equally in both systems, as the identical probability distributions of cluster sizes with $N_c < 10$ in Fig. 5(d) show.

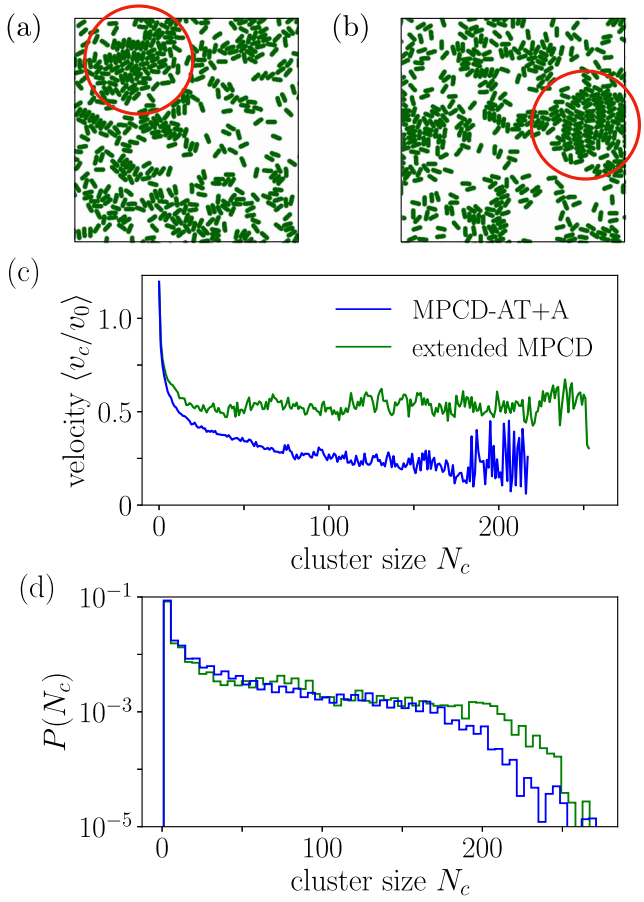

FIG. 5. Snapshots of simulations with (a) the traditional MPCD method and (b) the extended MPCD method. Both snapshots show a typical cluster/swarm, which is marked by a red circle. (c) Mean velocity of clusters with size N_c given in units of the squirmer velocity v_0 for squirmer rods with an aspect ratio of $\alpha = 2.5$ at a dilute area fraction of $\phi = 0.4$. (d) Probability density for a squirmer rod to lie in a cluster of size N_c. The system size is equal to Fig. 3 and also the systems used in Sec. V. The results are obtained with the traditional MPCD-AT+A algorithm (blue) and the extended MPCD algorithm (green).

Large clusters also exist in both systems, but they behave differently. Visual inspection of video V1 shows that clusters in simulations with traditional MPCD are formed rather by collisions between rods or other clusters and dissolve quickly. As a result, the mean cluster velocity v_c in Fig. 5(c) decreases drastically with the cluster size N_c. Furthermore, Fig. 5(d) shows that the clusters do not exceed a size of roughly $N_c = 200$.

In contrast, the formation of stable swarms in simulations with the extended MPCD method leads to the plateau value of the mean cluster velocity at $v_c \approx 0.6v_0$ for $N_c > 30$ [Fig. 5(c)]. In addition, the distribution $P(N_c)$ in Fig. 5(d) shows the existence of larger clusters. Both results indicate that these swarms are more ordered compared to the simulations with the traditional MPCD method. They accumulate new members during the collective swimming so that the polar order remains constant. Visual inspection of video V2 shows a dynamic swarming behavior where swarms still merge and dissolve, but overall they are more stable.

This is an interesting result because it shows that the extended MPCD method with its lower compressibility stabilizes clusters in the current system. Moreover, we conclude that the extended method mediates hydrodynamic interactions better such that rods align and form swarms.

V. COLLECTIVE DYNAMICS OF SQUIRMER RODS

We now present a thorough investigation of the collective dynamics of squirmer rods varying aspect ratio α and 2D area fraction ϕ. Overall, we observe four different dynamic states, which we briefly describe here based on visual inspections before turning to a detailed analysis in Subsections V A and V B. The state diagram together with exemplary snapshots is given in Fig. 6, and videos V3–V6 in the supplementary material illustrate the different dynamic states and correspond to the respective snapshots [Figs. 6(b)–6(e)].

At small densities and also at larger densities below a critical value of the aspect ratio, $\alpha_{\min} \approx 2$, we observe a disordered state with little variations in the local density. Thereby, we support the conclusion of Ref. 21 that the low fluid compressibility reduces clustering. Increasing α above 2 and also for sufficiently large density, swarms of squirmer rods form. They consist of clusters with inherent polar order such that the squirmer rods move collectively in one direction. However, as described already in Sec. IV B, the swarms are dynamic, meaning that they are not stable in time but frequently break apart and reform creating an interesting dynamics reminiscent of dynamic clustering found for spherical active particles in the presence of a chemical field.[92,93] Crossing the dashed black line in the state diagram by increasing density and/or aspect ratio further, the dynamic swarms merge into one large swarm, which is stable in time. Depending on the individual history of such a swarm, it can show either continuous translational or rotational motion. Further increasing area fraction ϕ, the global swarms grow bigger until they span over the whole system. In this situation, the cluster is jammed, where all movements inside the cluster are blocked and only some drift velocity of the whole cluster remains. Our findings generally show parallels to the surface dynamics of *B. subtilis* reported in Ref. 94. In particular, the dynamic swarms, single swarm, and the jammed cluster are observed. For systems of

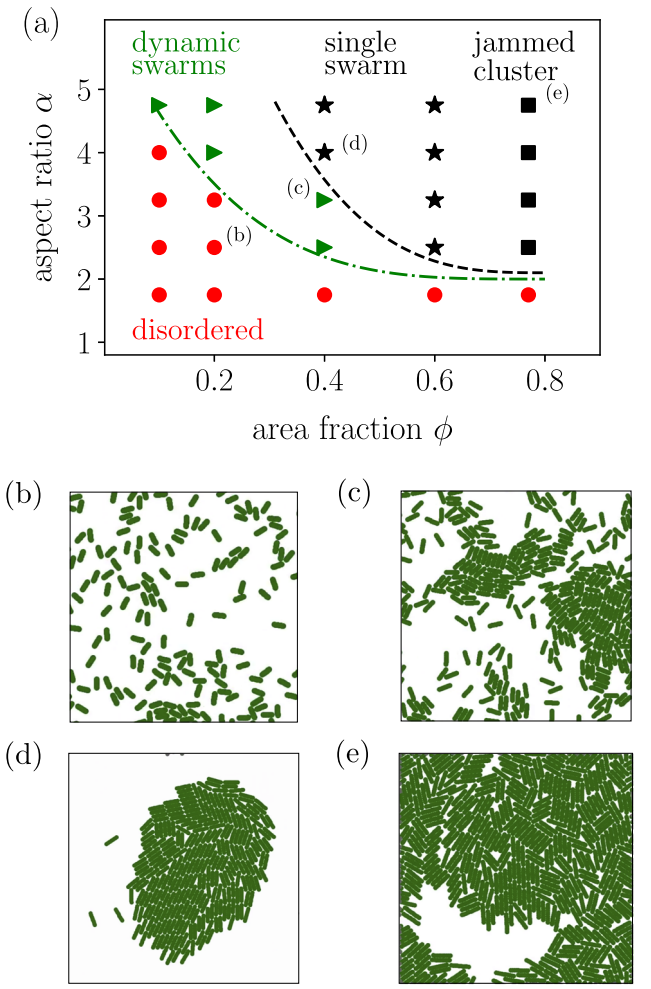

FIG. 6. (a) State diagram of squirmer rods of different aspect ratios α and at different area fractions ϕ. Red circles: disordered system (b), green circles: dynamic swarms (c), black stars: single moving swarm (d), and black squares: single jammed or drifting cluster (e). [(b)–(e)] Snapshots of the respective states for the points indicated in the state diagram.

elongated spheroidal squirmers, the disordered and single swarm states have been reported as well.[21]

For a detailed quantitative analysis of these dynamic states, we first study in Sec. V A the distribution of the local area fraction ϕ_{loc} as well as the cluster size and velocity. To analyze the alignment of the squirmer rods in the dilute and also cluster states, we use the spatial orientational pair-correlation function in Sec. V B.

A. Distributions of local area fraction, cluster size, and velocity

The observed swarms are clustered squirmer rods with additional polar order. Thus, to differentiate swarms from dilute regions in the system and to characterize the different states, we determine the distribution of local area fraction as well as cluster sizes and their velocities. To assign each squirmer rod a local area fraction ϕ_{loc}, we

use a Voronoi tessellation following our earlier work.[14] The concept is extended to the squirmer rods as follows and illustrated in Fig. 7(b). First, the ordinary Voronoi tessellation is calculated for all spherical squirmers. Here, periodic images are added around the central simulation box to achieve correct results across the periodic boundary conditions. Then, the Voronoi cells of the squirmers that belong to the same rod form the Voronoi cell of the rod, which are no longer convex polygons. Finally, the local area fraction follows from the ratio of the squirmer rod's cross section and the area of the Voronoi cell. In addition, we identify individual rod clusters and determine their velocity as described in Sec. IV B. To calculate the distribution of local area fractions $P(\phi_{\mathrm{loc}})$ and to identify clusters, we use all snapshots of the system after an equilibration time of $t_{\mathrm{eq}} = 10 \times 10^6 \Delta t$ in steps of $5 \times 10^4 \Delta t$.

We now characterize the different dynamic states using Fig. 7(a), where we plot the normalized distribution functions $P(\phi_{\mathrm{loc}})$ for different *global* or mean area fractions ϕ, always for squirmer rods with an aspect ratio of $\alpha = 3.25$. In addition, Fig. 7(c) shows individual clusters with their size N_c and velocity v_c so that for each area fraction a dynamic state is represented by a cloud of points. A dashed line is added for each area fraction ϕ, indicating the maximum possible cluster size equal to the total number of rods. Note that the distribution in the velocity is naturally broader for small clusters, which give rise to larger fluctuations.

Increasing ϕ from small to large values, we observe the following characteristics. At $\phi = 0.1$, the distribution $P(\phi_{\mathrm{loc}})$ is narrow and strongly peaked at the global value, which indicates the absence of pronounced clustering in the system. The distribution of cluster sizes in Fig. 7(c) reflects this behavior indicating only small groups of colliding squirmer rods. This is where we locate the disordered state, which is homogeneous in the local area fraction. At the larger area fraction of $\phi = 0.2$, $P(\phi_{\mathrm{loc}})$ shows the same trend but now the peak at low ϕ_{loc} is broader and a pronounced tail toward higher values of ϕ_{loc} is visible. Most of the system is still dilute, but small denser clusters are present, as shown in Fig. 7(c). This indicates that we are at the transition to the state of dynamic swarms. However, Fig. 7(c) indicates that these clusters are still mainly caused by collisions and not by longer lasting swarms with intrinsic rod alignment because their velocities are low.

At $\phi = 0.4$, we are right in the subsequent state of dynamic swarms. Here, the distribution $P(\phi_{\mathrm{loc}})$ becomes very broad and, in particular, bimodal. The bimodal distribution of area fractions has also been found for swarming *B. Subtilis*.[94] This signature is caused by parts of the system forming a dilute disordered background, while also dense dynamic swarms are visible. Their preferred area fraction indicated by the right peak of $P(\phi_{\mathrm{loc}})$ is close to the maximum $\phi_{\mathrm{loc}} = 1$. Thus, the clusters in the swarms are compact. Note that the peak for the dilute disordered background becomes more pronounced when decreasing the global area fraction and/or the aspect ratio toward the disordered state. The very broad distribution of cluster sizes and velocities in Fig. 7(c) also reflects this dynamic state of swarms. However, the size of the clusters always remains well below the total number of squirmer rods.

At the global aspect ratio of $\phi = 0.6$, we are in the state where the squirmer rods form a single moving swarm. Here, the distribution $P(\phi_{\mathrm{loc}})$ only shows one peak close to $\phi_{\mathrm{loc}} \approx 1$ and the dilute background is nearly absent. The distribution of cluster sizes in

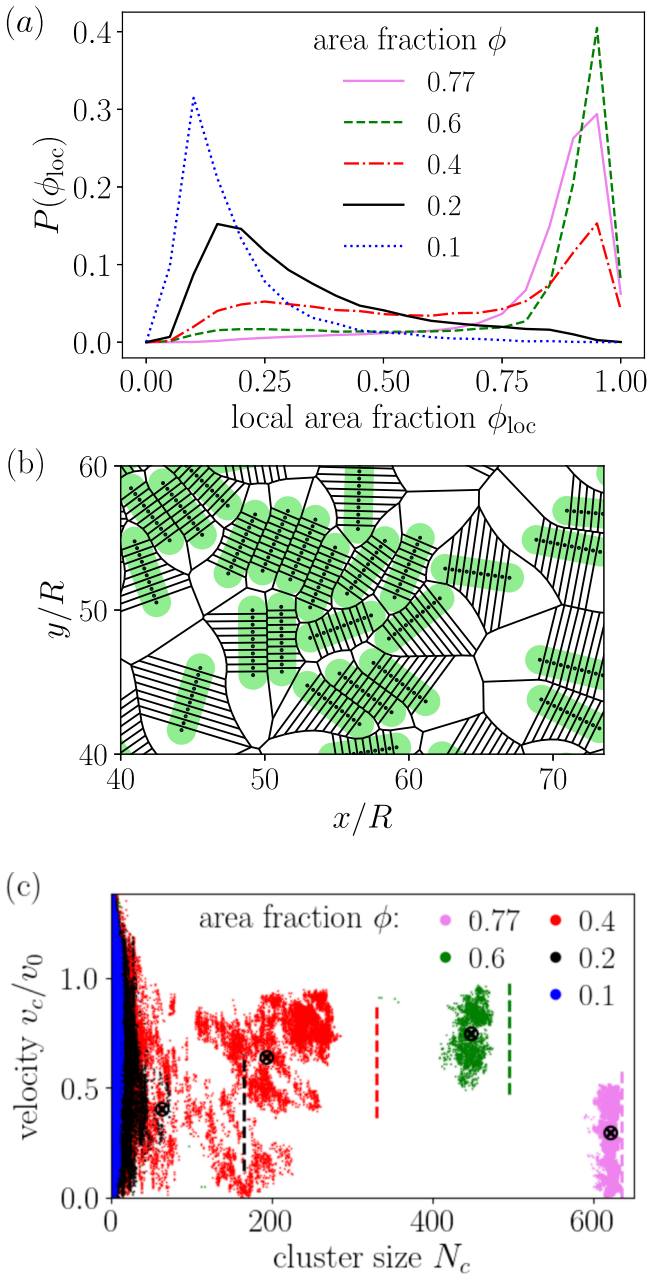

FIG. 7. (a) Distribution of local area fraction $P(\phi_{\mathrm{loc}})$ obtained from the Voronoi tessellation of the configurations of squirmer rods with an aspect ratio of $\alpha = 3.25$ at different global area fractions ϕ. (b) Demonstration of a Voronoi tessellation for squirmer rods with $\alpha = 3.25$ and at $\phi = 0.4$. The black dots mark the positions of the spherical squirmers, and the green circles mark their cross sections. Note that because always ten squirmers lie on a line, each squirmer rod creates nine parallel lines in the Voronoi diagram. (c) Cluster velocity v_c in units of the squirmer velocity v_0 plotted against the cluster size N_c. Each point represents a cluster determined from the snapshots. The colored dashed lines mark the total number of rods for the given area fraction ϕ. The black symbols ⊗ indicate the mean cluster velocity for clusters with size $N_c > 50$, which is chosen arbitrarily to exclude small collision groups.

Fig. 7(c) is narrow, meaning that this cluster is highly stable and its size almost reaches the total number of rods in the system. The jammed cluster at the highest aspect ratio $\phi = 0.77$ shows almost the same trend. However, the maximum of $P(\phi_{\text{loc}})$ slightly moved to the left and the distribution is broader compared to $\phi = 0.6$. This is in agreement with visual inspections, which show that the jammed clusters are less dense. When they form, the density is so high that they cannot all align properly as in the swarms, which we will confirm in Sec. V B. As shown in Fig. 7(c), the size of the cluster now reaches the total number of squirmer rods and the velocity of the jammed cluster is significantly smaller compared to the single swarm state.

For squirmer rods with other aspect ratios α, we observe the same behavior, with differences only in the quantitative description. At smaller aspect ratios $\alpha < 3.25$, the distributions $P(\phi_{\text{loc}})$ are broader and the bimodality in the swarming state is less pronounced. For higher aspect ratios $\alpha > 3.25$, the trend is inverted and also the peaks of $P(\phi_{\text{loc}})$ are more pronounced. Equally, the distribution of cluster sizes becomes more compact. This is a clear consequence of the fact that the rods tend to align better at larger aspect ratios α, which stabilizes the swarms.

B. Orientational correlations

As a second measure to characterize the different states of our system, we use the orientational pair-correlation function $\langle \hat{\mathbf{e}}_i \cdot \hat{\mathbf{e}}_j \rangle$, where $\hat{\mathbf{e}}_i$ and $\hat{\mathbf{e}}_j$ are the orientation vectors of two squirmer rods with a distance Δx. It helps us to distinguish the different swarming and jamming states by quantifying the degree of alignment in the clusters. Figure 8(a) presents the orientational pair-correlation function for different global area fractions for squirmer rods with an aspect ratio of $\alpha = 3.25$. The plot uses the same parameters as Figs. 7(a) and 7(c) in Sec. V A and supplements the results reported there.

For dilute rod suspensions with an area fraction of $\phi = 0.1$, we observe that the squirmer rods are indeed disordered. Although the orientational pair correlations have a pronounced peak at the side-by-side contact distance of two squirmer rods, they quickly decay to almost zero at two rod lengths. The strong correlations at a short distance make sense since the squirmer rods collide with each other even in the disordered state. Because of their active movement, pairs of squirmer rods are more likely to approach and collide if their swimming directions are already nearly aligned to each other. Moreover, a side-by-side configuration is more persistent, which causes the first peak with $\langle \hat{\mathbf{e}}_i \cdot \hat{\mathbf{e}}_j \rangle \approx 1$. At $\Delta x = l_S$, we observe a second smaller peak in the orientational pair correlations, which is due to two squirmer rods swimming behind each other. This configuration persists for longer times than a head on collision, and therefore, the correlation function is positive. At $\phi = 0.2$, we are close to the dynamic-swarm state. Still, the pair correlations are similar to $\phi = 0.1$, but overall they are increased. While the height of the first peak is almost the same, in particular, the second peak is more pronounced. This indicates the presence of small clusters with squirmer rods swimming side by side and also behind each other.

At $\phi = 0.4$, the orientational pair-correlations clearly change. They are of longer range, and the system is in the dynamic-swarm state. For example, the correlation only decays slowly to $\langle \hat{\mathbf{e}}_i \cdot \hat{\mathbf{e}}_j \rangle \approx 0.25$ at $4l_S$. The peak at $\Delta x = l_S$ for two squirmer rods swimming behind each other increases, and a careful inspection of the

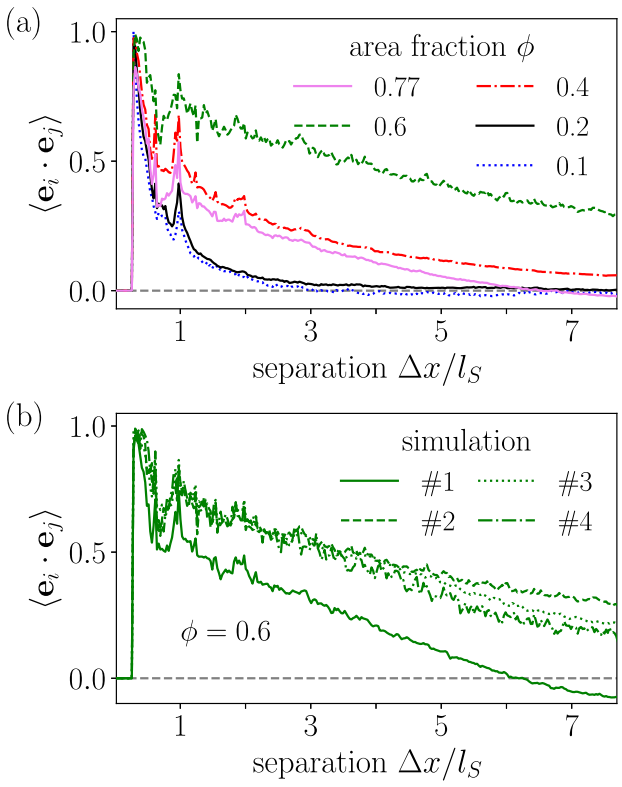

FIG. 8. (a) Orientational pair-correlation function $\langle \hat{\mathbf{e}}_i \cdot \hat{\mathbf{e}}_j \rangle$ of two squirmer rods plotted vs their distance Δx for different global area fractions ϕ. (b) Results of simulation runs with different initial conditions at $\phi = 0.6$ and $\alpha = 3.25$.

curve also shows an additional peak at $\Delta x = 0.62$, twice the side-by-side distance. This agrees with visual inspections, which show that squirmer rods tend to swim in successive rows within a swarm. Furthermore, the very weak peaks at $2l_S$ and $3l_S$ agree with the approximate extension of $R_S \approx 3l_S$ of the dynamic swarms. Note that the alignment is not perfect within clusters, and hence, the correlation reduces with increasing distance.

For the higher area fraction $\phi = 0.6$, the squirmer rods now form a single big swarm. Here, we see a further increase in the strength and range of the orientational correlations. Interestingly, Fig. 8(b) shows that the shape of the correlation function depends on the initial conditions. As described in Sec. II C, for $\phi \geq 0.6$, we only change the orientation randomly along one direction. As a result, in each simulation run, the cluster assumes a different shape and behaves differently. In particular, in the first simulation run the cluster of squirmer rods rotates rather than performing a straight motion as observed in simulation run 2. Thus, the rods at opposite sides of the cluster are anti-parallel to each other, causing the negative correlations $\langle \hat{\mathbf{e}}_i \cdot \hat{\mathbf{e}}_j \rangle$ at distances $\Delta x > 6l_S$. In simulation runs 3 and 4, the configuration of the cluster creates both straight motion and rotation so that it moves on a circle. Thus, the orientational pair-correlation function has an intermediate characteristic.

Increasing the area fraction further to $\phi = 0.77$, the cluster is jammed. Compared to the swarming cluster, the orientational correlations are weaker and of shorter range. This indicates that both local

and global alignments are reduced and swarming does not occur. The system is too dense to allow alignment during swimming, which initiated the swarm formation at lower densities. For $\alpha = 3.25$, the jammed cluster is not entirely stable and can partially break up and reform again, as observed by visual inspection. As a result, the orientational correlation function looks quite similar to that for the swarm state at $\phi = 0.4$. For the larger aspect ratios $\alpha = 4.0$ and $\alpha = 4.75$, the jammed cluster is entirely stable and the orientational correlation function decays to zero at even shorter distances.

For aspect ratios different from $\alpha = 3.25$, the results are qualitatively similar. For smaller aspect ratios, the orientational correlations are expectably lower and decay faster than for higher aspect ratios. For $\alpha > 3.25$, the orientational correlations are stronger at short distances $\Delta x < 2l_S$, especially in the dynamic-swarm state. However, in the single-swarm state, the squirmer rods cannot align as much as before, which results in lower cluster velocities.

VI. CONCLUSIONS AND OUTLOOK

In this article, we have tested the extended MPCD method introduced in our previous article[82] against known cases and also used it to explore the collective dynamics of squirmer rods. As we have demonstrated in Sec. III, the extended MPCD method accurately solves the Navier–Stokes equations in the Stokes limit. In particular, the hydrodynamic multipoles that occur due to the prescribed surface flow field of the pusher-type squirmer are correctly represented in the simulated velocity field. In both, the bulk fluid and Hele-Shaw geometry, the hydrodynamic source dipole and force dipole decay with the correct power law. In the simulations of the bulk fluid, we could also identify the source quadrupole, which becomes noticeable close to the squirmer.

Due to the non-linear equation-of-state, the MPCD fluid of the extended method is less compressible and, therefore, the density, viscosity, and pressure are significantly more uniform compared to traditional MPCD methods. Small variations in the fluid density remain since also in the extended model the fluid density encodes fluid pressure. Nevertheless, squirmer rods with a high aspect ratio $\alpha = 4$ show very similar clustering in both methods, which suggests that steric interactions due to the strongly elongated shape are dominant. To reduce the tendency to align and thereby increase the influence of hydrodynamic interactions, we lowered the aspect ratio to $\alpha = 2.5$. Interestingly, the observed swarming of dynamic clusters is more pronounced with the extended MPCD method. They have higher polar order, are more stable, and form larger clusters. Our understanding is that in a less compressible fluid where the fluid density is not reduced between nearby rods as in the traditional MPCD, the hydrodynamic flow reduces the occurrence of hard collisions, and thereby, the rods have the possibility to better align along each other. This favors the formation of swarms due to the prolonged duration of polar encounters.

Finally, we systematically investigated the collective dynamics of squirmer rods and found four different dynamic states with increasing aspect ratio α and area fraction ϕ, namely, a disordered state, dynamic swarms, a single swarm, and a jammed cluster. Similar states are identified for *B. Subtilis* in the experiments of Ref. 94. The disordered state and a global swarm also exist for spheroidal squirmers.[21] To characterize the dynamic states quantitatively, we determined the distribution of local area fraction $P(\phi_{\mathrm{loc}})$ as a measure for the degree of clustering in the system. Additionally, we identified clusters of squirmer rods and determined their mean velocities, while the intrinsic structure of the swarms was analyzed with the orientational pair-correlation function.

For low density ϕ and aspect ratio α, we observe a disordered state with homogeneous density in which squirmer rods only interact during frequent collisions. Above a critical value of $\alpha \approx 2$ and at larger densities, the squirmer rods form dynamic swarms, where the system clearly separates into a dilute background and very dynamic polar clusters with a broad size distribution. When the density is increased further, the dynamic swarms turn into a single stable swarm. The dilute background of squirmer rods disappears, and the swarm keeps a high polarization. Depending on the initial condition, the swarm can exhibit directed motion, rotation, or a combination of both, which results in a circular trajectory. At the highest density $\phi = 0.77$ in our simulations, the system is so crowded that the formation of highly ordered swarms is inhibited. The rod cluster becomes jammed and moves with a significantly lower velocity compared to the swarms. Our findings show similarities with previous studies[64–67] of dry active rods with different penetrability. In particular, the disordered and also motile cluster or swarming state is found in all systems. These states appear to originate from the rod shape and frequent collisions rather than the particular details of the steric interactions. Additionally, Refs. 64–67 found states of giant clusters of different nature. If particles cannot cross each other, also immobile giant clusters are observed.[65,67] In contrast, the giant clusters in our study are more polar and therefore more motile, which we attribute to the hydrodynamic interactions present in our work. In the case when rods are allowed to cross each other, the tendency to jam is reduced.[66] However, the mechanism for forming giant clusters is now different. Reference 65 adds an interesting study of hydrodynamically interacting flagella of pusher type. Thus, their collective dynamics is less comparable to our system.

In future investigations, we plan to extend our study to the collective dynamics of pusher- and puller-type squirmer rods as introduced in Ref. 17. In addition, it is straightforward to extend the squirmer-rod model to active flexible filaments by adding bending rigidity. This will provide valuable insights how hydrodynamic interactions influence the collective dynamics of active filaments and bridge between dry models[33,95] and models with implicit hydrodynamic interactions,[96,97] on the one hand, and continuum descriptions,[98,99] on the other hand. Clearly, the extended MPCD method will prove beneficial for simulations of dense suspensions of active filaments by providing a less compressible fluid environment in the regime of vanishing Reynolds numbers.

SUPPLEMENTARY MATERIAL

See the supplementary material for additional video files V1–V6, which show the dynamic evolution of the systems shown in Figs. 5(a), 5(b), and 6(b)–6(e), in the order of their occurrence.

ACKNOWLEDGMENTS

We thank Josua Grawitter for helpful discussions on the topic of the manuscript. We also acknowledge financial support from

the Collaborative Research Center 910 funded by the Deutsche Forschungsgemeinschaft.

AUTHOR DECLARATIONS

Conflict of Interest

The authors have no conflicts to disclose.

DATA AVAILABILITY

The data that support the findings of this study are available from the corresponding author upon reasonable request.

REFERENCES

[1] R. Kapral, "Multiparticle collision dynamics: Simulation of complex systems on mesoscales," Adv. Chem. Phys. **140**, 89 (2008).
[2] G. Gompper, T. Ihle, D. Kroll, and R. Winkler, "Multi-particle collision dynamics: A particle-based mesoscale simulation approach to the hydrodynamics of complex fluids," in *Advanced Computer Simulation Approaches for Soft Matter Sciences III* (Springer, 2009), pp. 1–87.
[3] A. Zöttl and H. Stark, "Simulating squirmers with multiparticle collision dynamics," Eur. Phys. J. E **41**, 61 (2018).
[4] A. Malevanets and R. Kapral, "Mesoscopic model for solvent dynamics," J. Chem. Phys. **110**, 8605–8613 (1999).
[5] J. T. Padding and A. A. Louis, "Hydrodynamic and Brownian fluctuations in sedimenting suspensions," Phys. Rev. Lett. **93**, 220601 (2004).
[6] A. Moncho-Jordá, A. A. Louis, and J. T. Padding, "Effects of interparticle attractions on colloidal sedimentation," Phys. Rev. Lett. **104**, 068301 (2010).
[7] M. Yang, A. Wysocki, and M. Ripoll, "Hydrodynamic simulations of self-phoretic microswimmers," Soft Matter **10**, 6208–6218 (2014).
[8] P. Kanehl and H. Stark, "Hydrodynamic segregation in a bidisperse colloidal suspension in microchannel flow: A theoretical study," J. Chem. Phys. **142**, 214901 (2015).
[9] P. Kanehl and H. Stark, "Self-organized velocity pulses of dense colloidal suspensions in microchannel flow," Phys. Rev. Lett. **119**, 018002 (2017).
[10] G. Rückner and R. Kapral, "Chemically powered nanodimers," Phys. Rev. Lett. **98**, 150603 (2007).
[11] I. O. Götze and G. Gompper, "Mesoscale simulations of hydrodynamic squirmer interactions," Phys. Rev. E **82**, 041921 (2010).
[12] P. de Buyl and R. Kapral, "Phoretic self-propulsion: A mesoscopic description of reaction dynamics that powers motion," Nanoscale **5**, 1337–1344 (2013).
[13] A. Zöttl and H. Stark, Phys. Rev. Lett. **112**, 118101 (2014).
[14] J. Blaschke, M. Maurer, K. Menon, A. Zöttl, and H. Stark, Soft Matter **12**, 9821–9831 (2016).
[15] A. Zöttl and J. M. Yeomans, "Enhanced bacterial swimming speeds in macromolecular polymer solutions," Nat. Phys. **15**, 554–558 (2019).
[16] J.-T. Kuhr, F. Rühle, and H. Stark, "Collective dynamics in a monolayer of squirmers confined to a boundary by gravity," Soft Matter **15**, 5685–5694 (2019).
[17] A. W. Zantop and H. Stark, "Squirmer rods as elongated microswimmers: Flow fields and confinement," Soft Matter **16**, 6400–6412 (2020).
[18] F. Rühle and H. Stark, "Emergent collective dynamics of bottom-heavy squirmers under gravity," Eur. Phys. J. E **43**, 26 (2020).
[19] T. Eisenstecken, J. Hu, and R. G. Winkler, "Bacterial swarmer cells in confinement: A mesoscale hydrodynamic simulation study," Soft Matter **12**, 8316–8326 (2016).
[20] M. Wagner and M. Ripoll, "Hydrodynamic front-like swarming of phoretically active dimeric colloids," Europhys. Lett. **119**, 66007 (2017).
[21] M. Theers, E. Westphal, K. Qi, R. G. Winkler, and G. Gompper, "Clustering of microswimmers: Interplay of shape and hydrodynamics," Soft Matter **14**, 8590–8603 (2018).
[22] F. J. Schwarzendahl and M. G. Mazza, "Hydrodynamic interactions dominate the structure of active swimmers' pair distribution functions," J. Chem. Phys. **150**, 184902 (2019).
[23] F. J. Schwarzendahl and M. G. Mazza, "Maximum in density heterogeneities of active swimmers," Soft Matter **14**, 4666–4678 (2018).
[24] A. Malevanets and J. M. Yeomans, "Dynamics of short polymer chains in solution," Europhys. Lett. **52**, 231 (2000).
[25] A. Zöttl and J. M. Yeomans, "Driven spheres, ellipsoids and rods in explicitly modeled polymer solutions," J. Phys.: Condens. Matter **31**, 234001 (2019).
[26] K. Qi, E. Westphal, G. Gompper, and R. G. Winkler, "Enhanced rotational motion of spherical squirmer in polymer solutions," Phys. Rev. Lett. **124**, 068001 (2020).
[27] H. Noguchi and G. Gompper, "Shape transitions of fluid vesicles and red blood cells in capillary flows," Proc. Natl. Acad. Sci. U. S. A. **102**, 14159–14164 (2005).
[28] H. Noguchi and G. Gompper, "Vesicle dynamics in shear and capillary flows," J. Phys.: Condens. Matter **17**, S3439 (2005).
[29] D. Alizadehrad, T. Krüger, M. Engstler, and H. Stark, "Simulating the complex cell design of *Trypanosoma brucei* and its motility," PLoS Comput. Biol. **11**, e1003967 (2015).
[30] S. B. Babu and H. Stark, "Modeling the locomotion of the African trypanosome using multi-particle collision dynamics," New J. Phys. **14**, 085012 (2012).
[31] S. Thutupalli, R. Seemann, and S. Herminghaus, "Swarming behavior of simple model squirmers," New J. Phys. **13**, 073021 (2011).
[32] J. Gachelin, A. Rousselet, A. Lindner, and E. Clement, "Collective motion in an active suspension of *Escherichia coli* bacteria," New J. Phys. **16**, 025003 (2014).
[33] Ö. Duman, R. E. Isele-Holder, J. Elgeti, and G. Gompper, "Collective dynamics of self-propelled semiflexible filaments," Soft Matter **14**, 4483–4494 (2018).
[34] V. Schaller, C. Weber, C. Semmrich, E. Frey, and A. R. Bausch, "Polar patterns of driven filaments," Nature **467**, 73–77 (2010).
[35] H. Wioland, F. G. Woodhouse, J. Dunkel, J. O. Kessler, and R. E. Goldstein, "Confinement stabilizes a bacterial suspension into a spiral vortex," Phys. Rev. Lett. **110**, 268102 (2013).
[36] D. Khoromskaia and G. P. Alexander, "Vortex formation and dynamics of defects in active nematic shells," New J. Phys. **19**, 103043 (2017).
[37] Y. Sumino, K. H. Nagai, Y. Shitaka, D. Tanaka, K. Yoshikawa, H. Chaté, and K. Oiwa, "Large-scale vortex lattice emerging from collectively moving microtubules," Nature **483**, 448–452 (2012).
[38] T. Sánchez, D. T. N. Chen, S. J. DeCamp, M. Heymann, and Z. Dogic, Nature **491**, 431 (2012).
[39] S. J. DeCamp, G. S. Redner, A. Baskaran, M. F. Hagan, and Z. Dogic, "Orientational order of motile defects in active nematics," Nat. Mater. **14**, 1110–1115 (2015).
[40] F. C. Keber, E. Loiseau, T. Sanchez, S. J. DeCamp, L. Giomi, M. J. Bowick, M. C. Marchetti, Z. Dogic, and A. R. Bausch, "Topology and dynamics of active nematic vesicles," Science **345**, 1135–1139 (2014).
[41] H. H. Wensink, J. Dunkel, S. Heidenreich, K. Drescher, R. E. Goldstein, H. Löwen, and J. M. Yeomans, Proc. Natl. Acad. Sci. U. S. A. **109**, 14308 (2012).
[42] J. Dunkel, S. Heidenreich, K. Drescher, H. H. Wensink, M. Bär, and R. E. Goldstein, "Fluid dynamics of bacterial turbulence," Phys. Rev. Lett. **110**, 228102 (2013).
[43] P. Guillamat, J. Ignés-Mullol, and F. Sagués, "Taming active turbulence with patterned soft interfaces," Nat. Commun. **8**, 564 (2017).
[44] A. Doostmohammadi, T. N. Shendruk, K. Thijssen, and J. M. Yeomans, "Onset of meso-scale turbulence in active nematics," Nat. Commun. **8**, 15326 (2017).
[45] D. Nishiguchi, I. S. Aranson, A. Snezhko, and A. Sokolov, "Engineering bacterial vortex lattice via direct laser lithography," Nat. Commun. **9**, 4486 (2018).
[46] V. M. Worlitzer, G. Ariel, A. Be'er, H. Stark, M. Bär, and S. Heidenreich, "Motility-induced clustering and meso-scale turbulence in active polar fluids," New J. Phys. **23**, 033012 (2021).
[47] H. Reinken, D. Nishiguchi, S. Heidenreich, A. Sokolov, M. Bär, S. H. Klapp, and I. S. Aranson, "Organizing bacterial vortex lattices by periodic obstacle arrays," Commun. Phys. **3**, 76 (2020).
[48] H. Reinken, S. H. Klapp, M. Bär, and S. Heidenreich, "Derivation of a hydrodynamic theory for mesoscale dynamics in microswimmer suspensions," Phys. Rev. E **97**, 022613 (2018).
[49] S. Heidenreich, J. Dunkel, S. H. Klapp, and M. Bär, "Hydrodynamic length-scale selection in microswimmer suspensions," Phys. Rev. E **94**, 020601 (2016).

[50]J. Toner and Y. Tu, "Long-range order in a two-dimensional dynamical XY model: How birds fly together," Phys. Rev. Lett. **75**, 4326 (1995).
[51] J. Swift and P. C. Hohenberg, "Hydrodynamic fluctuations at the convective instability," Phys. Rev. A **15**, 319 (1977).
[52]D. L. Koch and G. Subramanian, "Collective hydrodynamics of swimming microorganisms: Living fluids," Annu. Rev. Fluid Mech. **43**, 637–659 (2011).
[53]M. C. Marchetti, J.-F. Joanny, S. Ramaswamy, T. B. Liverpool, J. Prost, M. Rao, and R. A. Simha, "Hydrodynamics of soft active matter," Rev. Mod. Phys. **85**, 1143 (2013).
[54]N. Yoshinaga and T. B. Liverpool, "Hydrodynamic interactions in dense active suspensions: From polar order to dynamical clusters," Phys. Rev. E **96**, 020603 (2017).
[55]C. Hoell, H. Löwen, and A. M. Menzel, "Particle-scale statistical theory for hydrodynamically induced polar ordering in microswimmer suspensions," J. Chem. Phys. **149**, 144902 (2018).
[56]M. Bär, R. Großmann, S. Heidenreich, and F. Peruani, "Self-propelled rods: Insights and perspectives for active matter," Annu. Rev. Condens. Matter Phys. **11**, 441–466 (2019).
[57]M. R. Shaebani, A. Wysocki, R. G. Winkler, G. Gompper, and H. Rieger, "Computational models for active matter," Nat. Rev. Phys. **2**, 181–199 (2020).
[58]T. Vicsek, A. Czirók, E. Ben-Jacob, I. Cohen, and O. Shochet, "Novel type of phase transition in a system of self-driven particles," Phys. Rev. Lett. **75**, 1226 (1995).
[59]G. Grégoire and H. Chaté, "Onset of collective and cohesive motion," Phys. Rev. Lett. **92**, 025702 (2004).
[60]H. Chaté, F. Ginelli, G. Grégoire, F. Peruani, and F. Raynaud, "Modeling collective motion: Variations on the Vicsek model," Eur. Phys. J. B **64**, 451–456 (2008).
[61] H. H. Wensink and H. Löwen, "Emergent states in dense systems of active rods: From swarming to turbulence," J. Phys.: Condens. Matter **24**, 464130 (2012).
[62]R. Großmann, P. Romanczuk, M. Bär, and L. Schimansky-Geier, "Vortex arrays and mesoscale turbulence of self-propelled particles," Phys. Rev. Lett. **113**, 258104 (2014).
[63]M. C. Bott, F. Winterhalter, M. Marechal, A. Sharma, J. M. Brader, and R. Wittmann, "Isotropic-nematic transition of self-propelled rods in three dimensions," Phys. Rev. E **98**, 012601 (2018).
[64]F. Peruani, A. Deutsch, and M. Bär, "Nonequilibrium clustering of self-propelled rods," Phys. Rev. E **74**, 030904 (2006).
[65]Y. Yang, V. Marceau, and G. Gompper, "Swarm behavior of self-propelled rods and swimming flagella," Phys. Rev. E **82**, 031904 (2010).
[66]M. Abkenar, K. Marx, T. Auth, and G. Gompper, "Collective behavior of penetrable self-propelled rods in two dimensions," Phys. Rev. E **88**, 062314 (2013).
[67]S. Weitz, A. Deutsch, and F. Peruani, "Self-propelled rods exhibit a phase-separated state characterized by the presence of active stresses and the ejection of polar clusters," Phys. Rev. E **92**, 012322 (2015).
[68]M. Hennes, K. Wolff, and H. Stark, "Self-induced polar order of active Brownian particles in a harmonic trap," Phys. Rev. Lett. **112**, 238104 (2014).
[69]H. Jeckel, E. Jelli, R. Hartmann, P. K. Singh, R. Mok, J. F. Totz, L. Vidakovic, B. Eckhardt, J. Dunkel, and K. Drescher, "Learning the space-time phase diagram of bacterial swarm expansion," Proc. Natl. Acad. Sci. U. S. A. **116**, 1489–1494 (2019).
[70]J. de Graaf, H. Menke, A. J. T. M. Mathijssen, M. Fabritius, C. Holm, and T. N. Shendruk, "Lattice-Boltzmann hydrodynamics of anisotropic active matter," J. Chem. Phys. **144**, 134106 (2016).
[71] A. Pandey, P. B. Sunil Kumar, and R. Adhikari, "Flow-induced nonequilibrium self-assembly in suspensions of stiff, apolar, active filaments," Soft Matter **12**, 9068–9076 (2016).
[72]M. Kuron, P. Stärk, C. Burkard, J. De Graaf, and C. Holm, "A lattice Boltzmann model for squirmers," J. Chem. Phys. **150**, 144110 (2019).
[73]Z. Ouyang and J. Lin, "The hydrodynamics of an inertial squirmer rod," Phys. Fluids **33**, 073302 (2021).
[74]C.-C. Huang, G. Gompper, and R. G. Winkler, "Hydrodynamic correlations in multiparticle collision dynamics fluids," Phys. Rev. E **86**, 056711 (2012).
[75]A. Lamura, G. Gompper, T. Ihle, and D. M. Kroll, "Multi-particle collision dynamics: Flow around a circular and a square cylinder," Europhys. Lett. **56**, 319 (2001).
[76]D. A. Reid, H. Hildenbrandt, J. T. Padding, and C. K. Hemelrijk, "Flow around fishlike shapes studied using multiparticle collision dynamics," Phys. Rev. E **79**, 046313 (2009).
[77]S. B. Babu and H. Stark, "Dynamics of semi-flexible tethered sheets," Eur. Phys. J. E **34**, 1–7 (2011).
[78]E. Westphal, S. P. Singh, C.-C. Huang, G. Gompper, and R. G. Winkler, "Multiparticle collision dynamics: GPU accelerated particle-based mesoscale hydrodynamic simulations," Comput. Phys. Commun. **185**, 495–503 (2014).
[79]M. P. Howard, A. Z. Panagiotopoulos, and A. Nikoubashman, "Efficient mesoscale hydrodynamics: Multiparticle collision dynamics with massively parallel GPU acceleration," Comput. Phys. Commun. **230**, 10–20 (2018).
[80]E. Tüzel, M. Strauss, T. Ihle, and D. M. Kroll, "Transport coefficients for stochastic rotation dynamics in three dimensions," Phys. Rev. E **68**, 036701 (2003).
[81] T. Eisenstecken, R. Hornung, R. G. Winkler, and G. Gompper, "Hydrodynamics of binary-fluid mixtures—An augmented multiparticle collison dynamics approach," Europhys. Lett. **121**, 24003 (2018).
[82]A. W. Zantop and H. Stark, "Multi-particle collision dynamics with a non-ideal equation of state. I," J. Chem. Phys. **154**, 024105 (2021).
[83]J.-P. Hansen and I. R. McDonald, *Theory of Simple Liquids* (Elsevier, 1990).
[84]E. Tüzel, T. Ihle, and D. M. Kroll, "Constructing thermodynamically consistent models with a non-ideal equation of state," Math. Comput. Simul. **72**, 232–236 (2006).
[85]T. Ihle, E. Tüzel, and D. M. Kroll, "Consistent particle-based algorithm with a non-ideal equation of state," Europhys. Lett. **73**, 664 (2006).
[86]T. Ihle and D. M. Kroll, "Stochastic rotation dynamics: A Galilean-invariant mesoscopic model for fluid flow," Phys. Rev. E **63**, 020201 (2001).
[87]T. Ishikawa, M. P. Simmonds, and T. J. Pedley, J. Fluid Mech. **568**, 119–160 (2006).
[88]M. T. Downton and H. Stark, J. Phys.: Condens. Matter **21**, 204101 (2009).
[89]J. D. Weeks, D. Chandler, and H. C. Andersen, "Role of repulsive forces in determining the equilibrium structure of simple liquids," J. Chem. Phys. **54**, 5237–5247 (1971).
[90]A. J. T. M. Mathijssen, A. Doostmohammadi, J. M. Yeomans, and T. N. Shendruk, "Hydrodynamics of micro-swimmers in films," J. Fluid Mech. **806**, 35–70 (2016).
[91] N. Liron and S. Mochon, "Stokes flow for a stokeslet between two parallel flat plates," J. Eng. Mech. **10**, 287–303 (1976).
[92]I. Theurkauff, C. Cottin-Bizonne, J. Palacci, C. Ybert, and L. Bocquet, "Dynamic clustering in active colloidal suspensions with chemical signaling," Phys. Rev. Lett. **108**, 268303 (2012).
[93]O. Pohl and H. Stark, "Dynamic clustering and chemotactic collapse of self-phoretic active particles," Phys. Rev. Lett. **112**, 238303 (2014).
[94]A. Be'er, B. Ilkanaiv, R. Gross, D. B. Kearns, S. Heidenreich, M. Bär, and G. Ariel, "A phase diagram for bacterial swarming," Commun. Phys. **3**, 66 (2020).
[95]R. G. Winkler, J. Elgeti, and G. Gompper, "Active polymers—Emergent conformational and dynamical properties: A brief review," J. Phys. Soc. Jpn. **86**, 101014 (2017).
[96]A. Martín-Gómez, T. Eisenstecken, G. Gompper, and R. G. Winkler, "Active Brownian filaments with hydrodynamic interactions: Conformations and dynamics," Soft Matter **15**, 3957–3969 (2019).
[97]H. Jiang and Z. Hou, "Motion transition of active filaments: Rotation without hydrodynamic interactions," Soft Matter **10**, 1012–1017 (2014).
[98]J. Prost, F. Jülicher, and J.-F. Joanny, "Active gel physics," Nat. Phys. **11**, 111–117 (2015).
[99]T. B. Liverpool and M. C. Marchetti, "Bridging the microscopic and the hydrodynamic in active filament solutions," Europhys. Lett. **69**, 846 (2005).

Soft Matter

PAPER

Cite this: *Soft Matter*, 2022, **18**, 6179

Emergent collective dynamics of pusher and puller squirmer rods: swarming, clustering, and turbulence†

Arne W. Zantop * and Holger Stark *

Received 8th April 2022,
Accepted 30th June 2022

DOI: 10.1039/d2sm00449f

rsc.li/soft-matter-journal

We study the interplay of steric and hydrodynamic interactions in suspensions of elongated microswimmers by simulating the full hydrodynamics of squirmer rods in the quasi two-dimensional geometry of a Hele-Shaw cell. To create pusher or puller-type squirmer rods, we concentrate the surface slip-velocity field more to the back or to the front of the rod and thereby are able to tune the rod's force-dipole strength. We study a wide range of aspect ratios and area fractions and provide corresponding state diagrams. The flow field of pusher-type squirmer rods destabilizes ordered structures and favors the disordered state at small area fractions and aspect ratios. Only when steric interactions become relevant, we observe a turbulent and dynamic cluster state, while for large aspect ratios a single swarm and jammed cluster occurs. The power spectrum of the turbulent state shows two distinct energy cascades at small and large wave numbers with power-law scaling and non-universal exponents. Pullers show a strong tendency to form swarms instead of the disordered state found for neutral and pusher rods. At large area fractions a dynamic cluster is observed and at larger aspect ratio a single swarm or jammed cluster occurs.

1 Introduction

Microscopic unicellular organisms make up a major fraction of all life forms on our planet. They are involved in important natural processes such as photosynthesis[1–3] or industrial processes such as the production of enzymes[4,5] or biofuels,[6–8] or the recycling of wastewater.[9,10] Especially in photosynthesis, commonly viewed as the basis of life, unicellular phytoplankton accomplish about half of the worldwide natural turnover.[2,3] However, still many aspects of the behavior of unicellular organisms is not completely understood. In fact, many of these life forms are self-propelling microswimmers,[11–13] as, for example, the algae *C. reinhardtii*[14,15] or the bacterium *E. coli*.[16–18] From the perspective of physicists, their active motion gives rise to very interesting new collective phenomena. In this article we study the rich emergent collective dynamics of rod-shaped model microswimmers, which we can tune between the pusher and puller type.

Active motion is always performed in non-equilibrium and, therefore, gives rise to new and interesting phenomena. For example, specially designed boundaries can rectify the random motion of active particles,[19–23] or under gravity active particles develop polar order and even show inverted sedimentation profiles when they are bottom-heavy.[24,25] In addition, microswimmer suspensions are subject to long-range hydrodynamic interactions with characteristic power-law decay.[13,26,27] But also short-range steric interactions play an important role, in particular, for elongated particles, which align along each other.[12] The combination of these interactions gives rise to numerous interesting dynamic patterns. Common examples are the formation of swarms or flocks,[28–32] convection rolls and plumes,[25] fluid pumps,[33,34] vortices,[35–38] active nematic patterns,[39–41] and the emergence of the so-called active turbulence,[42,43] termed in analogy to classical inertial turbulence.[44,45] However, contrary to classical turbulence, where fluid flow is driven on the macroscopic scale, active turbulence is generated at the microscopic scale of the self-propelled particles and then energy is dissipated on larger scales. This mechanism causes a characteristic length scale for the formation of vortices and patterns, which is in contrast to the scale invariance of classical turbulence.[46–48] In particular, the specific model parameters now determine the scaling of the velocity power spectrum, which is no longer universal.[48–50] Active turbulence is found for microswimmers,[51,52] active bio-filaments, which exist in the cytoplasm,[39,53] and in growing tissue.[54,55]

Institut für Theoretische Physik, Technische Universität Berlin, Hardenbergstraße 36, 10623 Berlin, Germany. E-mail: a.zantop@tu-berlin.de, holger.stark@tu-berlin.de

† Electronic supplementary information (ESI) available: We provide eight videos of different collective dynamic states in the top view. Videos 1–3 show pusher rods in the turbulent (1), single swarm (2) and dynamic cluster state (3). Videos 4–8 show puller rods in the swarming (4 and 8), single swarm (5), jammed cluster (6), and dynamic cluster state (7). See DOI: https://doi.org/10.1039/d2sm00449f

On the theoretical side, the dynamics of active particles has been investigated at different levels of description. While the celebrated Vicsek model[56–58] uses coarse-grained alignment rules, also models with explicit steric interactions exist.[42,51,59–64] These models have also been generalized to active filaments[31,65,66] and models, which implicitly include hydrodynamic interactions.[67,68] Models, which directly simulate fluid flow and thereby explicitly include hydrodynamic interactions, use the method of multi-particle collision dynamics (MPCD)[25,30,32,69–79] or the lattice-Boltzmann method.[80–83] Continuum models combine elements of the Toner-Tu[84] and Swift-Hohenberg[85] equations to generate hydrodynamic equations for active suspensions.[46,86,87] Microswimmers are also distinguished by their swimming mechanisms and the flow field, they generate in the surrounding fluid.[11,13] While some microorganisms propel with cilia located all over their surface, common bacteria and algae propel with flagella that extent from the front or back of the cell body. In the first case, the flow field of a source dipole is realized, which decays as r^{-3}, while bacteria and algae are termed pusher or puller-type swimmers that generate a long-range force-dipole flow field, which decays as r^{-2}.[13,27] The specific form of these hydrodynamic multipole flow fields determines the collective dynamics of the microswimmers.[32,69,74,88–90]

In this context, we proposed in ref. 76 the squirmer rod as a realistic microscopic model for elongated microswimmers. It consists of overlapping squirmers and thereby extends the well-known spherical squirmer model for ciliary propulsion[26,91] and its implementation in MPCD.[92] Restricting the surface slip-velocity to the front or the back of the squirmer rod, puller and pusher-type squirmer rods can be realized, respectively. The hydrodynamic flow field is simulated using an efficient implementation of MPCD with a reduced compressibility such that also collective dynamics in large and dense systems can be studied.[93] Most recently, we presented the state diagram of neutral squirmer rods and identified with increasing area fraction and depending on the aspect ratio of the rods the disordered state, dynamic swarms, a single swarm, and ultimately a jammed cluster.[94]

In this article we generalize the squirmer-rod model to pushers and pullers with tunable force-dipole strength in the flow field. Compared to spheroidal squirmers it has the advantage that it better approximates real rodlike microswimmers such as *E. coli*. Using this model, we provide a comprehensive study of the state diagram for hydrodynamically interacting microswimmers over a wide range of aspect ratios, densities, and force-dipole strengths as the state diagrams in Fig. 3(a), 7(a) and 9(a) show. Hereby, we go well beyond previous works, which focused mainly on more dilute systems[95,96] or a single aspect ratio.[97] Thus, our work provides an overall view how hydrodynamics and shape determine the dynamic states of microswimmers. For example, our particle-based model nicely illustrates that the active turbulent state occurs as a compromise between the disordering hydrodynamic pusher–pusher interactions and aligning steric interactions. We also demonstrate that the two distinct energy cascades at low and large wave numbers in the power spectral density of velocity fluctuations exhibits non-universal exponents. Moreover, we find a dynamic cluster state at large densities. Besides this state all other states are also found in dry active rods.[98] But, in our case, they have a specific contribution from hydrodynamics as, for example, the turbulent and swarming states show. The overall appearance of the states in our state diagrams can be summarized as follows. For pushers we observe that the swarming states of neutral squirmer rods are destabilized. Instead, for smaller aspect ratio between the disordered and dynamic cluster state, we observe the turbulent state as already mentioned. At high aspect ratios, where steric interactions become more relevant, we recover the single swarm and jammed cluster state of neutral squirmer rods. For pullers, hydrodynamic interactions stabilize the swarming state even for our smallest area fraction. Thus, compared to neutral squirmer rods, states are shifted towards lower densities. Variation of the force-dipole strength at constant aspect ratio supports all these findings.

The article is organized as follows. In Section 2 we give a brief overview of the methods used in this paper. Section 3 provides a detailed study of the different dynamic states of the squirmer rods as a function of their area fraction, aspect ratio, and force-dipole strength. We end with a summary and conclusions in Section 4.

2 System and methods

We first introduce the squirmer-rod model and then summarize some details of the method of multi-particle collision dynamics, which we use to simulate the flow fields generated by the squirmer rods.

2.1 Model of the squirmer rod

To model shape-anisotropic microswimmers, we employ the squirmer rod model as introduced in our previous work.[76] Squirmer rods consist of N_{sq} overlapping spherical squirmers of radius R_{sq}, arranged on a line to form a single rigid body [see Fig. 1(a)]. By varying the distance d between neighboring squirmers, we can tune the aspect ratio of the squirmer rod, $\alpha = l_S/2R$, where l_S is the rod length. However, we do not exceed a distance of $d \approx 0.8R$ so that the surface of the rod is sufficiently smooth. With a number of $N_{sq} = 10$ squirmers in this work, this amounts to a maximum aspect ratio of $\alpha \approx 5$, which closely resembles the aspect ratio of bacteria such as *E. coli* or *B. subtilis*.

The squirmer rods propel through the axisymmetric and tangential slip velocity field at the surface of individual spherical squirmers,

$$\mathbf{v}_s = B_1^s[(\hat{\mathbf{e}}\cdot\hat{\mathbf{x}}_s)\hat{\mathbf{x}}_s - \hat{\mathbf{e}}], \quad (1)$$

which is imposed on the surrounding fluid.[26,92] Here, $\hat{\mathbf{e}}$ is the rod axis and $\hat{\mathbf{x}}_s$ the unit vector pointing from the center of a squirmer to a point on the squirmer surface. This generates a source-dipole flow field, which is a higher-order singular solution of the Stokes equations $\eta\nabla^2\mathbf{v} = \nabla p$ together with the incompressibility condition $\nabla\cdot\mathbf{v} = 0$, that govern fluid flow at

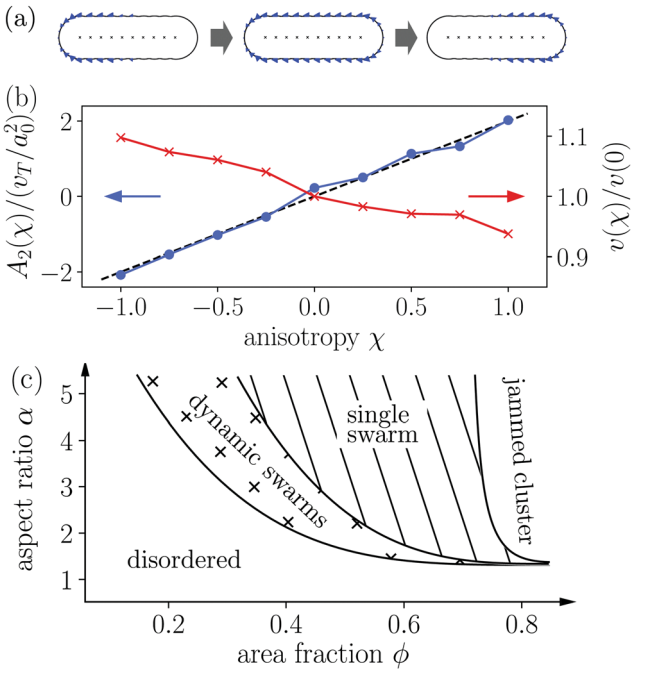

Fig. 1 (a) Sketch of the surface slip velocity of three squirmer rods with respective swimmer-type parameters $\chi = -1$, 0, and 1 (from left to right). The arrows within the squirmer rods indicate the swimming direction $\hat{\mathbf{e}}$. The parameter $\chi \in \{-1, 1\}$ can be used to smoothly vary the type of the squirmer rod from pusher to neutral to puller. (b) Force-dipole coefficient $A_2(\chi)$ (blue) and active velocity $v(\chi)/v(0)$ (red) as a function of the swimmer parameter χ. (c) Schematic state diagram for neutral squirmer rods adapted from ref. 94.

the microscale. Here, $\mathbf{v}$ and p are the respective fluid velocity and pressure fields, and η is the dynamic shear viscosity. The strength B_1^s controls the swimming velocity $v_0 = 2/3B_1^s$ of the spherical squirmer and hence of the squirmer rod. In ref. 76 we showed that the swimming velocity of the squirmer rods $v \approx 1.2v_0$ slightly exceeds the velocity of a single spherical squirmer. Additionally, the velocity of the rods varies by 10% in the range of aspect ratios used in this article. Although the increased velocity at the larger aspect ratios might augment clustering, we assume the effect to be negligible.

As described so far, the surface slip velocity of the squirmer rod resembles ciliated microorganisms such as *Paramecium*. In this realization, the profile of the slip velocity generates a flow field in the surrounding fluid, the far field of which can be described by a source dipole and an additional force quadrupole singularity, which both decay with $|\mathbf{u}_{sd}|, |\mathbf{u}_{fq}| \sim r^{-3}$, as we show in ref. 76.

However, other prominent microswimmers such as *E. coli* bacteria or *Chlamydomonas* algae propel by rotating or beating flagella that extent from the back or the front of their bodies, respectively. These modes of propulsion create a pair of opposing forces that generate the more long-ranged force-dipole flow field $|\mathbf{u}_{fd}| \sim r^{-2}$. To generalise the squirmer rod model to these pusher and puller-type microswimmers, we concentrate the surface slip velocity either to the back or the front of the squirmer rod [see Fig. 1(a)]. This is done by multiplying the surface flow field with the envelope function

$$f(\mathbf{x}_s^* \cdot \hat{\mathbf{e}}, \chi) = 1 + \chi \tanh(10\mathbf{x}_s^* \cdot \hat{\mathbf{e}}/l_S), \quad (2)$$

where $\mathbf{x}_s^*$ points from the rod center to a location on the rod surface. The parameter $\chi \in [-1, 1]$ determines the swimmer type and force-dipole strength, such that for $\chi < 0$ a pusher-type swimmer is realised and likewise a puller-type swimmer for $\chi > 0$. For either $\chi = -1$ or $\chi = 1$ this modification leads to a completely passive half of the rods [see Fig. 1(a)], while for intermediate values the relative contributions of the source dipole and force dipole to the flow field vary. For $\chi = 0$, the model again resembles the neutral squirmer rod.

In the present work, we consider the collective dynamics of squirmer rods confined between two parallel walls. In this so-called Hele-Shaw cell the radial decays of hydrodynamic multipoles are modified compared to the bulk fluid, such that the confined source dipole and force dipole decay as $|\tilde{\mathbf{u}}_{sd}| \sim \rho^{-2}$ and $|\tilde{\mathbf{u}}_{fd}| \sim \rho^{-3}$, respectively, where ρ is the polar distance[76,99] (see appendix of ref. 99). As a consequence, the source dipole has the longest range in the flow field and ultimately dominates the far field. However, already in our previous work we realized that a distance of $\Delta z = 6R$ between the walls, which we will use in our simulations, alters the relative strength of the source and force dipoles.[76] As a consequence, the force dipole dominates the flow field at short and medium distance as we will demonstrate in Section 3.2.

2.2 Method of multi-particle collision dynamics

To model the fluid flow in our simulations, we employ the meso-scale simulation technique of multi-particle collision dynamics (MPCD).[100–102] The MPCD method is particularly suited for solving the Navier–Stokes equations at the micro-scale, because it includes thermal fluctuations and is straightforward to implement boundary conditions for complex geometries.

The MPCD method uses a sequence of streaming and collision steps of the point-like fluid particles. In the streaming step the fluid particles move ballistically with their velocities during time step Δt. Then, the simulation box is divided into cubic cells with edge length a_0 and the velocities of the fluid particles in one cell are modified randomly but keeping the mean velocity or linear momentum fixed. In this work, we use a collision rule optimized to achieve a low compressibility of the fluid.[93] As in other MPCD methods, it includes angular momentum conservation and a thermostat. By choosing the MPCD fluid density $n_0 = 20/a_0^3$, *i.e.*, on average 20 fluid particles per cell, and the time step $\Delta t = 0.005a_0\sqrt{m_0/k_B T_0}$, we obtain a fluid viscosity of $\eta = 16.05\sqrt{m_0 k_B T_0}/a_0^2$, which is comparable to previous work.[74,76,96] Here, m_0 is the mass of one fluid particle.

The immersed squirmer rods are modeled with the mass density of the fluid $\rho_0 = m_0 n_0$. The radius of the constituting squirmers is chosen as $R_{sq} = 3a_0$ and the strength of the surface slip velocity as $B_1^s = 0.1$, which results in a Péclet number of Pe ≈ 350.[94] Steric repulsion is realized with a Weeks–Chandler–Andersen

potential[103] that acts between two squirmers of different rods. To ensure that there is no significant overlap between two squirmer rods, we choose a strong force constant $\varepsilon_{WCA} \approx 10^4 k_B T$.

The squirmer rods move because they acquire momentum from the surrounding fluid. In the MPCD streaming step, linear and angular momentum is transferred to the squirmer rod by collisions with the fluid particles. We achieve this by applying the so-called bounce back rule, which we also modify accordingly to implement the slip velocity in eqn (1) on the surface of the squirmer rods.[100,101] Squirmer rods also contain so-called "ghost" particles, which improve the implementation of no-slip boundary conditions.[101] During the MPCD collision step, they exchange momentum with the fluid, which is ascribed to the squirmer rod. Lastly, the equations of motion for the squirmer rods are integrated with a refined time step of $\delta t_{MD} = \Delta t/3$ using a symplectic splitting algorithm for rigid body molecular dynamics.[104]

For our simulations we use two different geometries. To determine how the force dipole strength A_2 depends on the swimmer-type parameter χ, we use a cubic box of linear size $L = 100a_0$ with periodic boundary conditions along all spatial directions. In this case we use the time $10^4\Delta t$ to equilibrate the MPCD fluid flow fields and then average the fluctuating flow fields over additional $5 \times 10^5 \Delta t$ time steps during simulations.

To simulate the collective dynamics of the squirmer rods, we consider the quasi two-dimensional geometry of a Hele-Shaw cell of linear size $L = 300a_0$ in the x and y direction. Along the z direction the system is confined by walls separated by a distance $\Delta z = 6R$ to mimic the experimental setups using microfluidic chambers[51,105] or liquid–oil interfaces.[106,107] It has also been used in previous work.[94,97] Additionally, this realization guarantees a strong contribution of the force-dipole interaction in the near field, as we will show in Section 3.2 and Fig. 2. In the x and y direction periodic boundary conditions are employed. In this geometry, the N squirmer rods are confined to only move in the midplane of the Hele-Shaw cell by a strong harmonic potential. The rods' initial positions are generated randomly for area fractions $\phi = NA_{sw}/L^2 < 0.6$, where A_{sw} is the two-dimensional cross section of one squirmer rod. For $\phi \geq 0.6$ squirmer rods are placed on a rectangular lattice, all with a randomly chosen orientation either parallel or anti-parallel to one of the major axis of the unit cell. We simulate for a time of $10^7\Delta t$ while saving snapshots every $2500\Delta t$ for further analysis. To ensure that the system is equilibrated, we omit the first 100 snapshots from the analysis.

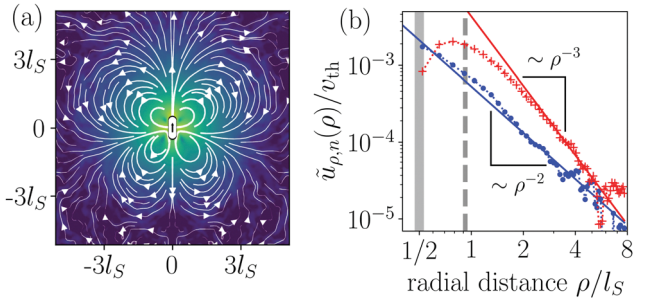

Fig. 2 Hydrodynamic flow field around a pusher-type squirmer rod ($\chi = -1.0$) swimming in the Hele-Shaw geometry with cell height $\Delta z = 6R$. (a) Flow field in the mid plane of the Hele-Shaw cell. The force dipole clearly dominates the near field. (b) Radial components $\tilde{u}_{\rho,n}(\rho)$ of the leading source-dipole (blue) and force-dipole (red) flow fields. They are normalized by the thermal velocity of fluid particles, $v_{th} = \sqrt{k_B T/m_0}$.

To improve statistics in the study of the emergent turbulent patterns of pusher-type squirmer rods, we perform two additional simulation runs for all turbulent states and their neighboring points in the (α, ϕ) parameter space. Furthermore, for all these cases we also perform three simulation runs with an increased system size of $L = 600a_0$ to investigate finite-size effects.

3 Results

In the following we report on our simulation results. First, we show that the anisotropy parameter χ of the surface slip-velocity field is directly proportional to the strength of the hydrodynamic force-dipole field and we illustrate the flow field of a single pusher-type squirmer rod in the Hele-Shaw cell. Then, we thoroughly discuss the state diagrams of the strongest pusher rod ($\chi = -1$) and the strongest puller rod ($\chi = 1$) depending on aspect ratio α and area fraction ϕ. We describe the different states using the velocity pair-correlation function, the power spectral density of the velocity fluctuations, and the orientational autocorrelation function. Finally, for a specific aspect ratio α, we show the state diagram in the space of χ *versus* ϕ.

3.1 Variation of the swimmer-type parameter χ

To extract the force-dipole coefficient A_2 from the flow field of the squirmer rod in the 3D bulk fluid, we follow the method described in detail in our previous article ref. 76. To do so, we consider the expansion of an axisymmetric flow field into a series of hydrodynamic multipoles $\mathbf{u}(\mathbf{r}) = \mathbf{u}_{FD}(\mathbf{r}) + \mathbf{u}_{SD}(\mathbf{r}) + \mathbf{u}_{FQ}(\mathbf{r}) + \ldots$, where the leading-order multipoles are the force dipole, source dipole, and force quadrupole, respectively. The radial velocity component with the general form $u_r(r,\theta) = \sum_{n=1}^{\infty} \left(A_n r^{-n} + B_n r^{-n-2}\right) P_n(\cos\theta)$ is measured from the simulations and then projected on the second Legendre polynomial $P_2(\cos\theta)$. From the resulting polynomial $\frac{5}{2}\int_0^\pi u_r(r,\theta) P_2(\cos\theta) \sin\theta \mathrm{d}\theta = A_2 r^{-2} + B_2 r^{-4}$, we determine the force-dipole coefficient A_2 by a polynomial fit in r^{-1}.

Indeed, we find a linear relation of the swimmer-type parameter χ and the force-dipole coefficient $\chi \sim A_2$ [Fig. 1(b)]. This is expected since the terminal values of the envelope function $f(x)$ in eqn (2), which determine the strength of the force dipole, are linear in χ. Furthermore, we find that due to the definition of the envelope function with $\langle f(x) \rangle = 1$, the swimming velocity is nearly independent of χ [*cf.* Fig. 1(b), red curve].

3.2 Force-dipole flow fields in the Hele-Shaw geometry

As already explained, our study of the collective dynamics of the squirmer rods is performed in a Hele-Shaw cell, which alters

the radial decay of the multipole far fields but also their strengths depends on the cell height Δz.[76,99] Thus, the multipole expansion for the radial component of the flow field becomes $\tilde{u}_\rho(\rho,\varphi) = \sum_{n=1}^{\infty} (\mathscr{A}_n + \mathscr{B}_n)\rho^{-(n+1)}\cos(n\varphi)$ for a microswimmer oriented along the x-axis.[76] Force multipoles dissipate momentum at the bounding walls, which increases for smaller Δz, *i.e.*, when they are closer to the walls.[99,108] In our notation this means that the coefficient of the force dipole in the Hele-Shaw cell scales as $\mathscr{A}_2 \sim A_2\Delta z$ with respect to the bulk coefficient A_2. In contrast, the fluid mass flux initiated by a point source in the Hele-Shaw geometry is distributed in a volume that is proportional to the cell height Δz. Hence, the coefficient of the source dipole, as all the other source multipoles, scales as $\mathscr{B}_2 \sim B_2/\Delta z$.[76,99]

Fig. 2(a) shows the flow field of a pusher-type squirmer rod ($\chi = -1.0$, $\alpha = 3.25$) swimming in Hele-Shaw geometry with wall distance $\Delta z = 6R$. The force-dipole field visibly dominates the flow field with its characteristic outwards directed streamlines along the rod and inwards directed streamlines at the side. From the simulated flow field, we extracted the radial parts of different hydrodynamic multipoles $\tilde{u}_{\rho,n}(\rho)$ following our previous work,[76] and arrived at the curves shown in Fig. 2(b). The radial part of the force dipole $\sim\rho^{-3}$ (red symbols) dominates the flow field up to a distance of *circa* $8l_S$, where it is exceeded by the more long-ranged field of the source dipole $\sim\rho^{-2}$ (blue symbols). For smaller cell heights Δz, this crossover occurs at smaller distances. Since we are interested in exploring the effect of the hydrodynamic force dipole, we keep $\Delta z = 6R$ for the rest of this work, such that the force dipole dominates the flow field close to the squirmer rod.

3.3 Pushers-type squirmer rods

3.3.1 State diagram. For the minimum dipole strength $\chi = -1$, *i.e.*, the pusher-type squirmer rods with the largest force dipole, we study the collective dynamical states as a function of the aspect ratio α and area fraction ϕ. A comparison between the state diagrams of neutral squirmer rods [*cf.* Fig. 1(c)] and pusher rods [*cf.* Fig. 3(a)] already illustrates the strong influence of the long-ranged hydrodynamic dipole–dipole interactions. Compared to neutral squirmer rods the transition line from the disordered to other states is shifted to larger area fractions and new dynamic states arise such as active turbulence and dynamic clustering. We provide an overview of the observed dynamic states before presenting a more quantitative analysis in Section 3.3.2.

Most interestingly, compared to neutral squirmer rods the flow field of the pusher rod obviously suppresses the formation of dynamic swarms and impedes the single swarm state, which only occurs for large $\alpha \geq 4.0$. This is in agreement with findings of Saintillan and Shelley,[88] who employ slender-body theory to show that polar and nematic order in systems of elongated pusher microswimmers is destroyed by their hydrodynamic flow fields. Likewise, explicit hydrodynamic simulations of collective dynamics of spherical squirmers show that pushers

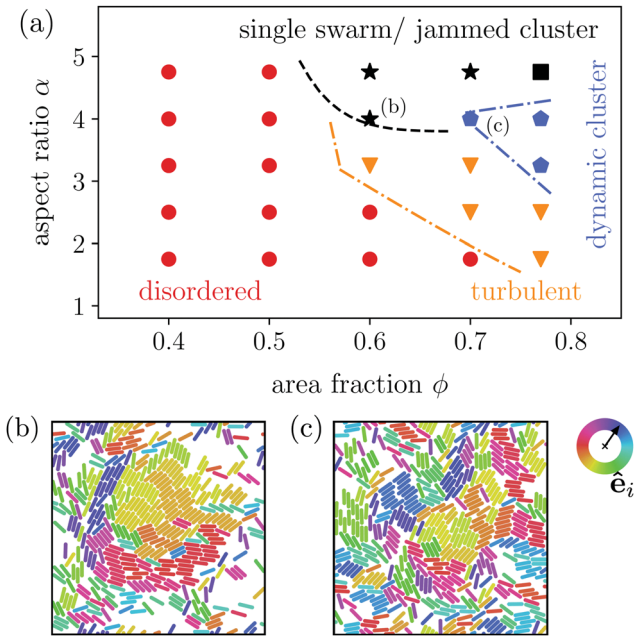

Fig. 3 (a) State diagram of the strongest pusher-type squirmer rods with $\chi = -1$ in the parameter space aspect ratio α *versus* area fraction ϕ. (b) Snapshot of a single swarm state at $\alpha = 4.75$ and $\phi = 0.6$, (c) snapshot of a dynamic cluster state at $\alpha = 4.0$ and $\phi = 0.7$ as indicated in the state diagram. The color of the individual squirmer rods encode their orientation $\hat{\mathbf{e}}_i$ in the xy-plane.

create disordered homogeneous systems,[13,109] while pullers show swarming.[109] An argument for this difference in the collective dynamic behavior is found in both implicit[90] and explicit[71] hydrodynamic simulations, which show that pushers are deflected during collision, while pullers align.

Instead of the suppressed swarming states for $\alpha \leq 3.25$, we find a very dynamic or turbulent state. A typical snapshot of a rod configuration is shown in Fig. 4(a), a video is provided in the Video 1 (ESI†). Here, the hydrodynamic dipole–dipole interactions compete with steric interactions that favor the formation of single swarms at large area fraction ϕ in the case of neutral rods.[94] Towards lower ϕ the turbulent state transitions to the disordered state and towards higher aspect ratio α to cluster or swarm states.

Similar to other examples of active turbulence in theory and experiments,[47,49–51,97] we find two cascades in the power spectral density of the squirmer velocities, as we will show in detail in Section 3.3.2. For the turbulent state at $\alpha = 3.25$ and $\phi = 0.6$ we construct a continuous velocity field $\mathbf{v}(x, y)$ to visualize the turbulent flow pattern and its vortices. A snapshot of the system and the resulting flow field are shown in Fig. 4(a) and (b), respectively. We also calculate the vorticity $\omega = (\nabla \times \mathbf{v})_z$, which is shown in Fig. 4(c). To easily obey the periodic boundary conditions, the vorticity was determined *via* a Fourier transformation. In all turbulent states, we observe that squirmer rods show a local alignment, which extends over short streaks, where squirmer rods swim side by side and head to tail. However, these streaks buckle and dissolve frequently, leaving a chaotic pattern of streaks and vortices.

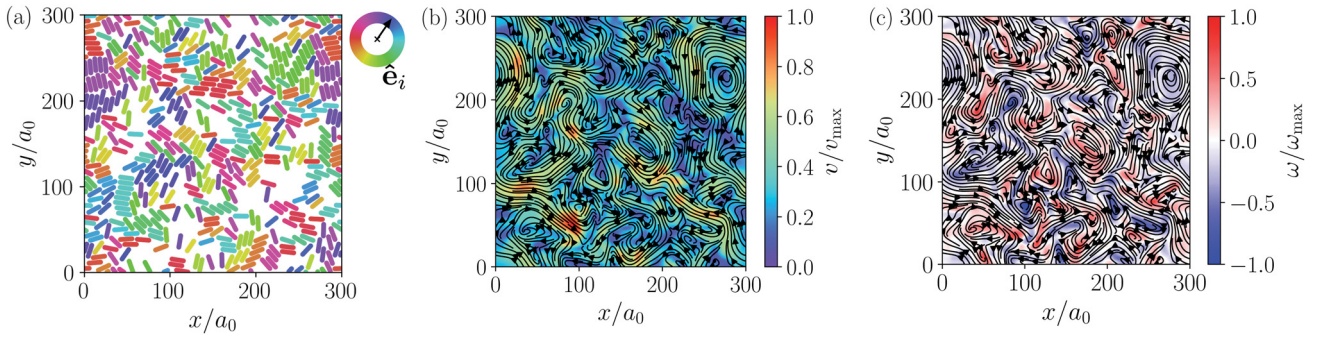

Fig. 4 Turbulent state of pusher-type squirmer rods with dipole strength $\chi = -1$, an aspect ratio $\alpha = 3.25$, and for an area fraction of $\phi = 0.6$. (a) Snapshot of the system with individual squirmer rods. Their orientation angles φ in the x/y-plane are color-coded to help identifying small groups with the same orientation. (b) Streamlines of the velocity field $\mathbf{v}(x, y)$ of the squirmer rods constructed from the snapshot in (a) with color-coded swimming velocity $v = |\mathbf{v}(x, y)|$. To construct the velocity field, each rod is represented by an elliptic Gaussian function with the standard deviations $\sigma_\parallel$ and $\sigma_\perp$ matching the shape of the squirmer rods. Each point on a regular grid is then assigned the average velocity of the surrounding rods weighted with the Gaussians. (c) Streamlines of the velocity field with color-coded vorticity $\omega = [\nabla \times \mathbf{v}(x, y)]_z$.

For large aspect ratio $\alpha \geq 4.0$ we still find the single swarm state [Fig. 3(b) and Video 2, ESI†], where a stable cluster moves through the system, and also a jammed cluster state. Since they are also found for neutral squirmer rods,[76] we deduce that they mainly arise from steric interactions. Indeed, they are also found for dry active rods.[98] For aspect ratios below $\alpha < 4.75$ and large area fractions clusters still form, but they deform dynamically while squirmer rods join or leave constantly [Fig. 3(c) and Video 3, ESI†]. However, the power spectral densities of this dynamic cluster state lacks the characteristic scaling behavior of the turbulent state, as we will show in Section 3.3.2. The absence of two power-law regimes (energy cascades) in the power spectra separated by a maximum, which defines a characteristic length scale, is our main criterion to distinguish the dynamic cluster state from the turbulent state. Hence, this state is intermediate between the jammed cluster and turbulent state. In the jammed cluster state observed for $\alpha = 4.75$ and $\phi = 0.77$ the average swimmer velocity is low, $\langle \mathbf{v}_i \cdot \hat{\mathbf{e}}_i \rangle \approx 0.18 v_0$, and rises to $\langle \mathbf{v}_i \cdot \hat{\mathbf{e}}_i \rangle \approx 0.4 v_0$ for the aspect ratio $\alpha \leq 4$ in the dynamic cluster state.

As already mentioned, the disordered state extends to higher densities compared to neutral squirmer rods. Here, velocity correlations between squirmer rods are short-ranged and the power spectral density decays without any algebraic behavior as we will show in Section 3.3.2. In other words, no patterns emerge because energy is not transported to larger scales.

All together, our results imply that the pusher-type flow fields inhibit or destabilize the steric alignment of swimmers that has been found for neutral squirmer rods. In intermediate regions of the state diagram, the competition of both effects lead to new dynamic states.

3.3.2 Velocity pair correlations and power spectral density. To investigate and classify the emergent dynamic states of pushers-type squirmer rods, we employ the velocity pair-correlation function $C_v(R)$ and the power spectral density of velocity fluctuations, $E(k)$. While the velocity pair correlation allows us to examine emerging patterns, the power spectral density quantifies the distribution of kinetic energy over different length scales $1/k$, which we will use to classify turbulent dynamics. To calculate the velocity pair-correlation function,

$$C_v(R) = \frac{\left\langle \sum_{i \neq j} \mathbf{v}_i \cdot \mathbf{v}_j \delta(|\mathbf{r}_{ij}| - R) \right\rangle}{\left\langle \sum_{i \neq j} \delta(|\mathbf{r}_{ij}| - R) \right\rangle}, \quad (3)$$

we use a histogram for the scalar product $\mathbf{v}_i \cdot \mathbf{v}_j$ with distance R between rods i and j, assuming our systems are isotropic, *i.e.*, $C_v(\mathbf{R}) = C_v(R)$. Here, $\langle \cdots \rangle$ means an average over time. The power spectral density is formally defined as $\langle |\tilde{\mathbf{v}}(\mathbf{k})|^2 \rangle$, where $\tilde{\mathbf{v}}(\mathbf{k})$ is the Fourier transform of the velocity field of the squirmer rods. According to the Wiener–Khinchin theorem, the power spectral density is related to the Fourier transform of the velocity pair-correlation function, $\langle |\tilde{\mathbf{v}}(\mathbf{k})|^2 \rangle = \mathscr{F}(C_v)(\mathbf{k})$. Due to the isotropy of the velocity fluctuations, we introduce the spectrum as a function of wave number k following ref. 51 and 110, $E(k) = \frac{k}{2\pi} \langle |\tilde{\mathbf{v}}(\mathbf{k})|^2 \rangle$. Then, using the zeroth-order Bessel function of the first kind, we arrive at

$$E(k) = \frac{k}{2\pi} \int_{L^2} C_v(\mathbf{R}) e^{-i\mathbf{k}\cdot\mathbf{R}} d^2R = k \int_0^{R_{\max}} C_v(R) J_0(kR) R dR, \quad (4)$$

where $R_{\max} = L$ is the system size.[111] Since for small R, $C_v(\mathbf{R})$ only exists for rods positioned side by side and thereby is highly anisotropic, we shift $C_v(\mathbf{R})$ by a length $l_S/2$ to smaller distances R when calculating $E(k)$, similar to ref. 97.

In Fig. 4 we compare the normalized velocity pair-correlation functions $\tilde{C}_v(R) = C_v(R)/\langle \mathbf{v}_i^2 \rangle$ of pusher-type squirmer rods for aspect ratio $\alpha = 3.25$ at different area fractions ϕ. A more complex behavior is observed for an area fraction in the range $\phi \in [0.4, 0.77]$, which allows for competing steric and hydrodynamic interactions and for which we show $\tilde{C}_v(R)$ in Fig. 5. The respective states are characterized as disordered ($\phi = 0.4/0.5$), turbulent ($\phi = 0.6/0.7$), and dynamic cluster $\phi = 0.77$, as we detail also further below. Generally, for larger ϕ,

the correlations extend to larger distances, which indicates that the size of ordered patterns increases with density. Distinctive for pushers we find that $\tilde{C}_v(R)$ is not purely positive but also shows distances where it becomes negative. In more detail, we observe the following characteristics. For distances, where steric interactions occur and dominate, $R < l_S$, $\tilde{C}_v(R)$ is positive. With increasing R it decays to zero around $R = l_S$ to $R = 3l_S$ and becomes negative for area fractions ϕ up to 0.7. In the turbulent states for $\phi = 0.6$ and 0.7, $\tilde{C}_v(R)$ returns to positive values at more than twice the first zero-crossing distance [inset of Fig. 5]. For $\phi = 0.6$ we even observe a third zero crossing. In the disordered states for $\phi = 0.4$ and $0.5\tilde{C}_v(R)$ does not show a second zero crossing but approaches zero from the negative region. Lastly, at $\phi = 0.77$ the system is in the dynamic cluster state with densely packed squirmer rods. This is in agreement with the pair-correlation function, which has the longest range and only exhibits anti-correlations for $R > 6l_S$. However, we find that the orientational autocorrelation function $\langle \hat{\mathbf{e}}(t)\cdot\hat{\mathbf{e}}(t+\delta t)\rangle$ (not shown) decays after the cluster moved a distance of 3–$5l_S$, considering its mean velocity of $\langle \mathbf{v}_i\cdot\hat{\mathbf{e}}_i\rangle \approx 0.4v_0$ for $\alpha = 4.0$. This clearly indicates that the clusters are dynamic. For other aspect ratios α only small quantitative changes occur. Especially, the correlation functions for the turbulent and disordered states are representative for all α and ϕ.

The power spectral densities $E(k)$ calculated from $C_v(R)$ are in accordance with the findings so far. In Fig. 6(a) we compare the power spectral densities $E(k)$ for three different aspect ratios $\alpha = 1.75$, 2.5, and 3.25 in dense systems. The velocity autocorrelation functions $\tilde{C}_v(R)$ show the same oscillating decay as already observed above for $\alpha = 3.25$ and $\phi = 0.6$. We called these states active turbulence since the power spectral density $E(k)$ shows a broad peak, which separates two regions from each other with power-law decays towards low and high k. This is characteristic of active turbulence. Close to the characteristic wave number $k_c = 2\pi/l_S$, where energy is inserted from the active motion of the squirmer rods, $E(k)$ decays to zero. The maxima of the power spectral density all roughly occur at $0.2k_c$, indicating that the pattern size scales with l_S, which makes sense when the density is roughly the same.

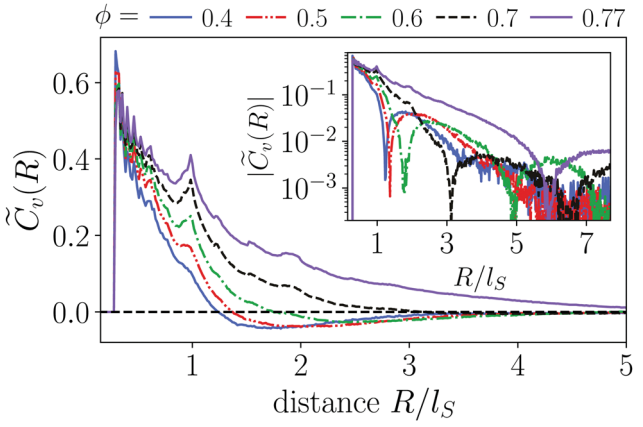

Fig. 5 Normalized velocity pair-correlation function $\tilde{C}_v(R)$ as a function of the rod distance R for pusher-type squirmer rods ($\chi = -1$) with aspect ratio $\alpha = 3.25$ at different area fractions ϕ. Inset: Plot of $|\tilde{C}_v(R)|$ *versus* R.

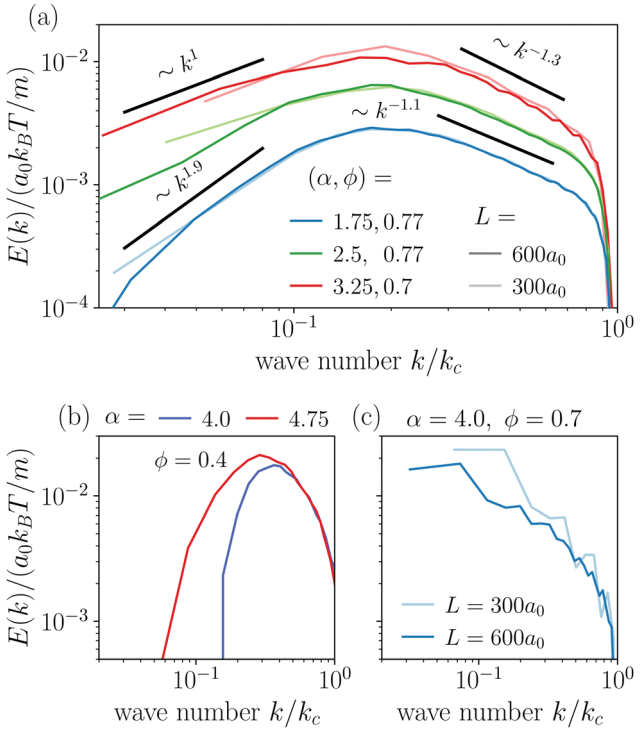

Fig. 6 (a) Power spectral density $E(k)$ in the turbulent state calculated from the velocity pair-correlation function $C_v(R)$. Light and dark colors correspond to small and large system sizes L, respectively. (b) Power spectral density $E(k)$ in the disordered state and (c) in the dynamic cluster state.

As reported in other experimental[51] and theoretical[50] studies on polar active fluids, the scaling exponents for the power laws in k are not universal. Towards smaller length scales (larger k), the exponent shows only a weak dependence on the aspect ratio α with values of -1.1 and -1.3, while towards larger length scales we observe a stronger variation of the scaling exponent with aspect ratio. For short squirmer rods with $\alpha = 1.75$, the power spectral density decays more rapidly with $E(k) \sim k^{1.9}$ and for a larger aspect ratio $\alpha = 3.25$, the power spectral density scales with $E(k) \sim k^1$. This indicates that for larger aspect ratio patterns at large length scales (small k) are observed more frequently.

For disordered states the power spectra do not follow power laws [*cf.* Fig. 6(b)]. Instead, they quickly decay towards smaller k, which indicates again that energy is not transported to larger length scales. In contrast, for the dynamic cluster state energy is concentrated at the larger length scales (small k) as expected, while $E(k)$ decays strongly towards smaller length scales [*cf.* Fig. 6(c)]. To investigate finite size effects, we compare the regular systems of size $L = 300a_0$ to systems with the increased system size of $L = 600a_0$ performed for $\alpha = 4$ and $\phi = 0.7$. In the bigger system the maximum of $E(k)$ shifts to smaller values of k roughly proportional to the change in L which suggests that the maximum correlation length always corresponds to the system size, and no characteristic length scale emerges. At the same time, we observe a decrease of max$[E(k)]$ indicating that the dynamic of the cluster slows down as L increases.

This behavior clearly distinguishes the dynamic cluster state from active turbulence, which has an intrinsic characteristic length scale. However, we note that data for larger systems would be necessary to show that the maximum correlation length $1/\mathrm{argmax}[E(k)]$ diverges for infinite system size. Though, this currently exceeds our computational capabilities. Note, the irregular behavior in the curve for $L = 300a_0$ is due to the fact that with increasing α close to the jammed cluster state the dynamics of the clusters slows down and longer simulation times are needed to smooth the curve.

3.4 Puller-type squirmer rods

3.4.1 State diagram. For strong puller-type squirmer rods with $\chi = 1$, we also investigate the system for varying aspect ratio α and area fraction ϕ and generate the state diagram as shown in Fig. 7(a). Here, we observe a completely different behavior compared to the pusher-type squirmer rods. Only for dense systems and at large aspect ratios, where steric interactions dominate, we observe the same single swarm/jammed cluster states for pusher and puller rods. Thus, the behavior resembles that of dry self-propelled rods,[98] although differences for pushers and pullers still remain. Otherwise, the state diagram is more similar to that of the neutral squirmer rods [Fig. 1(c)]. Only the disordered state is completely suppressed and replaced by the swarming state. This also means that the occurrence of all states are shifted towards smaller area fractions ϕ.

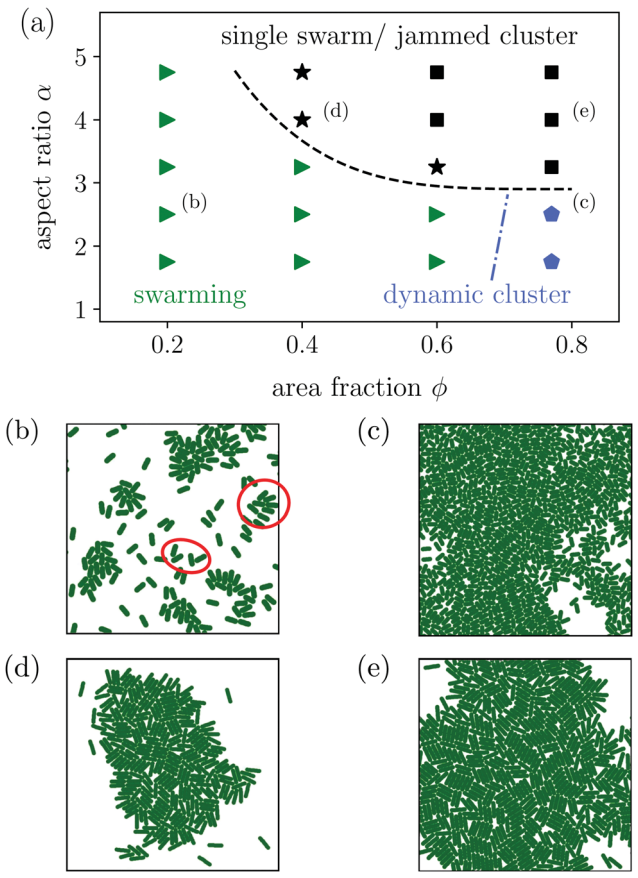

Fig. 7 (a) State diagram of the puller-type squirmer rods with $\chi = 1$ in the parameter space aspect ratio α *versus* area fraction ϕ. Snapshots of the system in (b) the swarming state at $\phi = 0.2$ and $\alpha = 2.5$ (only a part of the system is shown), (c) the dynamic cluster state at $\phi = 0.77$ and $\alpha = 2.5$, (d) the single swarm state at $\phi = 0.4$ and $\alpha = 4.0$, and (e) the jammed cluster state at $\phi = 0.77$ and $\alpha = 4.0$.

The most prominent feature of puller-type squirmer rods is that their flow fields strongly promote the formation of small swarms. Even for dilute systems with area fractions down to 0.2, the hydrodynamic interactions between the squirmer rods favor small swarms against the disordered state. Different from the purely steric alignment responsible for swarming neutral squirmer rods,[94] pairs of puller-type squirmer rods form T-shaped configurations, although deformed, when they collide. Examples are indicated in the snapshot of Fig. 7(b). This leads to small groups, where several squirmer rods follow a central leader of the group, arranged in a "comet tail" and pointing inwards [Fig. 7(b)]. A similar behavior is also found in ref. 95 and for dry active rods.[98] However, we observe that for the hydrodynamically interacting squirmer rods the swarming behavior extends to smaller densities and aspect ratios compared to dry self-propelled rods.[61,64] Often the swarms have an asymmetric shape, which then induces curved trajectories (Video 4, ESI†). With increasing area fraction, $\phi \geq 0.4$, swarms also increase in size. However, the overall alignment in the swarms rather decreases. This is due to the low polarity of the small swarms, which then merge in an unordered fashion with increasing ϕ.

For aspect ratios $\alpha \geq 3$ we also observe the formation of a single swarm, which collects all squirmer rods in the system [Fig. 7(d) and Video 5, ESI†]. For area fractions $\phi \geq 0.6$ and sufficiently large aspect ratios the single swarm becomes jammed and forms a static cluster state [Fig. 7(e) and Video 6, ESI†]. Reducing the aspect ratio at $\phi = 0.77$ to $\alpha \leq 2.5$, the jammed cluster becomes dynamic similar to the state observed in pusher-type squirmer rods [Fig. 7(c) and Video 7, ESI†].

3.4.2 Velocity pair correlations. For a quantitative study of the emergent states of the puller-type squirmer rods, we use again the velocity pair-correlation function. In Fig. 8(a) we compare results for the representative aspect ratio $\alpha = 4$, which exhibits most of the emergent states. We immediately notice the difference to the pusher-type squirmer rods; $\tilde{C}_v(R)$ does not become negative. This underlines the tendency of pullers to form two swarming states. To thoroughly distinguish these states, which both give very similar velocity correlation functions, we will further examine the orientational autocorrelations in Section 3.4.3.

We have already seen, that even in dilute systems with $\phi = 0.2$, the puller-type flow fields locally align the squirmer rods and thereby cause swarming. This is also visible in the velocity correlation function $\tilde{C}_v(R)$, which is more long-ranged compared to pusher-type rods [Fig. 5(a)]. Thus, squirmer rods are significantly correlated for distances up to $R = 2l_S$. As described in Section 3.4.1, the size of swarms increases with density. For the subsequent area fraction of $\phi = 0.4$ the system is already in the single swarm state at the chosen aspect ratio of 4.0. Hence, the velocity correlation function $\tilde{C}_v(R)$ becomes

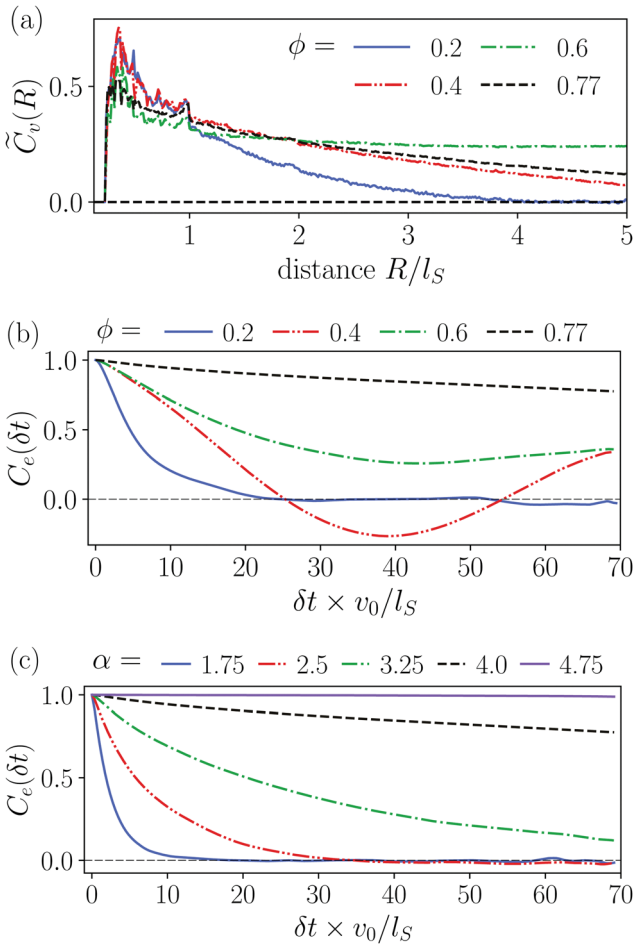

Fig. 8 (a) Normalized velocity pair-correlation function $\tilde{C}_v(R)$ plotted *versus* distance R for puller-type squirmer rods at constant aspect ratio of $\alpha = 4.0$. (b) Orientational autocorrelation function $C_e(\delta t)$ for constant aspect ratio $\alpha = 4.0$. (c) Orientational autocorrelation function $C_e(\delta t)$ in dense systems at area fraction $\phi = 0.77$.

more long-ranged. At $\phi = 0.6$ and $\phi = 0.77$, when the system is noticeably in the jammed cluster state, we observe two different features. For $\phi = 0.6$, $\tilde{C}_v(R)$ reaches a plateau, which indicates that the jammed cluster drifts in one direction since the squirmer rods are aligned, on average. At the highest density $\phi = 0.77$ the cluster formation takes place more quickly resulting in a disordered structure without drift. Here, the velocity correlation function $\tilde{C}_v(R)$ decreases and does not exhibit a plateau until $R/l_S = 5$.

3.4.3 Orientational autocorrelations. To further characterize and distinguish the single swarm, dynamic cluster, and jammed cluster states from each other, we employ the orientational autocorrelation function $C_e(\delta t) = \langle \mathbf{e}_i(t) \cdot \mathbf{e}_i(t + \delta t) \rangle$. In Fig. 8(b) we compare $C_e(\delta t)$ for different area fractions ϕ at constant aspect ratio $\alpha = 4$, and in Fig. 8(c) for different α at constant $\phi = 0.77$.

In dilute systems with $\phi = 0.2$, $C_e(\delta t)$ decays to zero at around $\delta t = 15 l_S/v_0$, meaning that swarms swim a distance of around $7 l_S$ until they either rotate, merge with other clusters or dissolve (Video 8, ESI†). For the single swarm state at $\phi = 0.4$, we observe a more long-ranged autocorrelation. After a swarm has formed it remains stable but also goes through configurational changes so that partially straight motion is observed interrupted by rotations or turns of the swarm (Video 5, ESI†). As a result, $C_e(\delta t)$ exhibits a damped oscillation, where the first minimum at $\delta t \approx 37 l_S/v_0$ means that the swarm has rotated by 180°. In the jammed cluster state, we again observe two different features. For $\phi = 0.6$, the cluster drifts due to its overall polar order. However, also configurational changes occur, which results in a decay of $C_e(\delta t)$ towards a non-zero value meaning that the cluster has reached some stable configuration within the observation window. At the higher density $\phi = 0.77$, the cluster now has a more random but static arrangement of the rods. Therefore, it hardly drifts and it only rotates very slowly, which causes a very slow decrease of $C_e(\delta t)$.

Comparing dense systems ($\phi = 0.77$) of different aspect ratios to each other, we observe the following characteristics from high to low α [Fig. 8(c)]. For the largest aspect ratio $\alpha = 4.75$ steric interactions between the rods are most dominant and we find an entirely jammed configuration with constant $C_e(\delta t) = 1$. Lowering the aspect ratio, the jammed cluster becomes more and more interrupted by occasional configurational changes, which results in the noticeable but slow decay of $C_e(\delta t)$ for $\alpha = 3.25$. In contrast, the dynamic cluster states at $\alpha = 1.75$ and $\alpha = 2.5$ show a fast exponential decay of $C_e(\delta t)$ due to the dynamic rearrangements within the cluster. The decay is faster for the lower aspect ratio, where the rods reorient more easily.

3.5 Variation from pusher to puller-type squirmer rod

In this section, we compare squirmer rods at a constant aspect ration $\alpha = 3.25$ and vary the swimmer type by the force-dipole strength χ. Furthermore, we performed simulations at different area fractions ϕ. The resulting state diagram is shown in Fig. 9(a). States of neutral squirmer rods are adapted according to ref. 94.

For puller-type squirmer rods with $\chi > 0$, we observe that already weak pullers with $\chi = 0.25$ show swarming at the small area fraction of $\phi = 0.2$, *i. e.*, the same state we observed in Section 3.4.1 for the highest strength $\chi = 1.0$. Obviously, the force-dipole field, which attracts nearby rods along the rod axis, promotes swarming. However, with increasing ϕ, swarming also extends to weak pusher rods. At higher area fractions $\phi \geq 0.6$, we find single swarm and jammed cluster states due to steric interactions between the rods, where neutral ($\chi = 0$) and puller-type squirmer rods show qualitatively similar behavior.

For pusher-type squirmer rods, $\chi < 0$, we observe a more diverse behavior, which we already noted for $\chi = 1$ in Section 3.3.1. While at $\phi = 0.2$ only the disordered state occurs, at $\phi = 0.4$ we find a transition from swarming to turbulent to disordered state with increasing pusher strength. The analysis of the power spectral density $E(k)$ reveals that the system with $\chi = -0.5$ is indeed in the turbulent state. Thus, the pusher flow field destabilizes swarming clusters. As a compromise between swarming and disordered states, active turbulence occurs in conjunction with steric repulsion. Increasing density further to $\phi = 0.6$, steric repulsion stabilizes swarming clusters and active turbulence is shifted to the largest pusher strength $\chi = -1$. Finally, at $\phi = 0.77$ the pusher flow field destabilizes the

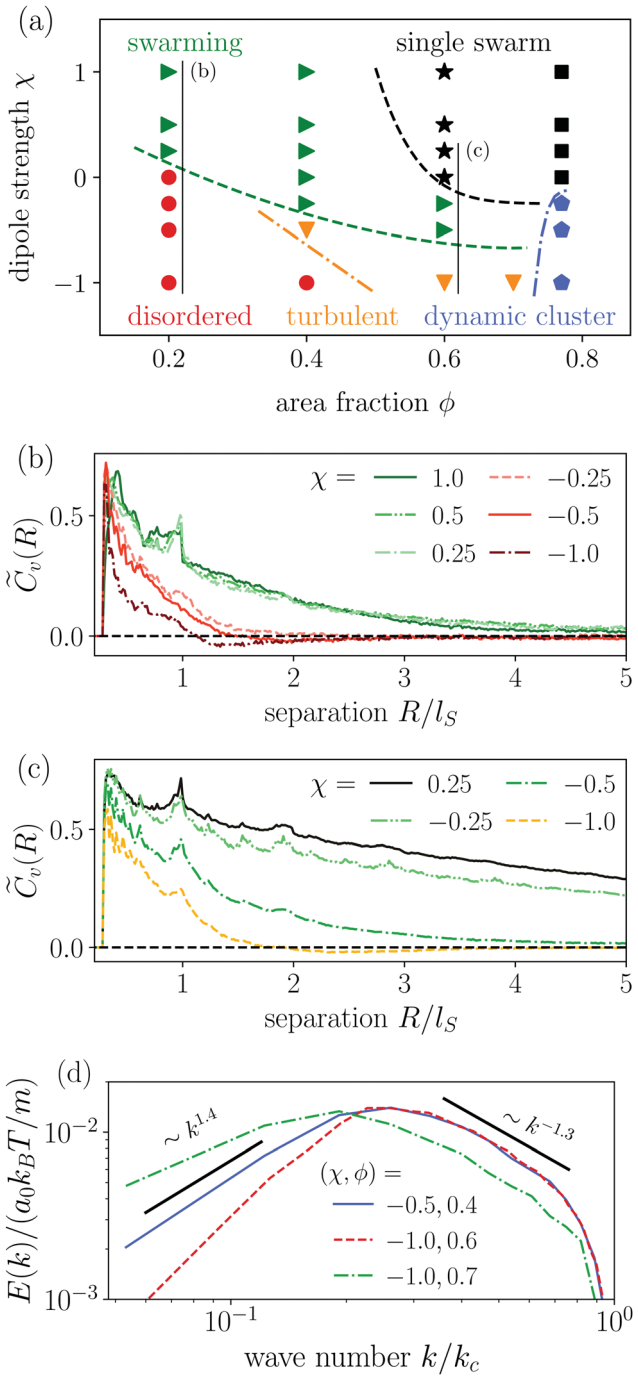

Fig. 9 (a) State diagram of the squirmer rods for different dipole-strengths χ and area fraction ϕ at an aspect ratio of $\alpha = 3.25$. The labeled vertical lines indicate the states for which the velocity correlation function is shown in (b and c). (b) Normalized velocity pair-correlation function $\tilde{C}_v(R)$ for dilute systems with $\phi = 0.2$ and different force-dipole strengths χ. Red curves belong to systems in the swarming state and green curves to the disordered state. (c) Normalized velocity pair-correlation function $\tilde{C}_v(R)$ for $\phi = 0.6$. The black curve belongs to the system in the single swarm state, green to the swarming state, and yellow to the turbulent case (d) Power spectral density $E(k)$ for the turbulent state at different χ, ϕ.

jammed cluster of neutral and puller-type squirmer rods, which then becomes dynamic.

3.5.1 Velocity pair correlations and power spectral density.

For a more quantitative analysis, we use the normalized velocity pair-correlation function $\tilde{C}_v(R)$ as defined in eqn (3). In Fig. 9(b) we compare $\tilde{C}_v(R)$ in dilute systems with $\phi = 0.2$ for different force-dipole strengths χ to each other. The collective dynamics is mainly governed by hydrodynamic interactions. Fig. 9(c) shows $\tilde{C}_v(R)$ for the larger area fraction $\phi = 0.6$, where a transition to the turbulent state occurs at $\chi = -1$.

In the dilute systems, all the velocity pair-correlation functions in the swarming state of puller-type swimmers ($\chi > 0$) are nearly identical and show correlations up to *circa* $2l_S$ [Fig. 9(b)]. This indicates that the mechanism behind swarm formation is fully established already at small dipole strength. Pusher-type squirmer rods ($\chi < 0$) only exhibit the disordered state and no swarms, so $\tilde{C}_v(R)$ is more short-ranged compared to pullers. Pushers prefer to order side by side and therefore pronounced peaks at closest distance $R = l_S/\alpha$ are observed compared to puller rods. Furthermore, we observe anti-correlations with $\tilde{C}_v(R) < 0$ starting at distances R between l_S and $2l_S$. They belong to pusher rods approaching each other head on.

At the higher area fraction $\phi = 0.6$, we observe the single swarm, swarming, and turbulent states [Fig. 9(c)]. In the single swarm state observed for weak pullers ($\chi = 0.25$), $\tilde{C}_v(R)$ is long-ranged and shows significant correlations for all recorded distances up to $R = 5l_S$. In the swarming state that emerges for pushers at $\chi = -0.25$ and -0.5 the correlation length of $\tilde{C}_v(R)$ decreases with increasing force-dipole strength. At $\chi = -0.5$ it is around $R = 2l_S$. In the turbulent state at $\chi = -1$, $\tilde{C}_v(R)$ becomes even more short-ranged and negative at $R = l_S$ due to the occurrence of vortices.

In Fig. 9(d) we compare the power spectral densities $E(k)$ for three systems in the turbulent state at $\alpha = 3.25$. All three spectra show a regular cascade towards large k (small scales) and a second cascade towards small k (large scales). At large k all three power spectral densities show roughly the same scaling behavior $E(k) \sim k^{-1.3}$. Furthermore, the curves for $(\chi, \phi) = (-0.5, 0.4)$ and $(\chi, \phi) = (-1.0, 0.6)$ coincide in the range from $k = 0.2k_c$ to k_c, which includes the maximum of both spectra. For the second cascade, different scaling exponents are observed. At $\chi = -1$ the power spectral density decays more rapidly in the system with $\phi = 0.6$ following a scaling $E(k) \sim k^2$, while in the denser system ($\phi = 0.7$) the scaling is $E(k) \sim k^1$. Furthermore, the maximum of $E(k)$ shifts to a smaller wave number k, which implies a larger intrinsic length scale of the turbulent pattern. For the system with the smaller pusher strength, $\chi = -0.5$, the scaling follows $E(k) \sim k^{1.4}$, thus, it is situated between the two cases just discussed.

4 Summary and conclusion

In this article, we investigated the dynamic states of pusher and puller-type squirmer rods. Varying the head-to-tail anisotropy parameter χ of the surface slip-velocity field of the squirmer rod, we are able to smoothly tune the force-dipole strength of the resulting flow field between a pusher and puller.

For pushers with largest force-dipole strength $\chi = -1$, we observe a new turbulent state along with other modifications in the state diagram compared to neutral squirmer rods. In dilute systems, where steric interactions are less important, the pusher flow field suppresses the formation of the swarming states so that the disordered state extends to larger area fractions and aspect ratios. When steric interactions and thereby steric alignment of the rods become more important with increasing area fraction, the turbulent state emerges at small aspect ratios. To observe it for weaker pusher strengths at constant aspect ratio, one has to decrease the area fraction, which confirms the importance of steric interactions for the turbulent state. The velocity pair-correlation function decays and exhibits negative regions after one or two swimmer lengths, which indicates a characteristic length scale. At the same time, the power spectral density of the velocity fluctuations shows two energy cascades at small and large wave numbers with power-law scaling and non-universal exponents as reported in other works on active turbulence in polar fluids.[49,50,97] Increasing the area fraction further, a transition to the dynamic cluster state occurs at medium aspect ratios, which is reminiscent of the turbulent state but without the characteristic energy cascades. This is in contrast to soft active rods, where jammed states occur,[42,63] which are, however, destroyed for strong enough self-propulsion.[112] At larger aspect ratios, steric interactions become more important. Here, pushers resemble the dynamics of neutral squirmer rods[94] and dry active rods,[61,62] such that, instead of the turbulent and dynamic swarm state, a single swarm and jammed cluster are observed.

For pullers at all studied force-dipole strengths χ and in the most dilute system at $\phi = 0.2$, hydrodynamic interactions already promote the swarming state instead of the disordered state observed for neutral rods. At smaller aspect ratios and the largest area fraction, the dynamic cluster state occurs, while for larger aspect ratios swarming and dynamic clustering are replaced by a single swarm and jammed cluster state.

Thus, our study clearly indicates the importance of the type of the swimmer flow field for the occurring states. Although comparable states are often found for dry self-propelled rods, for squirmer rods their occurrence in the state diagram crucially depends on the specific hydrodynamic flow field. Specifically, active turbulence is only found for pushers and puller type flow fields greatly enhance the formations of swarms. Additionally, the different scaling exponents in the turbulent state show that steric interactions, tuned by rod density, play an important role for this state. All in all, the turbulent state occurs as a compromise between disordering hydrodynamic pusher flow fields and aligning steric interactions. Therefore, with our work we contribute to the insights how various biological propulsion strategies determine the collective motion of microswimmers.

In future work, it will be interesting to investigate collective dynamics of pusher and puller-type squirmer rods also in the bulk fluid, where the hydrodynamic force-dipole has the most long-range or dominant flow field. Likewise, implementing a liquid–air interface using a slip-boundary condition at one wall of the Hele-Shaw geometry, would provide a realistic modeling of recent experiments, where bacteria move close to a fluid–air interface.[113]

Conflicts of interest

There are no conflicts to declare.

Acknowledgements

We thank Felix Rühle, Reinier van Buel and Josua Grawitter for helpful discussions on the topic of the manuscript. We also acknowledge financial support from the Collaborative Research Center 910 funded by Deutsche Forschungsgemeinschaft.

References

1 F. Partensky, W. R. Hess and D. Vaulot, *Microbiol. Mol. Biol. Rev.*, 1999, **63**, 106–127.
2 P. G. Falkowski, *Phys. Rev.*, 1994, **39**, 235–258.
3 C. B. Field, M. J. Behrenfeld, J. T. Randerson and P. Falkowski, *Science*, 1998, **281**, 237–240.
4 A. L. Demain, *Trends Biotechnol.*, 2000, **18**, 26–31.
5 I. M. Banat, A. Franzetti, I. Gandolfi, G. Bestetti, M. G. Martinotti, L. Fracchia, T. J. Smyth and R. Marchant, *Appl. Microbiol. Biotechnol.*, 2010, **87**, 427–444.
6 S. N. Naik, V. V. Goud, P. K. Rout and A. K. Dalai, *Renewable Sustainable Energy Rev.*, 2010, **14**, 578–597.
7 D. M. Alonso, J. Q. Bond and J. A. Dumesic, *Green Chem.*, 2010, **12**, 1493–1513.
8 H.-J. Huang, S. Ramaswamy, U. Tschirner and B. Ramarao, *Sep. Purif. Technol.*, 2008, **62**, 1–21.
9 M. Wagner, A. Loy, R. Nogueira, U. Purkhold, N. Lee and H. Daims, *Antonie van Leeuwenhoek*, 2002, **81**, 665–680.
10 I. Schmidt, O. Sliekers, M. Schmid, E. Bock, J. Fuerst, J. G. Kuenen, M. S. Jetten and M. Strous, *FEMS Microbiol. Rev.*, 2003, **27**, 481–492.
11 E. Lauga and T. R. Powers, *Rep. Prog. Phys.*, 2009, **72**, 096601.
12 M. C. Marchetti, J.-F. Joanny, S. Ramaswamy, T. B. Liverpool, J. Prost, M. Rao and R. A. Simha, *Rev. Mod. Phys.*, 2013, **85**, 1143.
13 A. Zöttl and H. Stark, *J. Phys.: Condens. Matter*, 2016, **28**, 253001.
14 M. Polin, I. Tuval, K. Drescher, J. P. Gollub and R. E. Goldstein, *Science*, 2009, **325**, 487–490.
15 J. Elgeti, R. G. Winkler and G. Gompper, *Rep. Prog. Phys.*, 2015, **78**, 056601.
16 H. C. Berg, *Annu. Rev. Biochem.*, 2003, **72**, 19–54.
17 R. Vogel and H. Stark, *Phys. Rev. Lett.*, 2013, **110**, 158104.
18 T. C. Adhyapak and H. Stark, *Phys. Rev. E*, 2015, **92**, 052701.
19 J. Tailleur and M. Cates, *Europhys. Lett.*, 2009, **86**, 60002.
20 C. O. Reichhardt and C. Reichhardt, *Annu. Rev. Condens. Matter Phys.*, 2017, **8**, 51–75.

21 R. Di Leonardo, L. Angelani, D. Dell'Arciprete, G. Ruocco, V. Iebba, S. Schippa, M. P. Conte, F. Mecarini, F. De Angelis and E. Di Fabrizio, *Proc. Natl. Acad. Sci. U. S. A.*, 2010, **107**, 9541–9545.
22 A. Sokolov, M. M. Apodaca, B. A. Grzybowski and I. S. Aranson, *Proc. Natl. Acad. Sci. U. S. A.*, 2010, **107**, 969–974.
23 M. Knežević and H. Stark, *New J. Phys.*, 2020, **22**, 113025.
24 M. Enculescu and H. Stark, *Phys. Rev. Lett.*, 2011, **107**, 058301.
25 F. Rühle and H. Stark, *Eur. Phys. J. E: Soft Matter Biol. Phys.*, 2020, **43**, 1–17.
26 J. R. Blake, *J. Fluid Mech.*, 1971, **46**, 199–208.
27 S. E. Spagnolie and E. Lauga, *J. Fluid Mech.*, 2012, **700**, 105–147.
28 S. Thutupalli, R. Seemann and S. Herminghaus, *New J. Phys.*, 2011, **13**, 073021.
29 J. Gachelin, A. Rousselet, A. Lindner and E. Clement, *New J. Phys.*, 2014, **16**, 025003.
30 M. Theers, E. Westphal, K. Qi, R. G. Winkler and G. Gompper, *Soft Matter*, 2018, **14**, 8590–8603.
31 Ö. Duman, R. E. Isele-Holder, J. Elgeti and G. Gompper, *Soft Matter*, 2018, **14**, 4483–4494.
32 J.-T. Kuhr, F. Rühle and H. Stark, *Soft Matter*, 2019, **15**, 5685–5694.
33 M. Hennes, K. Wolff and H. Stark, *Phys. Rev. Lett.*, 2014, **112**, 238104.
34 M. J. Kim and K. S. Breuer, *Small*, 2008, **4**, 111–118.
35 V. Schaller, C. Weber, C. Semmrich, E. Frey and A. R. Bausch, *Nature*, 2010, **467**, 73–77.
36 H. Wioland, F. G. Woodhouse, J. Dunkel, J. O. Kessler and R. E. Goldstein, *Phys. Rev. Lett.*, 2013, **110**, 268102.
37 D. Khoromskaia and G. P. Alexander, *New J. Phys.*, 2017, **19**, 103043.
38 Y. Sumino, K. H. Nagai, Y. Shitaka, D. Tanaka, K. Yoshikawa, H. Chaté and K. Oiwa, *Nature*, 2012, **483**, 448–452.
39 T. Sánchez, D. T. N. Chen, S. J. DeCamp, M. Heymann and Z. Dogic, *Nature*, 2012, **491**, 431.
40 S. J. DeCamp, G. S. Redner, A. Baskaran, M. F. Hagan and Z. Dogic, *Nat. Mater.*, 2015, **14**, 1110–1115.
41 F. C. Keber, E. Loiseau, T. Sanchez, S. J. DeCamp, L. Giomi, M. J. Bowick, M. C. Marchetti, Z. Dogic and A. R. Bausch, *Science*, 2014, **345**, 1135–1139.
42 H. Wensink and H. Löwen, *J. Phys.: Condens. Matter*, 2012, **24**, 464130.
43 J. Dunkel, S. Heidenreich, K. Drescher, H. H. Wensink, M. Bär and R. E. Goldstein, *Phys. Rev. Lett.*, 2013, **110**, 228102.
44 C. Dombrowski, L. Cisneros, S. Chatkaew, R. E. Goldstein and J. O. Kessler, *Phys. Rev. Lett.*, 2004, **93**, 098103.
45 C. W. Wolgemuth, *Biophys. J.*, 2008, **95**, 1564–1574.
46 S. Heidenreich, J. Dunkel, S. H. Klapp and M. Bär, *Phys. Rev. E*, 2016, **94**, 020601.
47 R. Alert, J.-F. Joanny and J. Casademunt, *Nat. Phys.*, 2020, **16**, 682–688.
48 B. Martnez-Prat, R. Alert, F. Meng, J. Ignés-Mullol, J.-F. Joanny, J. Casademunt, R. Golestanian and F. Sagués, *Phys. Rev. X*, 2021, **11**, 031065.
49 R. Alert, J. Casademunt and J.-F. Joanny, *Annu. Rev. Condens. Matter Phys.*, 2022, **13**, 143–170.
50 V. Bratanov, F. Jenko and E. Frey, *Proc. Natl. Acad. Sci. U. S. A.*, 2015, **112**, 15048–15053.
51 H. H. Wensink, J. Dunkel, S. Heidenreich, K. Drescher, R. E. Goldstein, H. Löwen and J. M. Yeomans, *Proc. Natl. Acad. Sci. U. S. A.*, 2012, **109**, 14308.
52 K. Qi, E. Westphal, G. Gompper and R. G. Winkler, *Phys. Rev. Lett.*, 2020, **124**, 068001.
53 A. Doostmohammadi, T. N. Shendruk, K. Thijssen and J. M. Yeomans, *Nat. Commun.*, 2017, **8**, 1–7.
54 S.-Z. Lin, W.-Y. Zhang, D. Bi, B. Li and X.-Q. Feng, *Commun. Phys.*, 2021, **4**, 1–9.
55 A. Doostmohammadi, S. P. Thampi, T. B. Saw, C. T. Lim, B. Ladoux and J. M. Yeomans, *Soft Matter*, 2015, **11**, 7328–7336.
56 T. Vicsek, A. Czirók, E. Ben-Jacob, I. Cohen and O. Shochet, *Phys. Rev. Lett.*, 1995, **75**, 1226.
57 G. Grégoire and H. Chaté, *Phys. Rev. Lett.*, 2004, **92**, 025702.
58 H. Chaté, F. Ginelli, G. Grégoire, F. Peruani and F. Raynaud, *Eur. Phys. J. B*, 2008, **64**, 451–456.
59 R. Großmann, P. Romanczuk, M. Bär and L. Schimansky-Geier, *Phys. Rev. Lett.*, 2014, **113**, 258104.
60 M. C. Bott, F. Winterhalter, M. Marechal, A. Sharma, J. M. Brader and R. Wittmann, *Phys. Rev. E*, 2018, **98**, 012601.
61 F. Peruani, A. Deutsch and M. Bär, *Phys. Rev. E: Stat., Nonlinear, Soft Matter Phys.*, 2006, **74**, 030904.
62 Y. Yang, V. Marceau and G. Gompper, *Phys. Rev. E: Stat., Nonlinear, Soft Matter Phys.*, 2010, **82**, 031904.
63 M. Abkenar, K. Marx, T. Auth and G. Gompper, *Phys. Rev. E: Stat., Nonlinear, Soft Matter Phys.*, 2013, **88**, 062314.
64 S. Weitz, A. Deutsch and F. Peruani, *Phys. Rev. E: Stat., Nonlinear, Soft Matter Phys.*, 2015, **92**, 012322.
65 H. Jiang and Z. Hou, *Soft Matter*, 2014, **10**, 1012–1017.
66 R. E. Isele-Holder, J. Elgeti and G. Gompper, *Soft Matter*, 2015, **11**, 7181–7190.
67 M. Hennes, K. Wolff and H. Stark, *Phys. Rev. Lett.*, 2014, **112**, 238104.
68 H. Jeckel, E. Jelli, R. Hartmann, P. K. Singh, R. Mok, J. F. Totz, L. Vidakovic, B. Eckhardt, J. Dunkel and K. Drescher, *Proc. Natl. Acad. Sci. U. S. A.*, 2019, **116**, 1489–1494.
69 A. Zöttl and H. Stark, *Eur. Phys. J. E: Soft Matter Biol. Phys.*, 2018, **41**, 61.
70 G. Rückner and R. Kapral, *Phys. Rev. Lett.*, 2007, **98**, 150603.
71 I. O. Götze and G. Gompper, *Phys. Rev. E: Stat., Nonlinear, Soft Matter Phys.*, 2010, **82**, 041921.
72 P. de Buyl and R. Kapral, *Nanoscale*, 2013, **5**, 1337–1344.
73 A. Zöttl and H. Stark, *Phys. Rev. Lett.*, 2014, **112**, 118101.
74 J. Blaschke, M. Maurer, K. Menon, A. Zöttl and H. Stark, *Soft Matter*, 2016, **12**, 9821–9831.
75 A. Zöttl and J. M. Yeomans, *Nat. Phys.*, 2019, **15**, 554–558.
76 A. W. Zantop and H. Stark, *Soft Matter*, 2020, **16**, 6400–6412.

77 T. Eisenstecken, J. Hu and R. G. Winkler, *Soft Matter*, 2016, **12**, 8316–8326.
78 M. Wagner and M. Ripoll, *Europhys. Lett.*, 2017, **119**, 66007.
79 F. J. Schwarzendahl and M. G. Mazza, *J. Chem. Phys.*, 2019, **150**, 184902.
80 J. de Graaf, H. Menke, A. J. Mathijssen, M. Fabritius, C. Holm and T. N. Shendruk, *J. Chem. Phys.*, 2016, **144**, 134106.
81 A. Pandey, P. S. Kumar and R. Adhikari, *Soft Matter*, 2016, **12**, 9068–9076.
82 M. Kuron, P. Stärk, C. Burkard, J. De Graaf and C. Holm, *J. Chem. Phys.*, 2019, **150**, 144110.
83 Z. Ouyang and J. Lin, *Phys. Fluids*, 2021, **33**, 073302.
84 J. Toner and Y. Tu, *Phys. Rev. Lett.*, 1995, **75**, 4326.
85 J. Swift and P. C. Hohenberg, *Phys. Rev. A*, 1977, **15**, 319.
86 V. M. Worlitzer, G. Ariel, A. Be'er, H. Stark, M. Bär and S. Heidenreich, *New J. Phys.*, 2021, **23**, 033012.
87 H. Reinken, S. H. Klapp, M. Bär and S. Heidenreich, *Phys. Rev. E*, 2018, **97**, 022613.
88 D. Saintillan and M. J. Shelley, *Phys. Rev. Lett.*, 2007, **99**, 058102.
89 A. Baskaran and M. C. Marchetti, *Proc. Natl. Acad. Sci. U. S. A.*, 2009, **106**, 15567–15572.
90 N. Yoshinaga and T. B. Liverpool, *Phys. Rev. E*, 2017, **96**, 020603.
91 M. Lighthill, *Commun. Pur. Appl. Math.*, 1952, **5**, 109–118.
92 M. T. Downton and H. Stark, *J. Phys.: Condens. Matter*, 2009, **21**, 204101.
93 A. W. Zantop and H. Stark, *J. Chem. Phys.*, 2021, **154**, 024105.
94 A. W. Zantop and H. Stark, *J. Chem. Phys.*, 2021, **155**, 134904.
95 K. Kyoya, D. Matsunaga, Y. Imai, T. Omori and T. Ishikawa, *Phys. Rev. E: Stat., Nonlinear, Soft Matter Phys.*, 2015, **92**, 063027.
96 M. Theers, E. Westphal, G. Gompper and R. G. Winkler, *Soft Matter*, 2016, **12**, 7372–7385.
97 K. Qi, E. Westphal, G. Gompper and R. G. Winkler, *Commun. Phys.*, 2022, **5**, 1–12.
98 M. Bär, R. Großmann, S. Heidenreich and F. Peruani, *Annu. Rev. Condens. Matter Phys.*, 2020, **11**, 441–466.
99 A. J. Mathijssen, A. Doostmohammadi, J. M. Yeomans and T. N. Shendruk, *J. Fluid Mech.*, 2016, **806**, 35–70.
100 A. Malevanets and R. Kapral, *J. Chem. Phys.*, 1999, **110**, 8605–8613.
101 A. Lamura, G. Gompper, T. Ihle and D. Kroll, *Europhys. Lett.*, 2001, **56**, 319.
102 I. O. Götze, H. Noguchi and G. Gompper, *Phys. Rev. E: Stat., Nonlinear, Soft Matter Phys.*, 2007, **76**, 046705.
103 J. D. Weeks, D. Chandler and H. C. Andersen, *J. Chem. Phys.*, 1971, **54**, 5237–5247.
104 A. Dullweber, B. Leimkuhler and R. McLachlan, *J. Chem. Phys.*, 1997, **107**, 5840–5851.
105 H. Jeckel, E. Jelli, R. Hartmann, P. K. Singh, R. Mok, J. F. Totz, L. Vidakovic, B. Eckhardt, J. Dunkel and K. Drescher, *Proc. Natl. Acad. Sci. U. S. A.*, 2019, **116**, 1489–1494.
106 J. Deng, M. Molaei, N. G. Chisholm and K. J. Stebe, *Langmuir*, 2020, **36**, 6888–6902.
107 L. Vaccari, M. Molaei, T. H. Niepa, D. Lee, R. L. Leheny and K. J. Stebe, *Adv. Colloid Interface Sci.*, 2017, **247**, 561–572.
108 N. Liron and S. Mochon, *J. Eng. Mech.*, 1976, **10**, 287–303.
109 N. Oyama, J. J. Molina and R. Yamamoto, *Phys. Rev. E*, 2016, **93**, 043114.
110 U. Frisch and A. N. Kolmogorov, *Turbulence: the legacy of AN Kolmogorov*, Cambridge University Press, 1995.
111 A. D. Poularikas, *Transforms and applications handbook*, CRC press, 2018.
112 R. Großmann, I. S. Aranson and F. Peruani, *Nat. Commun.*, 2020, **11**, 1–12.
113 D. Nishiguchi, I. S. Aranson, A. Snezhko and A. Sokolov, *Nat. Commun.*, 2018, **9**, 1–8.

CHAPTER 5

Conclusions and Outlook

Conclusions

Biological microswimmers exist in various shapes and employ different propulsion strategies to explore their environment. To model the particle shape of microswimmers, which is mostly elongated, we have introduced the squirmer-rod model. The squirmer rod consists of several spherical squirmers arranged on an straight line to form a rigid body. The surface slip-velocity of the squirmer thereby models the ciliary propulsion found for organisms such as *Paramecium*. To model also pusher and puller-type microswimmers, the surface slip velocity of the individual squirmers is modified such that the surface velocity is concentrated to either the back or the front of the rod. These realizations serve as model for *E. coli* bacteria and *C. reinhardtii* algae, respectively. To model the fluid surrounding the squirmer rods, we use the method of multi-particle collision dynamics (MPCD). This method solves the full Navier-Stokes equation including thermal fluctuations.

Performing simulations in the bulk fluid, we find that the neutral squirmer rod mainly results in the addition of a force quadrupole moment to the basic flow field of the spherical squirmer, which is a source dipole. The force quadrupole possesses the same radial decay $|\mathbf{v}^{\mathrm{FQ}}| \sim r^{-3}$ such that the overall radial decay of the flow field remains unchanged. For pusher-type squirmer rods we observe the additional flow field of a force dipole due to concentrating the surface velocity to the back of the rod. Consequently, the overall flow field of the pusher-type squirmer rod decays as $|\mathbf{v}| \sim r^{-2}$ in leading order.

In addition, we considered the Hele-Shaw geometry in which the fluid and microswimmer is confined in a narrow slit between to parallel plates. In this geometry the hydrodynamic multipoles are crucially altered and as a result, the flow fields show different characteristics. Most importantly the radial decay of the different multipoles is altered such that the source dipole, which now exists for all self-propelled

particles becomes the most long-ranged multipole field, $|\mathbf{v}^{\mathrm{SD}}| \sim \rho^{-2}$. At short and intermediate distances, however, we observe that the force dipole moment still dominates. Moreover, the force and source multipoles are affected by the confinement strength in an opposite way. Hence, the confinement strength introduces an interesting variation between the two hydrodynamic multipoles.

To create a less compressible model fluid, we introduced an extended collision rule for the MPCD method. The model generates an inherent momentum flux within each collision cell that contributes to the pressure. We showed that this extended rule results in a non-ideal equation of state and also derived analytic expressions for the shear viscosity. We find that these predictions are in good agreement with measurements obtained from equilibrium, constant shear, and Poiseuille flow simulations. Likewise, simulations of the flow fields of squirmers in the bulk fluid and Hele-Shaw geometry show good agreement with the analytic prediction. In simulations of the collective dynamics of squirmer rods, where the MPCD fluid is subject to strong forces, the comparison of the traditional MPCD-AT+a and the extended MPCD method shows a more homogeneous fluid density and viscosity in the context of clustering. For swarming squirmer rods we observe that the extended MPCD results in an increase in the size and velocity of emergent swarms compared to the traditional MPCD method.

In an in-depth study of neutral squirmer rods, we investigate the influence of their aspect ratio α and the density, given by the two-dimensional area fraction ϕ. We observe four different states going from small to large aspect ratio α. For short squirmer rods and low density we observe a disordered state with no correlations between the particles. At higher aspect ratio a state of dynamic swarms emerges, which is characterized by the frequent formation and break up of medium sized swarms. As the aspect ratio or density is further increased, the swarms become stable and the systems exhibits a single swarm state. For very high density the system becomes stationary and forms a jammed configuration.

The dynamic behavior becomes more diverse for pusher and puller-type squirmer rods. Here, we observe a new turbulent state for the pusher-type squirmer rods, as well as a dynamic clustering state, which is intermediate between turbulence and clustering. In dilute systems, where hydrodynamic interactions dominate, the pusher-type flow fields completely suppress the formation of swarms observed for neutral squirmer rods. Instead, a disordered state is found also for higher aspect ratio and density.

When steric interactions become more important at higher densities and aspect ratios, the turbulence state emerges as a compromise between the aligning and disordering interactions. In the turbulent state we observe a positive velocity pair-correlation at short distances which becomes negative at the length scale of a few

swimmer lengths. Then, again, it becomes positive after a few swimmer lengths, then negative again, and so on. The power spectral density of the velocity fluctuations shows two energy cascades at small and large wave numbers with power law scaling and non-universal exponents. When steric interactions dominate at high density and aspect ratio, the clustering and single-swarm states of neutral squirmer rods are recovered.

For puller-type squirmer rods we observe an increased tendency to form dynamic swarms for all aspect ratios. Here, the dynamic swarming state occurs already for very low densities, and the single-swarm state is shifted to lower densities and aspect ratios.

Investigating the swimmer-types for intermediate values of the force-dipole moment confirms our previous findings. Accordingly, also pushers rods exhibit the turbulent state, which, however, disappears for large values of the force-dipole strength. For pullers the tendency to form swarms sets in immediately when the force dipole is introduced.

Overall, we conclude that our study of the squirmer rod-model clearly indicates the importance of both the shape and hydrodynamic characteristic of the flow fields for the dynamics of elongated microswimmers. Although studies of dry self-propelled rods exhibit often similar states, our results clearly confirm previous work that the occurrence of, for example, active turbulence or the swarming state crucially depends on the type of hydrodynamic flow field [61]. As such, active turbulence is a characteristic of pushers, while swarms prevail for puller-type microswimmers. Furthermore, we observe that the scaling exponents, which characterize the turbulent state, depend on the aspect ratio and density and thus the strength of the interactions. This stresses again that the turbulent state emerges through a balance between aligning steric and disordering pusher-type hydrodynamic interactions. In contrast, we observe that neutral squirmer rods mainly exhibit swarming and jamming, which is more similar to dry active rods. Therefore, with our work we contribute to the understanding how biological propulsion strategies determine the collective motion of microswimmers.

Outlook

Below, we discuss a number of extensions for the squirmer rod models, which would be of interest for future studies. We have already implemented some of these extensions, such that we can discuss some preliminary results.

Rotlet dipole

A notable extension of the pusher-type squirmer rod is to improve the model for the actual propulsion mechanism of a rotating flagellum. For bacteria, the motor of the flagellar apparatus creates a torque that rotates the flagellum. At the same time,

the reverse torque rotates the cell body in the opposite direction. Resulting from the opposing torques, the flow field possesses the additional flow field of the rotlet dipole, as indicated in Sec. 2.2.5.1. This rotlet dipole results in circular trajectories when microswimmers are close to solid walls or liquid-air interfaces, where the orientation of rotation depends on the slip condition [234, 235].

To introduce the rotating flagellum in the squirmer-rod model, we add an azimuthal contribution to the surface slip velocity, which mimics the rotation of the flagellum. Preliminary research, which has been performed by the bachelor student Phillip Eisenhuth, showed that indeed circular trajectories emerge in the proximity of solid walls or liquid-air interfaces. We assume that this circular motion will be interesting in the context of the active turbulence that we observed for pusher-type squirmer rods. In particular, we assume an interaction between the radius of the circular trajectories of single squirmer rods and the characteristic vortex size of the active turbulence. However, more detailed simulations are required to investigate the statistics of the turbulent patters observed in the collective dynamics of these chiral pusher-type squirmer rods.

Flexible filaments

Another interesting extension of the squirmer-rods model is the realization of flexible filaments, as a model for polymer chains [43, 50], flagella [228], or elongated bacteria [236, 237] or the nematode worm *C. elegans* [238]. Our approach thereby provides an accurate description with explicit hydrodynamic interactions.

Similar work on filaments has been done using overdamped Langevin dynamics and implicit hydrodynamic interactions via the Rotne-Prager approximation [239–241], or inside the MPCD fluid without volume exclusion [242]. We have already conducted preliminary work on this topic, which we will discuss in the following. We begin with outlining the details of the flexible filament model and how it is coupled to the fluid.

To implement flexible filaments, the rigid-body constraint of the squirmer rod is partially released so that the constituting squirmers now move individually. In this way, the configuration of squirmers can deform and thereby model the deformation of a filament. To hold the squirmers in place and model the flexibility of filaments, we introduce additional potential forces between the individual squirmers. To introduce bending rigidity, we use the additional bending potential

$$V_{\text{bend}}(\mathbf{r}_1, ..., \mathbf{r}_{N_{\text{sq}}}) \;=\; -\frac{\epsilon_{\text{bend}}}{2} \sum_{i=2}^{N_{\text{sq}}-1} \left[\cos(\theta_i) + \theta_i^{12}\right] \tag{5.1}$$

where $\theta_i = \measuredangle(\mathbf{r}_{i-1}, \mathbf{r}_i, \mathbf{r}_{i+1})$ is the angle between the connecting vectors in the triplets of spherical squirmer, similar to Refs. [239, 240]. The additional θ_i^{12} term is added to avoids sharp angles above 90° in the configuration. For small $\theta \leqslant \pi/4$ this term

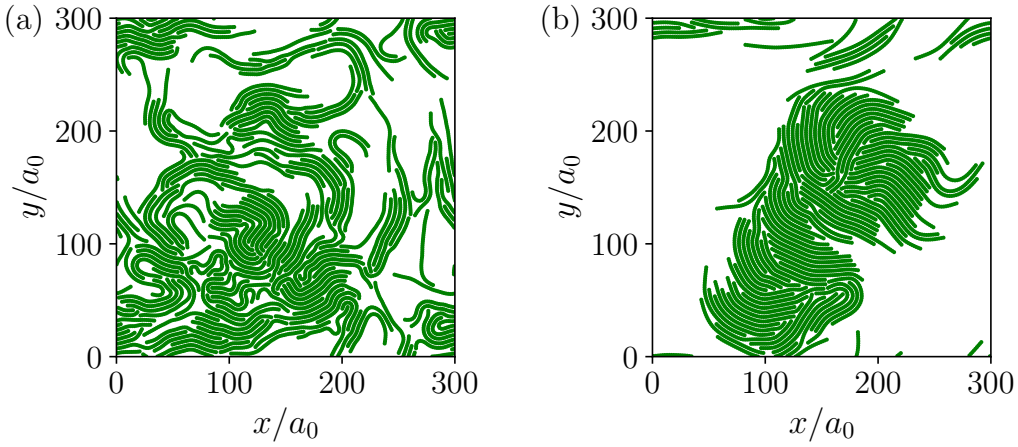

Figure 5.1: Snapshots of two simulations of flexible filaments for different bending energy ϵ_{bend}. (a) For a bending rigidity $\epsilon_{\text{bend}} \sim 10^3$ the filaments are rather soft and deform when they touch each other due to their active swimming. The softness thereby reduces the alignment due to steric interactions and hinders the formation of swarms. Moreover, filaments are able to escape dense configuration due to their flexibility. (b) For more stiff filaments with bending rigidity $\epsilon_{\text{bend}} \sim 10^4$ we see again the formation of swarms.

is negligible, and thus mostly does not affect the configuration. For long filaments the WCA potential of Eq. (3.17) is also applied between pairs of squirmers within a filament, when the index difference is greater than 10, which guarantees that the repulsion does not interfere with the bending potential. This avoids overlap of the filament with itself in compact configurations. To hold the bond length at the prescribed value, we use the constraint solver algorithm P-LINCS [243, 244], which is known from the simulation of molecules, *e.g.*, with the GROMACS package [245]. In other words, the P-LINCS algorithm keeps the distance between neighboring squirmers inside the filaments constant. Masses and moment-of-inertia tensors of the segments, which are required by P-LINCS, are taken from Ref. [125] presented in Sec. 4.2.

To couple the motion of the MPCD fluid to the flexible filament, we apply the momentum transfer of the squirmer i on the same squirmer. To apply the angular momentum transfer of the squirmer i to the filament, we consider triplets that include the two neighboring squirmers and are treated as rigid bodies during the angular momentum transfer. Furthermore, the orientation vector of the squirmer i is set to $\hat{\mathbf{e}}_i = (\mathbf{r}_{i-1,i} - \mathbf{r}_{i,i+1})/|\mathbf{r}_{i-1,i} - \mathbf{r}_{i,i+1}|$, such that we may define the surface slip-velocity of the spherical squirmer for every bead.

In Fig. 5.1 we compare two simulations of flexible filaments using different bending energies ϵ_{bend}. In both systems of size $L = 300a_0$ and thickness $\Delta z = 8a_0$, the filaments are constrained to move on in the center between the confining walls, similar to [206]. Filaments consist of $N_{\text{sq}} = 40$ squirmers of radius $R = 2$ and an

aspect ratio of $\alpha \approx 20$. The area fraction is given by $\phi = 0.6$ and individual squirmers propel with the typical slip-velocity parameter $B_1^{\mathrm{sq}} = 0.1$.

For the soft filaments shown in Fig. 5.1(a), the flexibility leads to strong shape changes upon collisions of the flexible filaments. Therefore, filaments are rather reoriented, than aligned, which suppresses the formation of swarms for this bending energy ϵ_{bend}. Likewise, the flexibility reduces the formation of clusters because filaments can escape dense regions in the system.

For the more rigid filaments shown in Fig. 5.1(b), we observe the formation of swarms again. Here, the increased rigidity allows an alignment of the filaments generally, while the deformations enables more aligned configurations and therefore more efficient formation of swarms. However, the deformation of filaments within swarms also leads to curved trajectories of the swarms.

Obstacles

In theory [106, 246] and experiments [174] with *E. coli* bacteria, it has been shown that the emerging active turbulence can be stabilized in regular patterns through the placement of obstacles in the domain of the microswimmers. It would be interesting to simulate our microscopic squirmer-rod model interacting with such pillars, since in the experiments microswimmers close to the pillars are not accessible for the microscopic imaging technique. [106].

In this context we performed preliminary research which, however, predates our latest articles including the investigation of active turbulence [185] and the more incompressible MPCD method [205, 206]. It would therefore be interesting to revisit this topic and explore pillars with structured surfaces, which prohibit the sliding motion of the microswimmers around the pillars. In our preliminary simulations, we immersed cylindrical pillars in the flow, which are realized with the WCA potential and no-slip boundary condition for the fluid. We show two exemplary simulations of pusher-type squirmer rods within the unit cell of a quadratic lattice in Fig. 5.2. Since active turbulence exhibits a characteristic length scale, the emergent dynamics is expected to couple to a specific lattice size [174], which is given by the different system sizes in Fig. 5.2(a) and (b).

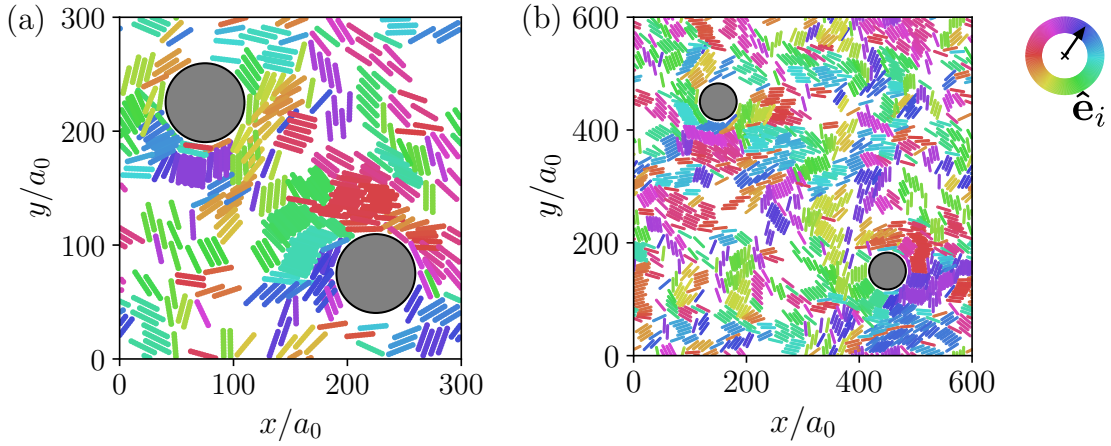

Figure 5.2: Snapshots of two simulations of pusher-type squirmer rods in the unit cell of a periodic square lattice with a pillar radius of $R_{\text{pillar}} = 1.25 l_S$ at different system sizes. (a) Small system size $L = 300 a_0$ and (b) large system size $L = 600 a_0$. The system height is $\Delta z = 18 a_0$ in both cases.

Bibliography

[1] F. Partensky, W. R. Hess, and D. Vaulot, "Prochlorococcus, a marine photosynthetic prokaryote of global significance", Microbiol. Mol. Biol. Rev. **63**, 106–127 (1999).

[2] P. G. Falkowski, "The role of phytoplankton photosynthesis in global biogeochemical cycles", Phys. Rev. **39**, 235–258 (1994).

[3] C. B. Field, M. J. Behrenfeld, J. T. Randerson, and P. Falkowski, "Primary production of the biosphere: integrating terrestrial and oceanic components", Science **281**, 237–240 (1998).

[4] P. B. Eckburg, E. M. Bik, C. N. Bernstein, E. Purdom, L. Dethlefsen, M. Sargent, S. R. Gill, K. E. Nelson, and D. A. Relman, "Diversity of the human intestinal microbial flora", Science **308**, 1635–1638 (2005).

[5] O. Tenaillon, D. Skurnik, B. Picard, and E. Denamur, "The population genetics of commensal escherichia coli", Nat. Rev. Microbiol. **8**, 207–217 (2010).

[6] J. L. Round and S. K. Mazmanian, "The gut microbiota shapes intestinal immune responses during health and disease", Nat. Rev. Immun. **9**, 313–323 (2009).

[7] I. Sekirov, S. L. Russell, L. C. M. Antunes, and B. B. Finlay, "Gut microbiota in health and disease", Physiol. Rev. (2010).

[8] A. L. Kau, P. P. Ahern, N. W. Griffin, A. L. Goodman, and J. I. Gordon, "Human nutrition, the gut microbiome and the immune system", Nature **474**, 327–336 (2011).

[9] J. G. LeBlanc, C. Milani, G. S. De Giori, F. Sesma, D. Van Sinderen, and M. Ventura, "Bacteria as vitamin suppliers to their host: a gut microbiota perspective", Current opinion in biotechnology **24**, 160–168 (2013).

[10] S. N. Naik, V. V. Goud, P. K. Rout, and A. K. Dalai, "Production of first and second generation biofuels: a comprehensive review", Renew. Sust. Ener. Rev. **14**, 578–597 (2010).

[11] D. M. Alonso, J. Q. Bond, and J. A. Dumesic, "Catalytic conversion of biomass to biofuels", Green Chemistry **12**, 1493–1513 (2010).

[12] H.-J. Huang, S. Ramaswamy, U. Tschirner, and B. Ramarao, "A review of separation technologies in current and future biorefineries", Separ. Purif. Technol. **62**, 1–21 (2008).

[13] P. Lorenz and J. Eck, "Metagenomics and industrial applications", Nat. Rev. Microbiol. **3**, 510–516 (2005).

[14] M. Schallmey, A. Singh, and O. P. Ward, "Developments in the use of bacillus species for industrial production", Canad. J. Microbiol. **50**, 1–17 (2004).

[15] A. L. Demain, "Microbial biotechnology", Trends Biotechnol. **18**, 26–31 (2000).

[16] I. M. Banat, A. Franzetti, I. Gandolfi, G. Bestetti, M. G. Martinotti, L. Fracchia, T. J. Smyth, and R. Marchant, "Microbial biosurfactants production, applications and future potential", Appl. Microbiol. Biotechnol. **87**, 427–444 (2010).

[17] J. Shafi, H. Tian, and M. Ji, "Bacillus species as versatile weapons for plant pathogens: a review", Biotechnol. & Biotechnol. Equip. **31**, 446–459 (2017).

[18] D. Fira, I. Dimkić, T. Berić, J. Lozo, and S. Stanković, "Biological control of plant pathogens by bacillus species", J. Biotechnol. **285**, 44–55 (2018).

[19] N. Ferrer-Miralles, J. Domingo-Espín, J. L. Corchero, E. Vázquez, and A. Villaverde, "Microbial factories for recombinant pharmaceuticals", Microbiol. Cell Fact. **8**, 1–8 (2009).

[20] N. A. Baeshen, M. N. Baeshen, A. Sheikh, R. S. Bora, M. M. M. Ahmed, H. A. Ramadan, K. S. Saini, and E. M. Redwan, "Cell factories for insulin production", Microbiol. Cell Fact. **13**, 1–9 (2014).

[21] J.-H. Martens, H. Barg, M Warren, and D. Jahn, "Microbial production of vitamin b12", Appl. Microbiol. Biotechnol. **58**, 275–285 (2002).

[22] M. Wagner, A. Loy, R. Nogueira, U. Purkhold, N. Lee, and H. Daims, "Microbial community composition and function in wastewater treatment plants", Antonie Van Leeuwenhoek **81**, 665–680 (2002).

[23] I. Schmidt, O. Sliekers, M. Schmid, E. Bock, J. Fuerst, J. G. Kuenen, M. S. Jetten, and M. Strous, "New concepts of microbial treatment processes for the nitrogen removal in wastewater", FEMS Microbiol. Rev. **27**, 481–492 (2003).

[24] M. C. Marchetti, J.-F. Joanny, S. Ramaswamy, T. B. Liverpool, J. Prost, M. Rao, and R. A. Simha, "Hydrodynamics of soft active matter", Rev. Mod. Phys. **85**, 1143 (2013).

[25] C. Bechinger, R. Di Leonardo, H. Löwen, C. Reichhardt, G. Volpe, and G. Volpe, "Active particles in complex and crowded environments", Rev. Mod. Phys. **88**, 045006 (2016).

[26] A. Zöttl and H. Stark, "Emergent behavior in active colloids", J. Phys.: Condens. Matter **28**, 253001 (2016).

[27] J. O'Byrne, Y. Kafri, J. Tailleur, and F. van Wijland, "Time irreversibility in active matter, from micro to macro", Nat. Rev. Phys., 1–17 (2022).

[28] H. C. Berg, "The rotary motor of bacterial flagella", Annu. Rev. Biochem. **72**, 19–54 (2003).

[29] R. Stocker, "Reverse and flick: hybrid locomotion in bacteria", Proc. Natl. Acad. Sci. **108**, 2635–2636 (2011).

[30] H. C. Berg, "Chemotaxis in bacteria", Annu. Rev. Biophys. Bioeng. **4**, 119–136 (1975).

[31] J. Adler, "Chemotaxis in bacteria", Annu. Rev. Biochem. **44**, 341–356 (1975).

[32] O. Pohl, M. Hintsche, Z. Alirezaeizanjani, M. Seyrich, C. Beta, and H. Stark, "Inferring the chemotactic strategy of p. putida and e. coli using modified kramers-moyal coefficients", PLoS Comp. Biol. **13**, e1005329 (2017).

[33] J. Stürmer, M. Seyrich, and H. Stark, "Chemotaxis in a binary mixture of active and passive particles", J. Chem. Phys. **150**, 214901 (2019).

[34] M. Seyrich, A. Palugniok, and H. Stark, "Traveling concentration pulses of bacteria in a generalized keller–segel model", New J. Phys. **21**, 103001 (2019).

[35] V. Kantsler, J. Dunkel, M. Blayney, and R. E. Goldstein, "Rheotaxis facilitates upstream navigation of mammalian sperm cells", eLIVE **3**, e02403 (2014).

[36] P. Denissenko, V. Kantsler, D. J. Smith, and J. Kirkman-Brown, "Human spermatozoa migration in microchannels reveals boundary-following navigation", Proc. Natl. Acad. Sci. **109**, 8007–8010 (2012).

[37] A. Zöttl and H. Stark, "Emergent behavior in active colloids", J. Phys.: Condens. Matter **28**, 253001 (2016).

[38] J. Elgeti, R. G. Winkler, and G. Gompper, "Physics of microswimmers—single particle motion and collective behavior: a review", Rep. Prog. Phys. **78**, 056601 (2015).

[39] S. Thutupalli, R. Seemann, and S. Herminghaus, "Swarming behavior of simple model squirmers", New J. Phys. **13**, 073021 (2011).

[40] J Gachelin, A Rousselet, A Lindner, and E Clement, "Collective motion in an active suspension of escherichia coli bacteria", New J. Phys. **16**, 025003 (2014).

[41] M. Theers, E. Westphal, K. Qi, R. G. Winkler, and G. Gompper, "Clustering of microswimmers: interplay of shape and hydrodynamics", Soft Matter **14**, 8590–8603 (2018).

[42] Ö. Duman, R. E. Isele-Holder, J. Elgeti, and G. Gompper, "Collective dynamics of self-propelled semiflexible filaments", Soft Matter **14**, 4483–4494 (2018).

[43] V. Schaller, C. Weber, C. Semmrich, E. Frey, and A. R. Bausch, "Polar patterns of driven filaments", Nature **467**, 73–77 (2010).

[44] H. Wioland, F. G. Woodhouse, J. Dunkel, J. O. Kessler, and R. E. Goldstein, "Confinement stabilizes a bacterial suspension into a spiral vortex", Phys. Rev. Lett. **110**, 268102 (2013).

[45] D. Khoromskaia and G. P. Alexander, "Vortex formation and dynamics of defects in active nematic shells", New J. Phys. **19**, 103043 (2017).

[46] Y. Sumino, K. H. Nagai, Y. Shitaka, D. Tanaka, K. Yoshikawa, H. Chaté, and K. Oiwa, "Large-scale vortex lattice emerging from collectively moving microtubules", Nature **483**, 448–452 (2012).

[47] F. Rühle and H. Stark, "Emergent collective dynamics of bottom-heavy squirmers under gravity", Eur. Phys. J. E. **43**, 1–17 (2020).

[48] M. Hennes, K. Wolff, and H. Stark, "Self-induced polar order of active brownian particles in a harmonic trap", Phys. Rev. Lett. **112**, 238104 (2014).

[49] M. J. Kim and K. S. Breuer, "Microfluidic pump powered by self-organizing bacteria", Small **4**, 111–118 (2008).

[50] T. Sanchez, D. T. Chen, S. J. DeCamp, M. Heymann, and Z. Dogic, "Spontaneous motion in hierarchically assembled active matter", Nature **491**, 431–434 (2012).

[51] S. J. DeCamp, G. S. Redner, A. Baskaran, M. F. Hagan, and Z. Dogic, "Orientational order of motile defects in active nematics", Nat. Mater. **14**, 1110–1115 (2015).

[52] F. C. Keber, E. Loiseau, T. Sanchez, S. J. DeCamp, L. Giomi, M. J. Bowick, M. C. Marchetti, Z. Dogic, and A. R. Bausch, "Topology and dynamics of active nematic vesicles", Science **345**, 1135–1139 (2014).

[53] H. H. Wensink, J. Dunkel, S. Heidenreich, K. Drescher, R. E. Goldstein, H. Löwen, and J. M. Yeomans, "Meso-scale turbulence in living fluids", Proc. Natl. Acad. Sci. **109**, 14308–14313 (2012).

[54] J. Dunkel, S. Heidenreich, K. Drescher, H. H. Wensink, M. Bär, and R. E. Goldstein, "Fluid dynamics of bacterial turbulence", Phys. Rev. Lett. **110**, 228102 (2013).

[55] P. Guillamat, J. Ignés-Mullol, and F. Sagués, "Taming active turbulence with patterned soft interfaces", Nat. Comm. **8**, 1–8 (2017).

[56] A. Doostmohammadi, T. N. Shendruk, K. Thijssen, and J. M. Yeomans, "Onset of meso-scale turbulence in active nematics", Nat. Comm. **8**, 1–7 (2017).

[57] D. Nishiguchi, I. S. Aranson, A. Snezhko, and A. Sokolov, "Engineering bacterial vortex lattice via direct laser lithography", Nat. Comm. **9**, 1–8 (2018).

[58] S. Heidenreich, J. Dunkel, S. H. Klapp, and M. Bär, "Hydrodynamic length-scale selection in microswimmer suspensions", Phys. Rev. E **94**, 020601 (2016).

[59] R. Alert, J.-F. Joanny, and J. Casademunt, "Universal scaling of active nematic turbulence", Nat. Phys. **16**, 682–688 (2020).

[60] B. Martínez-Prat, R. Alert, F. Meng, J. Ignés-Mullol, J.-F. Joanny, J. Casademunt, R. Golestanian, and F. Sagués, "Scaling regimes of active turbulence with external dissipation", Phys. Rev. X **11**, 031065 (2021).

[61] R. Alert, J. Casademunt, and J.-F. Joanny, "Active turbulence", Annu. Rev. Condens. Matter Phys. **13**, null (2022).

[62] V. Bratanov, F. Jenko, and E. Frey, "New class of turbulence in active fluids", Proc. Natl. Acad. Sci. **112**, 15048–15053 (2015).

[63] S.-Z. Lin, W.-Y. Zhang, D. Bi, B. Li, and X.-Q. Feng, "Energetics of mesoscale cell turbulence in two-dimensional monolayers", Comm. Phys. **4**, 1–9 (2021).

[64] A. Doostmohammadi, S. P. Thampi, T. B. Saw, C. T. Lim, B. Ladoux, and J. M. Yeomans, "Celebrating soft matter's 10th anniversary: cell division: a source of active stress in cellular monolayers", Soft Matter **11**, 7328–7336 (2015).

[65] E. Lauga and T. R. Powers, "The hydrodynamics of swimming microorganisms", Rep. Prog. Phys. **72**, 096601 (2009).

[66] E. Lauga, "Bacterial hydrodynamics", Annu. Rev. Fluid Mech. **48**, 105–130 (2016).

[67] K. Drescher, R. E. Goldstein, N. Michel, M. Polin, and I. Tuval, "Direct measurement of the flow field around swimming microorganisms", Phys. Rev. Lett. **105**, 168101 (2010).

[68] E. Lauga and R. E. Goldstein, "Dance of the microswimmers", Phys. Today **65**, 30 (2012).

[69] M. Lighthill, "On the squirming motion of nearly spherical deformable bodies through liquids at very small reynolds numbers", Commun. Pur. Appl. Math. **5**, 109–118 (1952).

[70] T. Ishikawa and M. Hota, "Interaction of two swimming paramecia", J. Exp. Biol. **209**, 4452–4463 (2006).

[71] D. Saintillan and M. J. Shelley, "Orientational order and instabilities in suspensions of self-locomoting rods", Phys. Rev. Lett. **99**, 058102 (2007).

[72] A. Baskaran and M. C. Marchetti, "Statistical mechanics and hydrodynamics of bacterial suspensions", Proc. Natl. Acad. Sci. **106**, 15567–15572 (2009).

[73] J. Blaschke, M. Maurer, K. Menon, A. Zöttl, and H. Stark, "Phase separation and coexistence of hydrodynamically interacting microswimmers", Soft Matter **12**, 9821–9831 (2016).

[74] A. Zöttl and H. Stark, "Simulating squirmers with multiparticle collision dynamics", Eur. Phys. J. E. **41**, 61 (2018).

[75] N. Yoshinaga and T. B. Liverpool, "Hydrodynamic interactions in dense active suspensions: from polar order to dynamical clusters", Phys. Rev. E **96**, 020603 (2017).

[76] J.-T. Kuhr, F. Rühle, and H. Stark, "Collective dynamics in a monolayer of squirmers confined to a boundary by gravity", Soft Matter **15**, 5685–5694 (2019).

[77] D. Nishiguchi and M. Sano, "Mesoscopic turbulence and local order in janus particles self-propelling under an ac electric field", Phys. Rev. E **92**, 052309 (2015).

[78] M. Schmitt and H. Stark, "Marangoni flow at droplet interfaces: three-dimensional solution and applications", Phys. Fluids **28**, 012106 (2016).

[79] C. C. Maass, C. Krüger, S. Herminghaus, and C. Bahr, "Swimming droplets", Annu. Rev. Condens. Matter Phys. **7**, 171–193 (2016).

[80] T. Vicsek, A. Czirók, E. Ben-Jacob, I. Cohen, and O. Shochet, "Novel type of phase transition in a system of self-driven particles", Phys. Rev. Lett. **75**, 1226 (1995).

[81] G. Grégoire and H. Chaté, "Onset of collective and cohesive motion", Phys. Rev. Lett. **92**, 025702 (2004).

[82] H. Chaté, F. Ginelli, G. Grégoire, F. Peruani, and F. Raynaud, "Modeling collective motion: variations on the vicsek model", Eur. Phys. J. B. **64**, 451–456 (2008).

[83] H. Wensink and H Löwen, "Emergent states in dense systems of active rods: from swarming to turbulence", J. Phys.: Condens. Matter **24**, 464130 (2012).

[84] R. Großmann, P. Romanczuk, M. Bär, and L. Schimansky-Geier, "Vortex arrays and mesoscale turbulence of self-propelled particles", Phys. Rev. Lett. **113**, 258104 (2014).

[85] F. Peruani, A. Deutsch, and M. Bär, "Nonequilibrium clustering of self-propelled rods", Phys. Rev. E **74**, 030904 (2006).

[86] Y. Yang, V. Marceau, and G. Gompper, "Swarm behavior of self-propelled rods and swimming flagella", Phys. Rev. E **82**, 031904 (2010).

[87] M. Abkenar, K. Marx, T. Auth, and G. Gompper, "Collective behavior of penetrable self-propelled rods in two dimensions", Phys. Rev. E **88**, 062314 (2013).

[88] S. Weitz, A. Deutsch, and F. Peruani, "Self-propelled rods exhibit a phase-separated state characterized by the presence of active stresses and the ejection of polar clusters", Phys. Rev. E **92**, 012322 (2015).

[89] M. Hennes, K. Wolff, and H. Stark, "Self-induced polar order of active brownian particles in a harmonic trap", Phys. Rev. Lett. **112**, 238104 (2014).

[90] H. Jeckel, E. Jelli, R. Hartmann, P. K. Singh, R. Mok, J. F. Totz, L. Vidakovic, B. Eckhardt, J. Dunkel, and K. Drescher, "Learning the space-time phase diagram of bacterial swarm expansion", Proc. Natl. Acad. Sci. **116**, 1489–1494 (2019).

[91] G. Rückner and R. Kapral, "Chemically powered nanodimers", Phys. Rev. Lett. **98**, 150603 (2007).

[92] I. O. Götze and G. Gompper, "Mesoscale simulations of hydrodynamic squirmer interactions", Phys. Rev. E **82**, 041921 (2010).

[93] P. de Buyl and R. Kapral, "Phoretic self-propulsion: a mesoscopic description of reaction dynamics that powers motion", Nanoscale **5**, 1337–1344 (2013).

[94] A. Zöttl and H. Stark, "Hydrodynamics determines collective motion and phase behavior of active colloids in quasi-two-dimensional confinement", Phys. Rev. Lett. **112**, 118101 (2014).

[95] T. Eisenstecken, J. Hu, and R. G. Winkler, "Bacterial swarmer cells in confinement: a mesoscale hydrodynamic simulation study", Soft Matter **12**, 8316–8326 (2016).

[96] M. Wagner and M. Ripoll, "Hydrodynamic front-like swarming of phoretically active dimeric colloids", Europhys. Lett. **119**, 66007 (2017).

[97] F. J. Schwarzendahl and M. G. Mazza, "Hydrodynamic interactions dominate the structure of active swimmers' pair distribution functions", J. Chem. Phys. **150**, 184902 (2019).

[98] J. de Graaf, H. Menke, A. J. Mathijssen, M. Fabritius, C. Holm, and T. N. Shendruk, "Lattice-boltzmann hydrodynamics of anisotropic active matter", J. Chem. Phys. **144**, 134106 (2016).

[99] A. Pandey, P. S. Kumar, and R Adhikari, "Flow-induced nonequilibrium self-assembly in suspensions of stiff, apolar, active filaments", Soft Matter **12**, 9068–9076 (2016).

[100] M. Kuron, P. Stärk, C. Burkard, J. De Graaf, and C. Holm, "A lattice boltzmann model for squirmers", J. Chem. Phys. **150**, 144110 (2019).

[101] Z. Ouyang and J. Lin, "The hydrodynamics of an inertial squirmer rod", Phys. Fluids **33**, 073302 (2021).

[102] S. Ramaswamy, "The mechanics and statistics of active matter", Annu. Rev. Condens. Matter Phys. **1**, 323–345 (2010).

[103] J. Dunkel, S. Heidenreich, M. Bär, and R. E. Goldstein, "Minimal continuum theories of structure formation in dense active fluids", New J. Phys. **15**, 045016 (2013).

[104] J. Toner and Y. Tu, "Long-range order in a two-dimensional dynamical xy model: how birds fly together", Phys. Rev. Lett. **75**, 4326 (1995).

[105] J. Swift and P. C. Hohenberg, "Hydrodynamic fluctuations at the convective instability", Phys. Rev. A **15**, 319 (1977).

[106] H. Reinken, D. Nishiguchi, S. Heidenreich, A. Sokolov, M. Bär, S. H. Klapp, and I. S. Aranson, "Organizing bacterial vortex lattices by periodic obstacle arrays", Comm. Phys. **3**, 1–9 (2020).

[107] V. M. Worlitzer, G. Ariel, A. Be'er, H. Stark, M. Bär, and S. Heidenreich, "Motility-induced clustering and meso-scale turbulence in active polar fluids", New J. Phys. **23**, 033012 (2021).

[108] M. Bär, R. Großmann, S. Heidenreich, and F. Peruani, "Self-propelled rods: insights and perspectives for active matter", Annu. Rev. Condens. Matter Phys. **11**, 441–466 (2020).

[109] D. L. Koch and G. Subramanian, "Collective hydrodynamics of swimming microorganisms: living fluids", Annu. Rev. Fluid Mech. **43**, 637–659 (2011).

[110] M. C. Marchetti, J.-F. Joanny, S. Ramaswamy, T. B. Liverpool, J. Prost, M. Rao, and R. A. Simha, "Hydrodynamics of soft active matter", Rev. Mod. Phys. **85**, 1143 (2013).

[111] C. Hoell, H. Löwen, and A. M. Menzel, "Particle-scale statistical theory for hydrodynamically induced polar ordering in microswimmer suspensions", J. Chem. Phys. **149**, 144902 (2018).

[112] M. Bär, R. Großmann, S. Heidenreich, and F. Peruani, "Self-propelled rods: insights and perspectives for active matter", Annu. Rev. Condens. Matter Phys. **11**, 441–466 (2019).

[113] M. R. Shaebani, A. Wysocki, R. G. Winkler, G. Gompper, and H. Rieger, "Computational models for active matter", Nat. Rev. Phys. **2**, 181–199 (2020).

[114] J. R. Blake, "A spherical envelope approach to ciliary propulsion", J. Fluid Mech. **46**, 199–208 (1971).

[115] F. Sciortino, A. Giacometti, and G. Pastore, "Phase diagram of janus particles", Phys. Rev. Lett. **103**, 237801 (2009).

[116] S. Jiang, Q. Chen, M. Tripathy, E. Luijten, K. S. Schweizer, and S. Granick, "Janus particle synthesis and assembly", Adv. Matter **22**, 1060–1071 (2010).

[117] I. Buttinoni, J. Bialké, F. Kümmel, H. Löwen, C. Bechinger, and T. Speck, "Dynamical clustering and phase separation in suspensions of self-propelled colloidal particles", Phys. Rev. Lett. **110**, 238301 (2013).

[118] T. J. Pedley, D. R. Brumley, and R. E. Goldstein, "Squirmers with swirl: a model for volvox swimming", J. Fluid Mech. **798**, 165–186 (2016).

[119] T. Ishikawa, M. Simmonds, and T. J. Pedley, "Hydrodynamic interaction of two swimming model micro-organisms", J. Fluid Mech. **568**, 119–160 (2006).

[120] M. T. Downton and H. Stark, "Simulation of a model microswimmer", J. Phys.: Condens. Matter **21**, 204101 (2009).

[121] G.-J. Li and A. M. Ardekani, "Hydrodynamic interaction of microswimmers near a wall", Phys. Rev. E **90**, 013010 (2014).

[122] J.-T. Kuhr, J. Blaschke, F. Rühle, and H. Stark, Soft Matter **13**, 7458–7555 (2017).

[123] F. Rühle, J. Blaschke, J.-T. Kuhr, and H. Stark, New J. Phys. **20**, 025003 (2018).

[124] J.-T. Kuhr, F. Rühle, and H. Stark, "Collective dynamics in a monolayer of squirmers confined to a boundary by gravity", Soft Matter **15**, 5685–5694 (2019).

[125] A. W. Zantop and H. Stark, "Squirmer rods as elongated microswimmers: flow fields and confinement", Soft Matter **16**, 6400–6412 (2020).

[126] A. Malevanets and R. Kapral, "Mesoscopic model for solvent dynamics", J. Chem. Phys. **110**, 8605–8613 (1999).

[127] C.-C. Huang, G. Gompper, and R. G. Winkler, "Hydrodynamic correlations in multiparticle collision dynamics fluids", Phys. Rev. E **86**, 056711 (2012).

[128] A. Lamura, G. Gompper, T. Ihle, and D. Kroll, "Multi-particle collision dynamics: flow around a circular and a square cylinder", Europhys. Lett. **56**, 319 (2001).

[129] D. A. Reid, H Hildenbrandt, J. Padding, and C. Hemelrijk, "Flow around fishlike shapes studied using multiparticle collision dynamics", Phys. Rev. E **79**, 046313 (2009).

[130] S. B. Babu and H. Stark, "Dynamics of semi-flexible tethered sheets", Eur. Phys. J. E. **34**, 1–7 (2011).

[131] H. Noguchi and G. Gompper, "Vesicle dynamics in shear and capillary flows", J. Phys.: Condens. Matter **17**, S3439 (2005).

[132] E Westphal, S. P. Singh, C.-C. Huang, G. Gompper, and R. G. Winkler, "Multiparticle collision dynamics: gpu accelerated particle-based mesoscale hydrodynamic simulations", Comp. Phys. Comm. **185**, 495–503 (2014).

[133] M. P. Howard, A. Z. Panagiotopoulos, and A. Nikoubashman, "Efficient mesoscale hydrodynamics: multiparticle collision dynamics with massively parallel gpu acceleration", Comp. Phys. Comm. **230**, 10–20 (2018).

[134] P. Kanehl and H. Stark, "Self-organized velocity pulses of dense colloidal suspensions in microchannel flow", Phys. Rev. Lett. **119**, 018002 (2017).

[135] P. Kanehl and H. Stark, "Hydrodynamic segregation in a bidisperse colloidal suspension in microchannel flow: a theoretical study", J. Chem. Phys. **142**, 214901 (2015).

[136] J. Padding and A. Louis, "Hydrodynamic and brownian fluctuations in sedimenting suspensions", Phys. Rev. Lett. **93**, 220601 (2004).

[137] A Moncho-Jordá, A. Louis, and J. Padding, "Effects of interparticle attractions on colloidal sedimentation", Phys. Rev. Lett. **104**, 068301 (2010).

[138] M. Yang, A. Wysocki, and M. Ripoll, "Hydrodynamic simulations of self-phoretic microswimmers", Soft Matter **10**, 6208–6218 (2014).

[139] A Malevanets and J. Yeomans, "Dynamics of short polymer chains in solution", Europhys. Lett. **52**, 231 (2000).

[140] A. Zöttl and J. M. Yeomans, "Driven spheres, ellipsoids and rods in explicitly modeled polymer solutions", J. Phys.: Condens. Matter **31**, 234001 (2019).

[141] K. Qi, E. Westphal, G. Gompper, and R. G. Winkler, "Enhanced rotational motion of spherical squirmer in polymer solutions", Phys. Rev. Lett. **124**, 068001 (2020).

[142] H. Noguchi and G. Gompper, "Shape transitions of fluid vesicles and red blood cells in capillary flows", Proc. Natl. Acad. Sci. **102**, 14159–14164 (2005).

[143] D. Alizadehrad, T. Krüger, M. Engstler, and H. Stark, "Simulating the complex cell design of trypanosoma brucei and its motility", PLoS Comp. Biol. **11**, e1003967 (2015).

[144] C. Hemelrijk, D. Reid, H Hildenbrandt, and J. Padding, "The increased efficiency of fish swimming in a school", Fish and Fisheries **16**, 511–521 (2015).

[145] T. Eisenstecken, R. Hornung, R. G. Winkler, and G. Gompper, "Hydrodynamics of binary-fluid mixtures—an augmented multiparticle collison dynamics approach", Europhys. Lett. **121**, 24003 (2018).

[146] K.-W. Lee and M. G. Mazza, "Stochastic rotation dynamics for nematic liquid crystals", J. Chem. Phys. **142**, 164110 (2015).

[147] T. N. Shendruk and J. M. Yeomans, "Multi-particle collision dynamics algorithm for nematic fluids", Soft Matter **11**, 5101–5110 (2015).

[148] S. Mandal and M. G. Mazza, "Multiparticle collision dynamics for tensorial nematodynamics", Phys. Rev. E **99**, 063319 (2019).

[149] K. Rohlf, S. Fraser, and R. Kapral, "Reactive multiparticle collision dynamics", Comp. Phys. Comm. **179**, 132–139 (2008).

[150] F. Peruani, "Active brownian rods", Eur. Phys. J.-Spec. Top. **225**, 2301–2317 (2016).

[151] A. Agrawal, H. M. Kushwaha, and R. S. Jadhav, *Microscale flow and heat transfer*, 2020.

[152] M. Kardar, *Statistical physics of fields*, 2007.

[153] J. Irving and J. G. Kirkwood, "The statistical mechanical theory of transport processes. iv. the equations of hydrodynamics", J. Chem. Phys. **18**, 817–829 (1950).

[154] L. G. Leal, *Advanced transport phenomena: fluid mechanics and convective transport processes*, 2007.

[155] G. Batchelor, *An introduction to fluid dynamics*, 2000.

[156] L. D. Landau and E. M. Lifshitz, *Fluid mechanics*, 1989.

[157] J. Happel and H. Brenner, *Low reynolds number hydrodynamics*, 1983.

[158] S. Kim and S. J. Karrila, *Microhydrodynamics: principles and selected applications*, 2005.

[159] C. Pozrikidis et al., *Boundary integral and singularity methods for linearized viscous flow*, 1992.

[160] D. J. Acheson, *Elementary fluid dynamics (corr.)* Oxford, 2005.

[161] J. K. Dhont, *An introduction to dynamics of colloids*, 1996.

[162] S. E. Spagnolie and E. Lauga, "Hydrodynamics of self-propulsion near a boundary: predictions and accuracy of far-field approximations", J. Fluid Mech. **700**, 105–147 (2012).

[163] J. de Graaf, H. Menke, A. J. Mathijssen, M. Fabritius, C. Holm, and T. N. Shendruk, "Lattice-boltzmann hydrodynamics of anisotropic active matter", J. Chem. Phys. **144**, 134106 (2016).

[164] E. Lauga, "Life around the scallop theorem", Soft Matter **7**, 3060–3065 (2011).

[165] E. M. Purcell, "Life at low reynolds number", Am. J. Phys. **45**, 3–11 (1977).

[166] J. V. Houten, "Paramecium biology", Evo-Devo: Non-model Species in Cell and Developmental Biology, 291–318 (2019).

[167] M. Polin, I. Tuval, K. Drescher, J. P. Gollub, and R. E. Goldstein, "Chlamydomonas swims with two "gears" in a eukaryotic version of run-and-tumble locomotion", Science **325**, 487–490 (2009).

[168] U. Rüffer and W. Nultsch, "High-speed cinematographic analysis of the movement of chlamydomonas", Cell motility **5**, 251–263 (1985).

[169] A. Oberbeck, "Ueber stationäre flüssigkeitsbewegungen mit berücksichtigung der inneren reibung.", J. Reine. Angew. Math. **81**, 62–80 (1876).

[170] D Edwardes, "Steady motion of a viscous liquid in which an ellipsoid is constrained to rotate about a principal axis", Quart. J. Math **26**, 68 (1892).

[171] G. B. Jeffery, "The motion of ellipsoidal particles immersed in a viscous fluid", Proc. R. Soc. Lond. A Math. **102**, 161–179 (1922).

[172] F. Rühle, J. Blaschke, J.-T. Kuhr, and H. Stark, "Gravity-induced dynamics of a squirmer microswimmer in wall proximity", New J. Phys. **20**, 025003 (2018).

[173] A. P. Berke, L. Turner, H. C. Berg, and E. Lauga, "Hydrodynamic attraction of swimming microorganisms by surfaces", Phys. Rev. Lett. **101**, 038102 (2008).

[174] D. Nishiguchi, I. S. Aranson, A. Snezhko, and A. Sokolov, "Engineering bacterial vortex lattice via direct laser lithography", Nat. Comm. **9**, 1–8 (2018).

[175] J. Blake, "A note on the image system for a stokeslet in a no-slip boundary", Math. Proc. Camb. Phil. Soc. **70**, 303–310 (1971).

[176] A. J. Mathijssen, A. Doostmohammadi, J. M. Yeomans, and T. N. Shendruk, "Hydrodynamics of micro-swimmers in films", J. Fluid Mech. **806**, 35–70 (2016).

[177] N. Liron and S Mochon, "Stokes flow for a stokeslet between two parallel flat plates", J. Eng. Mech. **10**, 287–303 (1976).

[178] J. Blake and A. Chwang, "Fundamental singularities of viscous flow", J. Eng. Mech. **8**, 23–29 (1974).

[179] T. Brotto, J.-B. Caussin, E. Lauga, and D. Bartolo, "Hydrodynamics of confined active fluids", Phys. Rev. Lett. **110**, 038101 (2013).

[180] H. Faxén, "Der widerstand gegen die bewegung einer starren kugel in einer zähen flüssigkeit, die zwischen zwei parallelen ebenen wänden eingeschlossen ist", Ann. Phys. (Berlin) **373**, 89–119 (1922).

[181] A. Zöttl and H. Stark, "Periodic and quasiperiodic motion of an elongated microswimmer in poiseuille flow", Eur. Phys. J. E. **36**, 1–10 (2013).

[182] T. Bickel, A. Majee, and A. Würger, "Flow pattern in the vicinity of self-propelling hot janus particles", Phys. Rev. E **88**, 012301 (2013).

[183] M. Kuron, P. Stärk, C. Burkard, J. De Graaf, and C. Holm, "A lattice boltzmann model for squirmers", J. Chem. Phys. **150**, 144110 (2019).

[184] K Kyoya, D Matsunaga, Y Imai, T Omori, and T Ishikawa, "Shape matters: near-field fluid mechanics dominate the collective motions of ellipsoidal squirmers", Phys. Rev. E **92**, 063027 (2015).

[185] A. W. Zantop and H. Stark, "Emergent collective dynamics of pusher and puller squirmer rods: swarming, clustering and turbulence", Soft Matter (2022).

[186] M. Theers, E. Westphal, G. Gompper, and R. G. Winkler, "Modeling a spheroidal microswimmer and cooperative swimming in a narrow slit", Soft Matter **12**, 7372–7385 (2016).

[187] L. J. Jones, R. Carballido-López, and J. Errington, "Control of cell shape in bacteria: helical, actin-like filaments in bacillus subtilis", Cell **104**, 913–922 (2001).

[188] K. C. Huang, R. Mukhopadhyay, B. Wen, Z. Gitai, and N. S. Wingreen, "Cell shape and cell-wall organization in gram-negative bacteria", Proc. Natl. Acad. Sci. **105**, 19282–19287 (2008).

[189] A. Einstein, "Zur theorie der brownschen bewegung", Ann. Phys. (Berlin) **324**, 371–381 (1906).

[190] M. M. Tirado, C. L. Martínez, and J. G. de la Torre, "Comparison of theories for the translational and rotational diffusion coefficients of rod-like macromolecules. application to short dna fragments", J. Chem. Phys. **81**, 2047–2052 (1984).

[191] B. ten Hagen, S. van Teeffelen, and H. Löwen, "Brownian motion of a self-propelled particle", J. Phys.: Condens. Matter **23**, 194119 (2011).

[192] Z Dogic, A. Philipse, S Fraden, and J. Dhont, "Concentration-dependent sedimentation of colloidal rods", J. Chem. Phys. **113**, 8368–8380 (2000).

[193] P. Wesseling, 2009.

[194] H. Noguchi, N. Kikuchi, and G. Gompper, "Particle-based mesoscale hydrodynamic techniques", Europhys. Lett. **78**, 10005 (2007).

[195] H. Noguchi and G. Gompper, "Transport coefficients of dissipative particle dynamics with finite time step", Europhys. Lett. **79**, 36002 (2007).

[196] J. J. Monaghan, "Smoothed particle hydrodynamics", Annual review of astronomy and astrophysics **30**, 543–574 (1992).

[197] S. Chen and G. D. Doolen, "Lattice boltzmann method for fluid flows", Annu. Rev. Fluid Mech. **30**, 329–364 (1998).

[198] K. Müller, D. A. Fedosov, and G. Gompper, "Smoothed dissipative particle dynamics with angular momentum conservation", J. Comp. Phys. **281**, 301–315 (2015).

[199] C. K. Aidun and J. R. Clausen, "Lattice-boltzmann method for complex flows", Annu. Rev. Fluid Mech. **42**, 439–472 (2010).

[200] R. Kapral, "Multiparticle collision dynamics: simulation of complex systems on mesoscales", Adv. Chem. Phys. **140**, 89 (2008).

[201] G Gompper, T Ihle, D. Kroll, and R. Winkler, *Multi-particle collision dynamics: a particle-based mesoscale simulation approach to the hydrodynamics of complex fluids*, 2009.

[202] A. Zöttl and J. M. Yeomans, "Enhanced bacterial swimming speeds in macromolecular polymer solutions", Nat. Phys. **15**, 554–558 (2019).

[203] F. J. Schwarzendahl and M. G. Mazza, "Maximum in density heterogeneities of active swimmers", Soft Matter **14**, 4666–4678 (2018).

[204] E Allahyarov and G Gompper, "Mesoscopic solvent simulations: multiparticle-collision dynamics of three-dimensional flows", Phys. Rev. E **66**, 036702 (2002).

[205] A. W. Zantop and H. Stark, "Multi-particle collision dynamics with a non-ideal equation of state. i", J. Chem. Phys. **154**, 024105 (2021).

[206] A. W. Zantop and H. Stark, "Multi-particle collision dynamics with a non-ideal equation of state. ii. collective dynamics of elongated squirmer rods", J. Chem. Phys. **155**, 134904 (2021).

[207] N Kikuchi, C. Pooley, J. Ryder, and J. Yeomans, "Transport coefficients of a mesoscopic fluid dynamics model", J. Chem. Phys. **119**, 6388–6395 (2003).

[208] T Ihle and D. Kroll, "Stochastic rotation dynamics: a galilean-invariant mesoscopic model for fluid flow", Phys. Rev. E **63**, 020201 (2001).

[209] I. O. Götze, H. Noguchi, and G. Gompper, "Relevance of angular momentum conservation in mesoscale hydrodynamics simulations", Phys. Rev. E **76**, 046705 (2007).

[210] J. F. Ryder, "Mesoscopic simulations of complex fluids", PhD thesis (University of Oxford, 2005).

[211] C.-C. Huang, A Chatterji, G. Sutmann, G. Gompper, and R. G. Winkler, "Cell-level canonical sampling by velocity scaling for multiparticle collision dynamics simulations", J. Comp. Phys. **229**, 168–177 (2010).

[212] H. Noguchi and G. Gompper, "Transport coefficients of off-lattice mesoscale-hydrodynamics simulation techniques", Phys. Rev. E **78**, 016706 (2008).

[213] T. Ihle, E Tüzel, and D. M. Kroll, "Consistent particle-based algorithm with a non-ideal equation of state", Europhys. Lett. **73**, 664 (2006).

[214] M. Yang, M. Theers, J. Hu, G. Gompper, R. G. Winkler, and M. Ripoll, "Effect of angular momentum conservation on hydrodynamic simulations of colloids", Phys. Rev. E **92**, 013301 (2015).

[215] C. Pooley and J. Yeomans, "Kinetic theory derivation of the transport coefficients of stochastic rotation dynamics", J. Phys. Chem. B **109**, 6505–6513 (2005).

[216] J.-P. Hansen and I. R. McDonald, *Theory of simple liquids*, 1990.

[217] J. D. Weeks, D. Chandler, and H. C. Andersen, "Role of repulsive forces in determining the equilibrium structure of simple liquids", J. Chem. Phys. **54**, 5237–5247 (1971).

[218] M. P. Allen and D. J. Tildesley, *Computer simulation of liquids*, Oxford, 2017.

[219] A. Dullweber, B. Leimkuhler, and R. McLachlan, "Symplectic splitting methods for rigid body molecular dynamics", J. Chem. Phys. **107**, 5840–5851 (1997).

[220] J. Padding, A Wysocki, H Löwen, and A. Louis, "Stick boundary conditions and rotational velocity auto-correlation functions for colloidal particles in a coarse-grained representation of the solvent", J. Phys.: Condens. Matter **17**, S3393 (2005).

[221] M. Resch, T. Bönisch, K. Benkert, T. Furui, Y. Seo, and W. Bez, *High performance computing on vector systems*, Heidlberg, 2006.

[222] T. Rauber and G. Rünger, *Parallel programming*, Heidlberg, 2013.

[223] D. A. Yuen, L. Wang, X. Chi, L. Johnsson, W. Ge, and Y. Shi, *Gpu solutions to multi-scale problems in science and engineering*, Heidlberg, 2013.

[224] T. H. Cormen, C. E. Leiserson, R. L. Rivest, and C. Stein, *Introduction to algorithms*, 2022.

[225] R. E. Ladner and M. J. Fischer, "Parallel prefix computation", J. ACM **27**, 831–838 (1980).

[226] K. D. Young, "The selective value of bacterial shape", Microbiol. Mol. Biol. Rev. **70**, 660–703 (2006).

[227] W. Margolin, "Sculpting the bacterial cell", Current Biology **19**, R812–R822 (2009).

[228] R. Vogel and H. Stark, "Rotation-induced polymorphic transitions in bacterial flagella", Phys. Rev. Lett. **110**, 158104 (2013).

[229] T. C. Adhyapak and H. Stark, "Zipping and entanglement in flagellar bundle of e. coli: role of motile cell body", Phys. Rev. E **92**, 052701 (2015).

[230] E Tüzel, M. Strauss, T. Ihle, and D. M. Kroll, "Transport coefficients for stochastic rotation dynamics in three dimensions", Phys. Rev. E **68**, 036701 (2003).

[231] E. Tüzel, T. Ihle, and D. M. Kroll, "Constructing thermodynamically consistent models with a non-ideal equation of state", Math. Comp. Sim. **72**, 232–236 (2006).

[232] T. Ihle, E Tüzel, and D. M. Kroll, "Consistent particle-based algorithm with a non-ideal equation of state", Europhys. Lett. **73**, 664 (2006).

[233] S. K. Upadhyay, *Chemical kinetics and reaction dynamics*, 2007.

[234] E. Lauga and T. M. Squires, "Brownian motion near a partial-slip boundary: a local probe of the no-slip condition", Phys. Fluids **17**, 103102 (2005).

[235] F. Fadda, J. J. Molina, and R. Yamamoto, "Dynamics of a chiral swimmer sedimenting on a flat plate", Phys. Rev. E **101**, 052608 (2020).

[236] H. Shi, B. P. Bratton, Z. Gitai, and K. C. Huang, "How to build a bacterial cell: mreb as the foreman of e. coli construction", Cell **172**, 1294–1305 (2018).

[237] Y. I. Yaman, E. Demir, R. Vetter, and A. Kocabas, "Emergence of active nematics in chaining bacterial biofilms", Nature communications **10**, 1–9 (2019).

[238] D. A. Gagnon and P. E. Arratia, "The cost of swimming in generalized newtonian fluids: experiments with c. elegans", Journal of Fluid Mechanics **800**, 753–765 (2016).

[239] H. Jiang and Z. Hou, "Motion transition of active filaments: rotation without hydrodynamic interactions", Soft Matter **10**, 1012–1017 (2014).

[240] A. Martín-Gómez, T. Eisenstecken, G. Gompper, and R. G. Winkler, "Active brownian filaments with hydrodynamic interactions: conformations and dynamics", Soft matter **15**, 3957–3969 (2019).

[241] R. G. Winkler, J. Elgeti, and G. Gompper, "Active polymers—emergent conformational and dynamical properties: a brief review", J. Phys. Soc. Jpn. **86**, 101014 (2017).

[242] J. L. Münch, D. Alizadehrad, S. B. Babu, and H. Stark, "Taylor line swimming in microchannels and cubic lattices of obstacles", Soft Matter **12**, 7350–7363 (2016).

[243] B. Hess, "P-lincs: a parallel linear constraint solver for molecular simulation", J. Chem. Theory Comput. **4**, 116–122 (2008).

[244] B. Hess, H. Bekker, H. J. Berendsen, and J. G. Fraaije, "Lincs: a linear constraint solver for molecular simulations", J. Comp. Comm. **18**, 1463–1472 (1997).

[245] M. J. Abraham, T. Murtola, R. Schulz, S. Páll, J. C. Smith, B. Hess, and E. Lindahl, "Gromacs: high performance molecular simulations through multi-level parallelism from laptops to supercomputers", SoftwareX **1**, 19–25 (2015).

[246] H. Reinken, S. Heidenreich, M. Bär, and S. H. Klapp, "Ising-like critical behavior of vortex lattices in an active fluid", Phys. Rev. Lett. **128**, 048004 (2022).

Danksagung

Zuallererst möchte ich mich bei Prof. Holger Stark für die durchgängige Unterstützung und Motivation über viele Jahre hinweg bedanken. Er war stets offen für Ratschläge, Anregungen und Diskussionen und hat mir ermöglicht an vielen Tagungen und Fortbildungen teilzunehmen. Ebenso möchte ich mich bei Prof. Roland Netz von der Freien Universität Berlin für die Beguachtung meiner Arbeit und der Teilnahme an der wissenschaftlichen Aussprache bedanken, sowie bei Prof. Dieter Breitschwerdt, den Vorsitzenden des Promotionsausschusses.

Außerdem bedanke ich mich bei der Deutschen Forgschungsgemeinschaft (DFG), welche mich im Rahmen des SFB 910 finanziell unterstützt hat.

Weiter gilt mein Dank auch allen derzeitigen und ehemaligen Mitgliedern der Arbeitsgruppe, wobei ich auch die gemeinsamen Mittagessen in der Mensa, Barabende oder Klettersessions hervorheben möchte. Für die angenehme Zusammenarbeit und interessanten sowie hilfreichen Diskussionen bedanke ich mich insbesondere bei meinen Büronachbarn Josua Grawitter sowie Reinier van Buel, Maximilian Seyrich und Christian Schaaf, ebenso wie für das Korrekturlesen bei Felix Rühle.

Zu guter Letzt möchte ich mich auch bei meine Familie bedanken, insbesondere meiner Partnerin Alice Faust, die mich wärend dieser Zeit sehr viel unterstützt und motiviert hat und stets ein offenes Ohr für mich hatte.